PERSONALIA

Igor' Orestovich Kulik (on his 70th birthday)

Fiz. Nizk. Temp. **31**, 1317 (November 2005)

[DOI: 10.1063/1.2127894]

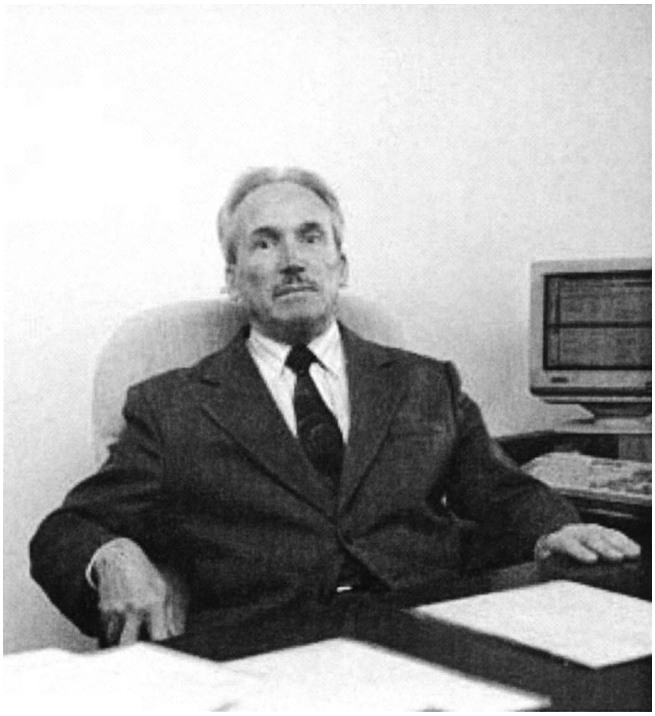

The prominent theoretical physicist, Corresponding Member of the National Academy of Sciences of Ukraine, and Laureate of the State Prize of Ukraine I.O. Kulik celebrated his 70th birthday on November 19, 2005. I. O. Kulik obtained basic scientific results in several areas of modern solid-state physics: the theory of superconductivity, the physics of mesoscopic systems, and spectroscopy.

I. O. Kulik became widely known and won worldwide acclaim, specifically, for his results in the theory of the electrodynamic properties of Josephson tunnel junctions, for the prediction of vortices of a special type ("Kulik vortices") in an inclined magnetic field, and for the theory of coherent current states in weak superconducting junctions with direct conduction. I. O. Kulik developed the basic concepts of mesoscopic physics: flux quantization and persistent currents in nonsuperconducting structures, charge-discreteness effects and Coulomb blockade in small metallic systems. I. O. Kulik constructed, together with his colleagues, the theory of point-contact spectroscopy of elementary excitations in solids (Discovery No. 328, registered by the Committee on Discoveries of the USSR).

I. O. Kulik's scientific work is reflected in many articles, reviews, talks, and monographs. As a brilliant spokesman for the Kharkov school of theoretical physics I. O. Kulik trained a pleiad of theoretical physicists, many of whom have become leaders of new scientific directions. Igor' Orestovich's many students are grateful to their teacher for the happiness and priceless benefits which they gained from their contact with him.

Dear Igor' Orestovich, we heartily congratulate you on your birthday and wish you good health, success, and many years of fruitful scientific work.

Editorial Board

Translated by M. E. Alferieff

Low-temperature phonon transport in 3*D* point-contacts (Review)

A. Feher

P. J. Safaric University, Park Angelinum 9, Kosice, Slovakia

A. A. Mamaluĭ and A. Ya. Dul'fan

National Technical University "Kharkov Polytechnical Institute," ul. Frunze 21, Kharkov 61002, Ukraine

E. S. Syrkin[a)] and A. G. Shkorbatov

B. I. Verkin Institute for Low Temperature Physics and Engineering of the National Academy of Sciences of Ukraine, pr. Lenina 47, Kharkov 61103, Ukraine

(Submitted December 24, 2004; resubmitted June 13, 2005)
Fiz. Nizk. Temp. **31**, 1211–1244 (November 2005)

This review is devoted to describing nonequilibrium carrier systems and relaxational and kinetic phenomena in three-dimensional point-contacts. Attention is focused on describing a phonon system which becomes substantially modified under conditions of ballistic transport. In such systems the energy fluxes are limited by the presence of weakly coupled layers of impurity atoms, planar defects, or microscopic-size contacts. The small size of point-contacts, ranging from several to 1000 nm, makes it possible to investigate low-temperature heat and charge transfer on scales less than the characteristic inelastic scattering lengths. A mechanism of phonon transport in the presence of an interface is analyzed, and various models of a planar defect are examined. The special features of interfacial phonon transport, where the transport coefficients are determined not by scattering processes in the volume of a bulk crystal but rather by the properties of the intercrystalline boundary, are studied. The quantum phonon thermal conductivity of point-contacts is studied in detail. © *2005 American Institute of Physics*. [DOI: 10.1063/1.2127874]

INTRODUCTION

The drive to miniaturize the components of electronic devices, sensors, and micromechanical systems has resulted in the development of different variants of nanotechnologies. These technologies make it possible to develop, on mesoscopic or atomic levels, composite materials and objects which include intercrystalline boundaries and regions of strong anisotropy or low dimension. As a rule, wave propagation in such systems is of interest. It is found that transport processes and kinetic effects are strongly modified, especially at low temperatures, compared with their manifestations in macroscopic uniform solid-state samples. The point is that at low temperatures (tens of degrees Kelvin and lower) the characteristic inelastic scattering lengths of heat and charge carriers start to exceed the dimensions of the components of nanostructures. Different variants of ballistic transport in nanostructures are realized.

In the present review, mainly crystalline nanosystems in the form of three-dimensional dielectric or conducting microbridges connecting bulk crystals are studied. Such systems are often said to be point-or microcontacts. These structures, as a rule, include interfaces or monomolecular impurity layers, which are described by the "planar defect" model. The small dimensions of point-contacts, ranging from several to 1000 nm, make it possible to investigate low-temperature heat and charge transport on scales less than the characteristic inelastic scattering lengths.

Point-contacts, realized as microscopic regions of short circuiting between bulk conductors, were introduced into scientific practice in Ref. 1. The investigation of weak inelastic scattering in the zone of a current-conducting point-contact has led to the development of a method of point-contact spectroscopy of the electron-phonon interaction.[2–6] The ballistic electronic thermal conductivity of a metallic point-contact was first measured in Ref. 7. The ballistic transport of phonons in point-contacts was first investigated experimentally in Refs. 8–10. The theoretical prediction of these effects is contained in Refs. 11–14.

Point-contacts have turned out to be unique physical devices, which can be used to study transport phenomena in strongly nonequilibrium electronic and phonon systems. In point-contacts the electrochemical potential or temperature drops over distances of the order of the diameter d of the contact. Any attempt to realize similar nonequilibrium conditions in macroscopic samples would in most cases destroy the experimental samples. Point-contacts make it possible to study the qualitative modification of the main kinetic phenomena as compared with similar processes in bulk conductors and dielectrics.

The present review is devoted to describing nonequilibrium carrier systems and relaxational and kinetic phenomena in nanostructures. Attention is focused on describing a phonon system which is strongly modified under conditions of ballistic transport. A general characteristic of transport phenomena in nanostructures, containing planar defect layers, interfaces, point contacts, and in strongly anisotropic crystals and low-dimension systems is that in these cases transport processes occur in systems containing weak links. The energy fluxes are limited by the presence of weakly coupled layers of impurity atoms, planar defects, or contacts of microscopic size.

The mechanism of phonon transport in the presence of a surface is analyzed, and various models of a planar defect are examined. The special features of interfacial phonon transport where the transport coefficients are determined not by scattering processes in the volume of a bulk crystal but rather by the properties of the intercrystalline boundary are studied. The quantum phonon thermal conductivity of point-contacts is studied in detail. The exposition starts with an analysis of ballistic transport of phonons. Then various phonon scattering processes are included and the thermal conductivity of dielectric point-contacts in various transport regimes is described. The results of promising investigations of phonon transport in two-dimensional and molecular contacts are examined. The modification of the phonon spectrum in mesoscopic contacts is described.[15] We note that the extensive review literature devoted to heat transfer (see, for example, Refs. 16–22 does not contain a systematic exposition of the experimental and theoretical works concerning low-temperature phonon transport in nanostructures, even though this area of research is still undergoing intensive development.[23–29] In addition, the greatest successes in obtaining an adequate theoretical description of the effects associated with phonon transport have been obtained precisely at low temperatures. Consequently, one of the main goals of the present review is to fill this lacuna in the review literature, and this is why some of the problems studied must be described in greater detail.

I. POINT-CONTACTS—ACTUAL OBJECTS OF SOLID-STATE PHYSICS

A. Ballistic transport in nanocontacts

Dimensional transport effects appear as the dimensions of nanostructures decrease. These effects are associated with the ratio between the geometric characteristics of the structures and the scattering lengths corresponding to various carrier scattering mechanisms. Ballistic charge and heat transport intensifies in point-contacts at low temperatures for values of the diameter of a contact ranging from 1000 nm to 10 nm.[12] Under these conditions the inelastic scattering lengths of charge and heat carriers become large compared with the dimensions of the contact. When the contact dimensions drop below 10 nm, size-quantization of phonons in a contact arises.[10,14] The influence of a disruption of the regular structure of the crystal lattice in the region of a contact on the form of the vibrational spectra of atoms becomes substantial for contact sizes ranging from 10 nm to 1 nm.[15] This effect is a mesoscopic phenomenon.

It has now been established that ballistic heat transport, calculated in Refs. 9 and 12, occurs in dielectric and semiconductor point-contacts and in metal-dielectric contacts.[23–29]

Diverse methods have been proposed to obtain point-contacts.[5,30] The "needle and anvil" method,[31] the method of crossed wedges,[32,33] and the break junction method[34,35] are used to investigate electron and phonon transport in point-contacts. Electrons and phonons in point-contacts cannot propagate through the surface of the vacuum gap bounding the surface of the contact.

A unique feature of transport phenomena in point-contacts is the possibility of producing strongly nonequilibrium states of the electron-phonon system in the region of narrowing. If a temperature difference is maintained on the edges of a contact, then the phonon system becomes strongly nonequilibrium.

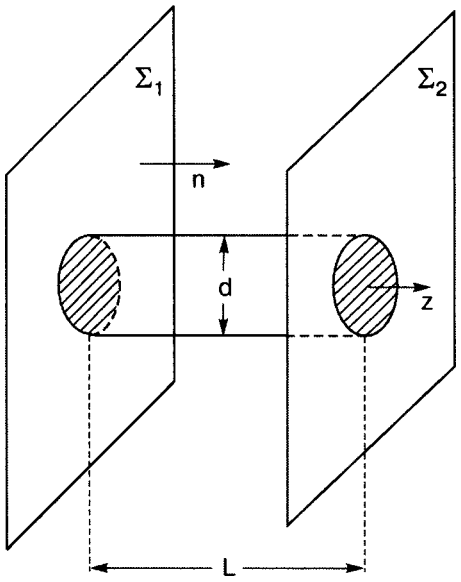

FIG. 1. Diagram of a point-contact in the form of a cylindrical short-circuit in a vacuum gap between the surfaces Σ_1 and Σ_2.

A nonequilibrium phonon system can be realized in a point-contact which is small compared with the phonon-phonon relaxation length $l_{\text{ph-ph}}$. Ballistic phonon transport occurs in point-contacts if the quasimomentum relaxation length is long compared with the diameter of the contact. A model of such a contact is shown schematically in Fig. 1.

Let us consider a situation where the bulk edges of the contact have different temperatures T_1 and T_2. Then groups of electrons and phonons in the region of the contacts are characterized by functions whose distributions have different temperatures T_1 and T_2. An average temperature cannot be established in a contact, since the inelastic scattering is weak ($d \ll l_{\text{ph-ph}}$). The low-temperature thermal conductivity of a contact gives clear evidence of the diffraction of phonons in point-contacts, which makes it possible to estimate the geometric parameters of the contacts. Obtaining point-contacts by the pressure of a microscopic needle results in the appearance of a polycontact structure. Thus heat flow can be studied between the edges of a contact as a result of transport through a number of parallel contacts.

B. Adiabatic method of measuring heat flux in a contact

A simple adiabatic method for measuring heat flux in dielectric contacts is proposed in Ref. 8. This method was used to measure the heat flux through NaCl–NaCl[8,9,36] and KBr–KBr[37] contacts. The point-contacts were produced between two NaCl single crystals, where the bottom NaCl-1 single crystal was suspended in vacuum under adiabatic conditions. The top NaCl-2 single crystal was in contact, via a copper heat guide, with a reservoir filled with liquid helium. External regulation of a clamp permitted varying the clamping force between the [001] plane of the NaCl-2 crystal and the trihedral angle in the [111] direction of a NaCl-1 crystal and thereby the size d of the point-contact.

To ensure adiabatic conditions both samples were placed in vacuum under pressure less than 10^{-4} Pa and surrounded by a heat screen. An electric heater-strain gauge was glued on the bottom surface of the NaCl-1 sample to heat the sample to a temperature of 80 K.

After the heater was switched off, the cooling curve of sample NaCl-1 was measured, i.e. the temperature dependence $T_1(t)$ was found, and the derivative dT_1/dt as a function of T_1 was found by numerical differentiation. Using the thermodynamic definition of the heat capacity the heat flux $\dot{Q}(T_1)$ can be calculated from the equation

$$\dot{Q}(T_1) = C(T_1)(dT_1/dt), \tag{1}$$

where $C(T_1)$ is the heat capacity of the sample NaCl-1 at temperature T_1.

In this setup of the experiment some of the heat flux is due to parasitic flux through electric wires, nylon filaments, and residual gas and to radiation. This parasitic background was measured without the point-contact included; this made it possible to calculate the pure heat flux through the point-contact. This experimental procedure can be used to measure, simply and with a small error ($<1.0\%$), the heat flux through a dielectric point-contact.

An experimental technique was later developed to obtain high-stability contacts. This technique included the production of metal-dielectric contacts.[10] In low-temperature experiments experiments ($T_1 \approx 0.1-10$ K) point-contacts were prepared using a high-purity silicon single crystal, secured on three thin microneedles, one of which was made of copper and the two others were made of Vespel polymer resin. The thermal conductivity of the Vespel resin is very low; it did not make an appreciable contribution to the heat flux, just as radiation. Immediately prior to the formation of a contact the copper needle was sharpened electrolytically in order to prevent the appearance of an oxide layer. The flat surface of the silicon was polished with diamond paste. The average roughness of the surface was 0.7 μm before polishing and about 2 nm after polishing. The silicon crystal with a temperature sensor glued to it was heated to 10 K. After heating, the crystal cooled as a result of heat flow through the point-contact, formed by the surface of the silicon and the copper needle. The time dependence of the silicon temperature was measured, using the value of the heat capacity of silicon, to calculate the heat flux.

C. Measurement of the thermal conductivity of contacts by the adiabatic method

Experiments with NaCl–NaCl contacts in the temperature range 4.2–65 K[8,9] have demonstrated that in contacts with effective diameters 150–350 nm the ballistic regime of heat conduction remains when the temperature T_1 of the "hot edge" of the contact increases right up to 60 K.

An experiment on the thermal conductivity of high-stability Si–Cu point-contacts[10] (see Fig. 2) reveals a well-defined peak in the temperature dependence of the reduced heat flux at $T_1=0.5$ K. This peak is associated with the diffraction effects accompanying phonon passage through a point-contact. For $T_1>2$ K phonon transport occurs in the geometric-optics limit, and the series of peaks demonstrates

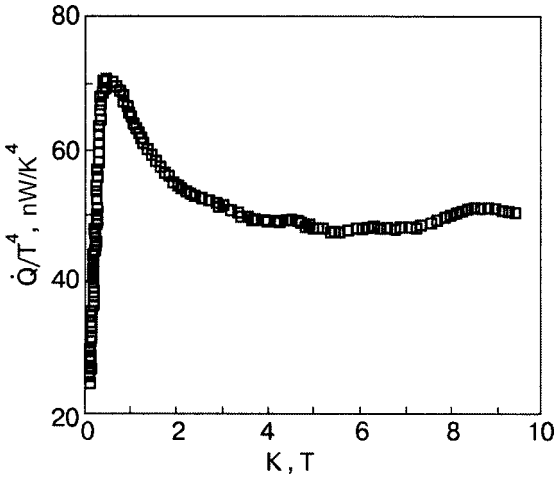

FIG. 2. Reduced heat flux measured in a Si–Cu point-contact.[10]

the presence of polycontacts. According to the spherical flow model, the diameter of contacts of this type is 30 nm and their length $L=4.5$.

The temperature dependence of the heat flux in Si–Cu point-contacts in the temperature range 4.2–25 K was investigated in Ref. 36 using the adiabatic method described in Sec. I B (see Fig. 3).

The geometric-optics regime was realized for phonons in these contacts. In this case the heat flux is proportional to T_1^4. The estimates based on the geometric-optics regime gave for the effective contact diameter $d_{\text{eff}}=5000$ nm.[36] We note that in the polycontact geometry the effective diameter is related with the average diameter d of an individual contact by the relation $d_{\text{eff}}=d\sqrt{n}$ (n is the number of individual contacts in a polycontact).

The adiabatic method has also been used to investigate the heat flux in KBr–KBr and KBr–Cu contacts.[38] The KBr crystals were prepared by the Czochralski method at the Institute of Single Crystals of the Ukrainian National Academy of Sciences. The purity of the samples was 99.99%. The temperature dependences of the heat flux through the KBr–KBr and KBr–Cu contacts are very similar to one another. They show the presence of a geometric-optics regime for phonons in a wide temperature range. The reduced heat flux

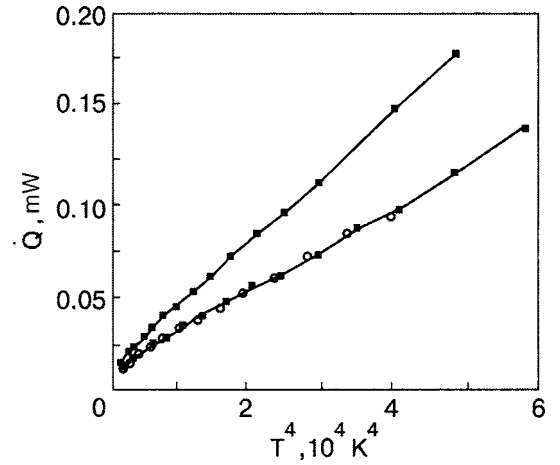

FIG. 3. Temperature dependence of the heat flux through a Si–Cu point-contact in the temperature range 4.2–25 K.[36]

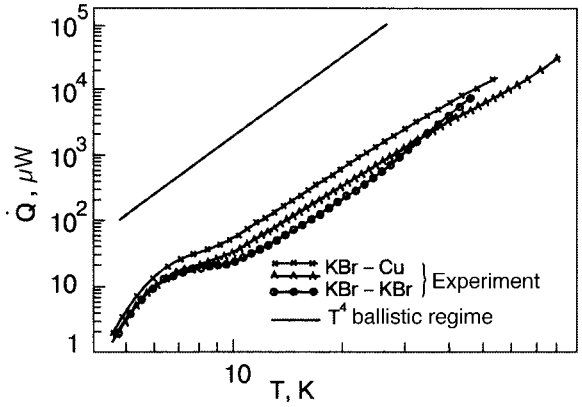

FIG. 4. Temperature dependence of the heat flux through KBr–Cu and KBr–KBr point-contacts.[36]

exhibits a low-temperature peak at $T_1=5.7\pm0.2$ K. Koestler *et al.* observed a similar anomaly.[39] The possible origin of such an anomaly as a result of resonance transport through a layer of weakly bound impurities was discussed in Refs. 38 and 40. This anomaly is reproduced well and has a similar form in KBr–KBr and KBr–Cu contacts. Finally, a strong temperature dependence of the reduced heat flux in the range 5–10 K was observed. This effect is due to intense scattering of low-frequency phonons in the static field of extended lattice deformations, associated with the production of point-contacts by the "needle-anvil" method. The upper temperature limit of intense phonon scattering (10 K) makes it possible to estimate the characteristic size of extended deformations to be 5 nm.

II. PHONON TRANSPORT IN 3*D* NANOCONTACTS

A. Nonequilibrium states of the phonon system in a contact

The theoretical description of strongly nonequilibrium nanosystems has required the development of special methods for solving problems of physical kinetics. This has made it possible to go far beyond the thermodynamics of nonequilibrium processes. The theory of ballistic phonon transport of heat in point-contacts was first developed in Ref. 12. In the present section the foundations of the theory of phonon transport in point-contacts is presented.

The condition for ballistic transmission of phonons through a dielectric point-contact presumes that the size (diameter) d of the contact is small compared with the phonon inelastic scattering length $l_{\rm ph}$ in the bulk sample. As a rule, for ballistic phonon transport to be realized at temperatures which are low compared to the Debye temperature Θ_D it is sufficient that the size of the contact not exceed 10 nm. An average temperature cannot be established in the contact because the inelastic phonon-phonon interaction is small ($d \ll l_{\text{ph-ph}}$).

An opening in an impermeable (for electrons and phonons) screen is used as the basic theoretical model of a contact connecting bulk edges. Unless otherwise stated the contact size is assumed to be large compared to the electron wavelength λ_e and phonon wavelength $\lambda_{\rm ph}(\lambda_e, \lambda_{\rm ph} \ll d)$.

The state of the phonon system of a dielectric point-contact can be described using the kinetic equation for the phonon distribution function N and boundary conditions that take account of the difference of the temperatures in the bulk edges:

$$N(z \to \pm\infty) = n_P(\omega, T_{1,2}). \tag{2}$$

Here z is the axis of the contact, oriented in a direction normal to the plane of the contact. The temperature of the left-hand bulk edge ($z \to -\infty$) is assumed to be T_1, the temperature of the right-hand edge ($z \to \infty$) is assumed to T_2, and n_P is the Planck distribution.

Heat is transported in a ballistic point-contact by two noninteracting groups of phonons, whose distribution functions are given by the temperatures of the bulk edges of the contact T_1 and T_2. Consequently, the kinetic equation for N can be solved by the method of characteristics in the zeroth order approximation in the phonon scattering integral.

B. Phonon flux in the geometric-optics approximation

The ballistic phonon heat flux $\dot{Q}_B(T_1, T_2)$ through a point-contact contains contributions of opposite sign, which correspond to the two groups of phonons arriving from different edges of the contact:[12]

$$\dot{Q}_B(T_1,T_2) = \frac{\hbar S_0}{2(2\pi)^3} \sum_\alpha \int d\mathbf{k}\, \omega^\alpha(\mathbf{k}) u_z^\alpha D_{1,2}^\alpha \{N(\omega^\alpha, T_1) - N(\omega^\alpha, T_2)\}. \tag{3}$$

Here S_0 is the area of the contact, $\omega(\mathbf{k})$ is the phonon dispersion law, $\mathbf{u}^\alpha = \partial\omega^\alpha(\mathbf{k})/\partial\mathbf{k}$, $\mathbf{k}$ is the wave vector of a phonon, and α is an index indicating the branch of the phonon spectrum. If the phonon distribution functions in the bulk edges are equilibrium functions, then $N = n_P(\omega, T) = [\exp(\hbar\omega/T) - 1]^{-1}$. The expression (3) contains the coefficient of phonon energy transfer $D_{1,2}^\alpha(\mathbf{k})$ from edge 1 to edge 2; the dispersion law is taken into account for edge 1. The magnitude of the heat flux remains unchanged if the corresponding quantities for edge 2 are used in Eq. (3). This is a consequence of the reciprocity theorem for the transmission of elastic waves through an ideal interface.[41]

The reciprocity theorem asserts that the fraction of the energy flux of the phonons which are associated with an elastic mode j in edge 1, transported by phonons of mode l in edge 2 $(1, j \to 2, l)$, is the same as the analogous fraction for the reverse process $(2, l \to 1, j)$. The quantity $D_{1,2}^\alpha(\mathbf{k})$ is determined by the law of refraction of phonons taking account of the conversion of the branches of the phonon spectrum at the contact boundary. For a ballistic planar contact the coefficients D_{mn}^α are determined by the properties of the crystal lattices of the edges and can be calculated by studying the problem of the transmission of a plane wave through an infinite planar boundary of two media.[42,43] At low frequencies, where the acoustic mismatch model can be used,[42] D_{mn}^α depends weakly on the frequency. For a contact between identical media, $D=1$ must be used in the ballistic regime of geometric optics. In this case the magnitude of the ballistic heat flux depends on the special features of the dispersion law for phonons and is independent of the mechanisms of phonon scattering in a bulk crystal. The relationship between the heat flux and the form of the phonon spectrum can be represented in an explicit form, expressing $\dot{Q}_B(T_1, T_2)$ as

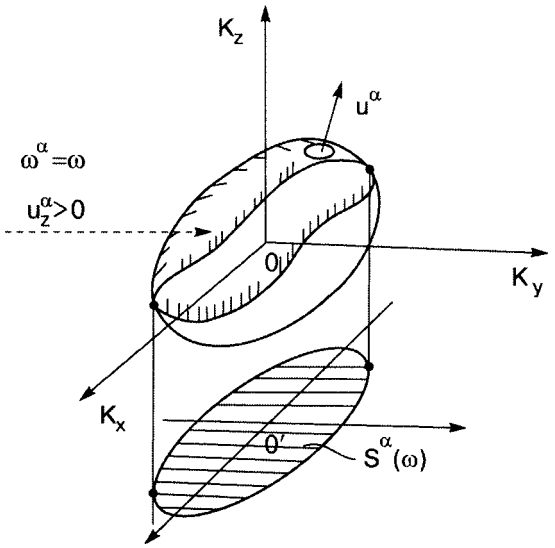

FIG. 5. Region of integration over an isoenergy surface in k space and geometric representation of the function S.

$$\dot{Q}_B(T_1,T_2)=\frac{\hbar S_0}{(2\pi)^3}\int d\omega\,\omega\,S(\omega)\{N(\omega,T_1)-N(\omega,T_2)\}. \tag{4}$$

The function $S(\omega)$ is determined by an integral over the constant-energy surfaces $\omega^\alpha(\mathbf{k})=\omega$ in the k-space of the phonon wave vectors:

$$S(\omega)=\sum_\alpha\int_{u_z^\alpha>0} d\mathbf{k}u_z^\alpha(\mathbf{k})\,\delta(\omega^\alpha(\mathbf{k})-\omega)$$
$$=\sum_\alpha\int_{u_z^\alpha>0} d\sigma_\omega^\alpha n_z(\sigma_\omega^\alpha), \tag{5}$$

σ_ω^α and $\mathbf{n}(\sigma)$ denote an element of the isoenergy surface and the unit normal to it, respectively.

It follows from the expression (5) that $S(\omega)=\Sigma_\alpha S^\alpha(\omega)$ has a simple geometric representation in k-space: for each α branch of the phonon spectrum $S^\alpha(\omega)$ is the area of the projection on the plane of the contact of that part of the isoenergy surface $\omega^\alpha(\mathbf{k})=\omega$ for which the condition $u_z^\alpha(\mathbf{k})>0$ holds (Fig. 5).

C. Low-temperature ballistic transport of phonons

At low temperatures, when the phonon dispersion law can be represented in the linear approximation $\omega_\alpha=u^\alpha(\mathbf{k}/k)\mathbf{k}$, $S(\omega)$ is quadratic in the frequency $S(\omega)=P\omega^2$, where

$$P=\sum_\alpha\int_{u_z^\alpha>0} d\Omega u_z^\alpha(\Omega)[\mathbf{u}^\alpha(\Omega)\mathbf{e}(\Omega)]^{-3}. \tag{6}$$

Here Ω denotes the angular coordinates of the unit vector $\mathbf{e}=\mathbf{k}/k$. The function $S(\omega)$ assumes its most compact form in the isotropic case: $S_{\text{is}}(\omega)=\pi\Sigma_\alpha k_\alpha^2(\omega)$.

Let us analyze the expression (4). At low temperatures ($T_{1,2}\ll\hbar\omega_D$) only low-frequency oscillations are excited and the heat flux is[12]

$$\dot{Q}_B(T_1,T_2)=\frac{\pi}{120}\frac{S_0}{\hbar^3}P(T_1^4-T_2^4). \tag{7}$$

For the simplest case of a uniform contact in the approximation of an isotropic dispersion law we have

$$P=\pi\sum_\alpha(u^\alpha)^{-2}. \tag{8}$$

This estimate is ordinarily used to calculate the effective area of ballistic contacts.[9]

In experiments studying phonon transport in point-contacts the situation where $T_1\gg T_2$ is often studied. In these cases we can set $T_2\simeq 0$, and the temperature T_1 of the "hot" edge of the contact can be denoted as T. The temperature dependence of the heat flux, proportional to T^4, serves as a criterion for the realization of the ballistic regime of geometric optics in a point-contact. The temperature dependence presented above for the phonon heat flux is analogous to the dependence obtained by Little[42] and Khalatnikov[44,45] for phonon heat transfer between two media. A temperature jump can occur at the boundary of two media if the contribution of boundary scattering of phonons to the heat resistance is larger than the heat resistance of the bulk edges. This effect was first observed in the experiments performed by Kapitsa on heat transfer between superfluid helium and a metal.[46] As the analysis of heat transport through a point-contact performed above shows, the presence of an interface of two media in the contact is not at all necessary for the formation of a contact jump in the temperature. This jump arises because of the scattering of phonons by the surface of the vacuum gap surrounding the point-contact.

We note that for high temperatures ($T_{1,2}\gg\hbar\omega_D$) the magnitude of the flux is a linear function of temperature difference $\Delta T=T_1-T_2$. For small ΔT a heat resistance R_T, determined from the formula $\dot{Q}=\Delta T/R_T$ in the entire temperature range, can be introduced. The expression for R_T is an analog of Sharvin's formula[47] for the ballistic resistance of a metal point-contact.

D. Reconstruction of the vibrational spectrum from the temperature dependence of the ballistic heat flux

If $\dot{Q}_B(T,0)$ is studied in a sufficiently wide temperature range, a formal procedure inverse to the transformation (5) can be indicated. Using the results presented in Ref. 48, the necessary integral transformation can be represented in the form[12]

$$S(\omega)=\frac{4\pi^2}{S_0}\left(\frac{\hbar}{\omega}\right)^{1/2}\int_{-\infty}^{+\infty}d\mu\left[\Gamma\left(\frac{3}{2}+i\mu\right)\zeta\left(\frac{3}{2}+i\mu\right)\right]^{-1}$$
$$\times\int_0^\infty dT\dot{Q}_B(T,0)T^{-5/2}\left(\frac{\hbar\omega}{T}\right)^{i\mu}. \tag{9}$$

Here $\Gamma(x)$ is the gamma function and $\zeta(x)$ is the Riemann zeta function. Mathematically, such transformations are ill-posed, i.e. small errors in determining $\dot{Q}_B(T,0)$ can result in strong distortions of the desired function $S(\omega)$. We note that a mathematically similar problem of inversion for determining the density of states from the temperature dependence of the heat capacity has been examined by I. M. Lifshits.[49]

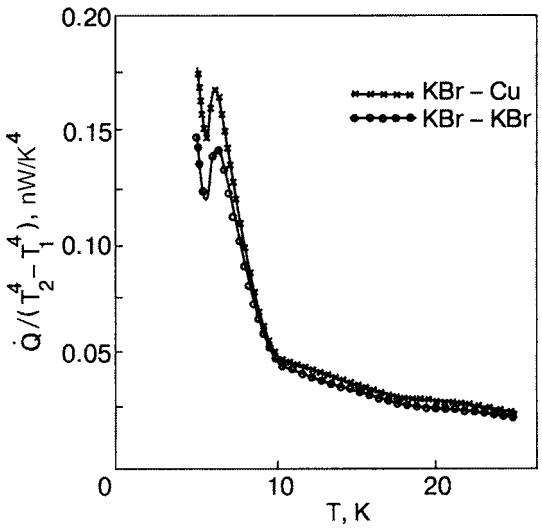

FIG. 6. Temperature dependence of the reduced heat flux in KBr–Cu and KBr–KBr point-contacts.[36]

III. PHONON SCATTERING IN THE NEAR-CONTACT REGION

The temperature dependence of the experimentally observed phonon heat flux through the boundary between solid bodies demonstrates a deviation from the temperature dependence predicted by Little's acoustic mismatch theory.[42] This is due to the physical processes occurring on the contact surface and in the layers near the surface (see Fig. 6).[17]

To analyze the phonon scattering processes in a point-contact it is convenient to use the following definition of the reduced heat flux:

$$\dot{q}_B(T_1,T_2) = \dot{Q}_B(T_1,T_2)/(T_1^4 - T_2^4). \tag{10}$$

The low-temperature reduced heat flux (10) calculated in the geometric-optics approximation is temperature-independent.

However, when measuring the thermal conductivity of dielectric point-contacts of the order of 100 nm in size the reduced thermal conductivity at low temperatures ($5\ \mathrm{K} < T < 10\ \mathrm{K}$) is observed to decrease with increasing temperature.[36] In the indicated temperature range, the temperature dependence of the thermal conductivity of a contact can be represented as $\dot{q}_B(T_1,T_2) = \mathrm{const}\, T_1^{-\varepsilon}$, where $\varepsilon \simeq 1$. Such a dependence attests to efficient phonon scattering in the contact.

A. Elastic scattering of phonons in a contact

The manifestation of low-temperature phonon scattering was first discovered in an investigation of metallic point-contacts. Although the point-contact spectra of metals demonstrate good agreement with the electron-phonon interaction functions and the phonon density of states found for bulk samples[4] a number of theoretical[50–53] and experimental[54,55] investigations have shown that the state of the near-contact region can strongly influence the phonon kinetics. Effects associated with "reabsorption" of nonequilibrium phonons,[50–53] attest to the possibility of strong elastic scattering of phonons in the near-contact region, caused by distortions produced in the crystal lattice when the contact is formed.

There is an extensive literature devoted to phonon scattering in bulk crystals (see, for example, Refs. 16 and 56). However, for point-contacts it is necessary to study the spatially nonuniform case and take account of the possibility of phonon scattering in the near-contact region by extended deformations of the lattice. In Ref. 9 a statistical description is proposed for the propagation of acoustic phonons in the field of extended lattice deformations under the assumption that the characteristic sizes of the distortions are large compared with the phonon wavelength.

We shall represent phonon propagation as a sequence of uncorrelated elastic scatterings by small angles for which the modulus of the phase velocity $\mathbf{u}$ remains unchanged. We shall examine the nonequilibrium distribution function $N_{\mathbf{q}}(\mathbf{r})$ for phonons with quasimomentum $\mathbf{q}$ at the point $\mathbf{r}$ (here the indices indicating the branches of the phonon spectrum are dropped). The Fokker-Planck differential equation[57,58] corresponding to a random walk in the space of orientations of the quasimomenta is

$$\frac{\partial}{\partial t} N_{\mathbf{q}} + u \frac{\partial}{\partial \mathbf{r}} N_{\mathbf{q}} = \frac{1}{2\tau_i} \Delta_\Omega N_{\mathbf{q}}, \tag{11}$$

where τ_i is the relaxation time over the orientations of the quasimomentum (and phase velocity), and Δ_Ω is the angular part of the Laplace operator in the space of the angular variables Ω of the quasimomentum $\mathbf{q}(\Omega)$.

Since Eq. (11) corresponds to the conservation of the modulus of the vector $\mathbf{q}$, for a linear dispersion law the time t can be replaced by a geometric parameter—the distance along the phonon "trajectory" $s = ut$. We introduce the notation $l_i = u\tau_i$ for the characteristic relaxation length of the orientation of the quasimomentum. Integrating Eq. (11) over spatial variables yields an equation describing only diffusion in the space of angular variables Ω for the quasimomentum vector $\mathbf{q}$. The Green's function for the latter equation is well known from the theory of rotational Brownian motion.[57,58]

The relaxation length l_i of the orientation of the quasimomentum in the presence of multiple scattering can be estimated from the characteristics of the nonuniformities of the medium in which the phonons propagate. If it is assumed that the nonuniformities are large-scale (on the scale of the characteristic wavelength of thermal phonons $\lambda \sim a\Theta_D/T$, where a is the lattice constant), they can be described by examining the variation of the local values of the velocity of sound $\mathbf{u}(\mathbf{r})$. It is convenient to introduce the dimensionless fluctuating quantity

$$\theta(\mathbf{r}) = [u^2(\mathbf{r}) - \langle u^2(\mathbf{r})\rangle]/\langle u^2(\mathbf{r})\rangle. \tag{12}$$

The geometric-optics method[57] yields the mean-square value of the deflection of a ray traversing a path s in a nonuniform medium:

$$\langle q^2(s)\rangle = \left(\frac{\pi}{2}\right)^{1/2} \frac{\sigma_\theta^2 s^3}{6R_\theta}. \tag{13}$$

Here σ_θ^2 and R_θ are, respectively, the normalized variance and the correlation radius for the random field $\theta(r)$, which is assumed to be Gaussian. On the other hand, a similar quantity can also be calculated in the space of angular variables in a diffusion model. For $s \ll l_i$ we find

$$\langle q^2(s)\rangle = \frac{2s^3}{3l_i}. \tag{14}$$

Comparing the expressions (14) and (15) gives the estimate

$$l_i \sim R_\theta/\sigma_\theta^2. \tag{15}$$

The expression (15) for the scattering length contains the low-frequency statistical characteristics of the elastic medium. The estimate (15) leads to the conclusion that the transmission coefficient D for acoustic phonons depends weakly on the frequency ω as long as the scattering nonuniformies can be regarded as large-scale ($\lambda \ll R_\theta$).

A different situation arises when the characteristic size δ of the scattering nonuniformities is small compared with λ. Then phonon scattering by point defects must be studied. The estimate found in the approximation of Rayleigh scattering of phonons (see, for example, Ref. 56) gives

$$l_i(\omega) \sim \frac{nu}{n_d\omega_D}\left(\frac{\omega_D}{\omega}\right)^4. \tag{16}$$

Here n is the number of unit cells per unit volume and n_d is the concentration of scattering defects. A sharp increase of the scattering length l_i with decreasing frequency should result in a large increase of the reduced point-contact heat flux with decreasing temperature.

The transition from Rayleigh scattering of phonons to the geometric-optics regime has been studied in detail for NaCl crystals containing inclusions of colloidal silver[59,60] and for doped KBr and KCl crystals.[61] The model calculations performed for scatterers in the form of spheres,[62,63] prolate spheroids[64] and cylindrical nonuniformities[65] have shown that in the region of the transition from Rayleigh scattering to the geometric-optics regime the phonon scattering cross section is a nonmonotonic function of the frequency. In the region $kb \simeq 1.5$, where b is the transverse size of a scatterer, the scattering cross section has a peak accompanied by a series of damped oscillations.

The model, which includes an analysis of heterocontacts, takes account of the fact that the phonon scattering lengths in different edges of a contact can be different (l_1 and l_2, respectively). Studying the balance of phonon energy transfer through the cross section of a contact assuming that the phonons undergo elastic scattering, a correction factor K can be found for the integrand in Eq. (17) for the heat flux, describing a transition to the diffusion regime of phonon scattering ($l_i \ll d$).

For elastic scattering of phonons, when the energy of the phonon system is not transferred from one frequency interval into another, the continuity equation for the energy flux can be written for each phonon frequency ω. We assume immediately that the elastic scattering is strong enough so that a diffusion regime is established in both edges of a heterocontact. Calculations show[36] that in this case the expression for the energy flux in the phonon system acquires an additional coefficient K corresponding to the elastic scattering of phonons by impurities in both edges of the contact:

$$\dot{Q}_B(T_1,T_2) = \frac{\hbar S_0}{2(2\pi)^3}\sum_\alpha \int d\mathbf{k}\,\omega^\alpha(\mathbf{k})u_z^\alpha D_{1,2}^\alpha K^\alpha \times \{N(\omega^\alpha,T_1) - N(\omega^\alpha,T_2)\}, \tag{17}$$

$$K^\alpha(l_1^\alpha,l_2^\alpha) = \frac{32}{3\pi d}\left(\frac{1}{l_1^\alpha}+\frac{1}{l_2^\alpha}\right)^{-1}. \tag{18}$$

The effective coefficient K of phonon scattering by nonuniformities becomes $K=(16/3\pi)(l/d)$, and the effective scattering length l is given by the expression $1/l=(1/2l_1)+(1/2l_2)$. The largest value of the parameter l corresponding to the ballistic regime can be obtained from the condition $K=1$, specifically, $l_{\text{ball}}=3\pi d/16$.

In heterocontacts the properties of the crystal lattices which are in contact with one another and the arrangement of the intercrystalline boundary determine the coefficient of phonon energy transfer.[66–72] In Little's work[42] the coefficient D was calculated for long-wavelength acoustic phonons on the basis of the acoustic mismatch model within the theory of elasticity. (A phenomenological "diffusion mismatch" model was also proposed there for the case of phonon transmission through a rough boundary of a contact.) The estimates for D are simplest for longitudinal oscillations, when D is determined by the ratio of the impedances Z_1/Z_2 (the ratio of the products of the densities $\rho_{1,2}$ and the sound velocities $u_{1,2}$ of the solid bodies in contact with one another). In this model the coefficients D are frequency-independent, and for the lattice with the higher sound velocity (for example, u_1) $D_{12} \simeq \min[(\rho_1u_1/\rho_2u_2),(\rho_2u_2/\rho_1u_1)]$ while for a lattice with the lower sound velocity $D_{21} \simeq D_{12}(u_2/u_1)^2$. In Ref. 43 the coefficients D were calculated for contacts of model fcc lattices with the same periods but different force matrices. It was shown that at frequencies commensurate to the Debye frequencies the coefficients D start to depend strongly on the frequency, vanishing at the lowest Debye frequency.

Deviations from the geometric-optics regime for phonon transport are very noticeable when the reduced heat flux (10) is used. The deviations of the first type consist of a monotonic decrease of the reduced heat flux at temperatures $T > 10$ K. This attests to a large increase in phonon scattering in the contact region with increasing temperature. The temperature dependence of the phonon scattering length l can be expressed as a power law $l(T) \simeq T^{-s}$, where, according to experimental data, $0.5 < s < 0.7$. Such a weak temperature dependence is typical for phonon scattering by static stresses of the crystal lattice near dislocations.[72] Since all contacts studied were obtained by the "needle and anvil" method, it is natural for stress fields to appear in the contact region.

B. Phonon-phonon scattering in point contacts

At sufficiently low temperatures ($T \leqslant \Theta_D/10$) the phonon-phonon scattering processes are substantial only for "large" ballistic point contacts ($d \geqslant 10^2$ nm).[9,73] If elastic phonon scattering occurs in the near-contact region (with characteristic scattering length $l_r \leqslant d$), then the contribution of phonon-phonon scattering becomes lage, since in this case the characteristic inelastic phonon scattering length is $l_{\text{in}} = (l_r l_{\text{ph-ph}})^{1/2}$.

The contribution of phonon-phonon scattering to the heat flux in a dielectric ballistic point-contact can be taken into account by introducing on the right-hand side of the kinetic equation for the phonon system (11) the phonon-phonon interaction integral $I_{\text{ph-ph}}$. Assuming that the characteristic phonon-phonon scattering length is large compared to the dimensions of the contact ($l_{\text{ph-ph}} \gg d$), we shall examine a phonon-phonon interaction integral where three-phonon interactions are taken into account.[56]

The heat flux $\dot{Q}$ transported by phonons and calculated to a first approximation in $I_{\text{ph-ph}}$ can be represented, introducing the point-contact scattering length $l^c_{\text{ph-ph}}$, according to the formula

$$\dot{Q} = \dot{Q}_B^{(0)} + \dot{Q}^{(1)}_{\text{ph-ph}} = \dot{Q}_B^{(0)}[1 - (d/l^c_{\text{ph-ph}})]. \tag{19}$$

Accordingly, the correction $\dot{Q}^{(1)}_{\text{ph-ph}}$ can be divided into a contribution $\dot{Q}_U^{(1)}$ due to scattering with umklapp (U processes) and a contribution $\dot{Q}_N^{(1)}$ due to normal scattering (N processes). The values obtained for the scattering lengths for N and U processes are

$$l^c_N = -d(\dot{Q}_B^{(0)}/\dot{Q}_N^{(1)}); \quad l^c_U = -d(\dot{Q}_B^{(0)}/\dot{Q}_U^{(1)}). \tag{20}$$

We take account of the fact that for this definition the relation $l^{-1}_{\text{ph-ph}} = l_N^{-1} + l_U^{-1}$ is valid.

Phonon propagation taking account of geometric constraints caused by the presence of a point-contact results in additional selection rules[73] for N scattering processes, compatible with the laws of conservation of quasimomentum and energy of the phonons.[74,75] Thus the contributions of scattering processes vanish for parallel vectors of the group velocity of the phonons. The maximum contribution obtains for oppositely directed velocities. Consequently, the decay process with the participation of long-wavelength phonons $t'' \rightarrow t + t'$ makes a negligibly small contribution to the point-contact phonon flux. (Here and below t and l denote the transverse and longitudinal branches of the phonon spectrum; t_1 and t_2 denote transverse phonons on different branches.) Normal processes of the type $l \rightarrow t + t'$, $l \rightarrow l' + t$ or $t_1 \rightarrow t_2 + l$ contribute to $\dot{Q}^{(1)}_{\text{ph-ph}}$, since in these processes one of the velocity vectors can be oriented in a direction opposite to the other two.

If the temperature difference between the contact edges is small ($T_1 - T_2 = \Delta T \ll T_1, T_1 \simeq T$), then the values of l^c_N and l^c_U can be assigned to a definite temperature T of the contact. The correction $\dot{Q}_N^{(1)}$ due to the normal processes can be estimated assuming the phonons participating in the scattering to be long-wavelength phonons, so that the condition $\hbar\omega < T$ is satisfied for all phonon frequencies, and $n_{\text{ph}}(\omega, T) \simeq T/\hbar\omega > 1$. We estimate the phonon-phonon interaction constant as $B(\mathbf{q}, \mathbf{q}', -\mathbf{q}'') \sim (a^3 u/\hbar^2 M) q q' q''$,[56] where M is the mass of an ion. Double summation over the phonon quasimomenta gives

$$\dot{Q}_N^{(1)} \sim -(d^3 a^3/\hbar^7 M)(T/u)^8 \Delta T. \tag{21}$$

Since the estimate $\dot{Q}_B^{(0)} \simeq (d^2/\hbar^3 u^2) T^3 \Delta T$ is valid for $\Delta T \ll T \ll \Theta_D$, we find by the definition (20) that

$$l^c_N \sim a(Mu^2/\Theta_D)(\Theta_D/T)^5. \tag{22}$$

We note that this estimate is identical to the result obtained for a bulk sample.

When U processes are taken into account, we must set $|\mathbf{q} - \mathbf{q}'| \sim G \sim \hbar/a$. Then the resulting quasimomentum is $q'' \sim G$ (G is a reciprocal lattice vector). The Planck distribution functions appearing in the phonon-phonon collision integral result in the appearance of the factor $\exp(-c\Theta_D/T)$, where $c \sim 1$, in the correction for inelastic phonon scattering.[73] We shall estimate the phase volume where the law of conservation of phonon energy is satisfied as done in Ref. 76. This results in the following estimate for the contribution of U processes to the inelastic correction to the phonon heat flux:

$$\dot{Q}_U^{(1)} \sim -\gamma d^3 a^{-5} (\hbar/M)(\Theta_D/T)^{1/2} \exp(-c\Theta_D/T)\Delta T. \tag{23}$$

The dimensionless coefficient $\gamma \sim 1$ depends on the degree to which the dispersion law for short-wavelength phonons deviates from linearity. However, the temperature dependence has a general form due to the possibility of describing the indicated deviations in the quadratic approximation. Taking account of the low-temperature estimate for $\dot{Q}_B$, the definition (20) in this case gives

$$l^c_U \sim \gamma^{-1} a(Mu^2/\Theta_D)(T/\Theta_D)^{7/2} \exp(c\Theta_D/T), \quad T \ll \Theta_D. \tag{24}$$

On account of the exponential factor l^c_U is a decreasing function of temperature in the range $0 < T \leqslant \Theta_D/3$. We note that the temperature dependences of l^c_N and l^c_U are studied in the temperature range where $\dot{Q}_B$ is proportional to $T^3\Delta T$. As a simple model calculation shows, this condition holds for $T \leqslant \Theta_D/10$. In the temperature range $T \leqslant \Theta_D/30$ the condition $l^c_N < l^c_U$ holds. The characteristic phonon-phonon scattering lengths are found to be of the order of the sizes of "large" point contacts ($d \geqslant 10^2$ nm). The N processes make the main contribution to scattering. It should be noted that for the indicated parameters of point-contacts a drift phonon distribution does not form in the contacts. The scattering lengths rapidly decrease with increasing temperature, and at $T \sim \Theta_D/3$ the phonon-phonon scattering, as a number of experiments show,[9,36] can make an appreciable contribution to the phonon heat flux in a point-contact.

An efficient interpolation procedure[73] makes it possible to calculate the phonon heat flux density in a point-contact in a wide temperature range according to the known temperature dependence of the phonon scattering length. Figure 7 shows the results of calculations of the phonon heat flux density (for small temperature differences) for a series of contacts of different size (10 nm $\leqslant d \leqslant 10^3$ nm). (The data on the phonon scattering lengths in crystalline quartz[77] were used.) It is evident that for small contacts ($d = 10$ nm) phonon scattering contributes only at quite high temperatures ($T \sim 100$ K). The ballistic phonon transport regime is established in the temperature range $T < 10$ K for all contacts studied.

C. Phonon transport in metal-dielectric point-contacts

In experiments studying phonon transport in point-contacts it is often convenient to use a metal-dielectric

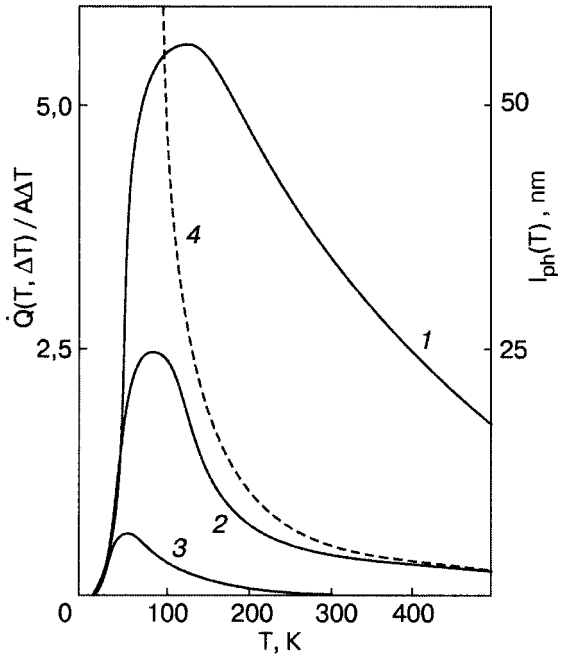

FIG. 7. Reduced thermal conductivity of a point-contact in the τ approximation for different values of d, nm:[53] 10 (1), 100 (2), and 1000 (3); l_{ph} (4)—phonon scattering length in crystalline quartz.

contact.[10,36,38] We shall analyze heat transport in metal-dielectric point-contacts for different phonon and electron transport regimes.

The electronic system in metal-dielectric point-contacts makes a small contribution to the heat transport process as long as the size d of the point-contact remains small compared with the effective phonon-electron scattering length l_a. For ballistic phonon transport l_a equals the phonon-electron scattering length $l_{\text{ph-}e}$ in a pure metal. For strong elastic scattering l_a depends on the relaxation length l_r of phonons over the quasimomentum, $l_a=(l_{\text{ph-}e}l_r)^{1/2}$. As shown in the preceding section, the phonon-phonon scattering effects at $T \sim 10$ K become substantial only for "large" point-contacts ($d>100$ nm). Metal "needles" make it possible to obtain stable metal-dielectric contacts 10–100 nm in size. In such contacts the phonon-phonon scattering contribution is negligibly small in the range $0<T<10$ K.

In a metal-dielectric point-contact phonons transport heat through the contact boundary. The electronic system can scatter and absorb the phonons. We shall denote by T_d and T_m the temperatures of the dielectric and metallic edges of the contact. We note that T_m in our problem denotes the temperature of the phonon and electronic systems of a bulk metal, since the small heat flux through the point-contact cannot destroy the equality of the temperatures of these systems.

The phonon energy transmission through the boundary of a contact as a result of the interaction of electrons with surface oscillations is analyzed in a number of works.[44,45,78–82] The parameter $\lambda_s/l_{\text{ph-}e}$, where λ_s is the penetration depth of the surface waves, determines the strength of this interaction. This parameter is small for most metals and, as a rule, essentially temperature-independent, $\lambda_s/l_{\text{ph-}e} \simeq \Theta_D/\varepsilon_F$ (ε_F is the Fermi energy of the metal). This heat-transport mechanism is important for contacts with strong acoustic mismatch.[80]

For contacts with good acoustic matching the contribution of the electron-phonon interaction in the bulk of the metal to heat transport becomes important. This contribution must be taken into account as a perturbation with respect to the small parameter $d/l_{\text{ph-}e}$, if $d \ll l_{\text{ph-}e}$ and $l_{\text{ph-}e}$ is smaller than all other phonon scattering lengths. We note that for contacts with diameter $d \simeq 100$ nm the condition $d>\lambda_s$ is ordinarily satisfied for $T>1$ K.

We shall use a kinetic equation to describe the electron-phonon system of the metallic edge of a point-contact. We shall use the distribution function $N_{\mathbf{q}}(\mathbf{r})$, where $\mathbf{q}$ is the quasimomentum of a phonon (just as in Eq. (11), here, the phonon branch index is dropped), to describe the state of the phonon system. The function f describes the state of the electronic system of the metallic edge. Since heat transfer through a point contact is weak, the function f can be taken as the equilibrium Fermi distribution, corresponding to the temperature T_m of the metallic edge. The kinetic equation for the phonon system of the metallic edge is

$$\mathbf{u}(\mathbf{q})(\partial/\partial\mathbf{r})N_{\mathbf{q}}(\mathbf{r}) = I_{\text{ph-}e}\{N_{\mathbf{q}}(\mathbf{r}), f\} + I_{\text{ph-}i}\{N_{\mathbf{q}}(\mathbf{r})\}. \qquad (25)$$

Here $I_{\text{ph-}e}$ is the phonon-electron interaction integral, and $I_{\text{ph-}i}$ is the integral of elastic scattering of phonons by distortions of the crystal lattice. We shall assume that $I_{\text{ph-}i}=0$ in the ballistic limit. The equation for $N_{\mathbf{q}}(\mathbf{r})$ in the dielectric edge does not contain $I_{\text{ph-}e}$ and, in addition, the dispersion law and the integral $I_{\text{ph-}i}$ can have a different form.

There is no need to write out the equation for the electronic system of the metallic edge, since the electron-phonon interaction near a point-contact perturbs the system only slightly. We shall assume below that electron reflection from the metal surface is specular, neglecting the interaction of the electrons with surface phonons. A consequence of the weak perturbation of the electronic system is an excess potential at the surface of the metal edge, calculated in Ref. 82.

The boundary conditions at infinity ensure that the phonon and electron distributions have an equilibrium form in the massive edges of the contact. It is assumed that electrons and phonons do not pass through the surface of the planar vacuum gap forming the contact.

The metal-dielectric interface is an additional phonon scatterer. A boundary condition can be introduced on the surface separating the metal and dielectric, making the assumption that a phonon propagating in the metal from the contact boundary can be transmitted through the interface with probability D^{α}_{dm} or be reflected from this surface with probability $1-D^{\alpha}_{dm}$.[82] The properties of the crystal lattices of the contact edges determine the coefficient $D^{\alpha}_{dm}(q)$, which can be calculated by analyzing the problem of the transmission of an elastic plane wave through the interface of two media, as the ratio of the squared moduli of the amplitudes of the waves refracted by and incident on the interface (see Sec. II C). In general, the phonon mode with index α, propagating in the edge d, can be excited by three different modes in the edge m. We must take the coefficient $D^{a}_{dm}(\mathbf{q})$ to be the average value over the indicated modes.

1. Ballistic regime of heat transport in a metal-dielectric contact

In a point-contact of size d ballistic phonon transport in the geometric-optics limit occurs if

$$\lambda_{\text{ph}} \ll d \ll l_{\text{ph-ph}}, l_{\text{ph-}e}, l_r, \tag{26}$$

When this condition is satisfied two noninteracting groups of phonons are responsible for the phonon heat flux $\dot{Q}(T_d, T_m)$ through the point-contact between the massive edges, whose temperatures are T_d and T_m. A single temperature of the phonon system cannot be determined near the point-contact. A general temperature of the phonon system is also not established for elastic scattering of phonons in the contact region; here, the condition $d \gg l_r$ can be satisfied.

In the ballistic limit, when $I_{\text{ph-}e}=0$ and $I_{\text{pn-}i}=0$ can be used, the solution of the kinetic equation for phonons (25), taking account of the transmission and reflection of phonons in the metallic edge, is

$$N_{\mathbf{q}}^{(0)\alpha}(\mathbf{r}) = \beta(\mathbf{u}^{\alpha}(\mathbf{q}),\mathbf{r}) D_{dm}^{\alpha}(\mathbf{q}) N_p(\omega^{\alpha}(\mathbf{q})/T_d) + [1-\beta(\mathbf{u}^{\alpha}(\mathbf{q}),\mathbf{r}) D_{dm}^{\alpha}(\mathbf{q})] N_p(\omega^{\alpha}(\mathbf{q})/T_m). \tag{27}$$

Here $N_p(x)=[\exp(\hbar x)-1]^{-1}$. The function $\beta(\mathbf{u}(\mathbf{q}),\mathbf{r})$ assumes the value 1 at all points r of the metal where phonons can arrive with group velocity $\mathbf{u}$ from the contact side. In other words, $\beta(\mathbf{u}(\mathbf{q}),\mathbf{r})=1$ within the solid angle under which the contact opening is visible. In all other cases $\beta=0$.

Using the phonon distribution function (27) it is easy to write an expression for the ballistic heat flux $\dot{Q}_B(T_d, T_m)$ transported by phonons from the dielectric into the metallic edge of a point-contact. This expression has the form of Eq. (3) where $T_1=T_d$, $T_2=T_m$, and $D_{12}^{\alpha}(\mathbf{q})$ is replaced by $D_{dm}^{\alpha}(\mathbf{q})$. We note that for a metal-dielectric contact it is convenient to examine in Eq. (3) the dispersion law of phonons for the metallic edge of the contact.

2. Phonon-electron scattering in the ballistic regime

The electronic thermal conductivity of a ballistic metal-metal point-contact can be represented as[83]

$$\dot{Q}_{EL}(T_1,T_2) = \frac{m_e}{12}\frac{S_0}{\hbar^3}\varepsilon_F(T_1^2-T_2^2). \tag{28}$$

Comparing this expresson with the expression for the phonon heat flux at low temperatures

$$\dot{Q}_B(T_1,T_2) = \frac{\pi^2}{40}\frac{S_0}{\hbar^3}\bar{D}(T_1^4-T_2^4)(\bar{u})^{-2}, \tag{29}$$

we obtain the relation

$$\dot{Q}_{EL}(T_1,T_2)/\dot{Q}_B(T_1,T_2) = \frac{10 m_e(\bar{u})^2}{3\pi^2\bar{D}}\varepsilon_F(T_1^2+T_2^2)^{-1} \gg 1, \tag{30}$$

where $\bar{D}$ and $\bar{u}$ are the average, over the branches of the phonon spectrum, low-frequency values of the energy transmission coefficient and the velocity of acoustic phonons, respectively. The latter inequality corresponds to the case where the electronic system has the higher low-temperature thermal conductivity.

Electrons in a metal-dielectric contact do not cross the contact boundary. Consequently, the presence of a metallic edge with high thermal conductivity has little effect on the magnitude of the heat flux. The phonon-electron scattering in the metallic edge of the contact can be taken into account in perturbation theory in the small parameter $d/l_{\text{ph-}e}$. The formal application of the formula for estimating the contribution of the phonon-electron scattering to the phonon heat flux gives a value of the order of

$$\dot{Q}_B\frac{d}{l_{\text{ph-}e}} \sim \dot{Q}_B\frac{dT}{a\varepsilon_F}. \tag{31}$$

However, the solution of the kinetic equation (25) shows that the contribution of phonon scattering by ballistic electrons vanishes to first order in $d/l_{\text{ph-}e}$.

Indeed, the phonon-electron collision integral can be written, using the ballistic phonon distribution function (the branch index is omitted), as

$$I_{\text{ph-}e}(\mathbf{q},\mathbf{r}) = \tau_{\text{ph-}e}^{-1}(\mathbf{q}) D_{dm}[N_p(\omega/T_m) - N_p(\omega/T_d)]\beta(\mathbf{u}(\mathbf{q}),\mathbf{r}). \tag{32}$$

Here $\tau_{\text{ph-}e}^{-1}(\mathbf{q})=2(m/\hbar)^2 W(\mathbf{q})[\omega(\mathbf{q})/q]$, W is the squared matrix element of the electron-phonon interaction, and m is the electron mass (a quadratic disperion law is assumed). We note that because of the factor $\beta(\mathbf{u}(\mathbf{q}),\mathbf{r})$ the collision integral is different from zero only at the points where injected phonons arrive from the dielectric.

The first-order correction $N^{(1)}$ to the ballistic distribution function has the form of an integral of $I_{\text{ph-}e}(\mathbf{q},\mathbf{r})$ along the trajectories of the ballistic phonons. It is convenient to calculate immediately the integral over the cross section of the contact:

$$\int_{z=0} d\mathbf{s}\,\mathbf{u}(\mathbf{q}) N^{(1)}(\mathbf{q},\mathbf{r}) = \int_{r_z>0} dr^3 \beta(-\mathbf{u}(\mathbf{q}),\mathbf{r}) I_{\text{ph-}e}(\mathbf{q},\mathbf{r}). \tag{33}$$

We note that the heat flux is calculated over the cross section of the contact assuming that the electrons which are elastically reflected from the boundary do not contribute to the thermal conductivity. Taking account of the possible reflection of phonons at the boundary, we find the correction $\dot{Q}^{(1)}$ to the heat flux:

$$\dot{Q}^{(1)} = \frac{1}{2\pi\hbar^2}\sum_{\alpha}\int dq^3 \omega^{\alpha}(\mathbf{q})(D_{dm}^{\alpha})^2 \times [N_p(\omega^{\alpha},T_d) - N_p(\omega^{\alpha},T_m)] \times \tau_{\text{ph-}e}^{-1}(\mathbf{q})\int_{z=0} dr^3 \beta(-\mathbf{u}^{\alpha}(\mathbf{q}),\mathbf{r})\beta(\mathbf{u}^{\alpha}(\mathbf{q}),\mathbf{r}). \tag{34}$$

This correction to the heat flux vanishes because

$$\beta(-\mathbf{u}(\mathbf{q}),\mathbf{r})\beta(\mathbf{u}(\mathbf{q}),\mathbf{r}) = 0. \tag{35}$$

Indeed, if in the ballistic regime one of the directions of the velocity $\mathbf{u}$ corresponds to a phonon arriving from the contact boundary (when $\beta=1$), then a phonon arrives along the opposite direction $-\mathbf{u}$ from the massive edge and $\beta(-\mathbf{u}(\mathbf{q}),\mathbf{r})=0$.

We note that the absence of an electronic contribution to the thermal conductivity, to first-order in $I_{\text{ph-}e}$, is associated precisely with the ballistic regime of phonon transport in a point-contact. In the case of diffusion transport of phonons in a metal, because of the smallness of the phonon elastic scattering length $d \gg l_r$ the isotropic parts of the function $\beta(\mathbf{u}(\mathbf{q}),\mathbf{r})$, i.e. $\beta_0(\mathbf{r})$, must be taken into account in the expression (34). In the diffusion regime $1-\beta_0(r) \sim (d/r)$. We obtain a divergence in the spatial integral appearing in the expression for $\dot{Q}^{(1)}$; this means that the problem must be solved in a variant which is nonlinear in $I_{\text{ph-}e}$.

It remains to estimate the contribution due to the inelastic electron scattering by the metal-dielectric boundary to the heat flux. Additional branches of the spectrum of the elementary excitations, such as, surface phonons, plasmons, and excitons, can exist on the surface of a metal. A detailed calculation of the effect of surface states on the state of the electronic system can be found in Refs. 84–86. The results of Refs. 85 and 86 lead to the conclusion that for transport effects the relative contribution of the interaction of electrons with surface phonons in a point-contact is small in the parameter λ_s/d compared with the contribution of volume phonons. The heat flux arising as a result of the inelastic electron scattering from the boundary of a metal-dielectric point contact can be estimated for $T_d > 1$ K and $T_d \gg T_m$ as

$$\dot{Q}_{\text{surf}} \sim \frac{S_0}{\hbar^3 \Theta_D} m_e T_d^4. \tag{36}$$

Under the above-indicated conditions the relative contribution of inelastic scattering of the boundary has the form

$$\dot{Q}_{\text{surf}}/\dot{Q}_B \sim \frac{m_e(\bar{u})^2}{\bar{D}\Theta_D} \sim \frac{\Theta_D}{\bar{D}\varepsilon_F}. \tag{37}$$

If the temperature T_d of the dielectric edge of a contact of size $d \sim 10$ nm decreases ($1\ \text{K} > T_d \gg T_m$), the case where $\lambda_s > d$ can occur. Then inelastic electron scattering by the boundary of the metal is determined by the parameter $d/l_{\text{ph-}e}$ calculated at the effective temperature T_d. The contribution of inelastic scattering by the boundary to the heat flux in this regime rapidly decreases with decreasing temperature:

$$\dot{Q}_{\text{surf}} \sim \frac{S_0 d}{\hbar^3 \Theta_D^3 \varepsilon_F a} m_e T_d^7. \tag{38}$$

We note that for $1\ \text{K} > T_d \gg T_m$ phonon diffraction effects accompanying transmission through the contact opening become substantial in contacts of size $d \sim 10$ nm.

3. Diffusion regime of phonon transport in a metal-dielectric contact

In the case of the diffusion regime of phonon transport in a metal-dielectric contact the electronic system can make a large contribution to the thermal conductivity.

As noted in Sec. III A, for elastic scattering of phonons, when the energy of the phonon system is not transferred from one frequency interval into another, the continuity equation for the energy flux can be written for each phonon frequency ω. If the elastic scattering is quite strong and a diffusion regime has been established in the edges 1 and 2 of a heterocontact, then the phonon distribution functions $N_{\mathbf{q},1,2}(\mathbf{r})$ are determined by their isotropic parts $\bar{N}_{1,2}(\omega,\mathbf{r}) = 0$. For an isotropic phonon dispersion law and an isotropic phonon momentum relaxation time $\tau_{\text{ph-}i}$, and assuming no sources of heat are present the continuity equation for the heat flux in the phonon system of each edge has the form div grad $\bar{N}_{1,2}(\omega,\mathbf{r}) = 0$. The boundary condition on the surface connecting the different edges can be constructed by examining the balance of phonon energy transport through the boundary at distances which are short compared with the elastic scattering length ($l_{1,2} \ll d$). If $\bar{N}_{1,2}(\omega,\mathbf{r})$ is continuous, once the energy flux has been calculated we obtain the result described by Eq. (17). We shall assume below that the index 1 or d corresponds to the dielectric edge, and the index 2 or m corresponds to the metallic edge.

When the conditions deviate from the ballistic regime, the condition (35) breaks down and the contribution of the phonon-electron interaction no longer vanishes. However, then, multiple phonon-electron scattering must be taken into account. It is convenient to do this using a method which was employed to describe the "reabsorption" of phonons in point-contacts.[53,87,88]

In the diffusion regime the phonon distribution function $N_{\mathbf{q},m}(\mathbf{r})$ can be sought as a sum of a symmetric S and antisymmetric $\mathbf{Mu}$ parts with respect to the directions of the group velocity vector u. The equations for $S(\omega,\mathbf{r})$ and $M(\omega,\mathbf{r})$ can be obtained from the kinetic equation (25) for phonons, using $I_{\text{ph-}e}$ and $I_{\text{ph-}i}$ in the τ approximation. These equations have their simplest form if it is assumed that the phonon dispersion law is linear and isotropic:

$$u^2 \operatorname{div} \mathbf{M} = 3\tau_{\text{ph-}e}^{-1}[N_P(\omega,T_m) - S(\omega,\mathbf{r})], \tag{39}$$

$$\operatorname{grad} S = -\tau_{\text{ph-}i}^{-1}\mathbf{M}. \tag{40}$$

If $\mathbf{M}$ is eliminated from Eq. (40), it becomes obvious that phonon propagation in the metal is accompanied by damping:

$$\Delta S = -l_{\text{tr}}^{-2}[N_P(\omega,T_m) - S(\omega,\mathbf{r})], \tag{41}$$

$$l_{\text{tr}} = (l_{\text{ph-}e} l_{\text{ph-}i}/3)^{1/2}. \tag{42}$$

Here $l_{\text{ph-}i} = u\tau_{\text{ph-}i}$ is the characteristic phonon momentum relaxation length.

Strong phonon-electron scattering has the effect that the nonequilibrium part of the phonon distribution function in the metal decays as $\exp(-r/l_{\text{tr}})$ away from the contact cross section ($r \gg d$). The characteristic decay length l_{tr} is close to l_a. The length l_{tr} has an obvious geometric meaning: if $d \gg l_{\text{tr}}$, then a region of width l_{tr}, where injected phonons decay, appears at the surface of the metallic edge. In this region heat is transferred from the phonon to the electron system.

The phonon energy flux at the contact boundary can be calculated using the continuity equation. The result is an expression similar to the one found in the diffusion regime for a dielectric-dielectric contact. However, in the case studied here the diffusion coefficient K depends on the decay length:

$$K^{-1} = \frac{3\pi}{32}\left(\frac{D_d^i d}{l_d^i} + \frac{D_m^i d}{l_m^i}\exp(-d/\pi l_{\text{tr}})\right). \quad (43)$$

It is obvious that the contribution of the metallic edge to the resistance becomes negligibly small for $l_{\text{tr}} \ll d$. However, we are interested in the more realistic case of weak volume decay of phonons, when $l_r = l_{\text{ph-}i} < d < l_{\text{tr}}$. Then

$$l_\alpha = 3^{-1/2} l_{\text{in}} = 3^{-1/2} l_{\text{ph-}e} l_{\text{ph-}d}^{1/2} (l_{\text{ph-}d} + l_{\text{ph-}e})^{-1/2}. \quad (44)$$

If it is assumed that because of the high impedance of the metal the condition $(\bar{D}_d/l_d) \ll (\bar{D}_m/l_m)$ is satisfied, then for $T_d \gg T_m \simeq 0$ we obtain the simple expression

$$\dot{Q}(T_d,0) = \dot{Q}^{(0)}(T_d,0)[1 + d\langle 1/l_\alpha\rangle_{T_d}] = \dot{Q}^{(0)} + \dot{Q}^{(1)}. \quad (45)$$

The notation $\langle 1/l_\alpha\rangle_{T_d}$ is introduced for the average value of the quantity $1/l_\alpha(\omega)$ at the temperature T_d corresponding to injected phonons. If the facts that in a metal l_r has a weak frequency dependence and in the diffusion regime $l_r \ll l_{\text{ph-}e}$ are taken into account, we obtain

$$\langle 1/l_\alpha\rangle_{T_d} \simeq \langle 1/(l_r l_{\text{ph-}e})^{-1/2}\rangle_{T_d}. \quad (46)$$

The quantity described by the formula (46) depends on the temperature of the phonons injected from the dielectric as $T_d^{1/2}$. Thus the temperature dependence of the heat flux $\dot{Q}$ in the diffusion regime deviates negligibly from the T^4 law: only the small correction to the phonon flux $\dot{Q}^{(1)}(T_d,0)$ depends on the temperature of the "hot" dielectric as $T_d^{4.5}$. The temperature dependence T^5 predicted in Ref. 78 can occur only if phonon-electron scattering in the contact is strong, when $l_r \gg l_{\text{ph-}e}$ and $l_{\text{in}} \simeq l_{\text{ph-}e}$.

IV. QUANTUM TRANSPORT OF PHONONS IN 3*D* CONTACTS

A. Diffraction of elastic waves by the opening of a 3*D* point-contact

Thus far we have described the calculation of ballistic transport of phonons under the assumption that the characteristic phonon wavelength is small compared with d (the geometric-optics approximation). The temperature dependence $\dot{Q}_B(T,0) \sim T^4$ can serve as a criterion for the occurrence of ballistic transport of phonons in the geometric-optics regime.

Low-temperature experiments[10,14,36] show that the temperature dependence of $\dot{Q}_B$, as a rule, has the more complicated form $\dot{Q}_B(T,0) \sim f(T)T^4$, where the function $f(T)$ has a sharp peak at $T \sim 1$ K (Fig. 2). It is natural to suppose that low-temperature anomalies appear as a result of the breakdown of the geometric-optics condition $d \gg \lambda$. Indeed, since at temperature T the characteristic phonon wavelength can be estimated as $\lambda \simeq a\Theta_D/T$ (where a is the lattice constant), it is easy to obtain the temperature T_{dif} at which the condition $d \sim \lambda$ is satisfied: $T_{\text{dif}} \sim \Theta_D a/d$. For $d \sim 100$ nm we obtain $T_{\text{dif}} \sim 1$ K. At this and lower temperatures phonon transport cannot be studied in the geometric-optics limit: the diffraction of elastic waves by the opening of the contact becomes substantial.

Let us consider a planar contact connecting two identical dielectric crystals. For $kd \leqslant 1$ the coefficient of energy transmission by an elastic plane wave through the contact is determined by diffraction effects and can be different from 1.[10,14]

In calculating the energy flux transported through a point-contact, the lattice oscillations are treated as an ensemble of bosons with energy $\hbar\omega(\mathbf{k})$, and diffraction by an opening makes the wave properties of the bosons important. Thus the calculation of the heat flux leads to the quantum problem of characteristic quasiparticles in a space with geometric constraints. As shown below, the quantum transport of heat is described by an expression similar to Landauer's formula for the electronic conductivity.[89,90] Just as in the case of quantum transmission of electrons through a point-contact, in our case the problem reduces to solving a stationary wave equation for a free particle. However, the boundary conditions on the surface of a contact, which are imposed on the solution of the wave equation, in the problem of the quantum transport of phonons, differ substantially from the standard zero boundary conditions (Dirichlet conditions). To obtain this boundary condition it is necessary to study the problem of the transmission of an elastic wave through a contact in the continuous-medium approximation.

When a plane wave with wave vector $\mathbf{k}$ is incident on the opening of a contact (we omit for the time being the branch index of the phonon spectrum) there arises an energy flux of the elastic wave appears. We denote by $\mathbf{W}(\mathbf{r},\mathbf{k})$ the flux density averaged over a period of a monochromatic oscillation. The total energy flux passing through the contact is $P(\mathbf{k}) = \int d\mathbf{S}_0 \mathbf{W}(\mathbf{r}(\mathbf{S}_0),\mathbf{k})$, where $d\mathbf{S}_0$ is an element of the surface of the chosen cross section of the contact. It is convenient to integrate $P(\mathbf{k})$ over the angular coordinates $\Omega(\mathbf{k})$ of the wave vector under the condition $u_z(\mathbf{k}) > 0$.

If diffraction effects can be neglected, then the elastic wave remains planar on the cross section of the contact and the following equality holds:

$$\int_{s_z(\mathbf{k})>0} d\Omega(\mathbf{k}) \int d\mathbf{S}_0 \mathbf{W}_0(\mathbf{k}) = \pi S_0 W_0(k) \quad (47)$$

(we confine our attention to a linear dispersion law for elastic waves $\omega = uk$; $\mathbf{W}_0(\mathbf{k})$ is the energy flux denity in the plane wave).

The ratio of the energy fluxes taking account of and neglecting diffraction is the energy transmission coefficient $\bar{D}(\mathbf{k})$

$$\bar{D}(\mathbf{k}) = \int_{u_z(\mathbf{k})>0} d\Omega(\mathbf{k}) \int d\mathbf{S}_0 \mathbf{W}_0(\mathbf{r},\mathbf{k})[\pi S_0 W_0(k)]^{-1}. \quad (48)$$

Now the heat flux through the contact can be written in the form

$$\dot{Q} = \hbar S_0 (8\pi^2)^{-1} \int dk k^2 u(k)\omega(k)\bar{D}(k) \times [n_P(\omega,T_1) - n_P(\omega,T_2)]. \quad (49)$$

Since we are talking about the heat flux transported by long-wavelength phonons, we shall calculate the energy fluxes, appearing in Eq. (48), in the approximation of a continuous elastic medium. Let us examine the harmonic oscil-

lations of the displacement vector **U** of the medium (with frequency ω). The energy flux density vector of an elastic wave has the form[91]

$$\mathbf{W} = -\sigma\mathbf{U}, \tag{50}$$

where the stress tensor σ_{ij} is expressed in terms of the tensor of elastic moduli and the tensor of deformations, i.e. in terms of the first derivatives of the displacements. In the simplest case of an isotropic medium, when the velocities of the transverse u_t and longitudinal u_l waves determine the tensor of the elastic moduli, we shall confine our attention to waves which are incident in the normal direction on the contact. Then, conversion of branches does not occur and the diffraction problem can be solved for each branch separately (we shall omit indices t and l). The energy flux $P(\mathbf{k})$, averaged over one period of the oscillations, on the cross section of the contact can be written in the form

$$P(\mathbf{k}) = -(\rho u^2\omega/2)\int d\mathbf{S}_0\,\mathrm{Im}[U^*(\mathbf{r})\,\nabla\,U(\mathbf{r})]. \tag{51}$$

Here $U(\mathbf{r})$ is a scalar function, appearing in the expression for the amplitude of the displacement vector,

$$\mathbf{U}(\mathbf{r},t) = \mathbf{e}_k U(\mathbf{r})\exp(i\omega t), \tag{52}$$

and ρ is the density of the crystal. Now the expression for the energy transfer coefficient $\bar{D}(k)$ becomes

$$\bar{D}(k) = -(\pi S_0 k)^{-1}\int d\Omega(\mathbf{k})\int d\mathbf{S}_0\,\mathrm{Im}(U^*\,\nabla\,U). \tag{53}$$

The quantity U satisfies the wave equation, which in stationary form is

$$-\Delta U_{\mathbf{k}}(\mathbf{r}) = k^2 U_{\mathbf{k}}(\mathbf{r}), \tag{54}$$

$k=\omega/u$, and the index k indicates that we are considering the solution of a wave equation corresponding to a plane wave with wave vector **k** incident on a half-space.

The boundary condition imposed on the solution of the wave equation assumes that **u** is a superposition of the plane wave arriving at and reflected from a screen Σ_1 and spherical waves propagating from the entrance and exit openings of the contact. The condition for the reflection of a wave from the free surfaces forming the contact (Σ_1 and Σ_2, see Fig. 1) is important. For elastic reflection the condition on the surface of a crystal which is not under any external pressure has the form

$$\sigma_{ij}n_j = 0. \tag{55}$$

(n is the normal to the surface of the crystal). Such a condition admits nonzero displacements on the surface of the contact. Strong damping of the waves at the surface of the contact can be described by requiring that the displacements U vanish on the surface (the Dirichlet condition).

We shall consider first the case of elastic reflection of waves from the boundary of a solid body. For normal incidence of waves on a contact the condition (55) for longitudinal and transverse branches assumes the form of the Neumann condition:

$$\mathbf{n}\ \mathrm{grad}\ U = 0. \tag{56}$$

To construct the solution of a wave equation in such a geometry an analogy can be used with the problem of the wave function of an electron passing through a contact. The three-dimensional variant of this problem was studied in Ref. 92, where the "spherical flow" model was used in the edges of the contact and cyclic harmonic conditions were used to solve the wave equation on the surface of the contact, which possesses axial symmetry.

The solution of the wave equation can be represented as a sum of normal modes corresponding to the boundary conditions imposed. In this case the energy transfer coefficient $\bar{D}$ is a sum over normal modes with index n (each mode is $(2n+1)$-fold degenerate because of the azimuthal symmetry of the problem):

$$\bar{D}(kd) = 4(kd)^{-2}\sum_{n=0}^{\infty}(2n+1)T_n(kd). \tag{57}$$

B. Quantum phonon thermal conductivity of a contact

The scheme presented above for calculating the energy transfer coefficient concerns low-frequency acoustic vibrations of a lattice. To calculate the total phonon flux the quantum statistics of the phonons must be taken into account. Then the expression for the heat flux through the contact becomes

$$\dot{Q}(T_1,T_2) = (\hbar/2\pi)\sum_{\alpha}\int d\omega\omega\Phi^{\alpha}(\omega)[n_P(\omega,T_1) - n_P(\omega,T_2)], \tag{58}$$

where $\Phi^{\alpha}(\omega)$ is the sum over normal oscillations

$$\Phi^{\alpha}(\omega) = \sum_{n=0}^{\infty}(2n+1)T_n(\omega d/u^{\alpha}).$$

Formulas of the type (58) possess great generality and a long history. The sets of resonance modes characteristic of waveguides with a variable cross section are conventionally studied by the methods of acoustics developed in detail in the mid-1900s.[93] The diffraction effects arising when an elastic wave enters the open end of a waveguide (for example, "horn cut-off") are well known in acoustics. However, the forced oscillations usually excited in acoustic waveguides when information is transmitted are far from the radiation of an equilibrium phonon thermostat. The balance of heat transport between thermostats separated by a phonon scattering boundary was first studied by Little[42] in connection with the calculation of the Kapitsa jump.[46] As a scattering mechanism Little examined the acoustic mismatch of continuous media in contact with one another. The next step in taking account of phonon scattering was taken in Refs. 94–96, where the wave propagation in discrete harmonic elastic chains containing a finite number of scattering impurities was investigated (see also Ref. 97). The model used in these works corresponds to heat transport between strongly anisotropic media separated by an impurity-containing layer. In such a system the scattering can be taken into account in a quite general form by introducing a set of coefficients $T_n(\omega)$, corresponding to different normal vibrations of the system

"chain with impurities." Just as in Little's model, there is no ballistic flow of phonons in the region near the contact in the chain model. Consequently, both models correspond to the case of small temperature differences. A general expression for the heat flux in the chain model can be obtained from Eq. (58) by expanding in the small parameter $(T_1-T_2)/(T_1+T_2)$. The expression (58) obtained in Ref. 14 corresponds to a different scattering mechanism—phonon diffraction by the aperture of a point-contact connecting three-dimensional phonon reservoirs with different temperatures. As a result of phonon flow, a "gigantic Kapitsa jump," equal to T_1-T_2, occurs in such a system. We also note that the structure of the expression (58) is similar to the expression for the quantized electric current in point-contacts.[98,99]

A thermostat which delivers equilibrium thermalized phonons into the contact region is not the most convenient source of phonons for studying phonon transport in a contact. In principle, in such investigations phonon sources with nonequilibrium quasimonochromatic distribution can be used.[100,101] In the limiting case when monochromatic phonons with distribution $N(\omega)=n\delta(\omega-\omega_0)$ transport the heat flux $\dot{Q}$ an expression similar to Landauer's formula[89,90] for the electronic conductivity is obtained

$$\dot{Q}=n(\hbar\omega_0/2\pi)\sum_{\alpha}\sum_{\mu,\nu}T^{\alpha}_{\mu,\nu}(\omega_0). \tag{59}$$

Here the indices μ and ν enumerate the transverse vibrational modes in a contact with transmission coefficients $T^{\alpha}_{\mu,\nu}$.

Apparently, when diffraction effects are taken into account in phonon transport in point-contacts, the picture becomes more complicated than in the case of electron transport. This is because the boundary conditions for elastic waves on the surface of a contact are more complicated. For real contacts these conditions may not reduce to the Neumann and Dirichlet problems stated here (a discussion of the choice of boundary conditions in quantum-mechanical problems can be found in Ref. 102.)

A form of the energy transfer coefficient that is convenient for performing calculations can be obtained by using the "spherical flow" model for the geometry of the contact.[92] This model can be obtained by rolling the initially flat surface of the screen into a tube and gluing the edges of the contact on the surface of a sphere. For a wave incident along the z axis the solution of the wave equation is symmetric with respect to this axis, and the Neumann condition is satisfied on the surface of the contact, rolled into a tube of vanishingly small diameter, as a result of the cylindrical symmetry.

The transmission coefficients T_n for $(2n+1)$-fold degenerate modes in the flow model for a planar "Sharvin" contact have the form

$$T_n^{-1}(kd)=1+S_n^2(kd), \tag{60}$$

$$S_n(kd)=2\sum_{m=0}^{n}\frac{(2n-m)!(2n-2m)!}{m![(n-m)!]^2}(n-m+1)\times(kd)^{2m-2n-1}. \tag{61}$$

The function $T_n(x)$ for $n>0$ has the form of diffuse steps; $T_n(x)\ll 1$ in the region $x\ll 2\sqrt{n(n+1)}$; $T_n(x)\simeq 1$ for $x\gg 2\sqrt{n(n+1)}$. Thus, $k_n=2\sqrt{n(n+1)}/d$ is the characteristic value of the wave number at which the normal mode with number $n>0$ starts to pass through the contact.

We call attention to the fact that the transmission coefficient for the zeroth mode is

$$T_0(kd)=(kd)^2/[4+(kd)^2]. \tag{62}$$

According to Eq. (62), $\bar{D}(0)=1$, i.e. long-wavelength phonons ($l\gg kd$) are essentially not reflected from the opening of the contact. This is due to the choice of the Neumann condition for solving the diffraction problem. The virtually complete transmission of a wave through the aperture with elastic reflection of a wave from the screen has been well studied.[103,104] For example, for normal incidence of a wave on a circular opening in a planar screen the variational principle applied to the Neumann problem gives the following expression for the energy transfer coefficient of a wave:[103]

$$D=8\pi^{-2}-\left[(2/3\pi)^2+\frac{8}{\pi^4}\right]k^2d^2. \tag{63}$$

It should be noted that the quantity $\bar{D}(kd)$ calculated according to Eq. (63) is essentially 1 in the entire range of values of the parameter kd.

For $kd\gg 1$ phonon transport can be studied in the geometric-optics approximation. In addition, the stepped character of the function $\Phi(\omega)$ of freqency becomes immaterial; it can be represented in the form

$$\Phi_{\text{geom}}(\omega)=\frac{S_0}{4\pi}\left(\frac{\omega}{u}\right)^2. \tag{64}$$

(We note that in the spherical flow model used here the contact area S_0 must be taken to be πd^2.)

The diffraction of a scalar wave by an ideally absorbing screen ($U=0$ on the screen) is, according to the expression in Ref. 105, an "archetypical" problem of wave mechanics. Although the solution of this problem has still not been found in closed form, for normal incidence of a wave on a screen the representation of the solution as a series is well known,[106,107] and the energy transfer coefficient $D(kd)$ has been calculated by the variational method.[105–108] Compared to the Neumann problem, a substantial difference in the results arises in the range $kd<5$.

The case of extremely long wavelengths ($kd\ll 1$) corresponds to Rayleigh emission of the incident wave through the opening in a contact. For a planar contact[108]

$$\bar{D}_{\text{Rayl}}=(9\pi)^{-2}(kd)^4. \tag{65}$$

For $kd>5$ the quantity $D(kd)$ undergoes negligible damping oscillations and then rapidly approaches 1 (the geometric-optics limit).

C. "Flow" model for the quantum thermal conductivity of channel contacts

The definition of the energy transfer coefficient for quantum transport of phonons leads us to calculations which are similar to finding the reflected and transmitted waves in channels in an elastic medium. The propagation of acoustic waves in long channels has been studied in detail (see, for example, Ref. 104). Taking account of edge effects system-

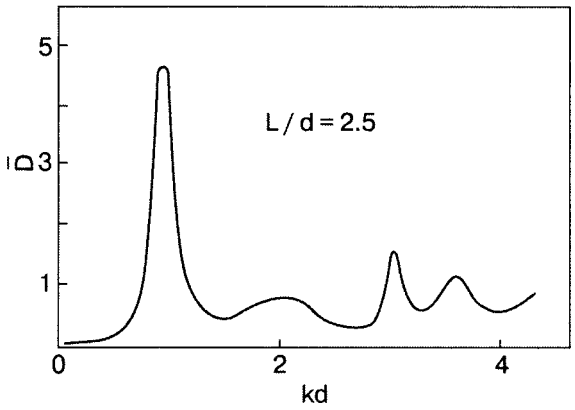

FIG. 8. Phonon energy transfer coefficient $\bar{D}$ for a channel contact with length to diameter ratio $L/d=2.5$.[14] The contact surface is assumed to be absolutely elastic. The calculation is performed in the spherical flow model.

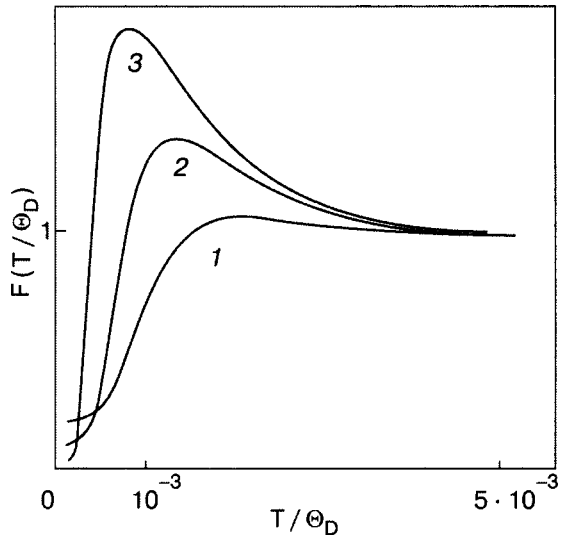

FIG. 9. Reduced phonon energy flux, calculated in the spherical flow model for cylindrical contacts with diameter d and length L.[14] The contact surface is assumed to be absolutely elastic. The calculation is performed for a cubic unit cell with period a, assuming a linear phonon dispersion law and $d=100a/\pi$ for different values of L/d: 1.5 (1), 2.5 (2), and 3.5 (3).

atically leads to the same difficulties as in the problem of a planar aperture. In Ref. 92 a contact in the form of a channel of length L is modeled by the condition that the corresponding points of the planar contact (in the spherical flow model) are connected by a one-dimensional transmission line of length L. The space of variables for the diffraction problem is the direct product of a sphere and a segment. This technique is justified, at least, for describing axial low-frequency vibrations, which can propagate in channels with absolutely rigid walls.[104] The transmission coefficient for low-frequency vibrations in this case is

$$T_0^L(kd)=\frac{(kd)^2}{(kd)^2+4\cos^2(kL)[1+\tan(kL)/kd]^2}. \tag{66}$$

It is evident that the function $T_0^L(x)$ is an irregular step for $L/d>1$ (for a sufficiently long channel). This is a consequence of the interference of waves reflected from the entrance and exit openings of the channel.

When the frequency of the incident wave equals the frequencies of longitudinal vibrations of the channel ($1+\tan(k_RL)/k_Rd=0$ or $k_R\simeq n\pi/L$ for $L\gg d$), the channel is an efficient transmitting device for acoustic waves. The planar sections of the screens Σ_1 and Σ_2 (see Fig. 1) at the entrance and exit of the channel can be regarded as horns, and at resonance, together with the channel, regions of the screens with area $S_R\sim(2\pi/k_R)^2$ participate in the vibrations. This increases the effective area of the contact in the ratio S_R/S_0 in the region of low-frequency resonances. We note that for very low frequencies (for $k\ll k_R$) the values of the energy transfer coefficient in the channel $\bar{D}^L$ decrease compared with the case of a planar contact, $\bar{D}^L(0)=\bar{D}(0)/(1+L/d)^2$ (see Fig. 8).

The discussion above referred to channels with absolutely rigid walls, which, mathematically, satisfy the Neumann condition. Channels with damping of a wave on the surface (the Dirichlet condition) have been studied in great detail in connection with the problem of quantum-mechanical ballistic electron transport in contacts.[109–115] Since it is impossible for low-frequency oscillations with $k>1/d$ to propagate in such channels, the "horn effect" does not arise in this case.

We shall describe the influence of diffraction effects on the thermal conductivity of contacts, considering the deviation of the heat flux from the T^4 law. For this we shall examine the function

$$F(T)=(60/\pi^6)(a^4/hu^2d^2)(\theta/T)^4Q(T,0), \tag{67}$$

normalized in a manner so that $F(T)\equiv 1$ in the geometric-optics limit ($kd\gg 1$). For a cubic lattice with lattice constant a we take $\Theta_D=hu/a$ (u is the sound speed).

Since these calculations are performed in the low-frequency range $\omega\ll\omega_D$, the details of the dispersion law at high frequencies are unimportant.

For the equilibrium (Planck) phonon distribution in the "hot" edge of a contact with temperature T the resulting temperature dependence of the heat flux no longer has oscillations which are characteristic of the energy transfer coefficient $\bar{D}$ of a wave. Only the peak corresponding to the low-frequency increase in the effective area of the channel contact remains. For realistic contact sizes ($d=100a/\pi$) and sufficiently long channels ($1.5<L/d<5$) diffraction effects become substantial at low temperatures $T_{\rm dif}\simeq 10^{-3}\Theta_D$ (see Fig. 9).

For zero boundary conditions on the contact surface (the case of strong damping) the diffraction effects reduce to a sharp decrease of the thermal conductivity of the contact for $T<T_{\rm dif}$. In the region of Rayleigh emission of waves through a planar contact

$$Q_{\rm Rayl}(T,0)=0.12\hbar^{-7}S_0d^4T^8\sum_\alpha u_\alpha^{-6}. \tag{68}$$

For small temperature drops on the contacts ($\Delta T\ll T_C$) the heat flux is proportional to ΔT with a coefficient to which the excited modes of quantum phonon transport contribute. At low temperatures the contribution of each quantum mode with unit amplitude, as follows from Eq. (58) (see Ref. 14) equals $(\pi^2/3h)T$. (We note that $3D$ contacts between three-dimensional heat reservoirs the modes are $(2n+1)$-fold de-

generate and the total flux in the multimode regime is proportional to T^3 and not T). The quantity $(\pi^2/3h)T$ is interpreted as a "quantum of thermal conductivity," although this expression is valid in the quite special case where the heat carriers are thermalized. In this connection, an expression obtained in Ref. 14 for the heat flux transported by phonons with fixed angular frequency ω_0 (59) can be analyzed. For a frequency-normalized distribution the coefficient $n=2\pi$, and each mode of the heat flux contributes an amount $\hbar\omega_0$. Thus the "quantum of spectral density of heat flux" is, as expected, $\hbar\omega$.

In 1998 two groups of authors[26,27] presented a calculation of quantized transport in a one-dimensional phonon system of a long contact ($L \gg d$) connecting two-dimensional heat reservoirs (see also Refs. 28 and 29). In long microbridges four quantum low-frequency modes exist for different types of elastic oscillations (longitudinal, two transverse, and torsional), and there are also optical-type shear modes (general with a two-dimensional reservoir). exist. The excitation energy E_0 of the optical modes depends on the thickness a_0 of the reservoirs and bridges. For $a_0=50$ nm in GaAs E_0 corresponds to 1.62 K. According to these calculations, the quantized phonon heat flux in long GaAs microbridges with cross section 50×50 nm at $T\sim 1$ K (when the first quantum mode determines the heat flux) becomes $4(\pi^2/3h)T\Delta T$. At lower temperatures the flux depends on the diffraction effects appearing at the junctions of the reservoirs and bridges; the "horn effect" does not arise in a one-dimensional phonon system. This picture, qualitatively similar to single-mode low-temperature quantized transport in three-dimensional contacts, is supplemented by the activation of optical nodes, which contribute to the heat flux at $T \sim 0.5$K.[23,24]

V. PHONON SCATTERING BY PLANAR DEFECTS OF A CRYSTAL LATTICE

A. Dynamics of a crystal surface with an adsorbed monolayer

It is completely obvious that the presence of defects (local or extended) greatly influences heat transport. We shall examine one of the interesting processes which occur with low-temperature heat transport with the participation of defects—the process of resonance transmission of phonons.

In situations where the conditions for ballistic transport presented above (see Sec. II) ae satisfied, the interface between contacts can be approximated, to a good approximation, by an infinite plane. In Refs. 116 and 117 the influence of a weakly coupled impurity monolayer on various low-temperature vibrational characteristics, including heat transport, was examined at a microscopic level. The model chosen was a fcc crystal where the interaction between the nearest neighbors in the volume of the crystal is described by a force constant α and the interaction of the impurity monolayer with the surface by the parameter $\gamma\alpha((\gamma \ll 1)$. In these works it is shown that when a wave with amplitude A and wave vector $\mathbf{k}(\chi,k_3)$ is incident on the surface from inside the volume of the solid body, the amplitude U_0 of the displacement of the surface impurity layer is given by the relation

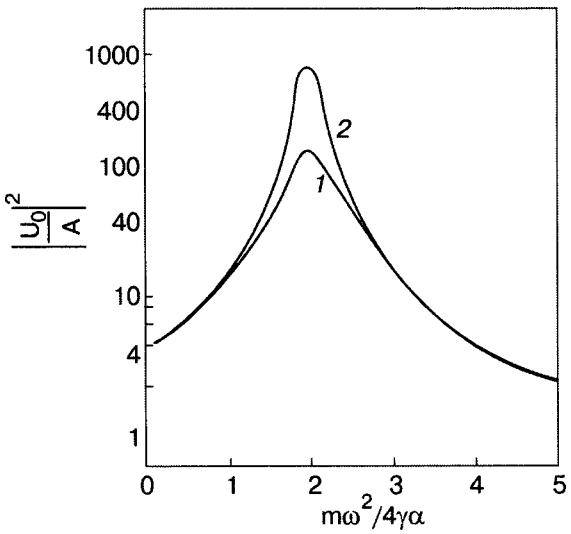

FIG. 10. $|U_0/A|^2$ versus the frequency of an incident volume wave at normal incidence: $M/m=0.5$; $\gamma=0.05$ (1) and 0.01 (2).[116]

$$\frac{U_0}{A} = 8i\gamma \sin k_3(\cos k_1 + \cos k_2)^2 \times\left\{-4\gamma^2(\cos k_1+\cos k_2)+\left(4\gamma-\frac{M\omega}{\alpha}\right)+\left[8+4\gamma-4\cos k_1\cos k_2-\frac{m\omega^2}{\alpha}-2(\cos k_1+\cos k_2)e^{-ik}\right]\right\}^{-1} \tag{69}$$

where $\chi(k_1,k_2)$ is a two-dimensional wave vector in the plane of the surface, m is the mass of the atoms in the crystal, and M is the mass of the atoms of the impurity monolayer. The quantity $|U_0/A|^2$, which determines the intensity of the acoustic radiation, is of interest. This quantity takes on its highest value in the long-wavelength region at

$$\omega_0^2 = \frac{4\alpha\gamma}{M} \tag{70}$$

and near this value it can be represented as

$$\left|\frac{U_0}{A}\right|^2 = \frac{64\gamma^2}{(4\gamma - M\omega^2/\alpha)^2 + 16\gamma^4/k^2\cos^2\theta}, \tag{71}$$

where θ is the angle of incidence of the wave on the surface. The maximum value of $|U_0/A|^2$ for normal incidence is $4m/\gamma M \gg 1$. Thus we are talking about resonance (quasisurface) vibrations of a semibounded crystal. In the limit $\omega \to 0$ the ratio $U_0/A \to 2$, which corresponds to a transition to a continuous medium. The typical frequency dependences of $|U_0/A|^2$ in the long-wavelength region are presented in Fig. 10.

Only surface states which are strongly localized at the boundary and are low-frequency states can make a substantial contribution to the low-temperature heat transfer through the boundary. Aside from these resonance states there is another surface state which is strongly localized at the boundary and which, to a first approximation in γ, possesses a frequency which is independent of χ (for sufficiently large χ)

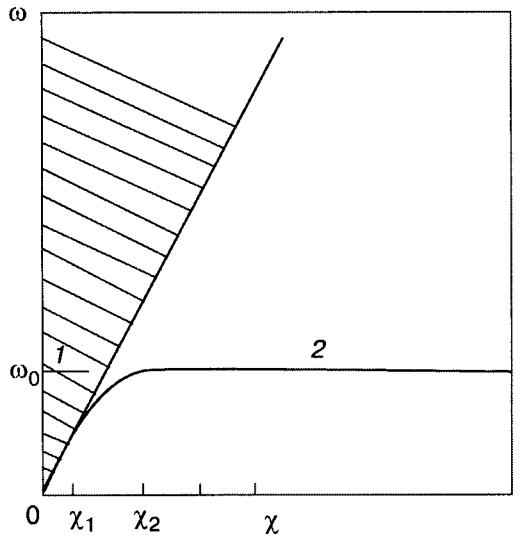

FIG. 11. Low-frequency spectrum in the model studied: 1—resonance state, 2—surface state.[116]

and equals ω_0 (71). In this approximation this state is a vibration of the impurity monolayer with and almost stationary substrate. The low-frequency spectrum in this model is presented schematically in Fig. 11.

If it is assumed that this crystal borders on a liquid (for example, liquid helium), then the vibrations of the surface layer of the crystal result in sound emission into the surrounding hydrodynamic medium.

We shall write the average intensity of the emitted sound with frequency ω in the form

$$\overline{W(\omega)} = 0.5\rho_f c_f \omega^2 |U_0(\omega)|^2 S. \tag{72}$$

The conservation laws for the energy and momentum of phonons limit the magnitude of the two-dimensional wave vector of a surface wave emitting sound into a liquid:

$$x^2 \leqslant \frac{\omega_S^2 a^2}{c_f^2} = \gamma \frac{c^2}{c_f^2}\frac{m}{M}, \tag{73}$$

where $a\sqrt{2}$ is the distance between the nearest neighbors. Thus the limiting short-wavelength surface states are nonradiating (we shall assume below that $\gamma(m/M)(c^2/c_f^2) < 1$).

Together with phonon emission there also occurs absorption of phonons incident from liquid helium on the surface; the difference of these two energy fluxes determines the resulting heat flux Q. Thus the coefficient of heat transfer of the boundary is

$$h = \frac{1}{S}\frac{d}{dt}\int \overline{W(\omega)} n(T) d\tau_\omega, \tag{74}$$

where $n(T)$ is the equilibrium phonon distribution function; $d\tau_\omega$ is an element of the phase volume. Using Eqs. (72)–(74) we obtain

$$h(T) = h_0(T) + h_r(T) + h_S(T), \tag{75}$$

$$h_0(T) = \frac{4\pi^2}{15h^3}\frac{\rho_f c_f}{pc^3} T^3 \text{ and } T \ll T_\gamma; \tag{76}$$

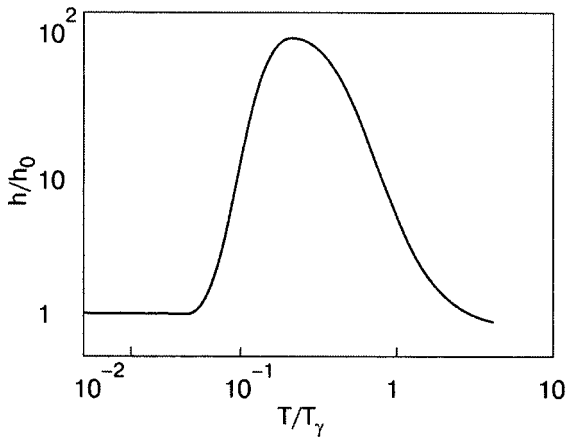

FIG. 12. Temperature dependence of the heat transfer coefficient of the boundary: $M/m = 0.5$; $\gamma = 0.01$; $(c^2/c_f^2) = 10$.[116]

$$h_r(T) = \frac{15}{16\pi^3}\frac{\rho_f c_f}{pc^3}\sqrt{\frac{m}{M_\gamma}}\left(\frac{T_\gamma}{T}\right)^5 \frac{\exp(T_\gamma/T)}{(\exp(T_\gamma/T)-1)^2} h_0(T); \tag{77}$$

$$h_S(T) = h_r(T)\frac{c^2}{c_f^2}. \tag{78}$$

Here

$$T_\gamma = \sqrt{\gamma \frac{m}{M}}\frac{\hbar c}{a}$$

($\hbar c/a$ is of the order of the Debye temperature). For $\gamma = 0.01$ and typical values of the Debye temperature $T_\gamma < 10$ K.

In the limit $T \to 0$ the quantity $h_0(T)$ in Eq. (75) corresponds to Khalatnikov's result[44,45] and makes the main contribution to $h(T)$. We note that even though the model is scalar, $h_0(T)$ agrees with Khalatinkov's result (obtained on the basis of the theory of elasticity taking account of volume waves of all polarizations and surface Rayleigh waves) to within a numerical factor close to 1.

The term $h_r(T)$ in Eq. (75) describes the contribution of resonance vibrations to heat transport, and $h_S(T)$ describes the contribution of surface vibrations. To calculate $h_S(T)$ the integration over χ was performed from 0; this gave a relatively small error.

For $T \sim T_\gamma$ we have $h_0(T) \ll h_r(T)$, which makes it possible to give in Eq. (76) the expression for $h_0(T)$ which is valid at extremely low temperatures.

Figure 12 shows the temperature dependence of the ratio $h(T)/h_0(T)$. Near $T = 1/5 T_\gamma$ a sharp increase in heat transport through the boundary as compared with the predictions of Khalatnikov's theory should be expected. Such an increase (by 1–2 orders of magnitude) has been observed in a number of experiments.[118–121]

The presence of one very sharp peak in the temperature dependence of heat transport is due to the choice of model—there is only one resonance frequency. In a real situation there can be several such frequencies, which should result in a smoother function (and even splitting) $h(T)$. We shall analyze examples of such situations below.

In conclusion, in the present section the mechanism of resonant low-temperature heat transport through a surface which adsorbs a weakly coupled impurity monolayer was described.

B. Resonance interaction of elastic waves with a two-dimensional defect on a boundary of a contact

Phonon transport through an intercrystalline boundary containing a layer of weakly bound impurities can be described using the "capillary" theory.[40,122–127] Using the terminology of the theory of an elastic medium we shall treat the impurity layer as a two-dimensional defect in the plane $z=0$, separating bulk crystals for which the elastic stresses and displacements are denoted by the indices (1) and (2). The characteristics of the planar defect are denoted by an index s. Boundary conditions can be obtained for the volume stresses $\sigma_{ik}^{(1,2)}$ and displacements $u_i^{(1,2)}$ in the $z=0$ plane by equating to zero the variation of the total (volume and surface) free energy of the intercrystalline boundary with respect to the independent dynamic variables $u_i^{(1,2)}$ and u_i^s:

$$\sigma_{\text{in}}^{(1)} = -\,\delta F_s/\delta u_i^{(1)}, \quad \sigma_{\text{in}}^{(2)} = \delta F_s/\delta u_i^{(2)}, \quad \delta F_s/\delta u_i^s = 0. \tag{79}$$

Here $\sigma_{\text{in}}=\sigma_{ik}^{n_k}$ and n_i is a unit vector normal to the interface and directed from the medium 1 into the medium 2.

Using Eq. (79) and taking account of the kinetic energy of the interface we obtain the following boundary conditions for the elastic stresses in the $z=0$ plane:

$$\sigma_{\text{in}}^{(1)} - \sigma_{\text{in}}^{(2)} = \rho_s \frac{\partial^2 u_i^s}{\partial t^2} + g_{\alpha\beta}\nabla_\alpha\nabla_\beta u_i^s + \delta_{i\beta}h_{\alpha\beta\gamma\delta}\nabla_\alpha u_{\gamma\delta}^s, \tag{80}$$

$$\sigma_{\text{in}}^{(1)} = A_{ik}^{(1)}(u_k^s - u_k^{(1)}), \tag{81}$$

$$\sigma_{\text{in}}^{(2)} = A_{ik}^{(2)}(u_k^{(2)} - u_k^s). \tag{82}$$

Combined with the boundary conditions (80)–(82) Eqs. (79) are a generalization to solids of the well-known Laplace formula for the excess capillary pressure. The equations (79)–(82) describe a linear relation between the displacements of the atoms of a planar defect and the corresponding elastic forces acting on the interface (Hooke's law for a two-dimensional defective layer).

The expressions (79)–(82) can be used to analyze the frequency and angular dependences of the coefficients of reflection r and transmission d and the magnitude of the surface displacement u_i^s for an elastic wave incident on an impurity layer separating two crystals.

We shall analyze a situation where an impurity two-dimensional layer separates two acoustically identical media ($Z_1=Z_2$, for example, a stacking fault in the bulk of a crystal). Using the conditions (79)–(82) of macroscopic dynamics of a two-dimensional defect, the following relations can be obtained[125] for the amplitudes of reflection, transmission, and surface displacement for a shear wave incident at angle θ to the normal to the surface and polarized in the plane of incidence xOz:

$$r = \frac{1}{\Delta_1}\left\{A_2C_{44}^2k\cos^2\theta - 0.5\left[\frac{\rho_s}{\rho}C_{44}k - (g_1+h_{66})k\sin^2\theta\right] \times (A_2^2 + C_{44}^2k^2\cos^2\theta)\right\}, \tag{83}$$

$$d = iA_2^{(2)}C_{44}k\cos\theta/\Delta_1, \tag{84}$$

$$u_0^s = \frac{u_0}{\Delta_1}(iA_2^2C_{44}k\cos\theta + A_2C_{44}^2k\cos^2\theta), \tag{85}$$

$$\Delta_1 = iA_2^2C_{44}k\cos\theta + A_2C_{44}^2k\cos^2\theta + 0.5 \times\left[\frac{\rho_s}{\rho}C_{44}k - (g_1+h_{66})k\sin^2\theta\right](A_2^2 + C_{44}^2k^2\cos^2\theta), \tag{86}$$

where $g_1=g_{xx}$, $h_{66}=h_{xyxy}$, and $A_2=A_{yy}^{(1)}=A_{yy}^{(2)}$.

The expressions (83)–(86) were obtained under the condition that the solutions of Eqs. (79)–(83) were sought in the form

$$u_y^{(1)} = u_0(\exp(ik\cos\theta z) + r\exp(-ik\cos\theta z)) \times \exp(ik\sin\theta x - i\omega t);$$

$$u_y^{(2)} = u_0 d\exp(ik\cos\theta z + ik\sin\theta x - i\omega t);$$

$$u_y^{(s)} = u_0^s\exp(-ik\sin\theta x - i\omega t);$$

$$\omega^2 = k^2C_{44}/\rho. \tag{87}$$

If the two-dimensional defect consists of a layer of light atoms, weakly coupled with the edges of the crystals, i.e. $A_2\rho_s \ll \rho C_{44}$ and $\omega \gg A_2(\rho C_{44})^{-1/2}$, then such a system of impurity atoms is characterized by the presence of low-frequency optical vibrations with resonance frequency

$$\omega \simeq \omega_0 \simeq (2A_2/\rho_s)^{1/2}. \tag{88}$$

At this frequency the amplitude of the displacements of the impurity atoms is much greater than the amplitude of the displacements of the crystal atoms:

$$u_0^s/u_{1,2} = (C_{44}\rho/A_2\rho_s)^{1/2} \gg 1. \tag{89}$$

A large increase of the amplitude of the vibrations in the intermediate layer (as compared with the edges of the contact) is extremely important for explaining the experimental results, which will be discussed below.

In this case the transmission and reflection amplitudes (83)–(86) have the following features. In the limit of very low frequencies ($\omega \ll \omega_0$) and long wavelengths ($kh \ll 1$) we have almost total nonreflection and total transmission of an incident elastic wave through a very thin layer in the volume of the crystal ($|r|<1, d\simeq 1$). At higher frequencies outside the resonance range ($\omega \neq \omega_0$) we have almost total reflection and nontransmission ($|r|\simeq 1, |d|<1$), which is due to the weak acoustic coupling between the equivalent crystals in contact with one another. In the resonance region ($\omega \approx \omega_0$), for nonglancing angles of incidence the coupling between the crystals in contact with one another effectively increases and total transmission of the wave through a planar defect occurs ($|r| \ll 1, d\simeq 1$) (Fig. 13).

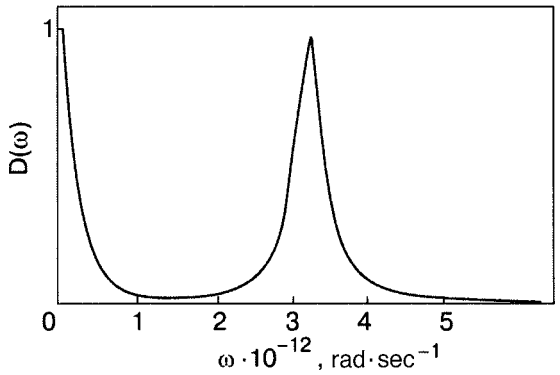

FIG. 13. Frequency dependence of the energy transfer coefficient in the presence of a weakly bound impurity layer between KBr–KBr crystals.[40]

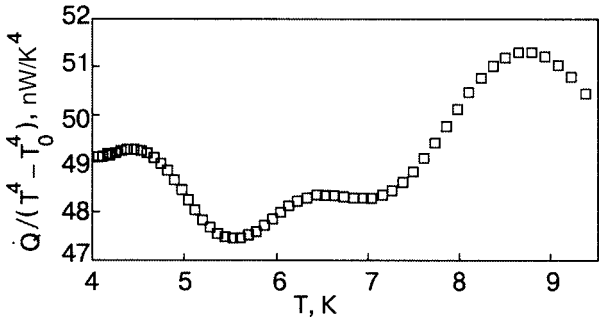

FIG. 15. Experimentally observed temperature dependence of the reduced heat flux in Si–Cu point-contacts above 2 K.[10,36]

C. Multichannel interfacial scattering in a point-contact

In Refs. 10 and 36 the heat flux in the ballistic regime in Si–Cu point contacts was studied in the temperature interval 0.1–10 K. (A model of such a contact is shown in Fig. 14.) An anomalously large peak in the reduced heat flux was observed in the interval 0.1–1 K. This peak was predicted theoretically in Ref. 14, where the theory of the quantum transport of phonons in point-contacts was developed. We note that an analogous theory of quantum transport of electrons was constructed in Refs. 26, 28, and 29 Additional peaks in the temperature dependence of the reduced heat flux were observed experimentally in Refs. 10 and 36 at temperatures above 2 K (Fig. 15). As follows from the theory of quantum point-contact transport of phonons,[14] in this temperature range phonon transport occurs in the geometric-optics regime.

Therefore these peaks cannot be due to quantum diffraction effects. Consequently, to explain them it is necessary to examine a different mechanism of ballistic transport of phonons through the interface between two media.

Analyzing the data of Refs. 10 and 36, using the model examined above, it can be concluded that the series of anomalous peaks in the reduced thermal conductivity above 2 K is due to multichannel resonance transmission of phonons through impurity layers located between two solid media in contact with one another. To describe phonon transport we shall employ the capillary theory of the transmission of elastic waves through a planar defect.[122–127]

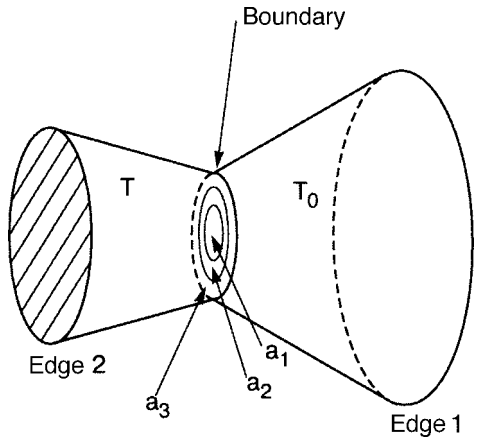

FIG. 14. Schematic model of a contact. T and T_0—temperatures of the massive edges of the contact; a_1, a_2, and a_3—zones with different composition of the interface layer.

A mechanism of resonance transmission of phonons through a planar defect was described in the preceding section under the assumption that there is one resonance frequency. This situation corresponds to the fact that the intermediate layer, through which resonance heat transfer occurs, is uniform with respect to both the composition of impurities and thickness along the entire contact boundary. However, in real experiments it is necessary to take account of the fact that the surface of a contact, as a rule, consists of a collection of sections on which the composition of the impurities and the thickness of the layer can be different. In this case it can be said that different channels of phonon transport correspond to different sections of the planar layer. Each channel has its own resonance frequency. Since phonon transport at temperatures above 2 K is being studied, it obeys the laws of geometric optics. Therefore the total phonon flux through the contact is a sum of fluxes in individual channels. Let S_n be the area of a part of the corresponding contact with number n and $D_n(\omega)$ the phonon energy transmission coefficient for the nth channel, characterized by the resonance frequency of transmission ω_n. Then the effective coefficient of multichannel resonance transmission of phonons is described by the expression

$$D(\omega) = \frac{\sum_n^{n_{\max}} D_n(\omega) S_n}{\sum_{n=1}^{n_{\max}} S_n}. \tag{90}$$

The capillary theory of phonon transport makes it possible to take account of different types of impurities and different channel thicknesses using a single parameter ρ_s. Assuming all channels to be uniform with respect to the impurity composition we can write

$$\rho_{sn} = \rho_{s1} n, \tag{91}$$

where ρ_{s1} is the excess surface density of the molecular layer with the smallest thickness and n is the number of molecular impurity layers in the channel, which serves as the channel number. The frequencies ω, which ensure resonance transmission through a point-contact, vary according to Eq. (88).

The theory developed above for multichannel resonance transport of phonons through an interface separating two media can be used to interpret experiments measuring the ballistic transport of phonons in a Si–Cu point-contact. Low-temperature quantum ballistic phonon transport was

observed in Ref. 18 in the temperature range 0.1–3 K. In addition, the reduced point-contact heat flux in the geometric-optics regime for phonons was measured in the temperature range 3–10 K. The results of this work have shown that in this temperature interval the reduced heat flux through a point-contact is a nonmonotonic function of the temperature and has sharp peaks at temperatures $T_1 = 4.46$ K, $T_2 = 6.53$ K, and $T_3 = 8.77$ K. It seems to us that the model developed in the preceding sections can be used to explain the series of peaks observed in Ref. 10 in the reduced heat flux. The appearance of the peaks is a characteristic consequence of resonant transport. The model of a narrow resonance peak was used for single-channel resonant transport, studied in Ref. 38. This model reduces to the following.

The total heat flux $\dot{Q}$ can be written as a sum of the ballistic flux $\dot{Q}_B$ and the resonance flux $\dot{Q}_R$. Assuming a narrow resonance peak at frequency ω_0^α we obtain the following formula for the temperature dependence of the heat flux:

$$\dot{Q}(T,T_0) = C(T^4 - T_0^4) + \sum_\alpha K_\alpha \left[\frac{1}{\exp(\hbar\omega_0^\alpha/T) - 1} - \frac{1}{\exp(\hbar\omega_0^\alpha/T_0) - 1} \right]. \quad (92)$$

To separate both contributions to the heat flux the heat flux must be divided $(T^4 - T_0^4)$. This model (using only one frequency) can be used to explain the experimental data with correlation coefficient 0.95. The resonance frequency ω_0 is related with $T_{\max}$ by the relation $\hbar\omega_0 = 3.89 T_{\max}$.

Using the multichannel resonant transport model, we shall modify the expression (92) as follows:

$$\frac{\dot{Q}}{T^4 - T_0^4} = \frac{1}{T^4 - T_0^4} \sum_{n=1}^{3} K_n \left\{ \left[\exp\left(3.89 \frac{T_n}{T} \left(1 + \frac{1}{T_s^2}(T - T_n)^2 \right) \right) - 1 \right]^{-1} - \left[\exp\left(3.89 \frac{T_n}{T_0} \right) - 1 \right]^{-1} \right\} + C. \quad (93)$$

The expression (93) takes account of the presence of three resonant transport channels. The temperature $T_0 = 0.15$ K is the constant temperature of the cold edge of the contact. The quantities T_n $(n = 1, 2, 3)$ correspond to the temperatures at which peaks are observed in the reduced heat flux. The constant C is the average reduced heat flux through a point-contact in the temperature range from 4 to 9 K. According to the experimental data, $C = 49.55$ nW/K^4. The coefficients K_n are proportional to the intensities of the peaks observed experimentally:

$$K_1 = 0.7 \text{ nW}, \quad K_2 = 2 \text{ nW}, \quad K_3 = 50 \text{ nW}. \quad (94)$$

The additional term containing T_s effectively takes account of the instability of the intermediate weakly coupled impurity layer near resonance. This is due to the fact that, according to the expression (89), $u_0^s/u_{1,2} \gg 1$. The role of the adsorption-desorption mechanism of impurity atoms is discussed in Ref. 116 (see also Ref. 17). The optimal agreement between the experimental and theoretical results is obtained at $T_s = 1.5$ K.

The results of a numerical calculation performed using Eq. (93), which are presented in Fig. 16, show that the proposed model describes in quite great detail the experimental results presented in Fig. 15. We note that the temperature T_s used in the calculations corresponds to the coupling energy between the impurity layer and the contact edges. The temperature T_s is two orders of magnitude lower than the Debye temperature of the crystals forming the edges of the contacts. This agrees with the fact that the constant characterizing the coupling of an impurity layer with the edges of a contact is two orders of magnitude smaller than the coupling constants inside the crystals forming this contact.[40]

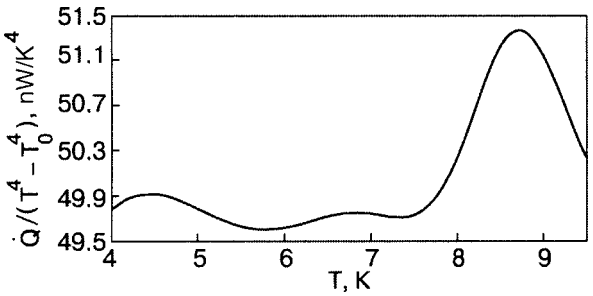

FIG. 16. Results of a numerical calculation using Eq. (93) in the model considered.

The formulas (91) and (92) make it possible to estimate the parameters of different phonon transport channels. The coefficients K are proportional to the areas of the different interfacial layers. Taking the area of the channel with the highest resonance frequency to be 1 we the ratios between the areas of the layers participating in resonant transport: 1:0.04:0.014. Combining the relations (91), (92), and (94) we obtain the relation

$$\left(\frac{T_{\max n}}{T_{\min m}} \right)^2 = \frac{\rho_f^m}{\rho_f^n} = \frac{L_m}{L_n}. \quad (95)$$

The experimental data yield

$$\frac{L_2}{L_3} = 1.8 \pm 0.2, \quad \frac{L_1}{L_3} = 3.8 \pm 0.2, \quad (96)$$

where L_3 corresponds to the number of layers in the channel with the highest resonance frequency (smallest ρ_s). It follows from the relation (96) that of the channels studied the lowest-frequency channel $(n = 1)$ contains the maximum number of layers (approximately 4 times greater than the relatively high-frequency channel with number $n = 3$), and the intermediate-frequency channel $(n = 2)$ actually contains two times more layers than the high-frequency layer with $n = 3$.

The mechanism of resonant phonon transport studied above is apparently characteristic for heat transfer between two media. Resonant heat transfer is substantial, for example, in heat transfer between a solid body and liquid helium in the presence of a matching layer.[116,17] In point-contacts molecules of water or solidified inert gases adsorbed on the interface can act as a resonance layer. The structure of water layers on the surface of crystalline silicon or silicon substrates was modeled theoretically in Refs. 128–130 and studied experimentally in Ref. 131. The results presented in the review give additional information on the dynamical properties of layers formed on the surface of silicon crystals.

Peaks in the reduced heat flux are also observed in other contacts, for example, KBr–KBr and KBr–Cu.[36] A low-

temperature peak at 5.7±0.2 K was observed in these contacts. This peak can also be explained using the theory of resonant transport.[132] We note that the phenomenon of resonant transport makes it possible to study the structure of interfacial layers and control heat transmission between two media, using controlled introduction of impurities, weakly bound with the contact edges, into the interface separating the layers.

VI. MODIFICATION OF THE PHONON SPECTRUM IN NANOSTRUCTURES

A. Contribution of the boundaries to the phonon spectral densities of bounded systems

Several types of size effects appear as the dimensions of contacts decrease. These effects are due to the characteristic scales in which different processes occur in solid bodies. For characteristic contact sizes from 100 to 10 nm, at low temperatures, a ballistic regime of charge and heat transport is established in point-contacts, since under these conditions the inelastic carrier scattering lengths are large compared with the dimensions of the contact. However, on these scales the carrier dispersion laws can still be regarded as close to the analogous dispersion laws in bulk solids.

For contact sizes ranging from 10 to 1 nm, the influence of distortions of the crystal structure in the contact region on the form of the vibrational spectrum of the lattice becomes substantial. Even when the crystal structure remains regular in the contact zone, the contribution of surface vibrational states can no longer be neglected. This effect is a mesoscopic phenomenon. Finally, for contact dimensions of the order of 1 nm ("single-atom contacts") effects due to size quantization of charge carriers in a point-contact appear.[133,134]

It is convenient to analyze the vibrational characteristics of the atoms of such systems by the methods based on the translational invariance of the lattice. These methods are suitable for describing crystalline and disordered systems. A very informative characteristic of the vibrations of disordered systems and complicated crystalline lattices or crystals with defects is the so-called local site density,[135] which describes the contribution of a given site to the vibrational spectrum of the entire system. The local densities can be calculated using the methods characteristic for calculations of the spectral characteristics of regular crystalline structures, for example, an expansion in plane waves.[135–137] However, as a rule, this approach leads to very great and often insurmountable mathematical difficulties when performing concrete calculations of given characteristics. The method of Jacobian matrices makes it possible to avoid these difficulties.[138–141] This method makes it possible to find, in the harmonic approximation, the frequency distribution of the vibrations without calculating the dispersion relations and the polarization vector. Moreover, this method makes it possible to find a more detailed information than that contained in the local densities about the frequency spectrum of the vibrations of the system.

In Ref. 142 it is shown on the basis of the results of numerical modeling that the local densities for the atoms comprising point-contacts differ substantially from the spectral density of a regular crystalline structure. A substantial relative increase of the number of low-frequency vibrations

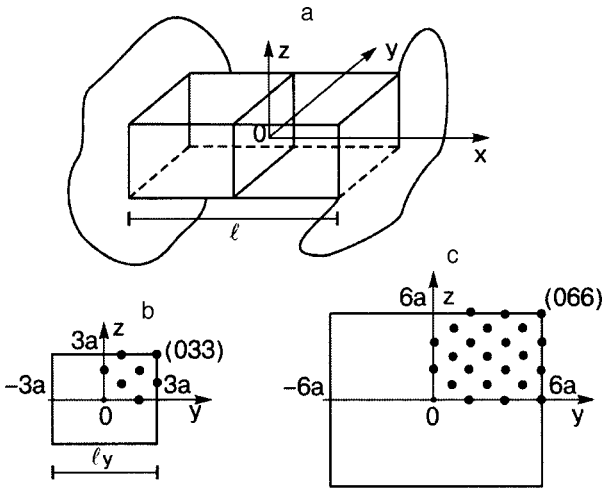

FIG. 17. Schematic model of a point-contact (a) in a contact section with edge 6*a* (b) and 12*a* (c).

of the atoms in the point-contact occurs. The differences between the local densities of "surface" and "edge" atoms in a contact were traced. Since the method of point-contact spectroscopy makes it possible to find the spectral function of the electron-phonon interaction, which is an integral characteristic of a crystal, a comparative estimate was made of the contributions to the point-contact spectrum of the contact region and its massive edges. It was shown that the modification of the point-contact spectra becomes substantial for contacts of the order of tens of interatomic distances in size. Here, the size modification of the spectrum is most effectively manifested in contacts in the form of an extended bridge.

The presence of a large number of "defect" atoms lying near the edges or faces of the bridge is characteristic for a contact. In addition, the vibrational characteristics of atoms located in the near-surface regions of the edges will be appreciably different from the corresponding characteristics of atoms in the bulk.

We shall assume that the contact edges in the contact itself are made of the same dielectric, possess fcc structure, and are commensurate with one another. We shall also assume that the contacts consist of a bridge, having a square cross section, between two surfaces of semibounded crystals, such that the surfaces are also the (100) crystallographic planes and are formed by breaking of the bonds between neighboring planes. The relaxation-related change in the interaction of atoms in the contact zone and on the contact surfaces and contact-edge surfaces was neglected.

The geometry of the contact and the coordinate system adopted are shown in Fig. 17. Numerical calculations were performed for contacts of length L equal to eight interlayer spacings. To study the influence of the dimensions of the cross section of the contact on its dynamical characteristics, contacts with a square cross section with edge length 6*a* and 12*a* (*a* is the lattice constant) were studied.

Figure 18 shows the results of a calculation of the function $\rho(\omega)$ for the atom (033) lying at the center of a contact edge with $l_z=6a$ (curve *1*). For comparison, the results of a calculation of similar functions for atoms located on a free

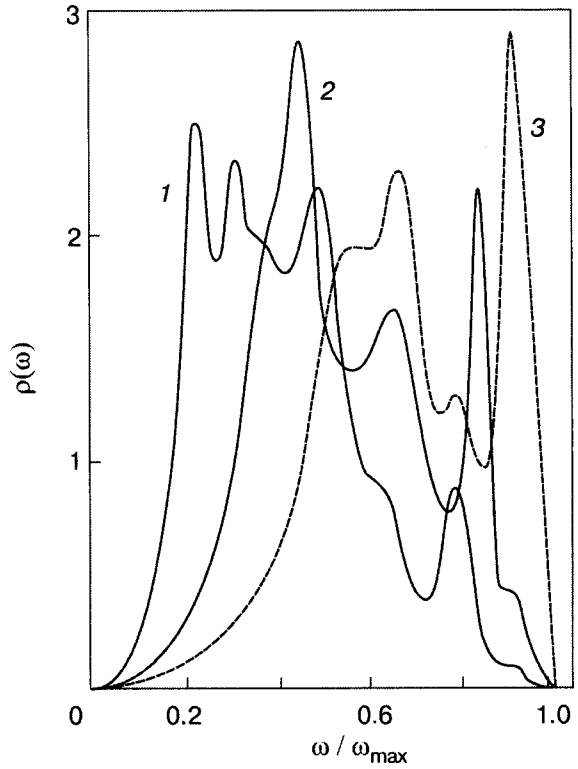

FIG. 18. Local densities for atoms lying at the center of a contact edge with $l_z=6a$ (1), on a free (001) surface of a fcc crystal (2), and in the bulk of a fcc crystal (3).[15]

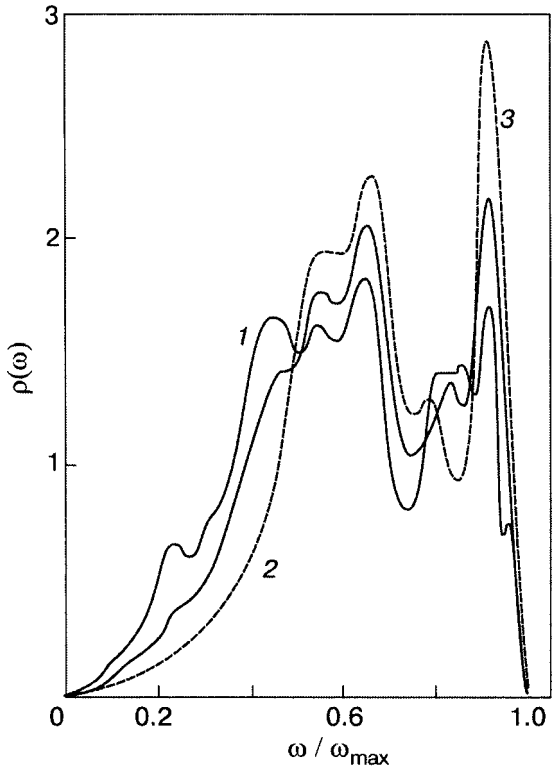

FIG. 19. Local densities averaged all atoms in the central section $x=0$. Curve 1—$l_z=6a$; curve 2—$l_z=12a$; curve 3—phonon density of states of an unbounded fcc crystal.[15]

surface (curve *2*) and in the bulk of a fcc crystal (curve *3*) are presented.

Undoubtedly, the character of the vibrations of the atoms depends not only on the positions of the atoms but also on the dimensions of the contact cross section. The calculations show that for atoms located at the centers of the cross sections $x=0$, doubling the dimensions of the cross section substantially decreases the number of low-frequency states: the local density at the site (000) of the bridge with cross section $l_z=12a$ is virtually identical to the local density of a bulk atom. However, for the (033) and (066) atoms lying on the edges, an increase in the size of the cross section does not produce an appreciable decrease in the number of low-frequency states. We also note that as the distance of an atom from the face of the bridge increases, the local density of the atom deforms to a form which is characteristic for the spectral density of free-surface atoms, and for atoms located on the face itself the density will depend strongly on the dimensions of the face.

The dependence of the local densities or atoms on the linear dimensions of the contact cross section is clearly seen in Fig. 19, which shows the results of a calculation of the local densities $\rho(\omega)$ averaged over all atoms of the cross sections $x=0$. As the dimensions of the contact increase, the number of low-frequency states appreciably decreases, which is obviously due to an increase in the fraction of atoms whose vibrational characteristics are close to those of bulk atoms. It is obvious that the number of such atoms will increase not only with increasing dimensions but also toward the edges of the contact. Therefore the largest increase in the number of low-frequency states obtains with a decrease of the cross section of a contact as the distance between the edges increases.

B. Electron-phonon interaction cross section in mesocontacts

If the conductivity of a point-contact is due to the presence of a degenerate electron gas, then the nonlinearities of the current-voltage characteristic which are caused by a weak electron-phonon interaction carry information about the vibrational spectrum of the crystal lattice.[2–6]

A voltage V applied to a point-contact (ordinarily, the characteristic phonon energies correspond to $V \approx 10-100$ mV) creates a condition for accelerating electrons which have arrived in the contact from one of the massive edges (viewed as a thermostat), and retarding the electrons arriving from the opposite edge of the contact. The point-contact current is transported by these two groups of electrons, which exchange energy with one another and with the phonon system only to a small degree, since the inelastic electron relaxation length l_ε in point-contacts is large compared to the characteristic size of the contact (for example, its diameter d):

$$d \ll l_\varepsilon, \tag{97}$$

If the contact size is small compared to the elastic electron scattering length in the conductor, then the electron transport regime in the contact is said to be ballistic.

The inelastic electron-phonon scattering gives a correction $I^{(1)}$, which is a nonlinear function of the applied voltage V, to the point-contact current. To describe this effect in point-contacts which are large compared to the deBroglie

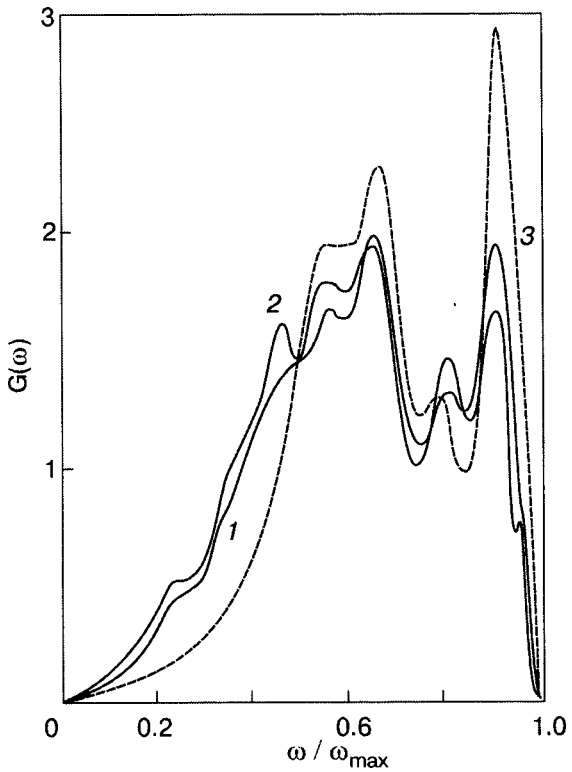

FIG. 20. Point-contact functions $G(\omega)$ for point-contacts of different length $l_x(l_y=l_z=6a)$. Curve 1—$l_x=8a$; curve 2—$l_x=La$, $L\gg 1$; curve 3—phonon density of states of an unbounded fcc crystal[15] (see Refs. 6 and 15 for the definition of the point-contact electron-phonon interaction function).

wavelength of an electron it is sufficient to use a system of coupled kinetic equations for the electron-phonon system of the contact. Treating the correction for the electron distribution function $f_{\mathbf{p}}(r)$ in first-order perturbation theory in the electron-phonon interaction integral, the inelastic correction to the point-contact current and point-contact electron-phonon interaction function $G(\omega)$ can be found.[6,143]

The spectra 1 and 2 in Fig. 20 are close to the point-contact spectra for a long channel.[143] The difference between these spectra reflects the increase of the length of the contact. It is evident that an increase of the length of the bridge results in an appreciable decrease of the contribution of the vibrations of the surface atoms of the contact, and the high-frequency region of the spectrum is almost identical to the spectrum of a "volume" contact.

The computational results show that all frequency anomalies of the point-contact spectrum, which are associated with the contribution of the vibrational states of the contact surface (see Fig. 20), should be observed in contacts in the form of a bridge of atomic dimensions. The calculations indicate the range of contact sizes where this effect can be expected to occur. The transfer size of a contact should not be much greater than 10 interatomic distances. The length of the bridge forming the contact should be at least of the same order of magnitude, although the effect is sharpest in contacts with the form of an elongated bridge between massive edges. Therefore if the diameter of a contact is greater than 10 interatomic distances, then the contact can be regarded as a "volume" contact.

The estimate made in Ref. 142 of the modification of the phonon spectra refers to the case where the contribution of surface vibrations becomes large, and the contact diameter d is chosen to be equal in order of magnitude to the damping depth λ_s of surface excitations. The limiting case ($d\gg\lambda_s$) is studied in Ref. 86, and it is shown that the inelastic interaction of conduction electrons with the surface vibrations of a crystal lattice can be taken into account, just as in the case of volume oscillations, using the kinetic equation where the surface scattering is taken into account via a boundary condition.[84,85] The form of this boundary condition is due to an effective summation over a near-surface layer of thickness λ_s. The contribution of surface vibrations to the point-contact spectrum in the latter case is found to be small in the parameter λ_s/d compared with the contribution of volume vibrations. We note that the expression obtained in Ref. 86 for the K factor of surface vibrations is virtually identical to the analogous quantity for volume vibrations in the case of a channel contact.

VII. CONCLUSIONS

The present review examined the problem of the effective removal of heat using point-contacts. Numerous measurements of the low-temperature ($T\leqslant 30$ K) phonon thermal conductivity of mechanical (clamped) contacts between solids show that the ballistic phonon transport regime is not at all exotic, even for macroscopic samples.[16–18,66–72] It is well known that in mechanical contacts the real area of a contact is 1–2% of the nominal area of the media which are touching one another.[18] At low temperatures a macroscopic contact must be viewed as a very large number of parallel point-contacts. In such a system, in contrast to a single point-contact, it is impossible to maintain a large temperature drop (Kapitsa jump) between the massive edges of the contact. However, in this case it is possible to introduce the thermal resistance of the contact R_T (see Sec. II C) which, according to Eq. (7), is found to be proportional to T^{-3}. This temperature dependence of the thermal resistance of a macroscopic contact serves as a criterion for realizing ballistic phonon transport in individual point-contacts.

The problem of phonon transport is also important in quasi-low-dimensional systems (including HTSCs). It should be noted that whatever the mechanism of superconductivity in HTSCs, the role of phonons in such systems is decisive,[144,145] which once again underscores the need for investigating the phonon properties of layered systems. Thus, for example, new magnetic materials,[146,147] which can be used to increase magnetic storage density and to develop quantum computers, are being developed based on layered structures. For such systems it is important to study the thermodynamic characteristics, including the heat capacity, which are due to phonons, since the correct identification of the lattice contribution is necessary for subsequently taking into account the contribution other excitations (specifically, magnetic excitations).

We note also that aside from quasi-low-dimensional compounds, structures with so-called fractional dimension, which contain inclusions which have a fractal geometry, are of interest.[148] In such systems the fracton-phonon interaction can make a large contribution to heat transfer.[149]

Heat transfer between two media (by means of point-contacts) in the presence of a controllable composition and

number of intermediate layers is now being studied as an elaboration of the results obtained in Refs. 150 and 151. This will make it possible to determine the dynamical coupling constants between the layers and the contact edges.

The experimental results and theoretical models examined in the present review refer to a wide range of important problems associated with quantum transport in the ballistic regime, and under conditions where various scattering mechanisms must be taken into account.[152] Previously, the quantum transport of charge[153,154] and heat[97] in contacts was studied when describing an electronic system. However, it is now clear that quantum heat transport can be described on the basis of a general formulism of the transfer of heat, entropy, and information, irrespective of the nature of the carriers.[155,156] The universal properties of heat transport, which do not depend on the carrier statistics, were demonstrated in Ref. 157. In the last few years of the last century the development of nanolithography made it possible to reproduce the experimental scheme with a suspended phonon reservoir, using long dielectric microbridges with controllable geometry.[21,158] It became clear that when the diameters of microbridges decrease to tens of nanometers quantization effects will make the determining contribution to the low-temperature phonon thermal conductivity of such systems. Quantum transport of phonons was first recorded using clamped Si–Cu $3D$ contacts,[10] and this phenomenon was soon investigated in experiments using long semiconductor microbridges.[23,24] As a result of the inclusion of optical modes, the interpretation of the experimental data on low-temperature thermal conductivity of such contacts requires a careful analysis of the dispersion laws for $2D$ structures.[159,160] Another important problem is taking account of quantum effects associated with scattering by the imperfect walls of long channels.[161]

Phonon transport in point-contacts and microbridges is increasingly becoming a subject of investigations which rely on the modern development of different variants of nanotechnology.[162–168] Thus experiments studying the thermal conductivity of individual carbon nanotubes have become possible.[169,170] In the last few years heat conducting point-contacts have been studied not only as objects of experimentation but also as components of nanodevices under development.[171–174]

Some of us (A.F., E.S.S., and A.G.Sh.) performed our work in Kosice at Safaric University (Slovakia) as part of projects APVT-20-009902 and APVT-20-005204 under grant No. 1(0430)03.

We thank L. A. Pastur for helpful discussions and support.

One of us (A.Sh.) dedicates his share of this work to Corresponding Member of the Ukrainian National Academy of Sciences, Igor' Orestovich Kulik, who was his first teacher in theoretical physics, in honor of Igor' Orestovich's 70th birthday.

[a)]E-mail: syrkin@ilt.kharkov.ua

[1]Yu. V. Sharvin, Zh. Éksp. Teor. Fiz. **48**, 984 (1965) [JETP **21**, 655 (1965)].
[2]I. K. Yanson, Zh. Éksp. Teor. Fiz. **66**, 1035 (1974) [JETP **39**, 506 (1974)].
[3]I. K. Yanson, Fiz. Nizk. Temp. **9**, 676 (1983) [Sov. J. Low Temp. Phys. **9**, 343 (1983)].
[4]I. K. Yanson and O. I. Shklyarevskiĭ, Fiz. Nizk. Temp. **12**, 899 (1986) [Sov. J. Low Temp. Phys. **12**, 509 (1986)].
[5]I. K. Yanson and A. V. Khotkevich, *Atlas of Point-Contact Electron-Phonon Interaction Spectra in Metals*, Naukova Dumka, Kiev (1986).
[6]I. O. Kulik, A. N. Omel'yanchuk, and R. I. Shekhter, Fiz. Nizk. Temp. **3**, 1543 (1977) [Sov. J. Low Temp. Phys. **3**, 740 (1977)].
[7]O. I. Shklyarevskiĭ, A. G. M. Jansen, and P. Wyder, Fiz. Nizk. Temp. **12**, 947 (1986) [Sov. J. Low Temp. Phys. **12**, 536 (1986)].
[8]P. Stefanyi, A. Feher, and A. Orendachova, Phys. Lett. A **143**, 259 (1990).
[9]P. Shtefani, A. Feher, and A. G. Shkorbatova, Fiz. Nizk. Temp. **18**, 153 (1992) [Sov. J. Low Temp. Phys. **18**, 107 (1992)].
[10]A. G. Shkorbatov, A. Feher, and P. Stefanyi, Physica B **218**, 242 (1996).
[11]É. N. Bogachek, I. O. Kulik, A. N. Omel'yanchuk, and A. G. Shkorbatov, JETP Lett. **41**, 633 (1985).
[12]É. N. Bogachek and A. G. Shkorbatov, Fiz. Nizk. Temp. **11**, 643 (1985) [Sov. J. Low Temp. Phys. **11**, 353 (1985)].
[13]É. N. Bogachek, I. O. Kulik, and A. G. Shkorbatov, Fiz. Nizk. Temp. **11**, 1189 (1985) [Sov. J. Low Temp. Phys. **11**, 656 (1985)].
[14]A. G. Shkorbatov, A. Feher, P. Shtefani, and T. Z. Sarkisyants, Fiz. Nizk. Temp. **19**, 1240 (1993) [Low Temp. Phys. **19**, 881 (1993)].
[15]I. A. Gospodarev, E. S. Syrkin, S. B. Feodos'ev, and A. G. Shkorbatov, Surface Investigation **13**, 1419 (1998).
[16]R. Berman, *Thermal Conduction in Solids*, Clarendon Press, Oxford (1976).
[17]E. T. Swartz and R. O. Pohl, Rev. Mod. Phys. **61**, 605 (1989).
[18]E. Gmelin, M. Asen-Palmer, M. Reuther, and R. Villar, J. Phys. D **32**, R19 (1999).
[19]M. A. Stroscio and M. Dutta, *Phonons in Nanostructures*, Cambridge University Press, New York (2001).
[20]E. K. Kalinin, G. A. Dreitser, I. Z. Kopp, and A. S. Myakochin, *Efficient Surfaces for Heat Exchangers. Fundamentals and Design*, Begell House Publ., New York (2001).
[21]D. G. Gahil, W. K. Ford, K. E. Goodson, G. D. Mahan, A. Majumdar, H. J. Maris, R. Merlin, and S. R. Phillpot, Appl. Phys. Rev. **93**, 793 (2003).
[22]G. Chen and A. Shakouri, J. Heat Transfer **124**, 242 (2002).
[23]K. Schwab, E. Henriskon, J. Worlock, and M. Roukes, Nature (London) **404**, 974 (2000).
[24]K. Schwab, J. L. Arlett, J. Worlock, and M. Roukes, Physica E (Amsterdam) **9**, 60 (2001).
[25]Q. Zheng, G. Su, J. Wang, and H. Guo, Eur. Phys. J. B **25**, 233 (2002).
[26]D. E. Angelescu, M. C. Cross, and M. L. Roukes, Superlattices Microstruct. **23**, 673 (1998).
[27]L. G. C. Rego and G. Kirczenov, Phys. Rev. Lett. **81**, 232 (1998).
[28]M. P. Blencowe, Phys. Rev. B **59**, 4992 (1999).
[29]A. Buldum, S. Ciraci, and C. Y. Fong, J. Phys.: Condens. Matter **12**, 3349 (2000).
[30]A. M. Duif, A. G. M. Jansen, and P. Wyder, J. Phys.: Condens. Matter **1**, 3157 (1989).
[31]A. G. M. Jansen, F. M. Mueller, and P. Wyder, Phys. Rev. B **16**, 1325 (1977).
[32]U. Gerlach-Meyer and H. J. Queisser, Phys. Rev. Lett. **51**, 1904 (1983).
[33]L. Weber, E. Gmelin, and H. J. Queisser, Phys. Rev. B **40**, 1244 (1989).
[34]C. J. Muller, J. M. van Ruitenbeck, and L. J. de Jongh, Physica C **191**, 485 (1992).
[35]H. Van Kempen and O. I. Shklyarevskiĭ, Fiz. Nizk. Temp. **19**, 816 (1993) [Low Temp. Phys. **19**, 583 (1993)].
[36]A. G. Shkorbatov, P. Stefanyi, E. Bystrenova, and A. Feher, J. Phys.: Condens. Matter **10**, 8313 (1998).
[37]A. Feher, P. Stefanyi, R. Zaboj, and A. G. Shkorbatov, in *Phonon Scattering in Condensed Matter YII*, M. Meissner and R. O. Pohl (eds.), Springer-Verlag, Berlin (1993), p. 143.
[38]A. Feher, P. Stefanyi, R. Zaboj, A. G. Shkorbatov, and T. Z. Sarkisyantz, Fiz. Nizk. Temp. **18**, 542 (1992) [Sov. J. Low Temp. Phys. **18**, 373 (1992)].
[39]L. Koestler, S. Wurdack, W. Dietsche, and H. Kinder, in *Phonon Scattering in Condensed Matter V*, M. Meissner and R. O. Pohl (eds.), Springer, Berlin (1986), p. 171.
[40]E. S. Syrkin, T. Z. Sarkisyants, and A. G. Shkorbatov, J. Phys.: Condens. Matter **5**, 5059 (1993).
[41]O. Weis, in *Phonon Scattering in Condensed Matter*, W. Eisenmenger, K. Lassman, and S. Dottinger (eds.), Springer, Berlin (1984), p. 179.
[42]W. A. Little, Can. J. Phys. **18**, 334 (1959).
[43]D. A. Young and H. J. Maris, Phys. Rev. B **40**, 3685 (1989).
[44]I. M. Khalatnikov, Zh. Éksp. Teor. Fiz. **22**, 687 (1952).

[45]I. M. Khalatnikov, *Theory of Superconductivity*, Nauka, Moscow (1971).
[46]P. L. Kapitsa, Zh. Éksp. Teor. Fiz. **11**, 1 (1941).
[47]Yu. V. Sharvin, Zh. Éksp. Teor. Fiz. **48**, 984 (1965) [JETP **21**, 655 (1965)].
[48]N. Wiener and R. Paley, *Fourier Transforms in the Complex Domain*, American Mathemactical Society, New York (1934), Nauka, Moscow (1964).
[49]I. M. Lifshits, Zh. Éksp. Teor. Fiz. **26**, 551 (1954).
[50]I. O. Kulik, Fiz. Nizk. Temp. **11**, 937 (1985) [Sov. J. Low Temp. Phys. **11**, 526 (1985)].
[51]I. F. Itskovich, I. O. Kulik, and R. I. Shekhter, Fiz. Nizk. Temp. **11**, 886 (1985) [Sov. J. Low Temp. Phys. **11**, 488 (1985)].
[52]I. F. Itskovich and R. I. Shekhter, Fiz. Nizk. Temp. **11**, 1176 (1985) [Sov. J. Low Temp. Phys. **11**, 649 (1985)].
[53]A. G. Shkorbatov and T. Z. Sarkisyants, Fiz. Nizk. Temp. **15**, 733 (1989) [Sov. J. Low Temp. Phys. **15**, 411 (1989)].
[54]Yu. G. Naĭdyuk, N. N. Gribov, and O. I. Shklyarevskiĭ, Fiz. Nizk. Temp. **11**, 1053 (1985) [Sov. J. Low Temp. Phys. **11**, 580 (1985)].
[55]Yu. G. Naĭdyuk and I. K. Yanson, Fiz. Tverd. Tela (Leningrad) **30**, 1535 (1988) [Sov. Phys. Solid State **30**, 888 (1988)].
[56]V. L. Gurevich, *Transport in Phonon Systems*, North-Holland, Publ. House, Amsterdam (1986).
[57]S. M. Rytov, Yu. A. Kravtsov, and V. I. Tatarskiĭ, *Introduction to Statistical Radiophysics*, Nauka, Moscow (1976), Part 1.
[58]S. M. Rytov, Yu. A. Kvartsov, and V. I. Tatarskiĭ, *Introduction to Statistical Radiophysics*, Nauka, Moscow (1978), Part 2.
[59]D. Walton, Bull. Am. Phys. Soc. **10**, 435 (1965).
[60]Y. M. Worlock, Phys. Rev. **147**, 636 (1966).
[61]J. W. Schwartz and C. T. Walker, Phys. Rev. **155**, 959 (1967).
[62]H. Van de Hulst, *Scattering of Light by Small Particles*, Wiley, New York (1957), Izd. Inostr. Lit., Moscow (1961).
[63]V. C. Anderson, J. Acoust. Soc. Am. **22**, 426 (1950).
[64]R. D. Spence and S. Granger, J. Acoust. Soc. Am. **23**, 701 (1951).
[65]R. M. White, J. Acoust. Soc. Am. **22**, 426 (1950).
[66]O. Weis, Z. Angew. Phys. **26**, 325 (1969).
[67]O. V. Lounasmaa, *Experimental Principles and Methods Below* 1 K, Academic Press, New York (1974).
[68]R. O. Pohl, in *Phonon Scattering in Solids*, L. J. Challis, V. W. Rampton, and A. F. G. Wyatt (eds.), Plenum, New York (1976), p. 107.
[69]J. A. Katenberg, C. L. Reynolds, and A. C. Anderson, Phys. Rev. B **16**, 673 (1977).
[70]D. S. Matsumoto, C. L. Reynolds,Jr., and A. C. Anderson, Phys. Rev. B **16**, 3303 (1977).
[71]F. Pobell, *Matter and Methods at Low Temperatures*, Springer, Heidelberg (1992).
[72]M. N. Wyborne and J. K. Wigmore, Rep. Prog. Phys. **51**, 923 (1988).
[73]A. G. Shkorbatov and T. Z. Sarkisyants, Fiz. Nizk. Temp. **16**, 725 (1990) [Sov. J. Low Temp. Phys. **16**, 427 (1990)].
[74]A. M. Kosevich, *Theory of Crystal Lattices*, Vishcha shkola, Khar'kov (1988).
[75]R. N. Gurzhi and A. O. Maksimov, Fiz. Nizk. Temp. **3**, 356 (1977) [Sov. J. Low Temp. Phys. **3**, 171 (1977)].
[76]R. N. Gurzhi, Usp. Fiz. Nauk **94**, 689 (1968) [Sov. Phys. Usp. **11**, 255 (1968)].
[77]R. C. Zeller and R. O. Pohl, Phys. Rev. B **4**, 2029 (1971).
[78]W. A. Little, Phys. Rev. **123**, 435 (1961).
[79]A. F. Andreev, Zh. Éksp. Teor. Fiz. **43**, 1535 (1962) [JETP **16**, 1084 (1963)].
[80]R. E. Peterson and A. S. Anderson, J. Low Temp. Phys. **11**, 639 (1973).
[81]E. T. Swartz and R. O. Pohl, Rev. Mod. Phys. **61**, 605 (1989).
[82]I. O. Kulik and A. G. Shkorbatov, Fiz. Nizk. Temp. **19**, 895 (1993) [Low Temp. Phys. **19**, 637 (1993)].
[83]É. N. Bogachek, A. G. Shkorbatov, and I. O. Kulik, Fiz. Nizk. Temp. **15**, 278 (1989) [Sov. J. Low Temp. Phys. **15**, 156 (1989)].
[84]L. A. Fal'kovskiĭ, Zh. Éksp. Teor. Fiz. **76**, 1358 (1979) [JETP **49**, 691 (1979)].
[85]Yu. A. Kolesnichenko and R. I. Shekhter, Fiz. Nizk. Temp. **15**, 959 (1989) [Sov. J. Low Temp. Phys. **25**, 530 (1989)].
[86]Yu. A. Kolesnichenko and R. I. Shekhter, Poverkhnost' **8**, 49 (1990).
[87]I. O. Kulik, JETP Lett. **41**, 370 (1985).
[88]I. O. Kulik, Fiz. Nizk. Temp. **11**, 937 (1985) [Sov. J. Low Temp. Phys. **11**, 516 (1985)].
[89]R. Landauer, Z. Phys. B: Condens. Matter **68**, 217 (1987).
[90]Y. Imry, *Directions in Condensed Matter Physics*, G. Grinstein and G. Mazenko (eds.), World Scientific, Singapore (1986).
[91]F. I. Fedorov, *Theory of Elastic Waves in Crystals*, Nauka, Moscow (1965).
[92]A. M. Zagoskin and I. O. Kulik, Fiz. Nizk. Temp. **16**, 911 (1990) [Sov. J. Low Temp. Phys. **16**, 533 (1990)].
[93]E. Skucik, *Fundamentals of Acoustics*, Mir, Moscow (1965), Vol. 1.
[94]R. J. Rubin and W. I. Greer, J. Math. Phys. **12**, 1686 (1971).
[95]A. Casher and J. Lebowitz, J. Math. Phys. **12**, 1703 (1971).
[96]A. O'Connor and J. Lebowitz, J. Math. Phys. **15**, 692 (1974).
[97]H. L. Engquist and P. W. Anderson, Phys. Rev. B **24**, 1151 (1981).
[98]B. J. van Wees, H. van Houten, C. W. J. Beenakker, G. Williamson, L. P. Kouwenhowen, D. van Marel, and C. T. Toxon, Phys. Rev. Lett. **60**, 848 (1988).
[99]D. A. Wharam, T. J. Thornton, R. Newbury, M. Pepper, H. Ahmed, J. E. F. Frost, D. G. Hasko, D. C. Peacock, D. A. Ritchie, and G. A. Jones, J. Phys. C **21**, L209 (1988); **22**, L887 (1988).
[100]W. E. Bron, Rep. Prog. Phys. **43**, 302 (1980).
[101]M. N. Wyborne and J. K. Wigmore, Rep. Prog. Phys. **51**, 923 (1988).
[102]A. D. Stone and H. Bruus, Physica B **189**, 43 (1993).
[103]P. M. Morse and H. Feshbach, *Methods of Theoretical Physics*, McGraw-Hill, New York (1953).
[104]E. Skucik, *Fundamentals of Acoustics*, Mir, Moscow (1965), Vol. 2.
[105]C. J. Bouwkamp, *Theoretische en Numereke Behemdelung van de Buiging Door Een Ronde Opening*, Dissertation, University of Groningen (1941).
[106]H. Levine and J. Schwinger, Phys. Rev. **74**, 958 (1948).
[107]H. Levine and J. Schwinger, Phys. Rev. **75**, 1423 (1949).
[108]I. F. Itskovich and R. I. Shekhter, Fiz. Nizk. Temp. **11**, 373 (1985) [Sov. J. Low Temp. Phys. **11**, 202 (1985)].
[109]J. A. Torres, J. I. Pascual, and J. J. Saenz, Phys. Rev. B **49**, 16581 (1994).
[110]L. I. Glazman, G. B. Lesovik, D. I. Khmel'nitskiĭ, and R. I. Shekhter, JETP Lett. **48**, 238 (1988).
[111]I. B. Levinson, JETP Lett. **48**, 301 (1988).
[112]E. G. Haanappel and D. van Marel, Phys. Rev. B **39**, 5484 (1989).
[113]E. A. Montie, E. C. Cosman, G. W. 't Hooft, M. B. van der Mark, and C. W. J. Beenakker, Nature (London) **350**, 594 (1991).
[114]A. G. Scherbakov, E. N. Bogachek, and U. Landman, Phys. Rev. B **53**, 4054 (1996).
[115]J. A. Torres and J. J. Saenz, Physica B **218**, 234 (1996).
[116]I. M. Gel'fgat and E. S. Syrkin, Fiz. Nizk. Temp. **4**, 141 (1978) [Sov. J. Low Temp. Phys. **4**, 69 (1978)].
[117]E. S. Syrkin and I. M. Gel'fgat, Fiz. Nizk. Temp. **12**, 525 (1986) [Sov. J. Low Temp. Phys. **12**, 295 (1986)].
[118]G. L. Pollack, Rev. Mod. Phys. **41**, 48 (1969).
[119]C. Anderson and W. L. Johnson, J. Low Temp. Phys. **7**, 1 (1972).
[120]J. C. A. van der Sluijs, E. A. Jones, and A. E. Alnaimi, Cryogenics **14**, 95 (1974).
[121]J. Weber, W. Sandman, W. Dietsche, and H. Kinder, Phys. Rev. Lett. **40**, 1469 (1978).
[122]A. F. Andreev and Yu. A. Kosevich, Zh. Éksp. Teor. Fiz. **81**, 1435 (1981) [JETP **54**, 761 (1981)].
[123]Yu. A. Kosevich and E. S. Syrkin, Kristallografiya **33**, 1339 (1988) [Sov. J. Crystallogr. **33**, 797 (1988)].
[124]Yu. A. Kosevich and E. S. Syrkin, Kristallografiya **33**, 1347 (1988) [Sov. J. Crystallogr. **33**, 801 (1988)].
[125]Yu. A. Kosevich and E. S. Syrkin, Fiz. Tverd. Tela (Leningrad) **33**, 2053 (1991) [Sov. Phys. Solid State **33**, 1156 (1991)].
[126]Yu. A. Kosevich and E. S. Syrkin, Phys. Rev. B **43**, 323 (1991).
[127]A. Kosevich, Prog. Surf. Sci. **55**, 1 (1997).
[128]Doo-In Kim, Hyo-Sopk Ahn, and Dong-Hoon Choi, Appl. Phys. Lett. **84**, 1919 (2004).
[129]Moon-Bong Song, Jai-Man Jang, and Chi-Woo Lee, Bull. Korean Chem. Soc. **23**, 71 (2002).
[130]D. A. Grigg, P. E. Russel, and J. E. Griffin, J. Vac. Sci. Technol. A **10**, 680 (1992).
[131]M. Heim, R. Eschrich, A. Hillebrand, H. F. Knapp, R. Gruckenberger, and G. Cevc, J. Vac. Sci. Technol. B **14**, 1998 (1996).
[132]E. S. Syrkin, A. G. Shkorbatov, and A. Feher, in *Phonon Scattering in Condensed Matter YII*, M. Meissner and R. O. Pohl (eds.) Springer-Verlag, Berlin (1993), p. 421.
[133]J. M. Krans, C. J. Muller, I. K. Yanson *et al.*, Phys. Rev. B **48**, 14721 (1993).
[134]C. J. Muller, J. M. van Ruitenbeck, C. W. J. Beenakeer, and R. de Brugn Ouboter, Physica B **189**, 225 (1993).
[135]J. Ziman, *Models of Disorder*, Cambridge University Press, New York (1979), Mir, Moscow (1982).
[136]D. M. Bercha, M. N. Botvinko, L. Yu. Germanskaya, and M. A. Ivanov, Fiz. Nizk. Temp. **12**, 287 (1986) [Sov. J. Low Temp. Phys. **12**, 162

(1986)].
[137] P. Knipp, Phys. Rev. B **43**, 6908 (1991).
[138] V. I. Peresada, *Physics of the Condensed State*, Institute for Low-Temperature Physics and Engineering, Academy of Sciences of the Ukrainian SSR, Khar'kov (1968).
[139] V. I. Peresada, V. N. Afanas'ev, and V. S. Borovikov, Fiz. Nizk. Temp. **1**, 461 (1975) [Sov. J. Low Temp. Phys. **1**, 227 (1975)].
[140] R. Haydock, in *Solid State Physics*, H. Ehrenreich, F. Seitz, and D. Turnbull (eds.), Academic Press (1980), p. 216.
[141] A. M. Kosevich, E. S. Syrkin, and S. B. Feodosyev, Phys. Lett. A **167**, 94 (1992).
[142] I. A. Gospodarev, E. S. Syrkin, S. B. Feodos'ev, and A. G. Shkorbatov, Poverkhnost'. Rentgenovskie, sinkhrotronnye i neĭtronnye issledovaniya **11**, 64 (1999).
[143] I. O. Kulik, R. I. Shekhter, and A. G. Shkorbatov, Zh. Éksp. Teor. Fiz. **81**, 2126 (1981) [JETP **54**, 1130 (1981)].
[144] V. L. Ginzburg, Usp. Fiz. Nauk **174**, 1240 (2004).
[145] E. G. Maksimov, Usp. Fiz. Nauk **170**, 1033 (2000).
[146] A. Orendacova, M. Orendac, V. Bondarenko, A. Feher, and A. G. Anders, J. Phys.: Condens. Matter **10**, 1125 (1998).
[147] M. Orendac, S. Zvyagin, A. Orendacova, M. Sieling, B. Luthi, A. Feher, and M. M. Meisel, Phys. Rev. B **60**, 4170 (1999).
[148] A. Dulfan, Functional Materials **9**, 559 (2002).
[149] R. Orbach, Science **231**, 814 (1986).
[150] E. S. Syrkin, A. G. Shkorbatov, P. A. Minaev, and A. Feher, Phys. Status Solidi C **1**, 2975 (2004).
[151] E. S. Syrkin, P. A. Minaev, A. G. Shkorbatov, and A. Feher, Microelectron. Eng. **81**, 503 (2005).
[152] I. M. Lifshits, S. A. Gredeskul, and L. A. Pastur, *Introduction to the Theory of Disordered Systems*, John Wiley and Sons, New York (1988).
[153] R. Landauer, Phys. Rev. **82**, 80 (1951).
[154] R. Landauer, IBM J. Res. Dev. **1**, 223 (1957).
[155] J. B. Pendry, J. Phys. A **16**, 2161 (1983).
[156] M. P. Blencowe and V. Vitelli, Phys. Rev. A **62**, 52104 (2000).
[157] L. G. C. Rego and G. Kirczenow, Phys. Rev. B **59**, 13080 (1999).
[158] T. S. Tighe, J. M. Worlock, and M. L. Roukes, Appl. Phys. Lett. **70**, 2687 (1997).
[159] N. Nishiguchi, Y. Ando, and M. N. Wybourne, J. Phys.: Condens. Matter **9**, 5751 (1997).
[160] M. C. Cross and R. Lifshitz, Phys. Rev. B **64**, 085324 (2001).
[161] D. H. Santamore and M. C. Cross, Phys. Rev. B **63**, 4306 (2001).
[162] M. A. Stroscio, V. Dutta, D. Kahn, and K. W. Kim, Superlattices Microstruct. **29**, 405 (2001).
[163] L. Shi and A. Majumdar, J. Heat Transfer **124**, 329 (2002).
[164] W. Wang and X. Yi, Chin. J. Phys. (Taipei) **41**, 92 (2003).
[165] D. Li, Y. Wu, P. Kim, L. Shi, P. Yang, and A. Majumdar, Appl. Phys. Lett. **83**, 2934 (2003).
[166] Y. Tanaka, F. Yoshuda, and S. Tamura, Phys. Status Solidi C **1**, 2625 (2004).
[167] V. A. Margulis and A. V. Shorokov, Phys. Status Solidi C **1**, 2642 (2004).
[168] S. Mizuno and O. Tokuda, Phys. Status Solidi C **1**, 2729 (2004).
[169] P. Kim, L. Shi, A. Majumdar, and P. L. McEuen, Phys. Rev. Lett. **87**, 215502 (2001).
[170] P. Kim, L. Shi, A. Majumdar, and P. L. McEuen, Physica B **323**, 67 (2002).
[171] O. Kwon, L. Shi, and A. Majumdar, J. Heat Transfer **125**, 156 (2003).
[172] L. Shi and A. Majumdar, in *Applied Scanning Probe Methods*, H. Fuchs, S. Hosaka, and B. Bhushan (eds.), Springer (2003), p. 27.
[173] L. Shi, in *Microscopy for Nanotechnology*, N. Yao and Z. O. Wang (eds.), Kluwer Academic Publishers (2005), p. 183.
[174] C. Yu., J. Vykoukal, D. Vykoukal, J. Schwartz, L. Shi, and P. R. C. Gascoyne, J. Microelectromech. Syst. **14**, 480 (2005).

Translated by M. E. Alferieff

QUANTUM LIQUIDS AND QUANTUM CRYSTALS

Solid solutions Ne–nD$_2$. Diagram of phase equilibrium

V. G. Belan, N. N. Gal'tsov,[a] A. I. Prokhvatilov, and M. A. Strzhemechnyĭ

B. I. Verkin Institute for Low Temperature Physics and Engineering of the National Academy of Sciences of Ukraine, pr. Lenina 47, Kharkov 61103, Ukraine

(Submitted March 5, 2005; resubmitted April 14, 2005)

X-Ray investigations of vacuum condensates of the binary mixtures Ne–nD$_2$ at temperatures from 6 K to the melting point of the solutions are performed. A diagram of phase equilibrium of the liquid and solid mixtures is proposed on the basis of the experimentally obtained and published data on the phase composition and mutual solubility of the components. The isotopic effect in the mutual solubility of the components is determined. A long-lived but metastable hexagonal phase is found, and the conditions for the formation and decomposition of this phase are determined. © *2005 American Institute of Physics*. [DOI: 10.1063/1.2127875]

I. INTRODUCTION

In the last few years investigators have been showing greater than usual interest in mixtures of quantum substances, such as helium and hydrogen, with inert elements or the simplest molecular substances. This is due to, on the one hand, the possibility of obtaining and studying matrix-isolated states in crystals of inert gases[1–6] and, on the other hand, the formation of quantum nanoclusters in helium-or hydrogen-enriched solid solutions[7,8] and the formation of solid bodies of a new type—double van der Waals crystals—on their basis.[9–12] In this connection, information on the mutual solubility of the components and on the complete diagram of phase equilibrium for such systems becomes especially important.

Among solutions of hydrogen with inert elements, the hydrogen-neon system is of special interest. In this system, because the Lennard-Jones parameters of neon (σ=2.788 Å, ε=36.7 K) are extremely close to those of hydrogen (deuterium) (σ=2.96 Å, ε=36.7 K)[13] the solutions can be regarded as quasi-isotopic and the mutual solubility can be expected to be unlimited or at least extremely high. However, because of the strong difference in the masses (a factor of 10 for Ne–H$_2$ and 5 for Ne–D$_2$) the degree of quantum behavior of the components is substantially different. This is manifested, specifically, in the their crystal lattice volumes. The volume of cubic fcc phase of neon at liquid-helium temperatures is 13.31 cm^3/mole,[14] while the volume of the hexagonal hcp lattice of normal deuterium is 19.86 cm^3/mole,[15] and the volume of normal hydrogen is 22.83 cm^3/mole.[16] Therefore the difference of the lattice volumes reaches 49% for neon and deuterium and 72% for neon and hydrogen. This latter circumstance greatly decreases the chances of observing a high mutual solubility of the components in neon-deuterium and neon-hydrogen systems.

Indeed, even in the first works it was found that the solubility is limited is not only in the solid[17,18] but also in the liquid[18,19] phases. Subsequent investigations[20,21] showed that the solubility of neon in solid hydrogen is low and is only 0.2 mole%. This result actually corresponded to the x-ray data,[12,17,22] according to which the limit of solubility of Ne in solid H$_2$ is 0.25 mole%. In Ref. 22 it was also established that the solubility of neon in solid deuterium at 5 K is twice that in hydrogen. An even higher solubility was observed in electron diffraction studies of thin Ne–H$_2$ films,[23] where a single-phase region of the hydrogen-based solutions was observed up to 3 mole%. At the same time estimates made on the basis of data on the influence of neon on the heat capacity and thermal conductivity of hydrogen[24,25] show that the maximum equilibrium content of a heavy impurity in H$_2$ crystals is of the order of or even less than 0.02 mole%.

The data on the solubility of hydrogen (deuterium) in solid neon likewise show a large interval of discrepancies. Structural investigations[17] show that the solubility of hydrogen in polycrystalline neon with crystallization of liquid mixtures is not less than 0.5 mole%. At the same time, for crystallization of mixtures from the gas phase[12,22,25] an order of magnitude higher maximum solubility of hydrogen in neon, reaching 2–5 mole%, was obtained; in order of magnitude, this is close to the estimate obtained in Ref. 5 as a result of an analysis of spectroscopic investigations performed by different groups of authors.[1–4] According to Ref. 5 the solubility of H$_2$ in solid Ne can reach 10 mole%. According to Refs. 5 and 6, the application of hydrostatic pressure to the samples decreases the limit of solubility of H$_2$ in Ne. In addition, it is noted that the solubility of hydrogen in crystals of inert gases is appreciably lower than in liquid phases. The large observed difference in the solubility data for the hydrogen-neon system is most likely due to the methodological features of the production of solid solutions in individual works.

The structure, phase composition, and properties of solid mixtures of neon with light hydrogen in Ne–nH$_2$ was recently investigated in a wide range of temperatures and concentrations.[26] The temperature-concentration limits of the equilibrium cubic and hexagonal phases of neon and hydrogen and also of the metastable hexagonal phase, discovered previously in Ref. 12, were determined. In the present work x-ray investigations were performed of solid mixtures of neon with heavy hydrogen Ne–nD$_2$ to obtain information about the isotopic effect in the solubility and in the properties

of the solutions in this system. A diagram of the phase equilibrium of the condensed phases of the system Ne–nD$_2$ is proposed on the basis of an analysis of the results obtained and of all of the previously published results.

II. PROCEDURE

Polycrystalline, 0.1 mm thick, snow-like samples were obtained by condensing small portions of room-temperature gas mixtures of normal deuterium and neon on a flat copper substrate at T=5 K. The condensation conditions were chosen so that the substrate would not heat up by more than 1–2 K when the mixture crystallizes. The purity of the initial components was at least 99.99%. The deuterium concentration in the mixtures was set by the P-V method to within 5% and varied in the range 2–70%.

Powder x-ray diffraction using a DRON-3M diffractometer with a helium cryostat was used for the structural investigations, which were performed in the temperature range 5–300 K. The temperature of the samples was measured and stabilized to within ±0.05 K. A personal computer was used to control the operation of the diffractometer and for data acquisition.

III. RESULTS

It was established that the formation of solid solutions in the system Ne–nD$_2$ qualitatively corresponds to the picture previously observed for solid mixtures of neon with light normal hydrogen.[22,26] Separation of the mixtures likewise occurs in a wide concentration range, but because of the smaller difference in the masses of the components the regions of mutual solubility are almost two times wider. Uniform solutions based on the hcp$_1$ lattice of deuterium are observed at concentrations up to 0.5 mole% Ne, and a single-phase region of solutions with the fcc lattice of neon was recorded with dissolution of up to 4.5 mole% nD$_2$ in it. Just as in mixtures of neon with light normal hydrogen, in the intermediate concentration range a metastable hexagonal hcp$_2$ phase with volume close to the volume of the neon lattice is observed together with the equilibrium hcp$_1$ and fcc phases. At liquid-helium temperatures this phase is long-lived, but near the melting temperature of deuterium it decomposes irreversibly into equilibrium phases. The volume of hcp$_2$ lattice is systematically somewhat smaller than the volume of the stable fcc phase of neon and, as in the case of light hydrogen, it is essentially concentration independent in its entire range of observation. The effect of isotopic substitution is manifested as a large positive deviation of the molar volumes of the solutions from pure neon and a somewhat smaller difference of the volumes of the two phases. These results are clearly demonstrated in Fig. 1. The larger than in the Ne–H$_2$ system deviation of the volumes of the fcc and hcp$_2$ phases from the lattice volume of pure neon is mostly due to the higher solubility of heavy hydrogen in the matrix. Quite close values are obtained with scaling to 1% impurity.

The observed constancy of the lattice parameters and volume of the fcc and hcp$_2$ phases in a wide concentration range corresponds to a suggestion which we made in Ref. 26 that the quantum nature of the hydrogen and, in this case, deuterium molecules is substantially suppressed when these molecules enter the neon lattice. Thus, as a result of the fact

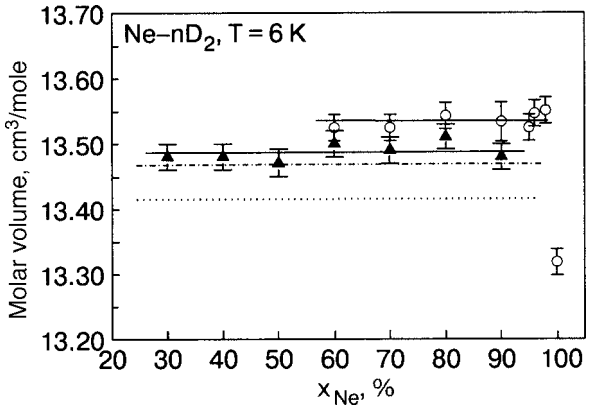

FIG. 1. Concentration dependences of the molar volumes of the equilibrium cubic fcc (○) and metastable hexagonal hcp (▲) phases of Ne–nD$_2$ solutions. The dot-dash and dotted lines show the concentration dependences of the volumes of the analogous phases of solutions in the system Ne–nH$_2$.[26]

that the molecular parameters σ and ε of neon and deuterium are essentially the same, even substantial changes in the composition of the phases should not appreciably influence the lattice of the solutions, as has in fact been observed experimentally. The introduction of nD$_2$ molecules into a neon lattice results, at concentrations $x(n\mathrm{D}_2) > 4.5$ mole%, in a transition of most of the sample into the hexagonal hcp$_2$ phase with average ratio of the lattice parameters $c/a = 1.641 \pm 0.0005$. The value obtained, just as the parameters and volume of the lattice, is essentially independent of the composition of the solution and is 0.004 higher than the value previously obtained for nH$_2$ impurity molecules.[26]

The presence of only two phases, in the samples condensed at low temperatures in a wide concentration range with lattice volume close to that of solid neon shows that as its concentration increases above 4.5 mole% deuterium completely dissolves in the metastable hcp$_2$ phase. In addition, as follows from the results obtained, the amount of the latter phase increases linearly and that of the fcc phase decreases with increasing concentration of nD$_2$ molecules (Fig. 2). The results presented in Fig. 2 were obtained by analyzing the ratios of the experimental intensities of both phases in the experimental concentration range. This procedure is described in detail in Ref. 26. It can be concluded from the data

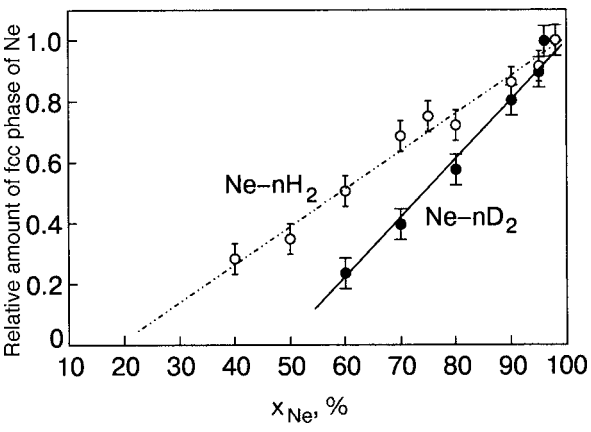

FIG. 2. Change of the relative amount of the equilibrium cubic fcc phase in Ne–nD$_2$ samples based on neon (○) with an increase of the deuterium concentration. The open circles show the data for Ne–nH$_2$ mixtures.[26]

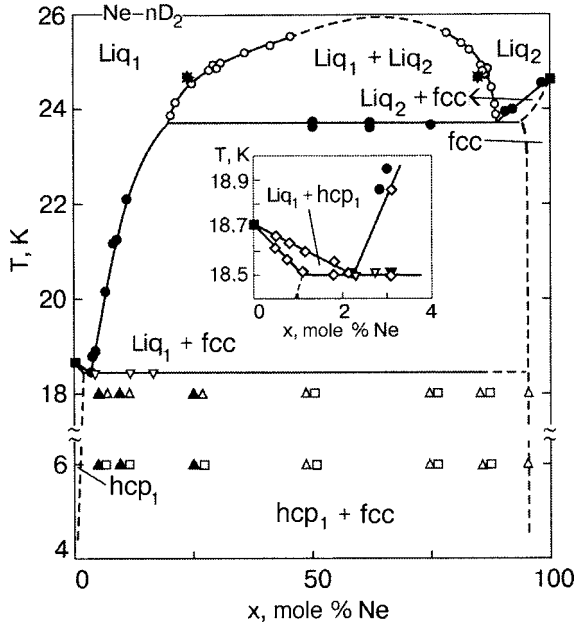

FIG. 3. Diagram of phase equilibrium of the binary mixtures Ne–nD$_2$. The diagram was constructed using the results of the present work and published data,[18–21] the curves of separation of the liquid mixtures (○),[18] (*),[19] the freezing temperature (●)[18] and melting temperature (▽),[18] the liquidus-solidus curves of deuterium-rich mixtures (◇).[20,21] The open and filled triangles correspond to the equilibrium cubic fcc and hexagonal hcp$_1$ phases observed in the present work; the open squares correspond to the metastable hexagonal phase hcp$_2$; the dashed lines show the boundaries of the regions of existence of the solid solutions based on the neon and deuterium lattices.

presented in Fig. 2 that isotopic substitution strongly influences the phase composition of freshly prepared condensates. If the cubic phase of neon in mixtures with nH$_2$ was actually observed in the concentration range 2–80% nH$_2$, then in mixtures with deuterium this range decreases to 5–50 mole% nD$_2$. However, it must be underscored once again that in this case we are talking about the nonequilibrium phase composition, since on heating up to temperatures 18–20 K the hexagonal hcp$_2$ phase decomposes into equilibrium hcp$_1$ and fcc solutions based on deuterium and neon, respectively.

The results of the present investigations, taken together with previously obtained data in a number of previous works,[1–6,12,18–22,26] made it possible to reconstruct the complete diagram of phase equilibrium of neon-deuterium mixtures and to indicate the region of existence and conditions for obtaining nonequilibrium states. As seen in Fig. 3, the phase diagram of the binary mixtures Ne–nD$_2$ is of the monotectic type.[13,27] It contains a critical point T_c=25.95 K and x_c=37±2 mole% D$_2$, below which liquid solutions separate into two phases with different density. Aside from the critical point (the point of equal concentrations), the diagram also contains two triple points. One of these points, the point of a monotectic transformation, lies in the region of neon-rich solutions and is characterized by T_1=23.8 K and x_1 ≈9.7 mole% D$_2$. The other eutectic transformation point lies in the region of deuterium-rich solutions with temperature T_2=18.52 K and concentration x_2≈2.3 mole% Ne. The parameters of the lower triple eutectic point near deuterium have been carefully investigated in Refs. 20 and 21. In these investigations not only the temperature and concentration of the eutectic were determined, but the boundaries of the two-phase liquid-crystal region were also determined reliably. In the diagram this region is Liq$_1$–hcp$_1$, where the influence of the Ne impurity atoms on the crystallization and melting temperatures of deuterium can be clearly seen. The authors of Refs. 20 and 21 also determined the maximum solubility of neon in solid deuterium, which at the temperature of the eutectic reaches 1.1 mole% (see inset in Fig. 3). The regions of solid solutions based on hcp$_1$ deuterium and fcc neon are bounded by the dashed lines. The concentration positions of the triple points of the eutectic and the monotectic and our values of the maximum solubility of the components in solid deuterium and neon were taken into account. The equilibrium and metastable phases of the solid solutions observed in the present work at temperatures below the line of the eutectic are designated in the diagram by different symbols (Fig. 3). The open and filled triangles correspond to an equilibrium cubic fcc and hexagonal hcp$_1$ phases of neon and deuterium and the open squares correspond to the metastable hexagonal hcp$_2$ phase based on neon. It is evident that for deuterium concentrations above 50 mole% the amount of the fcc phase in the samples with condensation on a substrate at temperature 6 K is so small (see also the data in Fig. 2) that to within the sensitivity of our experiment a diffraction pattern is not observed. In this concentration range, only two hexagonal phases—hcp$_1$ and hcp$_2$—are formed when the samples are condensed at low temperatures. This situation remains right up to 18 K, and at higher temperatures the hcp$_2$ phase with the neon volume decomposes and the ratio of the fcc and hcp$_1$ phases which corresponds to the equilibrium diagram is restored.

IV. CONCLUSIONS

A diagram of phase equilibrium of the binary mixtures neon-deuterium in the liquid and solid states was proposed on the basis of x-ray structural studies of solid mixtures Ne–nD$_2$ and analysis of published data. The diagram is complicated and contains a critical point of separation of the liquid mixtures and monotectic and eutectic points of a three-phase equilibrium, which lie in terms of the concentration near pure neon and deuterium.

A strong isotopic effect in the mutual solubility of components was observed. It was shown that for solid solutions at temperatures below the eutectic in the system Ne–nD$_2$ the mutual solubility on the basis of the lattices of both components is almost two times higher than in the system Ne–nH$_2$. This effect is mainly due to the fact that deuterium molecules, which have weaker quantum nature, are less ready to form a nonequilibrium hcp$_2$ phase, whose very existence the authors consider to be a quantum effect.

A long-lived metastable hexagonal hcp$_2$ phase with volume close to that of the pure-neon lattice was observed at low temperatures. When they dissolve in neon H$_2$ and D$_2$ molecules lose their quantum properties. As a result a substantial (tens of percent) quantity of hydrogen and deuterium dissolves in the hcp$_2$ phase without a change in the volume of the phase. The amount of this phase increases proportionally to the increase in the concentration of deuterium in the mixtures. Heating the condensates up to temperatures close

to the melting temperature of the solutions results in irreversible decomposition of hcp_2 into equilibrium phases based on the fcc neon and hcp_1 deuterium lattices.

The international science foundation CRDF provided partial financial support for this work under grant UP2-2445-KH-02.

[a)]E-mail: galtsov@ilt.kharkov.ua

[1]R. J. Kriegler and H. L. Welsh, Can. J. Phys. **46**, 1181 (1968).
[2]J. De Remigis and H. L. Welsh, Can. J. Phys. **48**, 1622 (1970).
[3]F. T. Prochaska and L. Andrews, J. Chem. Phys. **67**, 1139 (1977).
[4]K. D. Bier, H. J. Jodl, and H. Daufer, Can. J. Phys. **66**, 708 (1988).
[5]P. Loubeyre, R. LeToullec, and J. P. Pinceaux, Phys. Rev. Lett. **67**, 3271 (1991).
[6]P. Loubeyre, R. LeToullec, and J. P. Pinceaux, Phys. Rev. B **45**, 12844 (1992).
[7]Z. Li and V. A. Apkarian, J. Chem. Phys. **107**, 1544 (1997).
[8]R. Mazzarello and A. C. Levi, J. Low Temp. Phys. **127**, 259 (2002).
[9]W. L. Vos, L. W. Finger, R. J. Hemley, J. Z. Hu, H. K. Mao, and J. A. Schouten, Nature (London) **358**, 46 (1992).
[10]P. Loubeyre, M. Jean-Louis, R. LeToullec, and L. Charon-Gerard, Phys. Rev. Lett. **70**, 178 (1993).
[11]W. L. Vos and J. A. Schouten, Fiz. Nizk. Temp. **19**, 481 (1993) [Low Temp. Phys. **19**, 338 (1993)].
[12]A. S. Baryl'nik, A. I. Prokhvatilov, M. A. Strzhemechnyĭ, and G. N. Shcherbakov, Fiz. Nizk. Temp. **19**, 625 (1993) [Low Temp. Phys. **19**, 447 (1993)].
[13]V. G. Manzhelii, A. I. Prokhvatilov, I. Ya. Minchiina, and L. D. Yantsevich, *Handbook Binary Solutions of Cryocrystals*, Begell House, Inc., New York (1996).
[14]*Rare Gas Solids*, M. L. Klein and J. A. Venables (eds.), Academic Press, London (1966), Vol. 1; *ibid.*, Vol. 2 (1967).
[15]G. N. Shcherbakov, A. I. Prokhvatilov, and I. N. Krupskiĭ, Voprosy atomnoĭ nauki i tekhniki. Ser. Atomno-vodorodnaya énergetika i tekhnologiya, No. 3(19), 66 (1984).
[16]I. N. Krupskiĭ, A. I. Prokhvatilov, and G. N. Shcherbakov, Fiz. Nizk. Temp. **9**, 858 (1983) [Sov. J. Low Temp. Phys. **9**, 446 (1983)].
[17]C. S. Barrett, L. Meyer, and J. Wasserman, J. Chem. Phys. **45**, 834 (1966).
[18]J. P. Brouwer, L. J. Hermans, H. F. P. Knaap, and J. J. Beenankker, Physica (Amsterdam) **30**, 1409 (1964).
[19]M. Simon, Phys. Lett. **5**, 319 (1963); Physica (Amsterdam) **29**, 1079 (1963).
[20]N. G. Bereznyak, A. A. Sheĭnina, and L. V. Karnatsevich, Ukr. Fiz. Zh. (Russ. Ed.) **19**, 668 (1974).
[21]N. G. Bereznyak, A. A. Sheĭnina, and L. V. Karnatsevich, Fiz. Nizk. Temp. **1**, 780 (1975) [Sov. J. Low Temp. Phys. **1**, 376 (1975)].
[22]A. S. Baryl'nik, A. I. Prokhvatilov, and G. N. Shcherbakov, Fiz. Nizk. Temp. **21**, 787 (1995) [Low Temp. Phys. **21**, 607 (1995)].
[23]S. I. Kovalenko and A. A. Soldovnik, Fiz. Nizk. Temp. **19**, 1041 (1993) [Low Temp. Phys. **19**, 741 (1993)].
[24]M. I. Bagatskiĭ, I. Ya. Minchina, and V. G. Manzheliĭ, Fiz. Nizk. Temp. **22**, 52 (1996) [Low Temp. Phys. **22**, 37 (1996)].
[25]B. Ya. Gorodilov, A. I. Krivchikov, V. G. Manzheliĭ, N. N. Zholonko, and O. A. Korolyuk, Fiz. Nizk. Temp. **21**, 723 (1995) [Low Temp. Phys. **21**, 561 (1995)].
[26]N. N. Gal'tsov, A. I. Prokhvatilov, and M. A. Strezhemechnyĭ, Fiz. Nizk. Temp. **30**, 1307 (2004) [Low Temp. Phys. **30**, 984 (2004)].
[27]L. S. Palatnik and A. I. Landau, *Phase Equilibria in Multicomponent Systems*, Holt, Rinehart, and Watson, New York (1964), Izd-vo KGU, Khar'kov (1961).

Translated by M.E. Alferieff

Diffusion description of the kinetics of isotopic phase separation of ^{3}He–^{4}He solid solutions

V. N. Grigor'ev, I. A. Degtyarev,[a] and S. S. Sokolov

B. I. Verkin Institute for Low Temperature Physics and Engineering of the National Academy of Sciences of Ukraine, pr. Lenina 47, Kharkov 61103, Ukraine

(Submitted September 2, 2005)
Fiz. Nizk. Temp. **31**, 1250–1257 (November 2005)

The process of the separation of solid solutions of helium isotopes is examined using a diffusion approach with boundary conditions prescribed on the boundary of the inclusion of a new phase, the position of the boundary being a function of time. The diffusion processes occurring simultaneously outside and inside an inclusion are taken into account. The time dependence of the pressure is calculated on the basis of the time dependences of the concentration of the diffusing substance. A theoretical calculation using existing experimental data is performed. © *2005 American Institute of Physics*. [DOI: 10.1063/1.2127876]

I. INTRODUCTION

One of the most interesting manifestations of quantum effects in solid helium is isotopic phase separation. The discovery of this effect is an important step in the investigation of quantum crystals. The *T-C* phase diagram of ^{3}He–^{4}He solid solutions, which is presented in Fig. 1, has now been studied quite well. The kinetics of the separation process has been studied in less detail. Only the processes occurring in weak solutions of ^{3}He in ^{4}He (the "left-hand" part of the diagram) have been studied comparatively well. This is because ^{3}He impurities possess spin 1/2 and are easily detected in the spin-neutral ^{4}He matrix by the NMR method. The situation is much more complicated on the "right-hand" side of the phase diagram. In this case inclusions of zero-spin ^{4}He are formed in a ^{3}He matrix when the solution separates, and the NMR method is inapplicable. Information about the character of the motion of the impurity can be obtained only from indirect data. However, successfully developed quantitative methods for studying the kinetics of the decomposition of solid solutions at low temperatures, specifically, the method of high-precision measurement of pressure, make it possible to obtain information about the diffusion motion in a wide range of ^{3}He–^{4}He concentrations.

Experiments with weak solutions of ^{3}He in ^{4}He have shown that the kinetics of their decomposition in this case can be described completely adequately using the NMR values of the diffusion coefficients.[1,2] The experimental data for weak solutions of ^{3}He in ^{4}He have been successfully matched using the values of the diffusion coefficients calculated theoretically in Ref. 3. However, the situation remains intriguing for concentrated solutions. On the one hand it has been established experimentally that phase separation does occur in such solutions, and at not very high pressures over quite short time intervals. On the other hand it has been shown equally reliably that at least in uniform solutions the main mechanism of diffusion transport—tunneling—stops completely at impurity concentrations above 10%. Thus, at the present time the mechanism of mass transfer accompanying phase separation of concentrated solutions is completely unclear.

The situation described above makes it very urgent to investigate in detail the kinetics of the phase transition in concentrated ^{3}He–^{4}He solutions. There is hope that an analysis of the results of such investigations will make it possible to understand the mechanism of the motion of the atoms under these conditions. It is obvious that this possible only if the solution of the diffusion problem corresponding to the experimental conditions is known.

It should be noted that a spherically symmetric continuum approximation, where inclusions of a new phase are considered to be spherical formations of size R_1 separated from one another by a distance $2R_2$, was used in virtually all works where the kinetics of separation of solid solutions has been studied theoretically thus far. In this approximation only the radial part remains in the diffusion equation. This diffusion equation was solved assuming that the radius of the inclusions of the new phase is constant. In spite of such a serious simplification the solutions obtained for the diffusion equation explain many features of the experimentally observed phenomena. This substantiates further use of the spherically symmetric approximation for solving diffusion problems. At the same time it is obvious that an approxima-

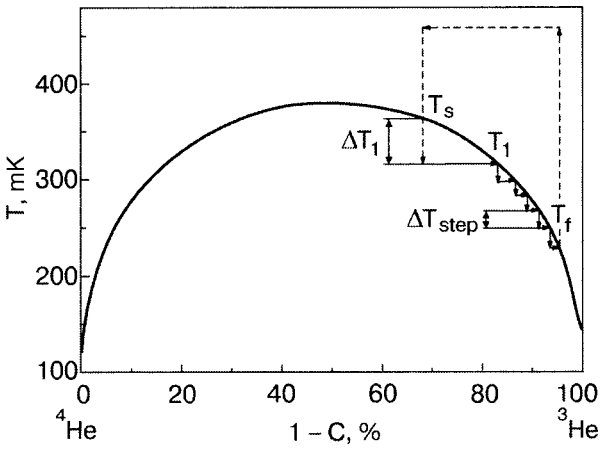

FIG. 1. Phase diagram of the solid solutions ^{3}He–^{4}He and schematic representation of the process studied.

tion where the radius of an inclusion is constant cannot be regarded as completely satisfactory, since the size of an inclusion changes strongly during the phase-separation process. Thus the boundary conditions of the diffusion problem must be posed on the surface, whose position is a function of time. In this case the conventional methods for solving diffusion problems, based on the separation of variables in a partial differential equation, are unsuitable and different approaches to solving the diffusion equations must be sought.

An additional condition arises when studying the decomposition of concentrated solutions. This condition is due to the fact that the volume of the phase formed can become comparable to the volume of the matrix. In this situation, when the coefficients of diffusion in different phases are different, the diffusion processes not only in the matrix but also in a nucleus must be taken into account. The objective of the present work is to solve the diffusion problem corresponding to the separation processes occurring in concentrated solutions.

II. DIFFUSION GROWTH OF AN INCLUSION OF A NEW PHASE

The process which we are studying is shown schematically in the phase diagram (Fig. 1). The solution is cooled from the homogeneous region to temperature T_1, corresponding to the "large" jump in temperature $\Delta T_1 = T_s - T_1$ (T_s is the separation temperature of the solution). After an equilibrium state is reached, further cooling is conducted in small steps $\Delta T_{\text{step}} < \Delta T_1$. This latter condition eliminates the additional formation of nuclei of a new phase on the "small" steps. It is assumed that an inclusion of a new phase is formed with a certain equilibrium concentration, which remains unchanged during the growth process. At the same time, when studying the subsequent coolings of an already partially separated solution the diffusion processes in two regions must be taken into account: outside and inside an inclusion.

To describe the separation of a solid solution of helium isotopes we assume that the volume of the sample is divided into individual cells (equivalent spheres), at the center of each of which an inclusion of a new phase grows. A theoretical analysis of the growth of an inclusion of a new phase in this formulation of the problem reduces to solving a spherically symmetric diffusion equation in the outer and inner regions taking account of the motion of the boundary of the new phase. The case of "large" cooling in such a formulation of the problem can always be obtained by passing to the limit where the diffusion processes inside an inclusion must be neglected.

We introduce the following notation: R_2 is the radius of an equivalent sphere, r is the running coordinate, and $R_1(t)$ is the radius of the spherical center of the new phase. The schematic diagram of the system being studied is presented in Fig. 2.

It is convenient to introduce the following dimensionless variables: the relative radius ρ and the generalized times τ^{out} and τ^{in}:

$$\rho = \frac{r}{R_2}, \quad \tau^{\text{out}} = \frac{tD^{\text{out}}}{R_2^2} \equiv \tau, \quad \tau^{\text{in}} = \frac{tD^{\text{in}}}{R_2^2} \equiv a\tau. \tag{1}$$

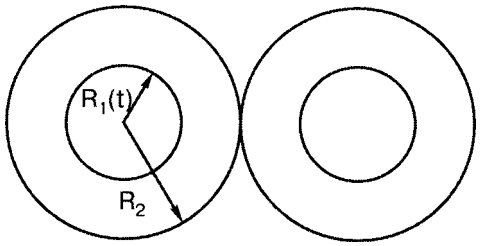

FIG. 2. Diagram illustrating the evolution of an inclusion of a new phase in spherically symmetric concentration fields.

The introduction of the parameter $a = D^{\text{in}}/D^{\text{out}}$, which is the ratio of the coefficients of diffusion, makes it possible to solve the system of equations with respect to one dimensionless time τ.

The concentration field in the inner and outer regions is described by the diffusion equation

$$\frac{\partial C^j}{\partial \tau} = \frac{\partial^2 C^j}{\partial \rho^2} + \frac{2}{\rho}\frac{\partial C^j}{\partial \rho}. \tag{2}$$

We shall solve the diffusion problems in the outer ($j = out$) and inner ($j = in$) regions. For each region we shall take account of the corresponding initial and boundary conditions:

Formulation of the boundary-value problem

1. Outer region

In the outer region the initial concentration is

$$C^{\text{out}}(\rho, 0) = C_i^{\text{out}}. \tag{3}$$

We shall assume that the total diffusion flux through the surface of an equivalent sphere is zero:

$$\left.\frac{\partial C^{\text{out}}}{\partial \rho}\right|_{\rho=1} = 0. \tag{4}$$

If the process is diffusion-limited, then on the outer side of the surface of a growing center the concentration corresponds to the phase diagram for the given supersaturation

$$C^{\text{out}}(\rho_1(\tau), \tau) = C_{pd}^{\text{out}}, \quad \rho_1(\tau) = R_1(\tau)/R_2. \tag{5}$$

2. Inner region

Here we have the initial condition

$$C^{\text{in}}(\rho, 0) = C_i^{\text{in}}. \tag{6}$$

Just as in the outer region, for a diffusion-limited process the concentration on the inner side of the surface of the growing center corresponds to the phase diagram:

$$C^{\text{in}}(\rho_1(\tau), \tau) = C_{pd}^{\text{in}}. \tag{7}$$

To close the system of diffusion equations (2) and couple the diffusion processes in the outer and inner regions, the equation of mass balance on the boundary of the inclusion of the new phase must be taken into account. We shall write this equation in the form

$$(C_{pd}^{\text{in}} - C_{pd}^{\text{out}})\frac{d\rho_1(\tau)}{d\tau} = \left.\frac{\partial C^{\text{out}}}{\partial \rho}\right|_{\rho=\rho_1(\tau)} + a\left.\frac{\partial C^{\text{in}}}{\partial \rho}\right|_{\rho=\rho_1(\tau)}. \tag{8}$$

This form of the mass-balance equation is associated with the presence of two fluxes of matter on the boundary of

the inclusion of a new phase. The expression (8) is obtained by switching from a vector representation for the fluxes of matter to projections of the fluxes on the radial direction.

In problems with nonstationary boundary conditions the solution is sought in a manner so that one of these conditions is satisfied automatically. It is convenient to choose the solution of Eqs. (2) for the outer region in the form[4]

$$C^{\text{out}}(\rho,\tau)=B(\tau)+\frac{1}{\rho}\sum_{n=1}^{\infty}\frac{(1-\rho)^{2n}}{(2n)!}\left[1-\frac{1-\rho}{2n+1}\right]\frac{d^nB(\tau)}{d\tau^n}. \tag{9}$$

This solution automatically satisfies the boundary condition (4); the unknown function $B(\tau)=C^{\text{out}}(1,\tau)$ describes the change in concentration at the boundary of the equivalent sphere. It follows from the initial condition (3) that

$$C(\rho,0)=C_i^{\text{out}}=B(0)+\frac{1}{\rho}\sum_{n=1}^{\infty}\frac{(1-\rho)^{2n}}{(2n)!}\left[1-\frac{1-\rho}{2n+1}\right]\times\left.\frac{d^nB(\tau)}{d\tau^n}\right|_{\tau=0}. \tag{10}$$

Thus the following limit is imposed on the derivatives of the function $B(\tau)$:

$$\lim_{\tau\to 0}\frac{d^nB(\tau)}{d\tau^n}=0. \tag{11}$$

To take account of diffusion processes inside a spherical inclusion of a new phase, Eq. (2) must be solved for the inner region. We chose this solution in the form

$$C^{\text{in}}(\rho,\tau)=A(\tau)+\frac{1}{\rho}\sum_{n=1}^{\infty}\frac{1}{a^n}\frac{\rho^{2n+1}}{(2n+1)!}\frac{d^nA(\tau)}{d\tau^n}. \tag{12}$$

The function $A(\tau)$ to be determined describes the change in concentration at the center of the inclusion of the new phase $A(\tau)=C^{\text{in}}(0,\tau)$. The initial condition (6) results in the following initial condition on the function $A(\tau)$:

$$C(\rho,0)=C_i^{\text{in}}=A(0)+\frac{1}{\rho}\sum_{n=1}^{\infty}\frac{1}{a^n}\frac{\rho^{2n+1}}{(2n+1)!}\left.\frac{d^nA(\tau)}{d\tau^n}\right|_{\tau=0}. \tag{13}$$

Thus the condition (13) is satisfied when

$$\lim_{\tau\to 0}\frac{d^nA(\tau)}{d\tau^n}=0. \tag{14}$$

Introducing new functions for the relative excess concentrations at the boundary of an equivalent sphere and at the center of an inclusion of a new phase

$$\beta(\tau)=\frac{B(\tau)-C_{pd}^{\text{out}}}{C_{pd}^{\text{in}}-C_{pd}^{\text{out}}},\quad \alpha(\tau)=\frac{C_{pd}^{\text{in}}-A(\tau)}{C_{pd}^{\text{in}}-C_{pd}^{\text{out}}}, \tag{15}$$

the following system of equations can be derived for the functions $\beta(\tau),\alpha(\tau)$, and $\rho_1(\tau)$:

$$\begin{cases}\beta(\tau)\rho_1(\tau)=-\sum_{n=1}^{\infty}\frac{(1-\rho_1)^{2n}}{(2n)!}\left[1-\frac{1-\rho_1}{2n+1}\right]\frac{d^n\beta(\tau)}{d\tau^n};\\ \alpha(\tau)\rho_1(\tau)=-\sum_{n=1}^{\infty}\frac{1}{a^n}\frac{\rho_1^{2n+1}}{(2n+1)!}\frac{d^n\alpha(\tau)}{d\tau^n};\\ \rho_1\frac{d\rho_1(\tau)}{d\tau}=\beta(\tau)-a\alpha(\tau)-\frac{1}{\rho_1}\sum_{n=1}^{\infty}\frac{1}{a^{n-1}}\frac{\rho_1^{2n}}{(2n)!}\frac{d^n\alpha(\tau)}{d\tau^n}\\ \quad-\frac{1}{\rho_1}\sum_{n=1}^{\infty}\frac{(1-\rho_1)^{2n-1}}{(2n-1)!}\left[1-\frac{1-\rho_1}{2n}\right]\frac{d^n\beta(\tau)}{d\tau^n}.\end{cases} \tag{16}$$

It follows from the conditions $B(0)=C_i^{\text{out}}$ and $A(0)=C_i^{\text{in}}$ that

$$\beta(0)=\frac{B(0)-C_{pd}^{\text{out}}}{C_{pd}^{\text{in}}-C_{pd}^{\text{out}}},\quad \alpha(0)=\frac{C_{pd}^{\text{in}}-A(0)}{C_{pd}^{\text{in}}-C_{pd}^{\text{out}}}. \tag{17}$$

Therefore the following conditions must be satisfied:

$$\lim_{\tau\to 0}\frac{d^n\beta(\tau)}{d\tau^n}=0;\quad \lim_{\tau\to 0}\frac{d^n\alpha(\tau)}{d\tau^n}=0. \tag{18}$$

The solutions (9) and (12) and the system of equations (16) with the conditions (17) and (18) completely determine the problem and make it possible to determine by numerical integration the functions $\alpha(\tau)$, $\beta(\tau)$, and $\rho_1(\tau)$ for arbitrary values of the initial concentrations.

III. RESULTS AND DISCUSSION

The system (16) was solved using the numerical method "BDF—implicit Backward Differentiation Formulas." To illustrate the solutions obtained we shall examine the separation of a solution of ^{3}He in ^{4}He when an inclusion already contains 2/3 of the ^{4}He. We recall that no detailed studies of concentrated solutions have been performed thus far. The typical solutions of the system (16) are presented as plots in Fig. 3 for several values of the parameter a and supersaturation with respect to the concentration $\Delta C=C_i^{\text{out}}-C_f^{\text{out}}$.

The functions $\alpha(\tau)$ and $\beta(\tau)$ are monotonically decreasing functions of their argument. The behavior of $\rho_1(\tau)$ is more complicated. If diffusion inside an inclusion is neglected ($\alpha(\tau)=\text{const}, a=0$), then ρ_1 increases monotonically with increasing τ and "saturates" at the value ρ_f. When diffusion processes inside an inclusion are taken into account for small values of a the function $\rho_1(\tau)$ is nonmonotonic. This function passes through a maximum and only then goes to the value $\rho_1(\tau)=\rho_f$. Such behavior of $\rho_1(\tau)$ can be seen clearly in Figs. 3b and 3c. For values of the parameter a of the order of 1, the maximum washes out. When a increases to $a\sim 30$ the nonmonotonic behavior reappears, but now a minimum is observed in the time dependence of the radius of the inclusion. After this minimum the radius of the inclusion takes on the equilibrium value. It should be noted that the characteristic values of τ for which an extremum is observed are appreciably greater for small a than for $a>10$. Moreover, in the latter case the absolute values of the extremum are also appreciably smaller (Fig. 3d).

When comparing the theoretical results with the experimental data it should be kept in mind that the separation kinetics are studied experimentally by the method of high-

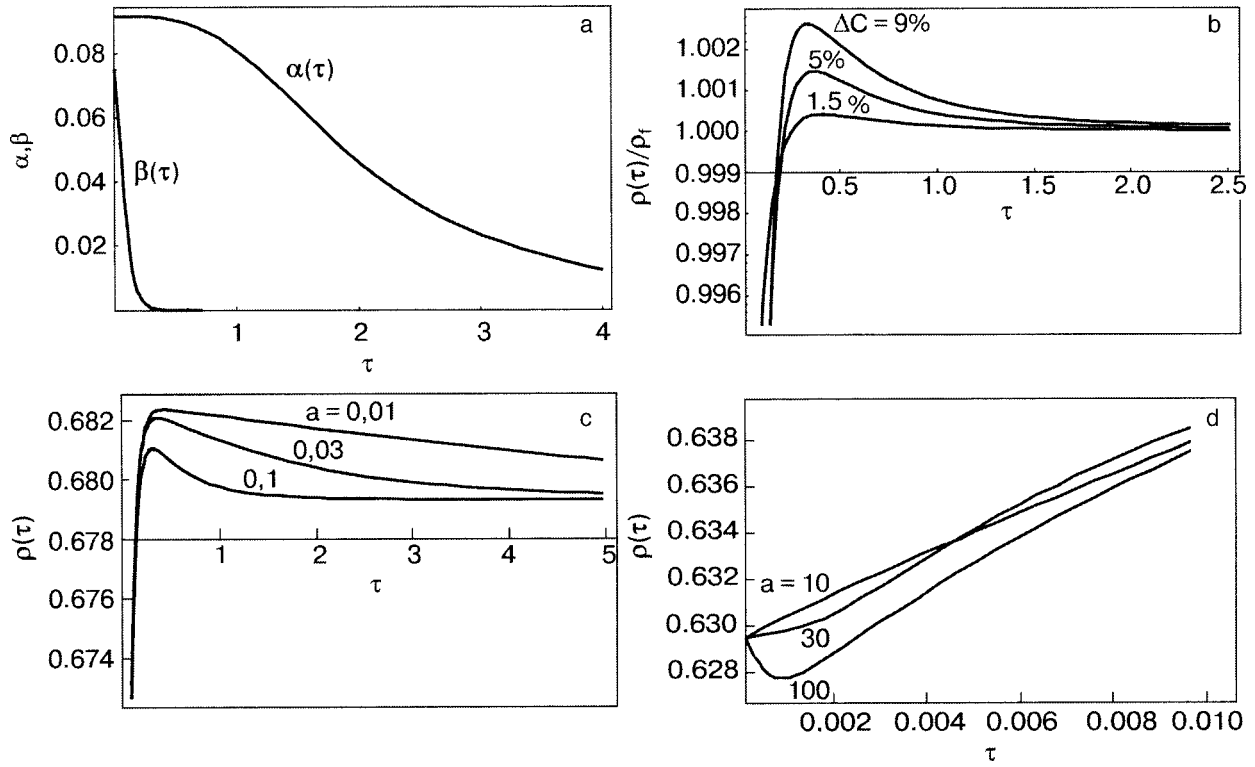

FIG. 3. Relative excess concentrations β and α versus the dimensionless time $\tau = D^{\text{out}}t/R_2^2$ ($a=0.3$; $\Delta C=0.09$) (a); $\rho(\tau)/\rho_f$, where ρ_f is the radius at saturation, for $a=0.1$ for several values of the supersaturation (b); radius of a spherical center of a new phase as a function of τ for supersaturation with respect to concentration 9% and various values of the parameter a (c, d).

precision pressure measurements.[3] For this reason, to compare with experiment it is necessary to switch from functions describing the concentration to functions describing the behavior of the change in pressure as a function of time.

The excess pressure resulting from the separation of the solution at constant volume can be written in the form

$$\Delta p = \frac{\Delta V_E}{\beta_T V}, \tag{19}$$

where β_T and V are the compressibility and molar volume of the solution and ΔV_E is the excess molar volume. Edwards and Balibar[5] showed that the theory of regular solutions describes the solid solutions ^{3}He-^{4}He with adequate accuracy. It was found in this approach that the excess molar volume on separation of a solution with initial concentration C_i to final concentration C_f is

$$\Delta V_E = 0.364[C_i(1-C_i) - C_f(1-C_f)], \tag{20}$$

where ΔV_E is measured in cm^3/mole. Taking account of Eq. (20) we obtain

$$\Delta p = \gamma[C_i(1-C_i) - C_f(1-C_f)], \tag{21}$$

where $\gamma = 0.364/\beta_T V$.

To describe the time evolution of the pressure we assumed that an expression of the type (21) remains valid in the course of the separation process also, if the average values, which are time dependent, are used for the concentrations. Then, assuming that the system in the initial state consists of a concentrated phase (nucleus) and a dilute phase (matrix) with volume fractions ρ_1^3 and $1-\rho_1^3$, respectively, we can write

$$\begin{aligned}\Delta p(t) = \gamma\{&\rho_{1i}^3 C_i^{\text{in}}(1-C_i^{\text{in}}) + (1-\rho_{1i}^3)C_i^{\text{out}}(1-C_i^{\text{out}}) \\ &- \rho_1^3(t)\overline{C^{\text{in}}}(t)(1-\overline{C^{\text{in}}}(t)) \\ &- (1-\rho_1^3(t))\overline{C^{\text{out}}}(t)(1-\overline{C^{\text{out}}}(t))\},\end{aligned} \tag{22}$$

where ρ_{1i} is the initial value of the radius of the inclusion.

Using the balance equation for ^{3}He

$$C_0 R_2^3 = R_1^3\overline{C^{\text{in}}} + (R_2^3 - R_1^3)\overline{C^{\text{out}}}, \tag{23}$$

(C_0 is the initial concentration of a uniform solution), we express $\overline{C^{\text{out}}}$ in terms of ρ_1 and $\overline{C^{\text{in}}}$:

$$\overline{C^{\text{out}}} = \frac{C_0 - \rho_1^3\overline{C^{\text{in}}}}{1-\rho_1^3}. \tag{24}$$

Substituting the expression (24) into Eq. (22) we obtain

$$\begin{aligned}\Delta p(t) = \gamma\Bigg\{&\rho_{1i}^3 C_i^{\text{in}}(1-C_i^{\text{in}}) + (1-\rho_{1i}^3)C_i^{\text{out}}(1-C_i^{\text{out}}) \\ &- C_0(1-C_0) + \frac{\rho_1^3(t)}{1-\rho_1^3(t)}(\overline{C^{\text{in}}}(t) - C_0)^2\Bigg\}.\end{aligned} \tag{25}$$

The results of a calculation using Eq. (25) are presented in Fig. 4. Here, of greatest interest are the values of the parameter a for the effects associated with the diffusion processes inside an inclusion are observed during a short time interval. Decreasing the parameter a strongly "protracts" the diffusion process inside an inclusion in time, while increasing the parameter a has the effect that the characteristic diffusion times in the inner and outer regions become close and therefore the process leading to a change in pressure pro-

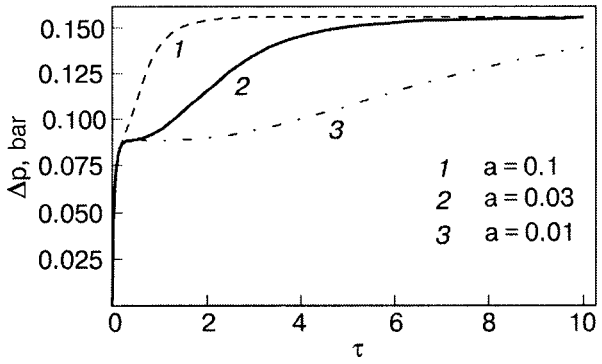

FIG. 4. Pressure change in the sample as a function of τ for a partially separated solution of ^{4}He in ^{3}He (initial concentration 0.3), and supersaturation $\Delta C = 0.09$.

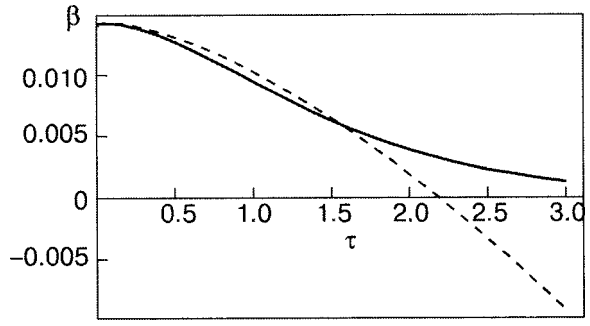

FIG. 5. Relative excess concentration β versus the dimensionless time $\tau = Dt/R_2^2$, on the boundary of an equivalent sphere. Solid line—numerical calculation, dashed line—analytical calculation using Eq. (26).

ceeds as if it occurred in a single region. This is evident from the curves 1 and 2 in Fig. 4. The appreciable difference in the functions $\Delta p(\tau)$ for different values of a provides a possibility for finding the values of a, when they are unknown, by comparing with the experimental data.

We note that in the calculation the concentrations were averaged in a simplified form as $C^{\text{in}}(t) = (A(t) + C^{\text{in}}_{pd})/2$. This simplification is based on the fact that for stepped cooling the concentration of the solution in each region does not change very strongly. Consequently, it can be expected that our expression can describe quite accurately the pressure-change process which is associated with separation of the solid solution of helium isotopes.

Since all calculations were performed numerically, it is of interest to compare our solutions with the results of an analytical solution of the system (16) by means of an expansion of the functions ρ_1 and β in a series in powers of $\beta_0^{1/2}$ neglecting the diffusion processes inside the inclusion of the new phase ($a = 0$, $\alpha(\tau) = \text{const}$):[4]

$$\rho_1(\tau) = \beta_0^{1/2}\varphi_1(\tau) + \beta_0\varphi_2(\tau) + \ldots\ .$$

$$\beta(\tau) = \beta_0\psi_1(\tau) + \beta_0^{3/2}\psi_2(\tau) + \ldots\ . \tag{26}$$

The solution of the system for the functions φ_i and ψ_i has the form

$$\varphi_1 = \sqrt{2\tau}; \quad \psi_1 = 1;$$

$$\varphi_2 = 0.2 + 2\sum_{k=1}^{\infty}\frac{1}{\mu_k^4} + 1.2\tau - 0.8\tau^2 - \frac{2}{\tau^{3/2}}\sum_{k=1}^{\infty}\frac{1}{\mu_k^3} + \frac{1}{\mu_k^5} \times D(\mu_k\sqrt{\tau})\mathrm{e}^{-\mu_k^2\tau};$$

$$\psi_2 = -2\sqrt{2}\tau^{3/2} - 2\sqrt{2}\tau^{1/2}\sum_{k=1}^{\infty}\frac{1}{\mu_k^2\sin\mu_k}D(\mu_k\sqrt{\tau})\mathrm{e}^{-\mu_k^2\tau}. \tag{27}$$

Here μ_k are the roots of the transcendental equation $\tan\mu_k = \mu_k$ and $D(x) = \int_0^x e^{t^2}dt$ is Dawson's integral.

The numerical and analytical solutions are compared in Figs. 5 and 6. According to the plots, for $\tau \gtrsim 1.5$ the numerical calculation of the system (16) differs strongly from the analytical calculation performed using Eqs. (26). The reason is that for long times τ the series (26) converge poorly, and a larger number of terms must be included in the series to obtain a correct description of the behavior of the system. According to Fig. 4, the strongest dependence of Δp on a occurs for $\tau > 1$. Consequently, a correct description of the process for large τ is a substantial advantage of the approach developed in the present work.

We shall now compare the solutions obtained for $\Delta p(t)$ with the experimental data. Since "stepped" dissolution has been studied in detail thus far for weak solutions of ^{4}He in ^{3}He, the comparison is made precisely with these results.[3] Figure 7 shows the experimental data for the first "large" cooling in the region of separation, the plots of the numerical and analytical calculation (26), and the results of fitting the exponential function $\Delta p \sim \exp(t/t_0)$ to the experimental data. As follows from the figure, only the solution obtained numerically gives a good description of the experimental data over the entire time interval. The agreement with the experimental dependence $\Delta p(t)$ for small t makes it possible to determine reliably the values of τ from the data obtained experimentally over a short initial time interval. Figure 8 shows the time dependence of the pressure change accompanying separation of the solution, corresponding to the subsequent steps in Ref. 3 in Fig. 1. The theory constructed agrees well with experiment in this case also.

IV. CONCLUSIONS

In the present work the diffusion approximation was used to investigate the growth of an inclusion of a new phase

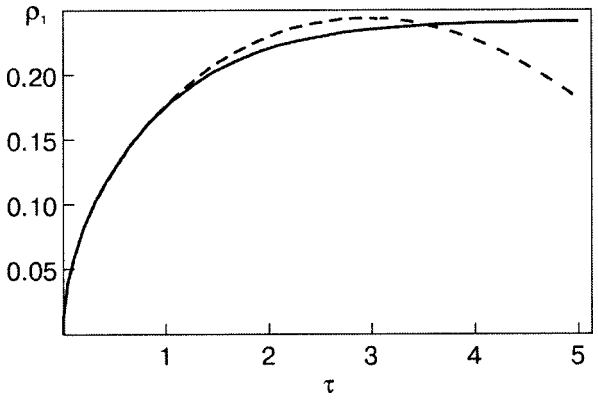

FIG. 6. Radius of a spherical center of a new phase with "large" cooling as a function of τ. Solid line—numerical calculation, dashed line—analytical calculation using Eq. (26).

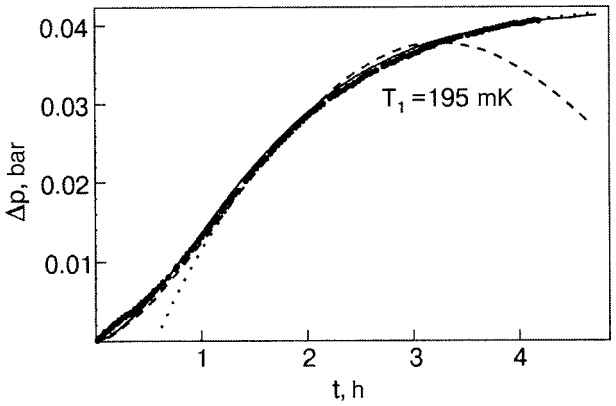

FIG. 7. Pressure change versus time for the first "large" cooling: solid line—numerical calculation; dashed line—analytical solution; dots—fit of an exponential to the experimental data.

in the process of separation of solid solutions of helium isotopes. The diffusion problem in the spherically symmetric approximation was solved numerically, taking account of the change in the size of an inclusion during its growth. Not only the general solutions of the diffusion equations but also the solution of the system of equations that makes it possible to determine the change in the radius of an inclusion under conditions where its growth is determined by the fluxes of matter both from outside and inside the inclusion were obtained for the first time. The concentrations of the diffusing substance at the boundary of an equivalent sphere, limiting the region of diffusion from outside the inclusion, and at the center of the inclusion are found simultaneously. The problem can be solved for an arbitrary ratio of the coefficients of diffusion outside and inside an inclusion. The results of the numerical calculation are compared with an analytical solution found previously for relatively small values of the dimensionless time neglecting diffusion inside the inclusion. This made it possible to estimate the time interval during which the approximate analytical solution gives results which are quite close to the results obtained by direct numerical integration of the system of differential equations. The use of formulas which are a generalization of the result obtained previously for the excess pressure accompanying the separation of regular solutions made it possible to determine, on the basis of the time dependences of the concentrations found using numerical methods, how the pressure changes as a function of time under conditions of constant volume. The dependences obtained are in good agreement with the experimental results found from a study of the decomposition of a solid solution of ^{4}He in ^{3}He by the method of high-precision pressure measurements. The method developed in the present work for solving the diffusion problem can be used in the future for studying diffusion processes occurring during the decomposition of concentrated solutions of helium isotopes and for obtaining information on the currently unknown diffusion coefficients in these systems.

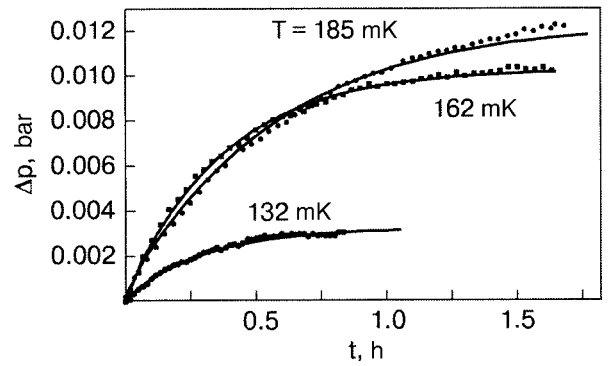

FIG. 8. Pressure change versus time for stepped coolings: solid line—numerical calculation. The temperatures correspond to the final temperature T_f of a cooling step (see Fig. 1).

[a)]E-mail: degtyaryov@ilt.kharkov.ua

[1]A. N. Gan'shin, V. N. Grigor'ev, V. A. Maĭdanov, N. F. Omelaenko, A. A. Penzev, É. Ya. Rudavskiĭ, A. S. Rybalko, and Yu. A. Tokar', Fiz. Nizk. Temp. **25**, 796 (1999) [Low Temp. Phys. **25**, 592 (1999)].
[2]A. Smith, V. Maidanov, E. Rudavskii, V. Grigor'ev, V. Slezov, M. Pool, I. Saunders, and B. Cowan, Phys. Rev. B **67**, 245314 (2003).
[3]V. N. Grigor'ev, V. A. Maĭdanov, A. A. Penzev, É. Ya. Rudavskiĭ, A. S. Rybalko, and E. V. Syrnikov, Fiz. Nizk. Temp. **29**, 1165 (2003) [Low Temp. Phys. **29**, 883 (2003)].
[4]B. Ya. Lyubov, *Diffusion Processes in Inhomogeneous Solid Media*, Nauka, Moscow (1972).
[5]D. O. Edwards and S. Balibar, Phys. Rev. B **39**, 4083 (1989).

Translated by M. E. Alferieff

SUPERCONDUCTIVITY, INCLUDING HIGH-TEMPERATURE SUPERCONDUCTIVITY

Enhancement of superconductivity in tin films of different widths by an external electromagnetic field

V. M. Dmitriev[a)]

B. I. Verkin Institute for Low Temperature Physics and Engineering of the National Academy of Sciences of Ukraine, pr. Lenina 47, Kharkov 61103, Ukraine; International Laboratory of High Magnetic Fields and Low Temperatures, 95 Gajowicka Str., Wroclaw 53-421, Poland

I. V. Zolochevskiĭ, T. V. Salenkova, and E. V. Khristenko

B. I. Verkin Institute for Low Temperature Physics and Engineering of the National Academy of Sciences of Ukraine, pr. Lenina 47, Kharkov 61103, Ukraine

(Submitted April 26, 2005)
Fiz. Nizk. Temp. **31**, 1258–1265 (November 2005)

The current-voltage characteristics of high-quality thin tin films, ranging in width from 7 to 50 μm, irradiated by microwave radiation are investigated. The behavior of the critical current I_c and of the maximum current I_m for the existence of a stationary flow of the characteristic vortices of the transport current (formation current of the first phase-slip line) is analyzed. The regimes of enhancement and suppression of the currents I_c and I_m by a microwave field are studied and analyzed. The criteria for separating films into narrow and wide are established. It is shown that the superconductivity enhancement effect is a general effect and is observed for uniform (narrow films) and nonuniform (wide films) distributions of the superconducting current over the film width. © *2005 American Institute of Physics*. [DOI: 10.1063/1.2127877]

I. INTRODUCTION

For a long time it was generally believed that the effect of an electromagnetic field on a superconductor should always result in the suppression of the energy gap Δ and other superconducting properties of the superconductor: the critical current I_c, the superconducting transition temperature T_c, and the critical magnetic field H_c, i.e. weakening of superconductivity. However, in 1966 the observation of an increase of the critical current of thin narrow superconducting bridges by microwave radiation was reported in Ref. 1. Subsequently, this effect was observed in virtually all types of superconducting weak links and in superconducting channels (single crystalline filaments and thin (thickness $d \ll \xi(T), \lambda_\perp(T)$) narrow (width $w \ll \xi(T), \lambda_\perp(T)$) films). Here $\xi(T)$ and $\lambda_\perp(T) = 2\lambda^2(T)/d$ are, respectively, the coherence length and the penetration depth of a weak perpendicular magnetic field into the film and $\lambda(T)$ is the London penetration depth.

A microscopic theory was proposed in 1970.[2] This theory examines the effect of electromagnetic radiation on the width of the energy gap Δ of a superconductor in the absence of vortices. To understand correctly the behavior of superconductors with an energy gap in an ac electromagnetic field it was necessary to take account of absorption of electromagnetic energy by quasiparticles (electrons) and inelastic processes resulting in dissipation of the absorbed energy. The theory showed that if a superconductor with a uniform spatial distribution of Δ is in an electromagnetic field whose frequency is higher than the inverse energy relaxation time τ_e of electrons, then the equilibrium distribution function of the electrons shifts to higher energies, which results in a stationary nonequilibrium state and increases the energy gap of the superconductor and, therefore, enhances its superconducting characteristics. The lower limiting frequency f_1 at which the superconductivity enhancement effect first appears is determined from the transcendental equation[2]

$$f_1^2 = \Delta/[\tau_\varepsilon h \ln(8\Delta/hf_1)]. \quad (1)$$

It should be noted that, in general, in the presence of an electromagnetic field Δ varies in space and time. However, for sufficiently thin and narrow superconducting samples the coordinate dependence of Δ can be neglected. In addition, near T_c the relaxation time of the order parameter $\tau_\Delta \approx 1.2\tau_\varepsilon/(1-T/T_c)^{1/2}$ is large compared with the reciprocal of the frequency of the enhancing microwave radiation ($\omega\tau_\Delta \gg 1$), so that the temporal oscillations of Δ can also be neglected. Consequently, the microscopic theory of Ref. 2 neglected the temporal and spatial variations of the order parameter in the sample.

To realize experimentally the case of a spatially uniform nonequilibrium state of a superconductor in a high-frequency field, the case studied in the theory of Ref. 2, it was necessary to ensure that the energy gap be constant over the volume of the sample ($w, d \ll \xi(T), \lambda_\perp(T)$). This is a purely technological problem. It was also important to ensure a uniform distribution of the transport current over the volume of the sample. Nonsatisfaction of this condition resulted in a nonuniform distribution of Δ not for technological reasons but rather because of the dependence of the energy gap on the magnitude of the transport current $\Delta(I)$. Finally, it was important to provide effective removal of heat. It was shown that narrow superconducting film channels sputtered on an appropriate substrate best satisfied these requirements. The

TABLE I. Parameters of film samples.

Sample	L, μm	w, μm	d, nm	$R_{4.2}$, Ω	$R^{\square}$, Ω	T_c, K	l_i, nm	R_{300}, Ω
Sn1	64	1.5	90	3.05	0.071	3.834	1743	59
SnW5	92	42	120	0.14	0.064	3.789	145	2.27
SnW6	81	17	209	0.185	0.039	3.712	152	3.147
SnW10	88	7	181	0.487	0.040	3.809	169	9.156

Note: L—sample length; w—sample width; d—sample thickness; l_i—electron mean free path length.

theory proposed in Ref. 2 was completely confirmed in experimental works investigating such samples (see, for example, Refs. 3 and 4).

The phenomenon of enhancement of superconductivity by an electromagnetic field in superconductors free of the characteristic vortices of the magnetic flux of the transport current is now a classical effect in solid-state physics.

For wide films the electrodynamic change of Δ over the width of a film with a nonuniformly distributed current and in the presence of characteristic vortices can no longer be neglected. Consequently, the theory of Ref. 2, strictly speaking, is inapplicable for wide films. Nonetheless, although the construction of a theory for a nonuniform distribution of Δ in a superconductor is a difficult problem, in principle the enhancement effect should occur in this case also.

In 2001 enhancement of superconductivity by an external magnetic field was also observed in wide ($w \gg \xi(T), \lambda_\perp(T)$) superconducting films with a nonuniform spatial distribution of $\Delta(I)$ over the width of the sample.[5] It was shown experimentally that under the action of an external electromagnetic field, the critical current I_c and the formation current of the first phase-slip line (PSL) increase. This current is denoted in Ref. 5 as I_c^{dp}. In Ref. 6 the temperature dependences of the current I_c^{dp} are analyzed taking account of the nontrivial distribution of the transport current and density of vortices across a wide film. As a result, it was shown that the current I_c^{dp} is the critical Ginsburg-Landau depairing current I_c^{GL}, if the film corresponds to the parameters of a vortex-free narrow channel at temperatures near T_c. Far from T_c this current is the maximum Aslamazov-Lempitskiĭ current I_m.[7] The physical meaning of the current I_m is that this is the maximum current for which a stationary uniform flow of the characteristic vortices of the transport current across a wide film is still possible. Above this current, $I > I_m$, the vortex structure collapses and a PSL structure arises in its place.[6] It is this structure that determines the resistance of the sample as the transport current increases further.

In this connection the problem of enhancement of superconductivity in wide films becomes especially interesting, since it requires studying the behavior of not only the critical current and critical temperature in an electromagnetic field. The current I_m and its ratio with I_c in an external electromagnetic field with different frequencies f and powers P become important objects of investigation.

The objective of the present work is to investigate the dependence of the enhancement of the critical current I_c and the formation current I_m of the first PSL on the power and frequency of an electromagnetic field in thin (thickness $d \ll \xi(T), \lambda_\perp(T)$) superconducting films as a function of their width w.

II. EXPERIMENTAL RESULTS AND THEIR DISCUSSION

To understand how the enhancement of superconductivity is manifested in a wide film we gradually increased the width of the sample, starting with a narrow channel, and observed how the effect under study changed in the process.

The objects of investigation consisted of thin ($d \ll \xi(T), \lambda_\perp(T)$) tin films. The method described in Ref. 6 was used to produce the films. The parameters of some of the films are presented in Table I.

It was shown in Ref. 5 that long ($L \gg \xi(T), \lambda_\perp(T)$) and wide ($w \gg \xi(T), \lambda_\perp(T)$) superconducting films exhibit an increase of the critical current under the action of external microwave radiation. Figure 1 shows a family of current-voltage characteristics (IVCs) of one such film (SnW5), 42 μm wide, for different power levels of the microwave irradiation at frequency $f = 12.89$ GHz. Here, just as in Ref. 6, $I_c(T)$ is the current at which a voltage appears on the sample as a result of the entry of vortices of the characteristic magnetic flux of the current and $I_m(T)$ is the maximum current at which a stable uniform flow of characteristic vortices exists or the formation current of the first phase-slip line.

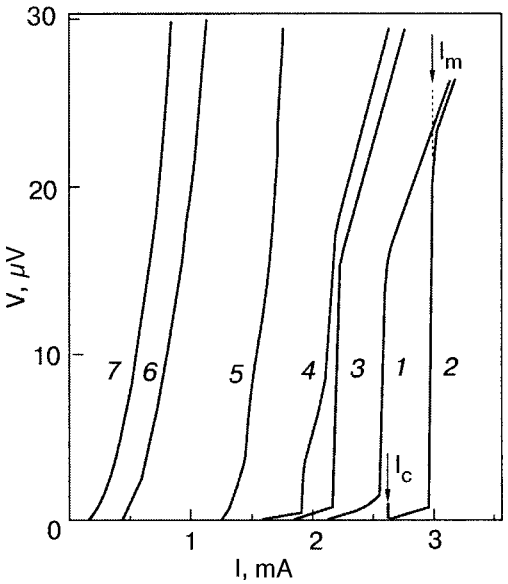

FIG. 1. Family of current-voltage characteristics of film sample SnW5 at $T = 3.745$ K and $f = 12.89$ GHz for various irradiation power levels: irradiation power equal to zero (1); the irradiation power increases with the numbers on the IVCs, (2-7).

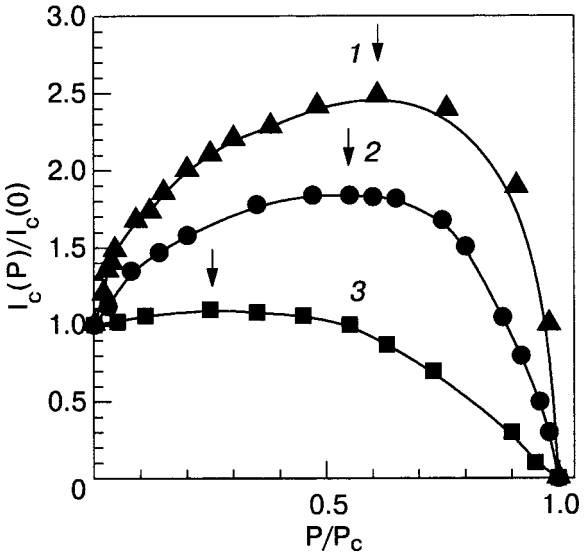

FIG. 2. Relative critical current $I_c(P)/I_c(0)$ of sample Sn1 versus the reduced microwave irradiation power P/P_c at $T=3.812$ K for various irradiation frequencies f, GHz: 15.4 (▲), 8.1 (●), 3.7 (■) ($I_c(0)$—critical current of a film at $P=0$; P_c—minimum power of the electromagnetic irradiation for which $I_c(P)=0$).

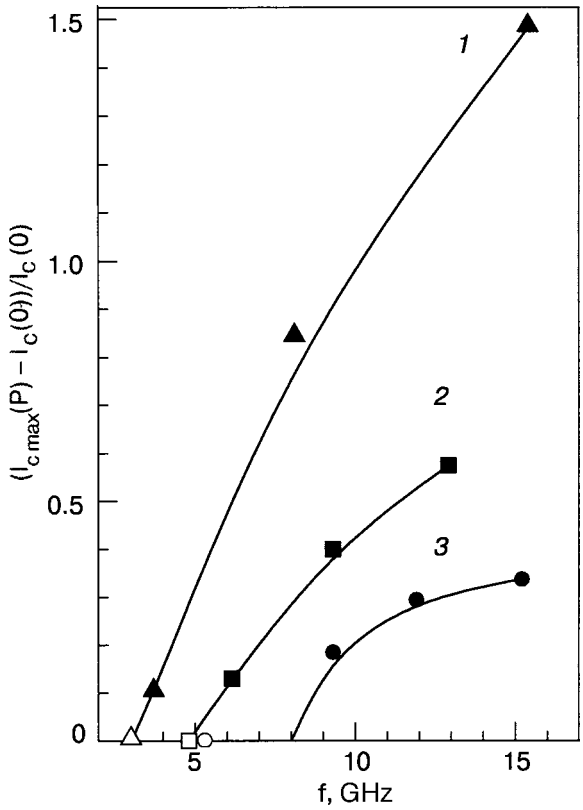

FIG. 3. Reduced excess of the maximum critical current $I_{cmax}(P)$ above $I_c(0)$ versus the irradiation frequency for samples Sn1(▲), SnW10(■), and SnW5(●) at $t=T/T_c\approx 0.99$; the values of the lower limiting superconductivity enhancement frequencies from Eq. (1) for samples Sn1(△), SnW10(□), and SnW5(○).

Figure 1 shows that the current $I_c(P)$ (2) is much greater than $I_c(0)$ (1), and the current $I_m(P)>I_m(0)$. Thus, external radiation increases I_c and I_m.

In addition, the following fact merits attention. With enhancement of superconductivity the differential resistance due to the stationary flow of vortices in the current range $I_c<I<I_m$ decreases (see Fig. 1). This could be related with a decrease in the density and effective velocity of the vortices.

A. Critical current I_c

Figure 2 shows for the narrow channel Sn1 of width $w=1.5$ μm with $T/T_c=0.994$ and $w/\lambda_\perp(T=3.812\text{ K})=0.28$ the relative magnitude $I_c(P)/I_c(0)$ of the enhancement of the critical superconducting current as a function of the reduced power P/P_c of the microwave irradiation for different frequencies of the external radiation. Here P_c is the minimum power for which $I_c(P=P_c)=0$, the curve *3* refers to a quite low irradiation frequency—3.7 GHz, the curve *2* is constructed for the irradiation frequency 8.1 GHz, and the curve *1* corresponds to the frequency 15.4 GHz. The arrows mark the powers for which the maximum enhancement of I_c is observed for each irradiation frequency. For irradiation frequency $f=3.7$ GHz the reduced power of the microwave irradiation for which the maximum effect is observed is $P/P_c=0.25$. The power ratio $P/P_c=0.51$ for $f=8.1$ GHz and 0.61 for $f=15.4$ GHz. It is evident that as the irradiation frequency increases, the reduced power at which maximum enhancement is observed increases. Unfortunately, the theory of enhancement given in Ref. 2 does not study the dropoff of the effect, following the peak, as the irradiation power increases. Consequently, the theory of Ref. 2 cannot explain the shift of the maximum enhancement of superconductivity by electromagnetic irradiation in the direction of higher powers with increasing frequency. The irradiation frequency dependences of the reduced increase of the critical current above its base value are presented in Fig. 3 for films of different width. It is evident that as the frequency increases, the excess of the critical current $I_{c\,max}(P)$ above $I_c(0)$ increases for narrow (curves *1* and *2*) and wide (curve *3*) films. As the frequency increases further, this dependence passes through a maximum and then starts to decrease (here this is not shown). It should be noted that the frequency at which the maximum enhancement of the critical current is observed decreases with increasing film width (the frequency of the maximum is about 30 GHz for Sn1 and about 15 GHz for SnW5).

It is interesting to note that for the Sn1 film (see Fig. 3, curve *1*) the calculation of the lower limiting frequency f_1 of enhancement from Eq. (1) gives 3 GHz (indicated by the symbol Δ in Fig. 3). This agrees well with experiment, as shown previously for narrow channels.[3] It is important to underscore that to calculate the lower limiting enhancement frequency of sample Sn1 we used the value $\tau_\varepsilon=8.3\cdot 10^{-10}$ s, characteristic for this sputtering series.

Figure 4 shows the curves of the reduced critical current $I_c(P)/I_c(0)$ versus the reduced power P/P_c of the microwave radiation for different irradiation frequencies for the wider sample SnW10 of width 7.3 μm at temperature $T=3.777$ K ($T/T_c=0.992$). At this temperature the ratio $w/\lambda_\perp=3.56$, i.e. less than 4. As shown in Ref. 6, at this temperature the sample SnW10 is still a narrow channel and its current-voltage characteristics do not show a resistive section due to the motion of vortices. Indeed, the curves *1* and *2* in Fig. 4 are qualitatively identical to the curves in Fig. 2. The arrows in Fig. 4 have the same meaning as in Fig. 2. It is evident in

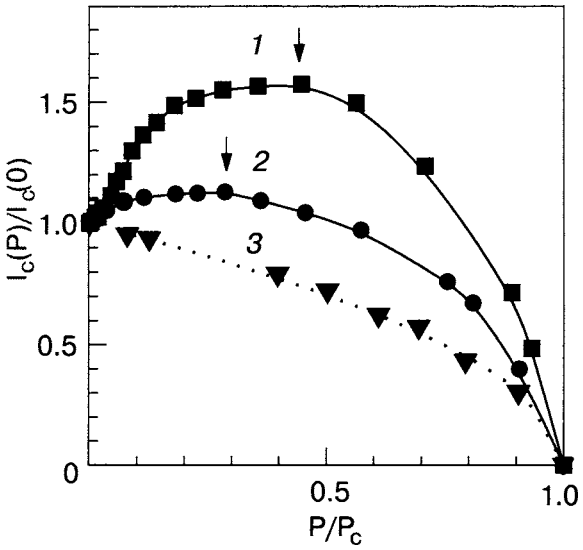

FIG. 4. Relative critical current $I_c(P)/I_c(0)$ of sample SnW10 versus the reduced microwave irradiation power P/P_c at $T=3.777$ K for different irradiation frequencies f, GHz: 12.91 (■), 6.15 (●), 0.63 (▼); dotted curve *3*—$I_c(P)/I_c(0)(P/P_c)$ computed using Eq. (2).

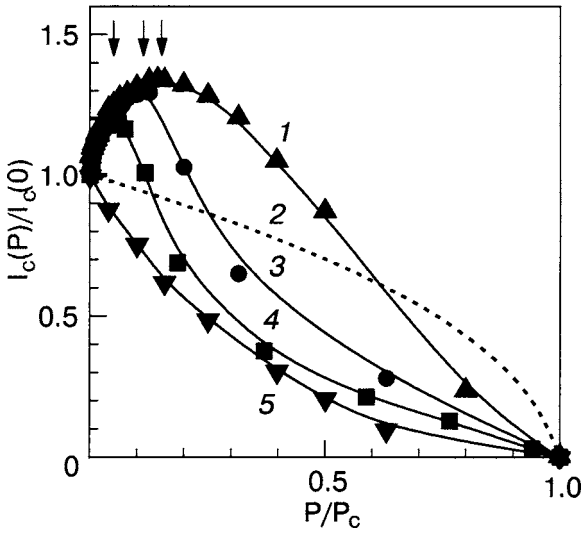

FIG. 5. Relative critical current $I_c(P)/I_c(0)$ of sample SnW5 versus the reduced microwave irradiation power P/P_c at $T=3.744$ K for different irradiation frequencies f, GHz: 15.2 (▲), 11.9 (●), 9.2 (■), and 5.6 (▼); dashed curve *2*—$I_c(P)/I_c(0)(P/P_c)$ computed using Eq. (2).

Fig. 4 that as the irradiation frequency increases, the reduced power at which the maximum enhancement of superconductivity is observed increases, as happened for a narrow channel. Moreover, the calculation of the lower limiting frequency from Eq. (1) gives 4.8 GHz (indicated by the symbol □), which also agrees quite well with the experimental value of f_1, as is evident in Fig. 3 (curve *2*). It is important to note that for the sample SnW10 we used the value $\tau_\varepsilon = 4.3\cdot 10^{-10}$ s, characteristic for this sputtering series, to calculate the lower limiting frequency of enhancement.

In Fig. 4 the experimental curve *3* (▼) was obtained for a relatively low irradiation frequency ($f=0.63$ GHz). This frequency is lower than the limiting frequency f_1 for the onset of enhancement of superconductivity, so that we observe only the suppression of I_c with increasing P. Since under these experimental conditions we consider the sample SnW10 to be a narrow channel, it is interesting to compare the experimental curve *3* (▼) with the theoretical curve. It is shown in Ref. 8 that for superconducting films, whose critical current equals the Ginsburg-Landau depairing current, the following dependence of the critical current on the power of the irradiating electromagnetic field holds:

$$I_c(P,\omega)/I_c(T) = (1-(P/P_c(\omega)))^{1/2} \times (1-(2P/((\omega\tau_\Delta)^2 P_c(\omega))))^{1/2} \qquad (2)$$

for $\omega\tau_\Delta \gg 1$. In our case $\omega\tau_\Delta \approx 24$ and the computed dependence (2) is presented in Fig. 4 (dotted line). Evidently, it agrees quite well with the experimental curve *3* and confirms our previous conclusion in Ref. 6 that films with the ratio $w/\lambda_\perp \leqslant 4$ are narrow channels. As the temperature of the sample SnW10 decreases below the crossover temperature T_{cros1}[6] the ratio $w/\lambda_\perp$ increases and exceeds 4, but not by much. This is due to the quite smooth decrease of $\lambda_\perp(T)$ as a function of temperature far from T_c. As a result, the distribution of the transport current over the width of the film becomes nonuniform, but not so much as to greatly influence the behavior of the film in an electromagnetic field and therefore the form of $I_c(P)$. To observe substantial differences the temperature must be decreased substantially, but in so doing the enhancement of superconductivity decreases appreciably. This is due to a decrease in the number of excited quasiparticles.[2–4]

Consequently, to study further the enhancement of superconductivity we chose at the outset a wider film—the sample SnW5, 42 μm wide. Figure 5 shows for this sample with $T/T_c=0.988$ and $w/\lambda_\perp(T=3.744\text{ K})=20$ the reduced critical current $I_c(P)/I_c(0)$ versus the reduced power P/P_c of the microwave field for different irradiation frequencies. The meaning of the arrows is the same as in Figs. 2 and 4. It is evident in Fig. 5 that as the irradiation frequency increases, the reduced power at which the maximum enhancement of superconductivity is observed increases. In addition, it is evident that the descending sections of the curves 1 and 3–5 in Fig. 5 differ qualitatively from those in Figs. 2 and 4 by the sign of the curvature: in Figs. 2 and 4 the descending sections of the curves are convex, whereas in Fig. 5 they are concave. Curve *5* was obtained at irradiation frequency $f=5.6$ GHz and the enhancement effect was not observed. The dashed curve shows the pressure dependence $I_c(P)$ calculated using Eq. (2) for the SnW5 film in which the the transport current is distributed uniformly over its width. It is evident that the curves *2* and *5* differ substantially from one another. Therefore we can attribute the concavity of the descending section of the experimental curve *5* completely to the nonuniform current distribution over the width of the film. In Fig. 5 the curves *1, 3*, and *4* were obtained for irradiation frequencies 15.2 GHz, 11.9 GHz, and 9.2 GHz. We attribute the concavity of their descending sections, just as for curve *5*, to the nonuniform current distribution over the width of the sample.

It is interesting that in the narrow film Sn1 the enhancement effect is very noticeable already at irradiation frequency $f=3.7$ GHz (see Fig. 2, curve *3*), while for the film SnW5 it was not observed even for $f=5.6$ GHz (see Fig. 5, curve *5*). A calculation of f_1 for the film SnW5 using Eq. (1)

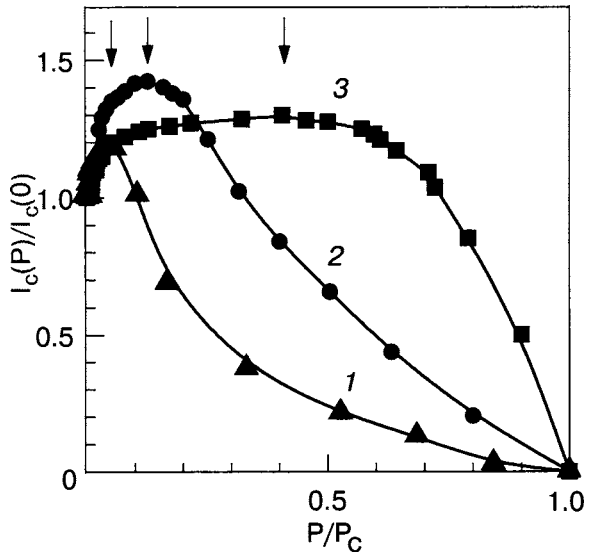

FIG. 6. Relative critical current $I_c(P)/I_c(0)$ versus the reduced microwave irradiation power P/P_c at frequency $f=9.2$ GHz at $t=T/T_c\approx 0.99$ for different samples: SnW5 (▲), SnW6 (●), and SnW10 (■).

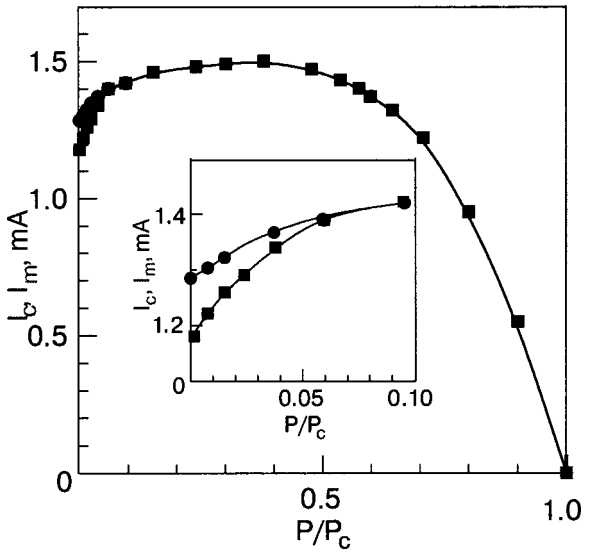

FIG. 7. Critical current I_c(■) and maximum current for the existence of vortex resistivity I_m(●) for sample SnW10 versus the reduced microwave power P/P_c at irradiation frequency $f=9.2$ GHz and $T=3.750$ K. Inset: Enlarged fragment of the dependences indicated above.

gives 5.1 GHz, which no longer corresponds to the experimental value 8.0 GHz. It is important to underscore the fact that to calculate the lower limiting enhancement frequency for the sample SnW5 the value $\tau_\varepsilon=4.5\cdot 10^{-10}$ s characteristic for this sputtering series was used.

The functions $I_c(P)$ in relative units for films of different widths and the same experimental conditions are presented in Fig. 6. The arrows in Fig. 6 have the same meaning as in Figs. 2 and 4. It is evident in Fig. 6 that as the film width increases, the ratio P/P_c for which the maximum enhancement effect is observed decreases. In addition, it follows from the data in the figure that as the film width increases, the power range ΔP where enhancement of superconductivity is observed decreases. Consequently, it can be supposed that for quite wide films the enhancement of superconductivity can be essentially unrealizable experimentally because of the very narrow power range of existence of this effect and because of the weakness of the effect. As the film width increases, the sign of the curvature of the descending sections of the curves changes (see Fig. 6). For the sample SnW6 of width $w=17$ μm the experimental value of twice the penetration depth of a longitudinal electric field into the superconductor is $2l_E=13.7$ μm, i.e. for this film $w>2l_E$, but not by much. The concavity of the curve *2* is not so great. It can be supposed that if the width of the sample were equal to $2l_E$, then the descending section of $I_c(P)$ would be rectilinear, separating the sections with positive and negative curvature, which are characteristic for narrow and wide films. We call attention to this circumstance because the authors of Ref. 9 already encountered a similar unusual scale ($2l_E$) for separation into narrow and wide films in their investigation of the density of non-Josephson generation currents. We believe that the current distribution over the film width plays a large role in this problem.

B. Maximum current of vortex resistance I_m

In the preceding section we determined how the electromagnetic radiation influences the critical current I_c of films of different widths. Another important characteristic current of a wide film is the so-called maximum current of vortex resistance I_m, whose physical meaning is determined in Refs. 6 and 7 and is mentioned above in the present work. The current I_m was investigated experimentally in Ref. 6 and has the form[7]

$$I_m(T) = CI_c^{GL}(T)\ln^{(-1/2)}(2\omega/\lambda_\perp(T)). \tag{3}$$

In this expression I_c^{GL} is the critical Ginsburg-Landau depairing current, and C is a numerical factor of the order of 1. On the basis of Eq. (3), obtained for an equilibrium current $I_m(T)$ (in the absence of external irradiation), it can be supposed that the behavior of $I_m(P,f)$ in an electromagnetic field is determined by the influence of this radiation on $I_c^{GL}(T)$ and $\lambda_\perp(T)$. When superconductivity is enhanced, $I_c^{GL}(T)$ increases and $\lambda_\perp(T)$, on the basis of general considerations (enhancement of T_c), should decrease. The degree to which $\lambda_\perp(T)$ decreases, other conditions being equal, also depends on how close the working temperature T is to T_c. Thus it is qualitatively understandable that the degree of growth of $I_m(P)$ should be less than that of $I_c(P)$.

Figures 7 and 8 show the experimental curves $I_c(P)$ and $I_m(P)$ for the films SnW10 and SnW5. The insets show the initial sections of the curves in order to show more clearly the degree to which $I_c(P)$ and $I_m(P)$ increase. It is evident from the figures that the critical currents $I_c(P)$ of the films do indeed increase more rapidly than the currents $I_m(P)$ with increasing irradiation power. There arises the question of whether or not the change of $\lambda_\perp$ under the action of the electromagnetic radiation is sufficient to suppress to such an extent the growth of $I_m(P)$ as compared with that of $I_c(P)$. Our estimates of the changes in $\lambda_\perp(P)$ at the relative temperatures at which the curves in Fig. 7 and 8 were measured show that they are quite small and, in accordance with Eq. (3), cannot slow the growth of $I_m(P)$ so greatly. Therefore there must be another reason. Analysis of the experimental data shows that this reason could be the nonuniformity of the

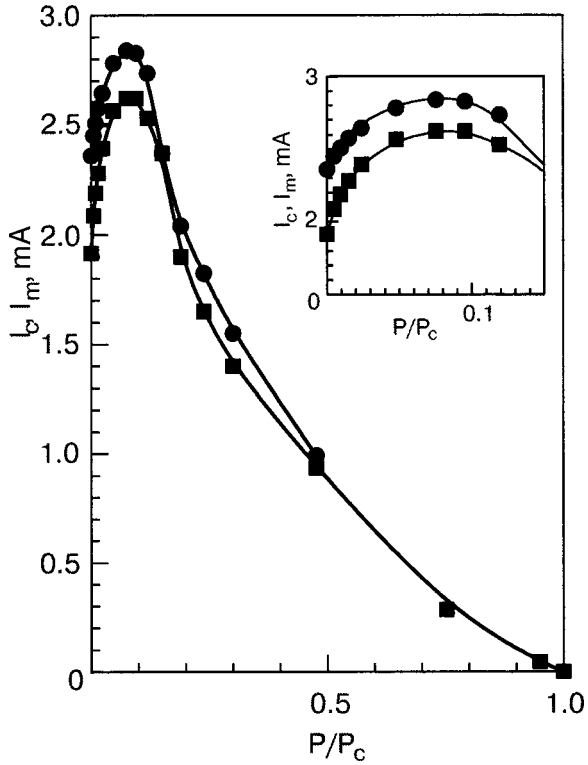

FIG. 8. Critical current I_c(■) and maximum current for the existence of vortex resistivity I_m(●) for sample SnW5 versus the reduced microwave power P/P_c at irradiation frequency $f=12.89$ GHz and $T=3.748$ K. Inset: Enlarged fragment of the dependences indicated above.

distribution of the currents over the film width and the presence of a vortex resistive background against which I_m grows. This background also depends (as already mentioned above, see Fig. 1) on the external radiation; Eq. (3) for the equilibrium current I_m does not take this into account. In this respect we call attention once again to a fundamental difference between I_c and I_m. I_c always arises against the background of a purely superconducting state. Consequently, on account of the transverse Meissner effect, it is always reached first at the edges of a film. The wider the film relative to $\lambda_\perp$, the more nonuniformly the transport current is distributed in it. In contrast to this, the current I_m is the maximum current for which there remains the possibility of uniform flow of vortices across the film. The presence of a moving lattice of vortices makes the distribution of the superconducting current across the film more uniform, though unique.[7] Thus the current in a wide film in a vortex-free state with $I \leqslant I_c$ is always more nonuniformly distributed over the width than in the same film in the presence of characteristic vortices with currents $I_c < I \leqslant I_m$.

For the reasons mentioned above the expression (3) is unsuitable for making an approximate calculation of the current I_m in a wide film exposed to an external electromagnetic field. A new theory of the nonequilibrium state of a wide film, taking account of the nonuniform distribution of the transport current and order parameter over the width of the film when calculating $I_c(P,f)$ and the presence of a vortex resistance $R(P,f)$ when calculating $I_m(P,f)$, is required.

III. CONCLUSIONS

Experimental investigations of films of different widths have shown that the enhancement of superconductivity is a general effect and is observed for uniform (narrow films) and nonuniform (wide films) distributions of the superconducting current over the film width.

Investigations in ac fields confirmed our previous conclusion based on studies using constant currents that films with $w/\lambda_\perp \leqslant 4$ are narrow channels. For them, the lower limiting frequences of enhancement of superconductivity computed using the theory of Ref. 2 correspond to the experimental values. In wider films a dependence of the characteristic parameters of the enhancement effect on film width appears. In this connection, to describe the nonequilibrium state of wide films ($w/\lambda_\perp > 4$) in electromagnetic fields it is necessary to construct a theory which, in contrast to Éliashberg's theory,[2] takes account of the nonuniform current distribution and the presence of vortices of its characteristic magnetic flux at the outset.

In the present work the behavior of the currents I_c and I_m in thin superconducting films of different widths in a microwave field was analyzed.

The main results of this work can be formulated as follows.

1. With enhancement of superconductivity not only the critical current I_c but also the current I_m—the formation current of the first phase-slip line—increase.

2. With enhancement of superconductivity the differential resistance of the vortex state of a film in the current range $I_c < I < I_m$ decreases. This could be due to a decrease of the density and the effective velocity of the vortices.

3. As the film width increases, the range of irradiation powers where enhancement of superconductivity is observed becomes narrower. The curvature of the descending section of the curve $I_c(P)$ also depends on the film width.

4. As the frequency of microwave irradiation increases, the power at which the maximum enhancement effect is observed increases.

5. The influence of an electromagnetic field on the current I_m does not reduce to its trivial effect on $I_c^{GL}(T)$ and $\lambda_\perp(T)$.

[a]E-mail: dmitriev@ilt.kharkov.ua

[1]A. F. G. Wyatt, V. M. Dmitriev, W. S. Moore, and F. W. Sheard, Phys. Rev. Lett. **16**, 1166 (1966).
[2]G. M. Éliashberg, JETP Lett. **11**, 114 (1970).
[3]V. M. Dmitriev and E. V. Khristenko, Fiz. Nizk. Temp. **4**, 821 (1978) [Sov. J. Low Temp. Phys. **4**, 387 (1978)].
[4]*Modern Problems in Condensed Matter Sciences, Nonequilibrium Superconductivity*, D. N. Langenberg and A. I. Larkin (eds.), Elsevier Science Publishers B. V. (North-Holland Physics Publishing), New York (1986), Vol. 12, Chaps. 5 and 6.
[5]A. B. Agafonov, V. M. Dmitriev, I. V. Zolochevskiĭ, and E. V. Khristenko, Fiz. Nizk. Temp. **27**, 928 (2001) [Low Temp. Phys. **27**, 686 (2001)].
[6]V. M. Dmitriev, I. V. Zolochevskiĭ, T. V. Salenkova, and E. V. Khristenko, Fiz. Nizk. Temp. **31**, 169 (2005) [Low Temp. Phys. **31**, 127 (2005)].
[7]L. G. Aslamazov and S. V. Lempitskiĭ, Zh. Éksp. Teor. Fiz. **84**, 2216 (1983) [JETP **57**, 1291 (1983)].
[8]E. V. Bezuglyĭ, V. M. Dmitriev, V. N. Svetlov, G. E. Churilov, and A. Yu. Azovskiĭ, Fiz. Nizk. Temp. **13**, 906 (1987) [Sov. J. Low Temp. Phys. **13**, 517 (1987)].
[9]G. E. Churilov, V. N. Svetlov, and V. M. Dmitriev, Fiz. Nizk. Temp. **12**, 425 (1986) [Sov. J. Low Temp. Phys. **12**, 242 (1986)].

Translated by M. E. Alferieff

LOW-TEMPERATURE MAGNETISM

Evolution of the spin state of a 3*d* ion in a pyramidal complex

E. S. Zhitlukhina, K. V. Lamonova,[a] S. M. Orel, and Yu. G. Pashkevich

A. A. Galkin Donetsk Physicotechnical Institute of the National Academy of Sciences of Ukraine, ul. R. Lyuksemburg 72, Donetsk 83114, Ukraine

(Submitted March 17, 2005; resubmitted May 13, 2005)
Fiz. Nizk. Temp. **31**, 1266–1276 (November 2005)

The evolution of the spin state of a metallic 3*d* ion in a pyramidal MeO_5 environment is studied. Ions of metals with $3d^6$ (Fe^{2+},Co^{3+}) and $3d^4$ configurations (Mn^{3+},Cr^{2+}) are studied. The change in the spin state of the metal ion from $S=0$ to $S=1$ and $S=2$ with a variation of the effective charge Z_{eff} of the metal ion and the displacements of the oxygen ions is investigated. The stability of the spin state as a function of the magnitude and symmetry of the displacements of the ligands is checked. Breathing-mode distortions, displacements of the 3*d* ion along the *Z* axis, Jahn-Teller distortions of the basal plane of the pyramid, and fluting distortions of the plane of the pyramid are studied. It is shown that different types of distortions produce different behaviors of the terms corresponding to a change in the spin states of all three types. It is found that the spin state of the coordination complex MeO_5 with the $3d^4$ configuration of the metal ion is most sensitive to breathing-mode distortions and Jahn-Teller type distortions stabilize the state with spin $S=1$ for the $3d^6$ configuration. © *2005 American Institute of Physics*.
[DOI: 10.1063/1.2127888]

I. INTRODUCTION

The interest in spin transitions which has reappeared in the last ten years is due to the appearance of high-quality single crystals of perovskite-like cobalt-containing compounds of the type $RCoO_3$ and $RBaCo_2O_{5+\delta}$ (R is a rare-earth ion, $0 \leqslant \delta \leqslant 1$). It has become clear that the anomalous transport properties of these compounds, the cascade of phase magnetic transitions, and the gigantic magnetoresistance are due to a change in the spin state of the magnetic ions and not to the quality of the polycrystals.[1–16] The presence of trivalent Co^{3+} ions and the special structural features of the unit cell of a metal oxide make it possible for three different spin states to appear: low-spin (LS)—the state with spin $S=0$ ($t_{2g}^6 e_g^0$), intermediate-spin (IS)—the state with spin $S=1$ ($t_{2g}^5 e_g^1$), and high-spin (HS)—the state with spin $S=2$ ($t_{2g}^4 e_g^2$). The appearance of a specific state depends on the ratio between the intra-atomic and interatomic energies: the electron-electron energy E_{ee}, the spin-orbit energy E_{SO}, and the interaction energy E_{CF} of an ion interacting with the crystal field. The spin states are distinguished by the ionic radii, the character of the interatomic bonds, and the magnetic properties. Transitions between these three states can be induced by a change in the external parameters, such as the temperature, pressure, and magnetic field. One of the interesting questions which are now being actively discussed in the literature is the stability of the intermediate-spin state.[13,17–21]

One of the first theoretical calculations of the electronic terms of the compound $SrCoO_3$ to explain the spin transitions was performed in Ref. 3. Using the fact that in compounds of the type $RCoO_3$ and $R_{1-x}Sr_xCoO_3$ the crystal field energy is comparable to that of the Hund exchange interaction energy,[1] the authors investigated the conditions for the existence of a ground state with intermediate spin in $3d^5$ and $3d^6$ electronic systems. The calculations of the atomic multiplets, taking account of the crystal field and hybridization between the orbitals of the cobalt ion and the ligand environment, showed that in $SrCoO_3$ compounds this state can be a ground state because of the redistribution of the electron density. The calculation of the electronic spectrum of the compound $LaCoO_3$ by the Local Density Approximation +Correlation Energy (LDA+U) method[4] confirmed that at liquid-helium temperatures the crystal is a nonmagnetic insulator with spin $S=0$. However, it was found that there exist two excited states with spin $S=1$ and $S=2$ close to the ground state, and as temperature increases these states become occupied. The authors of the article believe that this is due to the special features of the band structure of the compound studied: the e_g levels of the Co ion form a quite wide band, whose origin is due to the substantial overlapping of the electron density of the Co ion with the valence states of the oxygen ions surrounding it. We note that the crystal structure of $SrCoO_3$ and $LaCoO_3$ is such that the Co ions are in an octahedral ligand environment and form CoO_6 complexes.

Other authors have also investigated the electronic spectrum of the trivalent Co ion and its evolution as a function of the external parameters.[21–29] For example, the compound of layered Sr_2CoO_3Cl, where the Co^{3+} ions are in a pyramidal environment of oxygen ions, forming CoO_5 complexes, was investigated in Ref. 21. The calculation of the real crystal structure of Sr_2CoO_3Cl by the LDA+U method showed that the IS state is an excited state, but it can become the ground state if the Co ion is shifted out of the basal plane of the pyramid. The magnitude of the shift should not exceed the critical value $\Delta_{Co} \sim 0.15$ Å, because for large values of Δ_{Co}

the HS state once again becomes the ground state. In Ref. 4 the spin transition IS→HS is attributed to a decrease in the magnitude of the crystal field, which, in turn, results in a lower degree of hybridization between the $3r^2-z^2$ orbital of the ion Co^{3+} and the p_z orbital of the oxygen ion O^{2-}.

Other interesting objects for investigating spin transitions are compounds of rare-earth cobaltites $RBaCo_2O_{5+\delta}$ with orthorhombic group symmetry. For $\delta=0.5$ some cobalt ions lie at the centers of the octahedra formed by oxygen ions and some lie in the basal plane of pyramids. This case is of greatest interest for studying spin evolution, because pyramids and octahedra behave differently when the sample is heated and therefore engender different spin states under identical conditions. For example, in Refs. 11 and 27 it was suggested, on the basis of diffraction and magnetic measurements performed on single crystal and ceramic samples of $RBaCo_2O_{5.5}$, that at low temperatures ($T<108$ K) the ground state of Co^{3+}, which lies in an octahedral environment, is a low-spin state, while for Co^{3+}, which lies in the plane of a pyramid, the ground state is an intermediate-spin state. As temperature increases, the sample undergoes a series of magnetic phase transitions and an insulator-metal transition, which the authors believe is provoked by changes of its spin state. The effective magnetic moment calculated per Co atom at $T=400$ K corresponds to a situation where 50% of the Co ions are in a state with spin $S=1$ and 50% are in a state with spin $S=2$. The authors attribute the high-spin state to Co ions in octahedra and the intermediate-spin state to Co ions in pyramids.

The objective of the present work is to investigate the possible spin states of a metal ion (Me) with the electronic configuration $3d^4(3d^6)$, placed in the basal plane of a pyramidal complex MeO_5. Iron-group ions with the electronic configuration $3d^6(Fe^{2+},Co^{3+})$ or $3d^4(Mn^{3+},Cr^{2+})$ can be taken as the metal ions. The problem was solved using the crystal field theory (CFT), as the simplest but quite effective method among a number of methods used for solving multiparticle problems. The main assumption of the crystal field theory concerning the electrostatic character of the influence of ligands on the central ion strongly limits its range of application, because the electronic structure of the ligand ions is neglected. In spite of this the CFT makes it possible to make a qualitative and sometimes, with an appropriate choice of parameters, quantitative analysis of the splittings and the symmetry of the states and to follow the evolution of the relative energies and the spin under a change of the external conditions without using a computational apparatus which is too cumbersome, for example, the *ab initio* and LDA+U calculations.

The problem of taking account of the inner structure of ligands is important for heteronuclear molecules with a covalent bond. The error associated with ignoring the overlapping of the electron clouds of the central ion and ligands is determined by the degree of covalence λ of the bond, which in turn depends on the relative arrangement of the ligands with respect to the central atom, the magnitudes of the ligand charges, and the magnitude of the effective charge of the central atom. In Ref. 29 it is shown for the coordination complex $[NiF_6]^{-4}$ of the crystal $KNiF_3$ that covalence contributes no more than 10–20% to the splitting parameter Δ_{CF}.

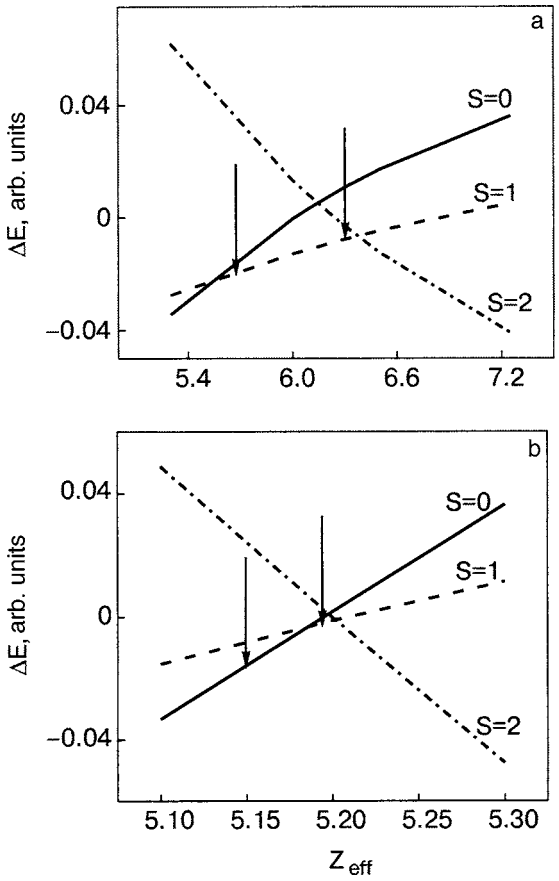

FIG. 1. Energies of the electronic levels of the central ion ΔE, which correspond to different spin states, versus the effective charge Z_{eff} of the metal ion in a regular pyramid for electronic configurations $3d^6$ (a) and $3d^4$ (b). The metal-oxygen distance is 1.95 Å.

A rough estimate of λ for the complex MeO_5 ($Me=Fe^{2+}$, Co^{3+}, Mn^{3+}, and Cr^{2+}) gives ~0.3–0.5.[30] We note that a conventional ionic bond is characterized by $\lambda<0.4$. Therefore assuming the Me–O bond to be ionic we admit an error within the indicated limits. This deficiency can be partially eliminated by varying the magnitude of the effective charge compared to Z_{eff} for a free ion. Charge transfer from O^{2-} to Me^{x+} lowers the ligand charge and, correspondingly, decreases the effective charge Z_{eff} of the central ion. It is obvious that a change of Z_{eff} reflects a change in the degree of covalence of the bond which arises as a result of the redistribution of electron density in the space of the complex. In this connection the dependence of the terms of metal ion on the magnitude of its effective charge was analyzed in this work (Fig. 1). It was shown that there exist points of accidental degeneracy near which negligible changes in the magnitude of the crystal field can result in a change of the spin state.

Another factor which greatly influences the spin state of the central ion is the symmetry of the ligand environment. In the present work the evolution of the ground spin state of a metal ion under the action of distortions of the ligand complex of different symmetry is investigated. Two types of distortions are studied: distortions which a change of the volume of the pyramid and distortions which leave the initial volume unchanged. Breathing-mode displacements are of the first type. Displacements of the central ion along the Z axis,

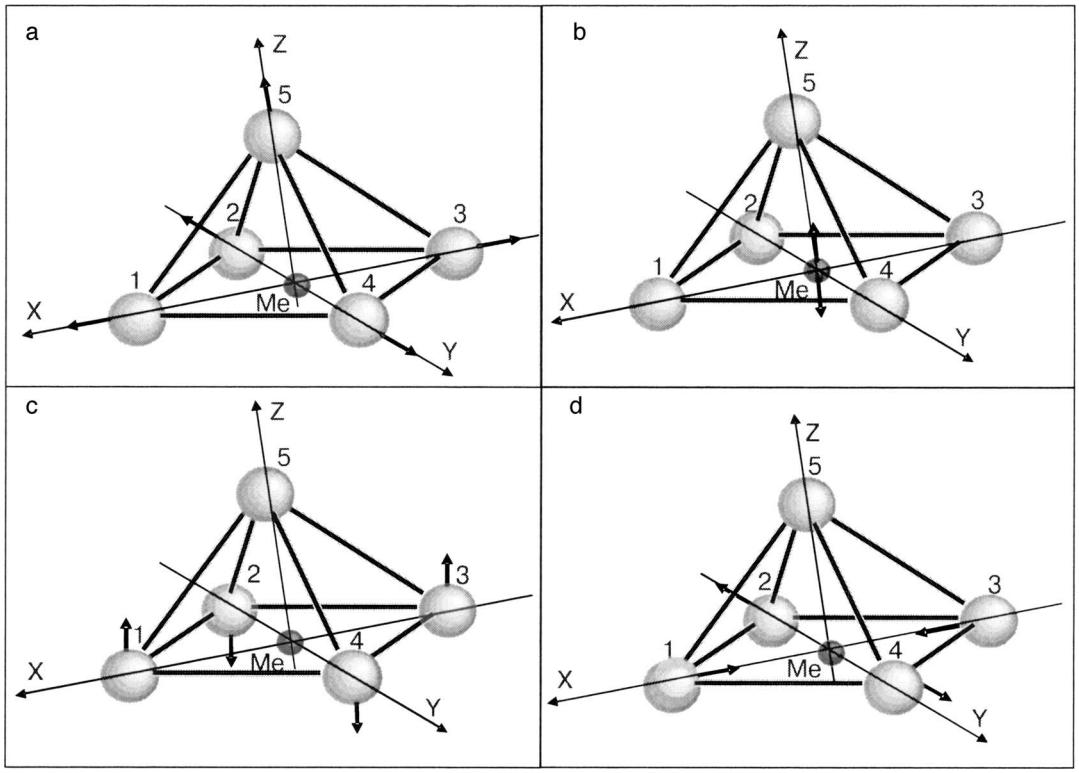

FIG. 2. Types of displacements of the ions comprising the complex MeO_5.

Jahn-Teller displacements, and surface fluting distortions are of the second type (Fig. 2).

The calculations of the ground spin state of the metal ion as a function of the magnitude of the displacements of the oxygen atoms showed that the different types of distortions of the ligand complex result in different scenarios of the behavior of the terms corresponding to the three main spin states (Figs. 3–6).

II. THEORETICAL MODEL

We shall examine an inorganic coordination complex MeO_5 consisting of five oxygen ions occupying the vertices of a pyramid and a central ion with the electronic configuration $3d^4$ ($3d^6$) lying in the basal plane of the pyramid. We shall study the central ion taking account of its inner structure, and we shall consider the ligands—fixed point charges—to be sources of an external electrostatic field. In such a model the main effects of the interaction of the central ion and the ligands are the splitting of the energy levels (terms) of the central ion ^{2S+1}L into a series of crystal terms $^{2S+1}\Gamma$ and the mixing of terms with the same symmetry and multiplicity ($^{2S+1}L\Gamma - {}^{2S+1}L'\,'\Gamma$).

The Hamiltonian of a multielectronic atom in a crystal field can be represented in the form

$$\mathcal{H} = \mathcal{H}_0 + V, \tag{1}$$

where $\mathcal{H}_0$ includes the kinetic energy operators of the electrons and the nucleus of the central ion and also the electrostatic interaction of the core electrons with one another and the valence d electrons; $V = V_{ee} + V_{SO} + V_{CF}$ is the sum of operators of the interelectronic V_{ee} and spin-orbit V_{SO} interactions of the d electrons and their interaction V_{CF} with the electrostatic field of the ligands. An estimate of the contributions of these interactions has shown that for transition metals $V_{SO} \ll V_{CF} + V_{ee}$. This made it possible to limit the excitation operator to the operator $V = V_{CF} + V_{ee}$, which for an ion with the electronic configuration $3d^4(3d^6)$ has the form

$$V = \sum_{k=1}^{N} \sum_{i=1}^{4(6)} \frac{eq_k}{|\mathbf{r}_i - \mathbf{r}_k|} + \sum_{i>j}^{4(6)} \frac{e^2}{r_{ij}}, \tag{2}$$

where N is the number of ligands and $\mathbf{r}_k$ is the radius vector of an ion with the charge q_k.

To calculate the eigenvalues of the operator $V_{CF} + V_{ee}$ we choose the complete (for the electronic configuration under study) system of multielectronic wavefunctions in the zeroth approximation. Since we are interested in the relative arrangement of the terms corresponding to different spin states, we shall proceed from the average crystal field scheme[31,32] and choose as the basis functions the eigenfunctions of the atomic Hamiltonian $\Psi(\gamma SLM_S M_L)$ with configuration $3d^4(3d^6)$ in the Russell-Saunders coupling approximation. We note that for the electronic configuration studied there are 16 terms of different multiplicity, corresponding to 210 states.[33] The ground term is five-fold degenerate with respect to the orbital angular momentum of the ^5D terms. Taking account of the interaction of the central ion with the ligand environment results in an interaction of terms with the same symmetry and multiplicity, and the perturbation matrix $V = V_{CF} + V_{ee}$ decomposes into three independent blocks of dimension $5 \times 5, 45 \times 45$, and 50×50. The first block corresponds to the ^5D term with spin $S=2$, and the two other blocks correspond to terms with spin $S=1$ and $S=0$, respectively. The matrix elements of the perturbation have the form

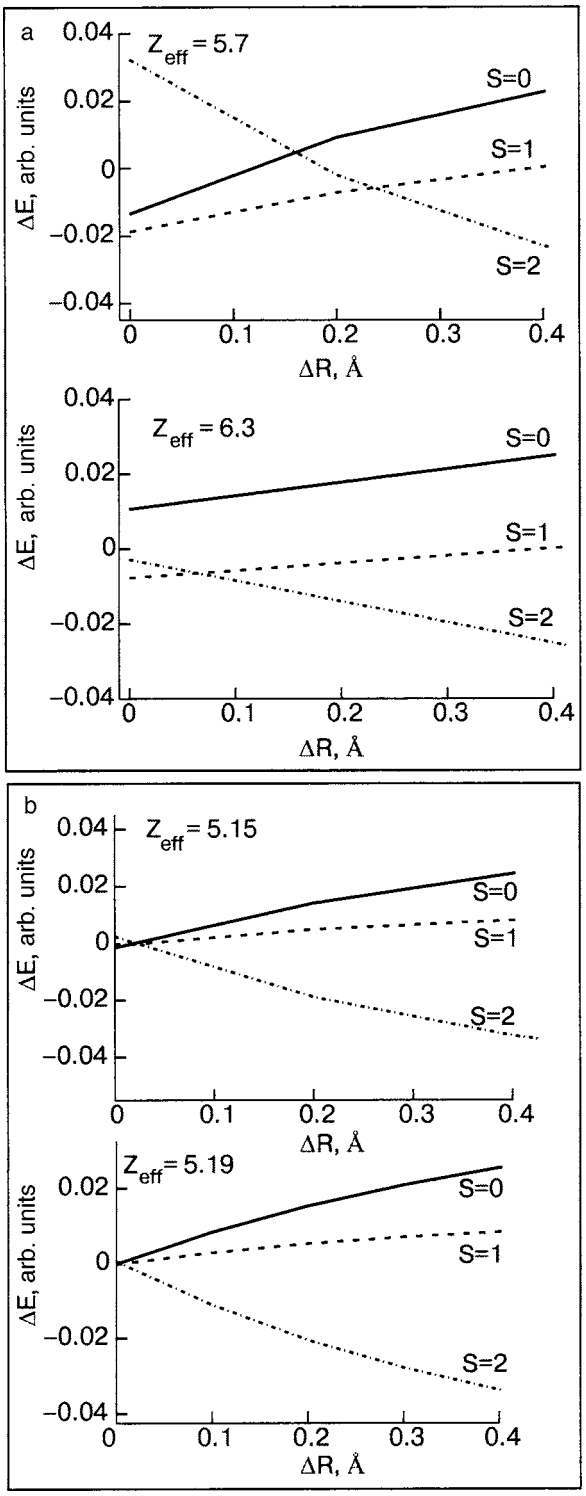

FIG. 3. Energies of the lowest spin states of the central ion ΔE versus the uniform expansion ΔR for different values of the effective charge for the configurations $3d^6$ (a) and $3d^4$ (b).

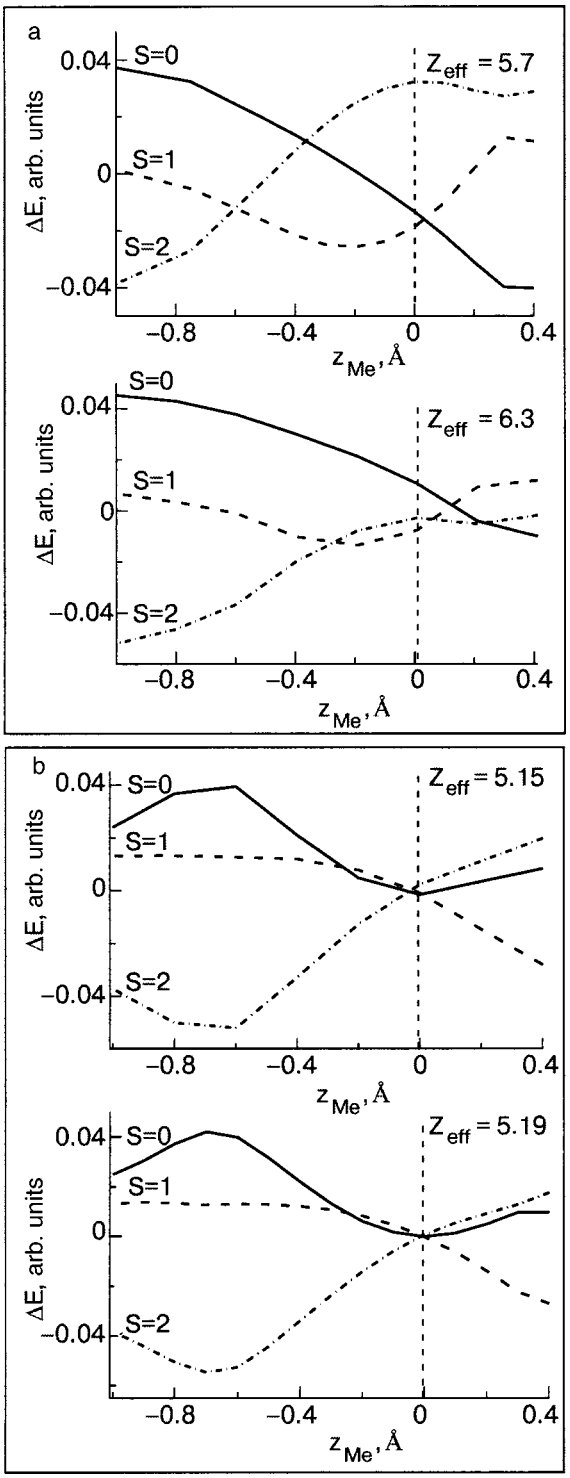

FIG. 4. Energy levels ΔE of the central ion which correspond to different spin states versus the displacement of the central ion Z_{Me} with respect to the basal plane for different values of the effective charge for the configurations $3d^6$ (a) and $3d^4$ (b).

$$V_{\mu\nu} = \langle \Psi(\gamma SLM_S M_L) | V | \Psi(\gamma' SL' M_S M'_L) \rangle, \quad (3)$$

where the wavefunctions of the terms $\Psi(\gamma SLM_S M_L)$ are linear combinations of multielectronic determinant functions $\Phi(1,2,\ldots,4(6))$ (the numbers designate the single-electron wavefunctions $\psi_i(nlm_l m_s)$ for each of the $3d$ valence electrons). The indices μ and ν run through the values corresponding to the dimensions of the computed blocks. The single-electron wavefunctions were taken to be hydrogen-like with the effective parameter $\alpha = Z_{\text{eff}}/na_0$ (n is the principal quantum number and a_0 is the Bohr radius). Thus the matrix elements (3) of the perturbation V and therefore the eigenvalues of the corresponding systems of secular equations depend on Z_{eff}, the ligand charges q_k, and the ligand coordinates $\mathbf{r}_k$. Thus, in addition to the values of the lengths and angles, characterizing the Me–O bond, and the ligand charges there is also another effective parameter—Z_{eff}, which

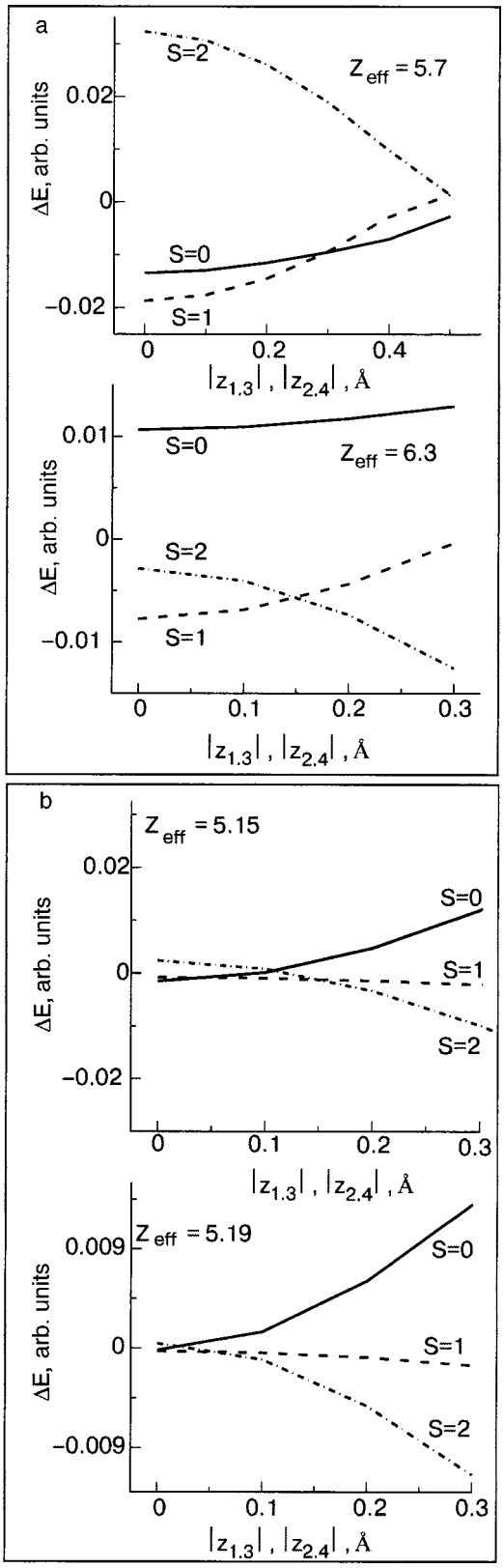

FIG. 5. Energy levels of the central ion ΔE which correspond to different spin states versus the magnitude of fluted-plane type displacements for different values of the effective charge for the configurations $3d^6$ (a) and $3d^4$ (b).

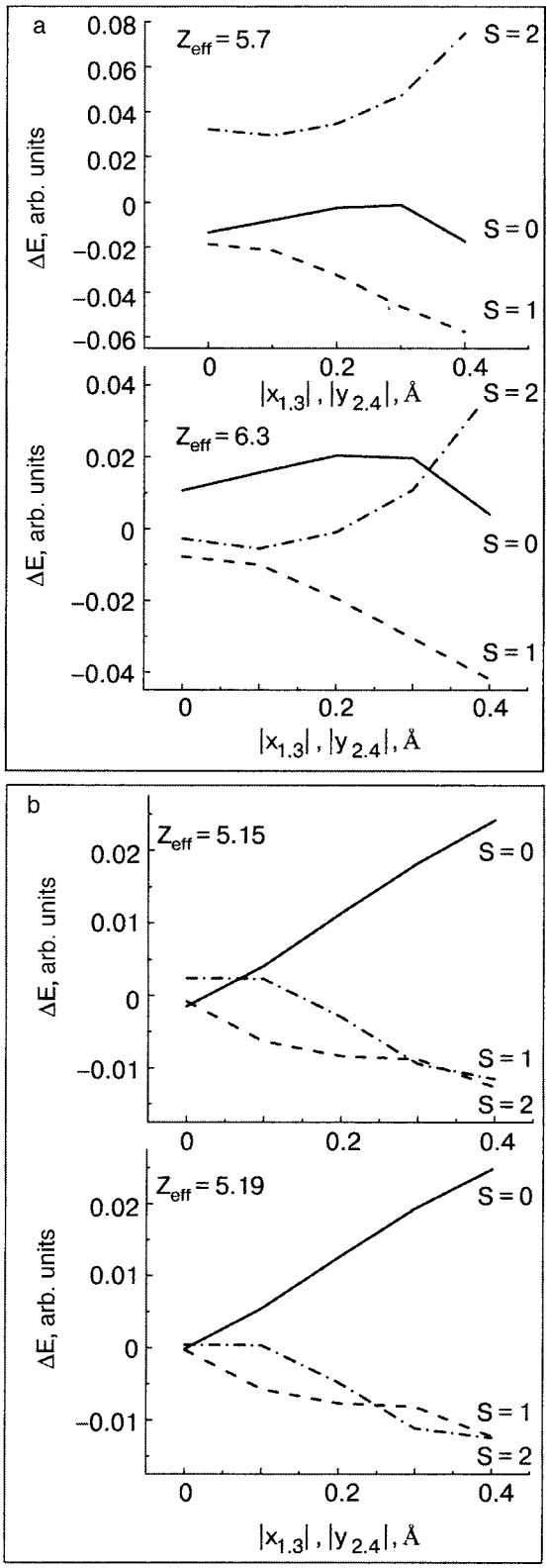

FIG. 6. Energy levels of the central ion ΔE which correspond to different spin states versus the magnitude of Jahn-Teller type displacements for different values of the effective charge for the configurations $3d^6$ (a) and $3d^4$ (b).

makes it possible to take into account implicitly the influence of the ligand environment on the state of the metal ion.

In concluding this section, it should be noted that a change of the effective charge Z_{eff} of the metal ion has a much stronger effect on the change in the covalence of the bond than a change in the ligand charge q_i. Consequently, we shall assume below that the ligand charge is constant and equal to −2 and the effective charge Z_{eff} and ligand coordinates are variable.

III. DISCUSSION

The curves in Fig. 1 demonstrate the changes occurring in the lowest electronic levels, corresponding to different spin states of the central ion, as a function of the effective charge for the electronic configurations $3d^6$ (Fig. 1a) and $3d^4$ (Fig. 1b). As a starting model we shall consider a regular pyramid with metal-oxygen distances 1.95 Å for both configurations. We note that for a fixed electronic configuration of the free ion Me the values of Z_{eff} for different ions will be different. For example, for the electronic configuration $3d^6$ $Z_{\text{eff}}=6.25$ for the Fe^{2+} ion and 7.25 for the Co^{3+} ion. For the $3d^4$ configuration $Z_{\text{eff}}=5.95$ corresponds to the Mn^{3+} ion and 4.95 corresponds to the Cr^{2+} ion. (The effective charges of free ions are calculated according to Slater's rules.[34]) Figure 1 shows that as the effective charge increases both systems undergo a series of transitions between the spin states of the central ion: HS→IS→LS. For a prescribed metal-oxygen bond length (1.95 Å) the IS state as the ground state is realized for both configurations but much more so for the $3d^6$ configuration. In the first case it is sufficient to change the effective charge by 0.4% for a transition into a low-spin state, while in the second case changes near 13% are required. Thus the state with spin $S=1$ for the $3d^4$ configuration is less stable with respect to a change in the degree of bond covalence.

The points $Z_{\text{eff}}=6.38$ and 5.56 for $3d^6$ in Fig. 1a and $Z_{\text{eff}}=5.2$ and 5.15 for $3d^4$ in Fig. 1b are points of accidental degeneracy. Therefore, as soon as the effective charge of the central ion is equal to one of these values, negligible changes in the magnitude of the crystal field can result in fluctuations of the spin state of the system. We note that different distortions of the crystal structure of the complex can initiate these changes.

We shall investigate the stability of the ground spin state of a metal ion with respect to the magnitude and symmetry of the distortions of the ligand environment for prescribed values of the effective charge Z_{eff}, noted in Fig. 1 by arrows. Since we are studying the evolution of the spin state under distortions of the ligand complex, the effective charges were chosen on the basis of the proximity to the points of accidental degeneracy. We shall consider two types of distortions of the complex MeO_5: displacements of atoms resulting in a change of the pyramid volume and displacements which leave the initial volume unchanged. Breathing-mode type displacements (Fig. 2a) distortions of the first type. Displacements of the central ion along the Z axis (Fig. 2b), fluting distortions of the plane (Fig. 2c), and Jahn-Teller type displacements (Fig. 2d) are distortions of the second type.

We shall investigate the influence of the breathing-mode type distortions on the behavior and relative arrangement of the energy levels of the central ion, which correspond to different spin states. First, we note that distortions of this type model the thermal compression/expansion of the lattice with a change in temperature and hydrostatic compression. Figure 3 shows the energy levels of a Me ion which depend on the magnitude of the uniform expansion ΔR. Such distortions are accompanied by an increase in the volume of the pyramid. The dependence of the relative change in the volume of the pyramid on the magnitude of the uniform expansion ΔR is expressed by the equality $\Delta V/V=3(\Delta R/R)$. Calculations show that the magnitude of the effective charge determines the values of ΔR and therefore ΔV which are necessary to change the spin state of a metal ion. It is evident that for the $3d^6$ configuration with $Z_{\text{eff}}=5.7$ the volume of the pyramid must be increased by approximately a third, while for $Z_{\text{eff}}=6.3$ the increase in the volume of the pyramid need be less than 10% (Fig. 3a) of the initial value in order for the state with high spin $S=2$ to replace the state with intermediate spin $S=1$. In the case of the $3d^4$ configuration only a negligible change in volume of the pyramid $\Delta R\sim 0-3\%$ is needed (Fig. 3b) to establish the term order which is characteristic for a free ion. It is evident that for the $3d^4$ configuration and for large values of the effective charge for the $3d^6$ configuration an increase in the volume of the pyramid results in a decrease of the interaction between the central ion and the ligands, i.e. a decrease of the strength of the crystal field. Thus the energy Δ_{ex} for d electrons becomes greater than Δ_{CF}, and the associated rearrangement of the electronic spectrum has the effect that the high-spin state becomes the ground state.

We shall now examine the influence of other types of distortions on the relative arrangement of the terms of the central ion. First we investigate the influence of a displacement of the central ion with respect to the basal plane of the pyramid (see Fig. 4). We note that in real compounds containing pyramidal metal-oxide complexes, as a rule, the metal ion is shifted into the pyramid. Distortions of this form do not change the volume or symmetry of the complex, but they do change the degree of covalence of the Me–O bond as a result of a redistribution of the electronic charge. The direction of motion of the metal ion determines the character of the change in the strength of the crystal field. A displacement of the ion in the positive direction along the Z axis of the pyramid increases the crystal field and a displacement in the negative direction decreases the field. Thus, one would expect the system to make a transition from a state with spin $S=1$ into states with $S=0$ and $S=2$ with the metal ion shifting in the positive and negative directions, respectively. Indeed, such behavior of the terms is observed for $Z_{\text{eff}}=5.7$ (see Fig. 4a). A small shift of the central ion (0.02–0.05 Å) in the direction of the apical oxygen transfers the system into a state with spin $S=0$. The intermediate-spin state occurs with a displacement of the Co ion in the opposite direction by about 0.6 Å, after which a high-spin state is established. This calculation agrees completely with the calculations performed in Ref. 21. The authors showed that the intermediate-spin state of the real crystal structure of Sr_2CoO_3Cl is stabilized by a displacement of the Co^{3+} ion along the axis of the pyramid. The critical magnitude of this displacement calculated by the LDA+U method is 0.15 Å.

For a large effective charge ($Z_{\text{eff}}=6.3$) the pattern of alternation of the ground levels is more complicated. It is evident that starting with an intermediate-spin state the system passes into a high-spin state with the metal ion shifting to the outside of the pyramid, while a displacement of the ion in the opposite direction results in a cascade of spin transitions IS →HS→LS. The levels with configuration $3d^4$ exhibit a similar feature but for much smaller displacements of the metal ion (Fig. 4b). The region of the intermediate spin state for the $3d^4$ configuration degenerates practically to zero, so

that negligible displacements in both directions initiate transitions of the type HS→LS→IS (Z_{eff}=5.15) or HS→IS (Z_{eff}=5.19).

To explain the anomalous behavior of the curves in Fig. 4a we shall determine the type of wavefunction describing the lowest spin state. It is known[35] that the splitting of the term ^5D by the crystal field of an undistorted pyramid has the effect that the ground state is a doubly degenerate level described by wavefunctions of the type d_{xz} and d_{yz}. The first excited level is the term d_{xy}, followed by d_{z^2} and $d_{x^2-y^2}$, respectively. When the Me ion shifts in one or another direction along the Z axis the symmetry of the crystal field does not change, but the Me–O bond lengths do change, which results in a redistribution of the electron density of the complex. Thus with the character of the splitting of the levels remaining unchanged their mutual arrangement within a term changes. When a metal ion occupies a point with the coordinate z_{Me}=−0.6 Å a state with spin S=2, described by a wavefunction of the type d_{z^2}, is realized. Indeed, the maxima of the electronic density of the function d_{z^2}, just as for $d_{x^2-y^2}$, lie on the coordinate axes, so that an increase of the Me–O bond lengths has the effect that the d electrons of the metal ion undergo a smaller electrostatic repulsion from the ligands than in the case where the ion lies at the center of the basal plane of the pyramid. Therefore the state described by a wavefunction of the type d_{z^2} becomes the ground state and the level drops substantially. Wavefunctions of the type d_{xy}, d_{xz}, and d_{yz} do not undergo large changes, because the maxima of the electronic density of these wavefunctions lie between the coordinate axes. A shift of the Me ion in the direction of an apical oxygen results in a further redistribution of the electron density of the complex, and for z_{Me}= −0.2 Å a transition occurs into a state with spin S=1. The high-spin state once again becomes the ground state when z_{Me}=0.14 Å, and the lowest doubly degenerate level is now described by wavefunctions of the type d_{yz} and d_{xz}. It is evident that a displacement of the metal ion is accompanied by similar transformations within the terms corresponding to the spin states S=1 and S=0, although these changes are more difficult to interpret. A further displacement of the central ion into a point with the coordinate z_{Me}=0.4 Å makes the high-spin state unfavorable: the ground state becomes a state with spin S=0, and the first excited state is a high-spin level described by a wavefunction of the type d_{xy}. It should be underscored that the lowest high-spin state of the central ion is described by wavefunctions which have different symmetry depending on the position of the metal ion. This fact is explains the nonlinearity of the curves in Fig. 4.

In conclusion we note that a distinguishing feature of the $3d^4$ configuration is the stabilization of the intermediate-spin state accompanying a shift of the metal ion into the pyramid. This behavior of the terms is probably characteristic for this configuration, since an increase in the value of Z_{eff} does not produce any substantial differences.

Next, we shall examine how fluting distortions of a plane influence the spin state of a metal ion (see Fig. 5). Such displacements of the ligand ions do not change the size of the complex but they do lower its symmetry. Comparing Figs. 5a and 5b shows that the terms of the configurations being studied respond differently to ligand displacements of this type. For the $3d^6$ configuration the magnitude of the splitting of the levels which correspond to different spin states under the action of such distortions decreases for Z_{eff}=5.7; conversely, for a larger value of Z_{eff} it increases. For the $3d^4$ configuration the magnitude of the splitting by the crystal field increases irrespective of the magnitude of the effective charge. Another nontrivial feature of distortions of this type should be noted for the configuration $3d^6$. For Z_{eff}=5.7 a series of transitions IS→LS→HS is once again observed, just as for displacements of the metal ion along the axis of the pyramid. The behavior of the terms for a higher value of the effective charge is conventional: the state with spin S=1 is replaced by a high-spin state (S=2). The behavior of terms of the configuration $3d^4$ is also characteristic: as the degree of fluting of the plane increases, the low-spin state is replaced by an intermediate-spin state and then a high-spin state. An increase of Z_{eff} only decreases the region of stability of the intermediate-spin state.

Finally, the last form of distortions which we investigated are Jahn-Teller type distortions (Fig. 6). Atomic displacements of this type also leave the volume of the complex unchanged, but, just as the fluting distortions of a plane, they substantially lower its symmetry since the basal plane transforms into a rhombus. The Me–O bonds along the diagonals of the rhombus become nonequivalent, and therefore Jahn-Teller type distortions increase the degree of covalence in one direction and decrease it in the other. Figure 6a shows that terms of the $3d^6$ configuration exhibit a characteristic feature—the spin state S=1 is the ground state for any Jahn-Teller type distortions.

An increase of Z_{eff} lowers the level corresponding to spin S=2 and, ultimately, results in a conventional Hund filling of the levels for undistorted and weakly distorted pyramids. Conversely, a decrease of Z_{eff} lowers the spin S =0 level, so that for $Z_{\text{eff}}<5.7$ the low-spin state becomes the ground state. The behavior of the terms in the $3d^4$ configuration is also characteristic. It is evident (see Fig. 6b) that irrespective of its starting state the system undergoes a series of transitions of the type LS→IS→HS→IS (for Z_{eff}=5.15) and IS→HS→IS (for Z_{eff}=5.19). Apparently, the nature of such transitions lies in the alternation of the terms, similar to a displacement of a metal ion along the axis of the pyramid.

In conclusion, it should be noted that in real layered cobaltites the Co^{3+} ions lying in the basal planes of pyramids are in states with spin S=1 in the temperature range 50–400 K. The distortions which can be used to model the temperature transformations of pyramidal complexes are predominantly of the Jahn-Teller type.

IV. CONCLUSIONS

A calculation of the ground spin state of a metal ion as a function of the magnitude of the displacements of oxygen ions has shown that different types of distortions of the ligand complex result in different scenarios of the behavior of the terms corresponding to the three main spin states of the $3d$ ion.

1. The spin state of the coordination complex MeO_5 with a metal ion with configuration $3d^6$ is most sensitive to distortions of the breathing-mode type. A negligible expansion of the pyramid (~0.3%) is sufficient to establish an order of

the terms corresponding to Hund's rule. The magnitude of the effective charge does not play a determining role. Conversely, for a complex containing a metal ion with the $3d^6$ configuration Z_{eff} plays an important role: for large values of Z_{eff} the complex becomes more sensitive to a uniform thermal expansion/compression of the pyramid.

2. The behavior of the electronic subsystems of the $3d^6$ and $3d^4$ configurations demonstrates large differences accompanying a displacement of the Me ion out of the basal plane into the pyramid. In the first case a low-spin state is realized, while in the second case an intermediate-spin state is realized irrespective of the value of Z_{eff}. This state can become stable with displacements of the metal ion in one or another direction by ~30% from the initial bond lengths for the $3d^6$ configuration and ~1% for the $3d^4$ configuration.

3. For fluting distortions of a plane the intermediate-spin state remains the ground state with a change in bond length of about 3–7% for the $3d^4$ configuration and 7–14% for the $3d^6$ configuration. An increase of Z_{eff} decreases the range of stability of the intermediate-spin state for both configurations.

4. The most interesting feature of the behavior of the spin state of a metal ion in a pyramidal complex is that in the case of the $3d^6$ configuration Jahn-Teller distortions stabilize the intermediate-spin state for a wide range of values of the effective charge. This situation is in complete agreement with the actual behavior of layered cobaltites on heating.

[a)]E-mail: lamonova@kinetic.ac.donetsk.ua

[1]P. M. Raccah and J. B. Goodenough, Phys. Rev. **155**, 932 (1967).
[2]M. A. Senaris-Rodriguez and J. B. Goodenough, J. Solid State Chem. **116**, 224 (1995).
[3]R. H. Potze, G. A. Sawatskii, and A. Abbate, Phys. Rev. B **51**, 11501 (1995).
[4]M. A. Korotin, S. Yu. Ezhov, I. V. Solovyev, V. I. Anisimov, D. I. Khomskii, and G. A. Sawatzky, Phys. Rev. B **54**, 5309 (1996).
[5]T. Saitoh, T. Mizokawa, A. Fujimori, M. Abbate, Y. Takeda, and M. Takano, Phys. Rev. B **56**, 1290 (1997).
[6]W. S. Kim, E. O. Chi, H. S. Choi, N. H. Hur, S.-J. Oh, and H.-C. Ri, Solid State Commun. **116**, 609 (2000).
[7]F. Fauth, E. Suard, and V. Caignaert, Phys. Rev. B **65**, R060401 (2001).
[8]H. Kusuya, A. Machida, Yu. Moritomo, K. Kato, E. Nishibor, M. Takata, M. Sakata, and A. Nakamura, J. Phys. Soc. Jpn. **70**, 3577 (2001).
[9]C. Frontera, J. L. Garcia-Munoz, A. Llobet, M. A. G. Aranda, J. Rodriguez-Carvajal, M. Respaud, J. M. Broto, B. Raquet, H. Rakoto, and M. Goiran, J. Alloys Compd. **323–324**, 468 (2001).
[10]C. Zobel, M. Kriener, D. Bruns, J. Baier, M. Gruninger, T. Lorenz, P. Reutler, and A. Revcolevchi, Phys. Rev. B **66**, 020402 (2002).
[11]C. Frontera, J. L. Garcia-Munoz, A. Llobet, and M. A. G. Aranda, Phys. Rev. B **65**, R180405 (2002).
[12]S. Roy, M. Khan, Y. Q. Guo, J. Craig, and N. Ali, Phys. Rev. B **65**, 064437 (2002).
[13]P. G. Radaelli and S.-W. Cheong, Phys. Rev. B **66**, 094408 (2002).
[14]D. D. Khalyavin, S. N. Barilo, S. V. Shiryaev, G. L. Bychkov, I. O. Troyanchuk, A. Furrer, P. Allenspach, H. Szymczak, and R. Szymczak, Phys. Rev. B **67**, 214421 (2003).
[15]J.-Q. Yan, J.-S. Zhou, and J. B. Goodenough, Phys. Rev. B **69**, 134409 (2004).
[16]V.-P. Gnezdilov, Yu. G. Pashkevich, P. Lemmens, K.-Y. Choi, G. Güntherodt, S. V. Shiryaev, G. G. Bychkov, and S. N. Barilo, Fiz. Nizk. Temp. **29**, 1269 (2003) [Low Temp. Phys. **29**, 963 (2003)].
[17]K. Asai, O. Yokokura, M. Suzuki, T. Naka, T. Matsumoto, H. Takahashi, N. Mori, and K. Kohn, J. Phys. Soc. Jpn. **66**, 967 (1997).
[18]H. Takahashi, F. Munakata, and M. Yamanaka, Phys. Rev. B **57**, 15211 (1998).
[19]M. Zuang, W. Zhang, An Hu, and N. Ming, Phys. Rev. B **57**, 13655 (1998).
[20]I. A. Nekrasov, S. V. Streltsov, M. A. Korotin, and V. I. Anisimov, Phys. Rev. B **68**, 235113 (2003).
[21]Z. Hu, Hua Wu, M. W. Haverkort, H. H. Hsieh, H.-J. Lin, T. Lorenz, J. Baier, A. Reichl, I. Bonn, C. Felser, A. Tanaka, C. T. Chen, and L. H. Tjeng, Phys. Rev. Lett. **92**, 207402 (2004).
[22]K. Asai, A. Yoneda, O. Yokokura, J. M. Tranquada, G. Shirane, and K. Kohn, J. Phys. Soc. Jpn. **67**, 290 (1998).
[23]H. Wu, Phys. Rev. B **62**, R11953 (2000).
[24]I. O. Troyanchuk, D. D. Khalyavin, T. K. Solovykh, H. Szymczak, Q. Huang, and J. W. Lynn, J. Phys.: Condens. Matter **12**, 2485 (2000).
[25]S. K. Kwon, J. H. Park, and B. I. Min, Phys. Rev. B **62**, R14637 (2000).
[26]T. Vogt, P. M. Woodward, P. Karen, B. A. Hunter, P. Henning, and A. R. Moodenbaugh, Phys. Rev. Lett. **84**, 2969 (2000).
[27]Y. Moritomo, T. Akimoto, M. Takeo, A. Machida, E. Nishibori, M. Takata, M. Sakata, K. Ohoyama, and A. Nakamura, Phys. Rev. B **61**, R13325 (2000).
[28]H. Wu, Phys. Rev. B **64**, 092413 (2001).
[29]R. E. Watson and A. J. Freeman, Phys. Rev. A **134**, 1526 (1964).
[30]S. S. Batsanov and R. A. Zvyagin, *Overlap Integrals and the Problem of Effective Charges*, Nauka, Moscow (1966).
[31]H. Bethe, Ann. Phys. **3**, 133 (1929).
[32]S. V. Vonsovskiĭ, S. V. Grum-Grzhimaĭlo, V. I. Cherepanov, A. N. Men', D. T. Sviridov, Yu. F. Smirnov, and A. E. Nikiforov, *Crystal Field Theory and the Optical Spectra of Impurity Ions with an Unfilled d-Shell*, Nauka, Moscow (1969).
[33]I. I. Sobel'man, *Introduction to the Theory of Atomic Spectra*, Pergamon Press, New York (1972), Fizmatgiz, Moscow (1963).
[34]J. Slater, Phys. Rev. **36**, 57 (1930).
[35]S. Nagakura and T. Nakajima, *Quantum Theory in Chemistry*, Iwanami Shoten Publishers (1979).

Translated by M. E. Alferieff

Hidden ferrimagnetism in pniktides $(Fe-Mn)_{1.95}As$

V. I. Val'kov,[a] I. F. Gribanov, A. V. Golovchan, and B. M. Todris

A. A. Galkin Donetsk Physicotechnical Institute of the National Academy of Ukraine, ul. R. Lyuksemburg 72, Donetsk 83114, Ukraine

(Submitted March 23, 2005; resubmitted May 30, 2005)
Fiz. Nizk. Temp. **31**, 1277–1287 (November 2005)

The results of experimental investigations of the magnetic properties of the antiferromagnetic alloy $Fe_{0.765}Mn_{1.185}As$ are presented. They show that at atmospheric pressure and temperatures below 65 K the antiferromagnetic state is not the only stable state, since the imposition of a magnetic field in this temperature range makes it possible to observe irreversible induced transitions into a state with a canted ferrimagnetic structure. This is a second stable state for the experimental sample. As the temperature increases, this state vanishes via a first-order phase transformation at 65 K. Above 65 K reversible induced first-order transitions from the antiferromagnetic into a canted ferrimagnetic structure are observed. The results are discussed on the basis of a phenomenological expression for the free energy of a system with two interacting magnetic-order parameters. It is shown that a simple phenomenological model qualitatively describes the behavior of the system investigated. A single-band Hubbard model is used to give a microscopic substantiation of the phenomenological approach. © *2005 American Institute of Physics*. [DOI: 10.1063/1.2127889]

I. INTRODUCTION

Experimental investigations of the effect of a strong magnetic field on solid solutions of transition-metal pniktides $Mn_{a-y-x}Fe_yCo_xAs$ with $a \approx 1$ have made it possible to observe the existence of metastable magnetically ordered states and construct their phase $(P-T-H)$ diagrams.[1–3]

Today, such studies are important because the effects accompanying the magnetization process in these materials could have practical applications. For example, there is a strong magnetocaloric effect which appears when the ferromagnetic phase reversibly induced by a magnetic field vanishes.[4,5]

However, the applied interest does not push into the background certain fundamental features which appear in the process of magnetization of pniktides such as, for example, solid solutions of the system $Fe_{a-x}Mn_xAs$ with $a > 1.95$. Alloys of this system possess $C38$ tetragonal crystal structure $C38$, whose spatial symmetry group $(P4/nmm)$ reflects the existence of two types of crystallographic positions occupied by the magnetically active manganese and iron ions. It is possible that the crystal-structural and electronic characteristics of $Fe_{a-x}Mn_xAs$ systems with $1.95 \leqslant a \leqslant 2.35$ are responsible for the existence of low-temperature $(T=T_1<T_N)$ magnetic order-order phase transitions from the antiferromagnetic (AF) state $(T<T_N)$ into an angular or canted ferrimagnetic (CFM) state $(T<T_1)$.[6,7]

The magnetic structure of CFM can be regarded as the coexistence of uniform and periodic components of the magnetic moment of the crystal-chemical cell.[8]

Investigations of spontaneous AF–CFM transitions in alloys of this system made it possible to increase our understanding of the mechanisms of order-order transitions and call attention to the possibility of the role of interacting ferromagnetic and antiferromagnetic modes which coexist in systems with itinerant magnetism carriers.[9]

Two magnetic phase transitions have been observed in most previously studied samples of the system $Fe_{a-x}Mn_xAs$. A high-temperature PM-AF transition occurs as a second-order transformation at T_N of the order of 460 K. The low-temperature first- and second-order transformations are observed at $T=T_1$, where 127 K $\leqslant T_1 \leqslant$ 330 K depends on the parameters a and $\eta=x/a-x$.[7] In a sample with parameters closest to those of the experimental sample ($a=1.95$, $\eta=1.56$) a distinct first-order transformation is observed at $T_1=127$ K; in this transformation the appearance of spontaneous magnetization is accompanied by a sharp and anisotropic change of the crystal lattice parameters c and a. According to Ref. 6, $\Delta c/c=+3\%$, $\Delta a/a=-0.85$, and $\Delta V/V=+1.9\%$.

The present work is devoted to an experimental investigation of the magnetic properties of the antiferromagnetic alloy $Fe_{0.765}Mn_{1.185}As$, where magnetic-field induced reversible and irreversible transitions into a canted ferrimagnetic state have been observed.

The results are discussed on the basis of a phenomenological expression for the free energy of a system with two interacting magnetic-order parameters. A single-band Hubbard model is used to give a microscopic substantiation of the expression.

II. EXPERIMENTAL PROCEDURE

The main experimental results were obtained during investigations of the temperature $\sigma(T)$ and field $\sigma(H)$ dependences of the magnetization measured in static and pulsed magnetic fields. The temperature dependences in a static magnetic field were performed using a Domenicali-type balance. The field dependences were obtained in static and pulsed magnetic fields. In the first case Faraday magnetic balance with a superconducting solenoid as the magnetic field source was used.[10] The measurements in a pulsed mag-

netic field were performed using a pulsed magnetometer, similar to the one described in Ref. 11. A DRON-1.5 x-ray diffractometer was used to obtain the temperature dependences of the crystal-lattice parameters.

III. RESULTS

We established certain general characteristics of the canted ferrimagnetic phase (type of anisotropy and special features of the magnetization curve), arising spontaneously as a result of a low-temperature phase transition, in measurements of the magnetization of samples in strong static and pulsed magnetic fields.

According to our measurements the anisotropic properties are determined by the plane of easy magnetization (the plane perpendicular to the tetragonal axis).

The most important characteristic feature of the magnetization curve of the samples in the CFM phase is a linear increase of the saturation magnetization with increasing intensity of the magnetic field. As an example, the field dependences of a single-crystal sample $Fe_{0.65}Mn_{1.3}As$ are presented (see Fig. 1). In this sample two types of transitions characteristic of the system $Fe_{1.95-x}Mn_zAs$ are observed as temperature decreases: disorder-order (PM–AF) at $T=T_N$ and order-order at $T=T_1=140$ K (AF–CFM). Both transitions are second-order magnetic phase transformations.

In the investigation of the magnetic properties of a $Fe_{0.765}Mn_{1.185}As$ sample in a 10 kOe static magnetic field, a decrease of temperature results in only one PM–AF second-order transition. The ordering temperature $T=T_N\approx 470$ K was identified as the temperature at the maximum of the temperature dependence of the magnetic susceptibility $\chi(T)$ (Fig. 2). Below this temperature the magnetic and x-ray measurements do not show any substantial changes in the state of the sample (the temperature dependence of only the parameter c is presented in Fig. 2b; this parameter undergoes its maximum change at a AF–CFM transition.) Thus, preliminary measurements show that the state of the experimental sample can be determined as an antiferromagnetic state.

However, this characteristic is not unique. Indeed, reversible and irreversible induced first-order transitions from the antiferromagnetic state into a state whose characteristics are the same as those of the canted ferrimagnetic phase are observed in measurements of the field dependences of the magnetization of the sample in strong static and pulsed magnetic fields. The field dependences $\sigma(H)$ presented in Fig. 3 show that certain magnetization curves of the experimental sample describe an irreversible field-induced first-order AF–CFM transition. The form of the magnetization curves attests to this: a smooth reversible increase of magnetization in fields with intensity below the critical value $H_1(T)\geqslant 20$ kOe, a sharp increase of the magnetization when this value is reached with an irreversible change of its magnitude (the final value of the magnetization remains after the field is reduced to zero). The field-induced state remains as long as desired, and repeated magnetization of the sample at this or lower temperature (curve *2*) is described by a curve which reflects the characteristics of the induced ferrimagnetic state CFM—spontaneous magnetization and linear increase of its magnitude with increasing intensity of the magnetic field. In weak fields ($H<20$ K) the irreversibly induced CFM state

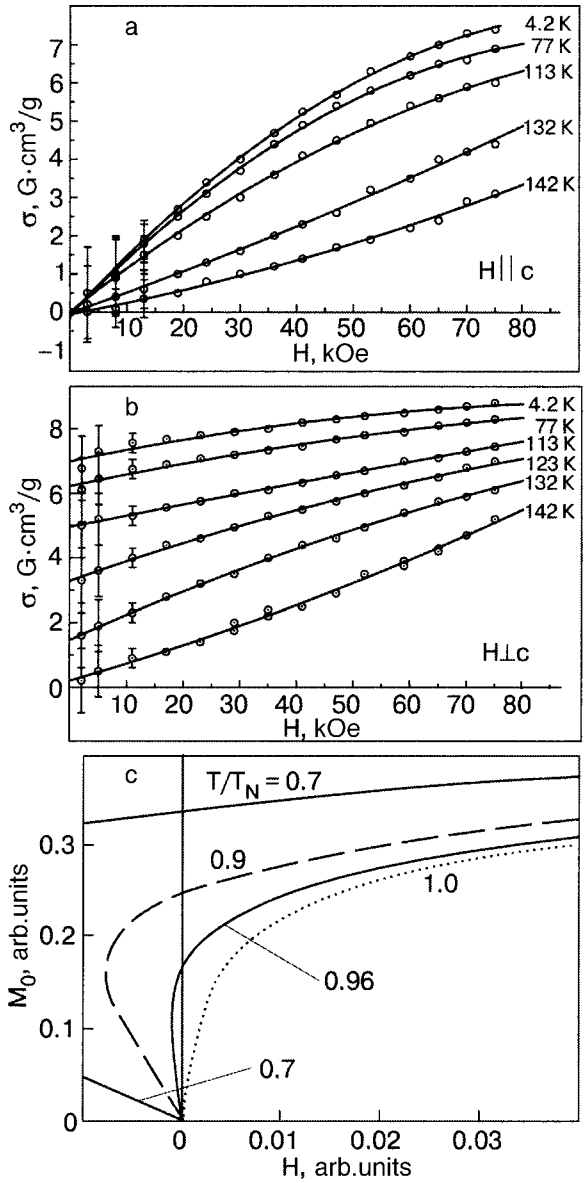

FIG. 1. Experimental (a,b) and computed (c) field dependences of the magnetization of a sample where the AF–CFM transition is of second order. The experimental curves were measured for a single crystal sample $Fe_{0.65}Mn_{1.3}As$ for two orientations of the field with respect to the tetragonal axis c and at different temperatures.

remains stable with temperature increasing up to $T_2=65$ K. At T_2 an irreversible spontaneous first-order transition CFM$\rightarrow$AF occurs; this transition is accompanied by cracking of the sample. This shows that strong spontaneous magnetostriction accompanies such a transition. The term "irreversible spontaneous transition" is associated with the fact that decreasing the temperature from 65 K does not restore the magnetization. At temperatures above T_2 the application of a magnetic field can result in reversible induced first-order AF–CFM transitions. The existence of two critical fields is characteristic for these transitions: $H_1<H_2$, the CFM appears in the first field and vanishes in the second. We investigated these transitions in measurements performed in pulsed magnetic fields. The temperature dependences $H_1(T)$ and $H_2(T)$, characterizing the temperature change of the field boundaries for the appearance of the AF and CFM states, are presented in Fig. 4.

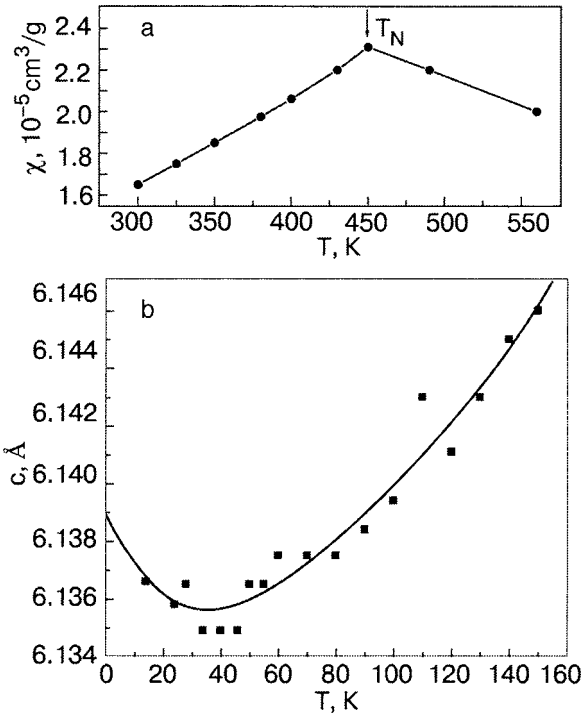

FIG. 2. Temperature dependences of the inverse magnetic susceptibility (a) and the crystal lattice parameter c (b) of a single crystal sample $Fe_{0.765}Mn_{1.185}As$ with a hidden ferrimagnetic phase.

A special feature of the curve $H_1(T)$ is the presence of a minimum near 50 K. The fact that the AF state of the sample has no structural or magnetic anomalies at this temperature (Fig. 2) means that such behavior is due to the topology of the boundary of the appearance of the "hidden" canted phase in pressure-temperature coordinates.

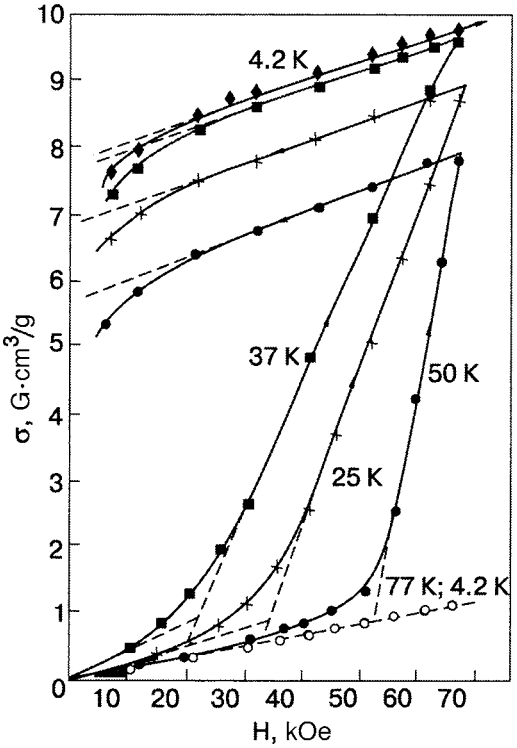

FIG. 3. Isothermal curves of the magnetization versus the field ($\mathbf{H}\|\mathbf{c}$) in a single crystal sample $Fe_{0.765}Mn_{1.185}As$. At T=4.2 K the behavior of the antiferromagnetic (○) and the irreversibly induced canted ferrimagnetic (♦) phases is shown.

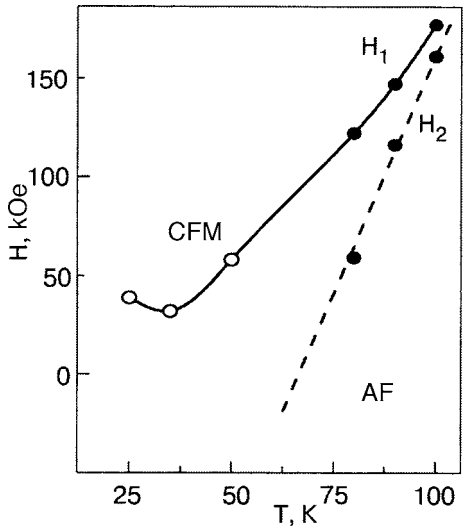

FIG. 4. Experimental H-T diagram of a $Fe_{0.765}Mn_{1.185}As$ sample. The boundaries of lability with respect to the field $H_1(T)$ and $H_2(T)$ for induced transitions AF→CFM and CFM→AF correspond to values of the field for which the isothermal values of the differential susceptibility $(\partial\sigma/\partial H)(H)$ have an extremum; (○) and (●)—measurements in static and pulsed magnetic fields.

The observation of irreversible induced transitions fundamentally changes the picture of the antiferromagnetic state of the sample as the only stable state. Our measurements show that the range $0 \leqslant T \leqslant T_2$ for the experimental sample is the region of metastable states.

IV. DISCUSSION

Such metastable regions arise in systems where two conditions are satisfied.

The first (necessary) condition is the existence of an interval in P–T space that separates the boundaries of lability of two magnetically ordered states. This condition can always be satisfied for systems where the order-order transitions are of first-order.

The second (sufficient) condition is the existence of blocking of the formation of nuclei of one or both phases. For real systems, where spontaneous transitions are accompanied by a large spontaneous deformation of the lattice, such blocking is achieved by a magnetostriction mechanism.[12,13] In this case at any temperature and pressure the system behaves as a uniform system and the P–T boundaries of the appearance of these phases can approach the boundaries of lability of the magnetically ordered states.

In the present paper we shall discuss only the necessary condition for the appearance of the region of metastable states that separates the absolutely stable AF and CFM phases. We assume that the second condition is satisfied as a result of the presence of strong magnetostriction.

A. Phenomenological model of order-order transitions with coexisting magnetic-order parameters

We shall start our analysis from the assumption that the CFM structure is due to the coexistence of two magnetic-order parameters M_0 and M_Q. These two parameters can be taken as the ferromagnetism and antiferromagnetism vectors

TABLE I. Value of the coefficients in P–T coordinates

Transition type AF-CFM	$P_1(T)$	T_C	$T_N = K_3/K$	K	K_1	K_2	K_Q	$\bar{a}_3 \cdot 10^2$	$a_5 \cdot 10^3$	$\bar{b}_3 \cdot 10^3$	$b_5 \cdot 10^3$	$\delta \cdot 10^3$
Second-order	>0	1	1.0844	0.971	−1	3.1	1/3	0.6	2.4	6	1.212	1
First-order	>0	1	1.0844	0.971	−1	3.1	1/3	−3.15	2.4	6	1.212	3.5
First-order	<0	1	1.0844	0.971	−1	3.1	1/3	−3.15	2.4	6	1.212	3.8

or the Fourier components of the magnetic moment of the crystal-chemical cell with wave vectors $\mathbf{q}=0$ and $\mathbf{q}=\mathbf{Q}$. The expression for the free energy F of such a system under the condition $\mathbf{M}_0 \perp \mathbf{M}_Q$ and neglecting anisotropic properties has the form

$$F = \frac{1}{2!}a_1 M_0^2 + \frac{1}{4!}a_3 M_0^4 + \frac{1}{6!}a_5 M_0^6 + \ldots - HM_0 + \frac{1}{2!}b_1 M_Q^2 + \frac{1}{4!}b_3 M_Q^4 + \frac{1}{6!}b_5 M_Q^6 + \frac{1}{2!}\delta M_0^2 M_Q^2. \quad (1)$$

We assume that the coefficients are linear functions of the temperature and pressure, but only the coefficients $a_1(T)$ and $b_1(T)$ are sign-changing:

$$a_1 = T - T_C + P, \quad b_1 = (TK - K_3 - Pk_Q),$$

$$a_3 = \bar{a}_3(1 + K_1 T), \quad b_3 = \bar{b}_3(1 + K_2 T),$$

$$T_C < T_N \equiv K_3/K. \quad (2)$$

Analysis of the equations of state $(\partial F/\partial M_0)=0$ and $(\partial F/\partial M_Q)=0$ for certain values of the coefficients a, b, and δ

$$a_1 M_0 + \frac{1}{3!}a_3 M_0^3 + \frac{1}{5!}a_5 M_0^5 + \delta M_0 M_Q^2 = 0, \quad (3)$$

$$b_1 M_Q + \frac{1}{3!}b_3 M_Q^3 + \frac{1}{5!}b_5 M_Q^5 + \delta M_Q M_0^2 = 0 \quad (4)$$

shows that for $H=0$ (depending on the temperature and pressure) a minimum of F can correspond to the following states from the set of solutions of the system (3) and (4): paramagnetic PM ($M_0=M_Q=0$), antiferromagnetic AF ($M_0=0$, $M_Q=M>0$), and mixed ($M_0>0$, $M_Q=m>0$), which can be interpreted as the CFM state under the condition $M_0 \perp m < M$. This set of solutions corresponds to a sequence of magnetic phase transitions with decreasing temperature PM→AF→CFM. The high-temperature transition PM→AF at $T=T_N$ is a second-order transition if $b_3>0$, and the transition AF→CFM at $T_1(P)$ can be of second or first order. In the latter case, as temperature increases, the reverse order-order transition CFM→AF occurs at $T_2>T_1$. The condition for the transition AF→CFM to occur as a first-order magnetic phase transformation is the inequality

$$D = \left(\frac{\partial^2 F}{\partial M_0^2}\frac{\partial^2 F}{\partial M_Q^2} - \left(\frac{\partial^2 F}{\partial M_0 \partial M_Q}\right)^2\right)_{M_0 \to 0, M_Q = M_Q(T_1)} = M_0^2 M_Q^2 \left(a_3(T_1)b_3(T_1) - 36\delta^2 + \frac{|a_1(T_1)|a_3(T_1)b_5(T_1)}{10\delta}\right) \leqslant 0. \quad (5)$$

The temperature T_1 is determined from Eq. (4) as $M_0 \to 0$ after substituting the expression $M_Q^2(T_1) = |a_1(T_1)|/\delta$.

For $T_1(P) < T < T_2(P)$ both solutions, AF and CFM, minimize the free energy if

$$D(M_0 > 0,\ M > 0) > 0 \ [D(M_0 > 0,\ m > 0) > 0]. \quad (6)$$

For $T < T_1(P)$ only the CFM solution corresponds to an energy minimum if

$$D(M_0 > 0,\ m > 0) > 0 \ [D(M_0 > 0,\ M > 0) < 0]. \quad (7)$$

At the same time, for $T_N + Pk_Q/k > T > T_2(P)$ a minimum of F will correspond only to a purely antiferromagnetic solution if

$$D(M_0 = 0,\ M > 0) > 0 \ [D(M_0 > 0,\ m > 0) < 0]. \quad (8)$$

It can be shown that depending on the values of the coefficients a, b and δ (see Table I) three types of phase diagrams can be realized in P–T coordinates. For chosen values of a and b the smallest value $\delta_1 = 3.5 \cdot 10^{-3}$ corresponds to a diagram where the boundaries of the appearance and vanishing of the CFM state ($T_1(P)$ and $T_2(P)$) encompass a region of positive pressures, and when the conditions (5) are satisfied the AF–CFM transition is of first order. For the larger value $\delta_2 = 1.086\delta_1$ the temperatures $T_1(P)$ are always negative and the theoretical P–T diagram will have the form shown in Fig. 5a. The computed curves of the magnetization as a function of the temperature (Fig. 6) describe

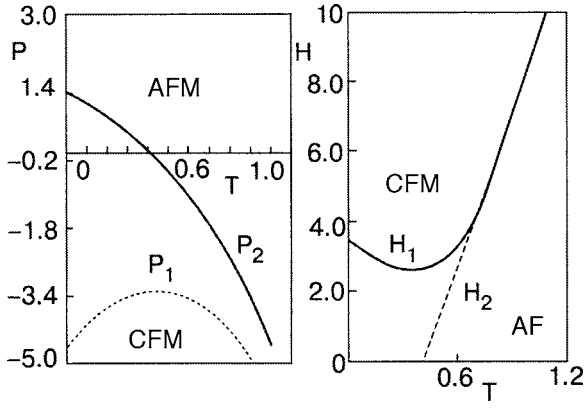

FIG. 5. Comparison of the theoretical P–T and H–T diagrams, illustrating the presence of a minimum in the experimental dependence $H_1(T)$.

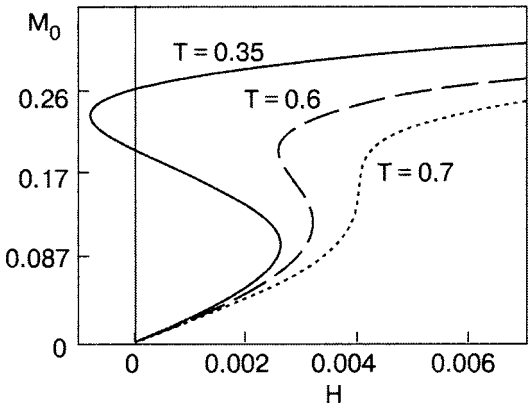

FIG. 6. Theoretical curves of magnetization versus the field: irreversible (—), reversible (--), induced (···) AF–CFM transitions.

reversible and irreversible induced AF–CFM transitions and are qualitatively similar to the experimental curves (Fig. 3). For $\delta=\delta_3=10^{-3}$ and when the condition (5) is not satisfied the AF–CFM transition is of second order; the curves cross the region $P>0$. This case describes the properties of the sample $Fe_{0.65}Mn_{1.3}As$, whose experimental and computed magnetization curves are presented in Fig. 1.

The curves of the critical fields in our model (Fig. 5b) are similar to the experimental curves (Fig. 4). Comparing Figs. 5a and 5b shows that the minimum of the function $H_1(T)$ is associated with the topology of the boundary of the appearance of the CFM phase, which is hidden in the region of negative pressures.

Thus, our simple model correctly reflects the behavior of a real system. However, the questions of the microscopic interpretation of the model solution of CFM and the relation of the coefficients, responsible for the conditions (5)–(8) being satisfied, with the microscopic parameters of the spin-polarized electronic band structure of the crystal remain unclear. It is convenient to resolve these questions for an electronic system described by the Hubbard Hamiltonian.

B. Free energy of an electronic system in the uniform local field approximation

For our purposes it is convenient to examine a system of degenerate d electrons in external uniform $H_0=(0,0,H_0)$ and periodic $H_{Qj}=(H^x_{Qj},H^y_{Qj},0)$ fields which is described by a single-band Hubbard Hamiltonian (see Appendix). The Stratonovich–Hubbard transformation[14,15] and the uniform local field approximation[16,17] make it possible to obtain an expression for the free energy in the form

$$F=\psi_0+\psi_1+\mu N+\Omega_0, \tag{9}$$

where

$$\psi_0=\left|\eta^Z_{00}-\frac{H_0}{2\sqrt{J}}\right|^2+\left|\eta^X_{00}-\frac{H^X_Q}{2\sqrt{J}}\right|^2+\left|\eta^Y_{00}-\frac{H^Y_Q}{2\sqrt{J}}\right|^2+\sum_{q\omega\neq 0}(\mathbf{r}_{q\omega})^2, \tag{10}$$

$$\psi_1=L-T\sum_{q\omega\neq 0}\sum_{\alpha=X,Y,Z}\ln r^\alpha_{q\omega}+\sum_{q\omega\neq 0}\{X^{ZZ}_{q\omega}(r^Z_{q\omega})^2+X^{+-}_{q\omega}[(r^X_{q\omega})^2+(r^Y_{q\omega})^2]\}, \tag{11}$$

$$L\{\eta,\varphi,\varphi_1\}=-\frac{1}{\beta}\sum_{k,\sigma}\ln\{1+\exp[-\beta(E_\sigma(k,\eta)-\mu)]\}-\Omega_0, \tag{12}$$

$$E_\sigma(k,\eta)=\frac{1}{2}\{\varepsilon_{k+Q/2}+\varepsilon_{k-Q/2}+\sigma\times\sqrt{(\varepsilon_{k+Q/2}-\varepsilon_{k-Q/2}+2\eta^Z\sqrt{J})^2+4J[(\eta^X)^2+(\eta^Y)^2]}\}, \tag{13}$$

$$(\eta^\alpha)^2=|\eta^\alpha_{00}|^2+x^\alpha,\quad x^\alpha=\sum_{q\omega\neq 0}|r^\alpha_{q\omega}|^2. \tag{14}$$

Here ψ_0 describes the energy of external (H) and static average exchange (η) fields [see Eq. (A8)] after the Hamiltonian of the system is transformed to local coordinates X,Y,Z [see Eq. (A2)]; Ω_0 is the thermodynamic potential of a system of noninteracting electrons. The last sum in ψ_1 describes a second-order correction to the uniform local field approximation, in which the energy spectrum of the electrons has the form (13). The temperature dependence of the spectrum is determined by the mean-square fluctuations of the exchange fields x^α.

Proceeding from the definition of the average value of the ferromagnetic (M_0) and periodic (M_Q) Fourier components of the magnetic moment of the system we obtain a relation between these macroscopic quantities and the static (Z,X,Y) Fourier components of the saddle-point values [see Eq. (A15)] of the exchange fields:

$$\eta^Z_{q=0,\omega=0}\equiv\eta^Z_0,\quad \eta^{(X,Y)}_{q=0,\omega=0}\equiv\eta^{(X,Y)}_0,$$

$$M_0=-g\mu_B\langle S^Z_0\rangle=-g\mu_B\frac{\partial F}{\partial H_0}=g\mu_B\left(\eta^Z_0-\frac{H_0}{2\sqrt{J}}\right)\frac{1}{\sqrt{J}},$$

$$M^{X,Y}_Q=-g\mu_B\langle S^{X,Y}_Q\rangle=-g\mu_B\frac{\partial F}{\partial H^{X,Y}_Q}=g\mu_B\left(\eta^{X,Y}_0-\frac{H^{X,Y}_Q}{2\sqrt{J}}\right)\frac{1}{\sqrt{J}}. \tag{15}$$

The expression for the free energy in the form (9) can be regarded as a nonequilibrium free energy $F(\eta^Z_0,\eta^{X,Y}_0)$ of a magnetically active system which is described by nonequilibrium order parameters η^Z_0 and $\eta^{X,Y}_0$. Then the saddle-point equations (A15) are identical to the equations of state of the system.

Expressions for the phenomenological coefficients a, b, and δ can be obtained on the basis of the microscopic approach examined here by switching from the free energy as a function of the exchange fields $F(\eta^Z_0,\eta^{X,Y}_0)$ to an expression for the free energy in the form of a power series in the uniform and periodic components of the magnetic field $F(M_0,M^{X,Y}_Q)$ (see Appendix). For example, the coefficients a_1 and b_1 have the form

$$a_1=\frac{1}{\chi^2_0(x)}-2J,\quad b_1=\frac{1}{\chi^0_Q(x)}-2J,$$

$$\chi_0^0(x) = \chi_0^0(0) + \delta\chi_0^0(x), \quad \chi_Q^0(x) = \chi(0) + \delta\chi(x),$$

where

$$\chi_0^0(0) = g(\varepsilon_F)/2, \quad \chi_Q^0(0) = -\frac{1}{2}\int^{\varepsilon_F} \frac{g(\varepsilon)d\varepsilon}{\varepsilon}$$

are the uniform and alternated susceptibilities of a system of noninteracting electrons at $T=0$. The corrections $\delta\chi_{0,Q}^0(x)$ due to the interaction of the fluctuations of the exchange fields cause these quantities to be strongly temperature-dependent.

The pressure dependence of these coefficients is due to the dependence of the transfer integral t_{lj} and, correspondingly, the density of states $g(\varepsilon)$ of the noninteracting electrons on the interatomic distance $\Delta R_{lj}=R_j-R_l$.

In conclusion, we note that the fundamental possibility of the coexistence of two interacting magnetic-order parameters as two components of the magnetic moment is due to the specific property of a system of itinerant electrons to allow the coexistence of different types of exchange splitting of the spin-polarized electronic spectrum (13). The presence of a minimum of the free energy with $M_0 \neq 0$ and $M_Q \neq 0$ is a sufficient condition for such coexistence. As shown in Ref. 19 this condition can be satisfied for certain values of the intra-atomic exchange interaction parameter J, the number n of electrons per site, and a definite form of the density of states.

Such is the qualitative interpretation of the phenomenological ideas concerning the coexistence of ferromagnetism and antiferromagnetism in magnets with itinerant electrons.

A quantitative analysis of the results of the present experimental investigations will be performed on the basis of first-principles calculations of the ground-state energy of a series of pniktides with $C38$ crystal structure.

APPENDIX

We start with the single-band Hubbard Hamiltonian for a system of electrons in a crystal of arbitrary symmetry:

$$H = H_0 + H_{\text{int}} + H_{\text{ex}},$$

$$H_0 = \sum_{l,j,\sigma} t_{lj} a_{l\sigma}^+ a_{j\sigma}, \quad H_{\text{ex}} = \mathbf{H}_0 \sum_j \mathbf{S}_j + \sum_j \mathbf{H}_{Qj}\mathbf{S}_j,$$

$$H_{\text{int}} = -J\sum_j \mathbf{S}_j^2, \tag{A1}$$

where $\mathbf{H}_0=(0,0,H_0)$ and $\mathbf{H}_{Qj}=(H_{Qj}^x, H_{Qj}^y, 0)$ are, respectively, the uniform and periodic components of the field applied at the site j; t_{lj} is the transfer matrix element; $a_{l\sigma}$ is the operator annihilating an electron with spin σ at site l; $\mathbf{S}_j$ is the spin density operator; J is the effective intra-atomic exchange integral. For subsequent calculations it is convenient to transform into the local (X,Y,Z) coordinate system:[19]

$$a_{j\sigma} = c_{j\sigma}\exp(-i\sigma\mathbf{Q}\mathbf{R}_j/2),$$

$$\begin{bmatrix} H_{Qj}^x \\ H_{Qj}^y \end{bmatrix} = \begin{bmatrix} \cos(\mathbf{Q}\mathbf{R}_j) & -\sin(\mathbf{Q}\mathbf{R}_j) \\ \sin(\mathbf{Q}\mathbf{R}_j) & \cos(\mathbf{Q}\mathbf{R}_j) \end{bmatrix} \begin{bmatrix} H_{Qj}^X \\ H_{Qj}^Y \end{bmatrix}. \tag{A2}$$

Under this transformation the forms of H_{int} and H_{ex} do not change, but the operators $\mathbf{S}_j$ are now expressed in terms of new electronic operators $c_{j\sigma}$. In the new operators the noninteracting part of the Hamiltonian becomes

$$H_0 = \sum_{k,\sigma} \varepsilon_{k-1/2\sigma Q} \cdot c_{k\sigma}^+ c_{k\sigma}, \tag{A3}$$

where

$$\sum_k = \frac{V}{(2\pi)^3}\int d^3k$$

$$c_{j\sigma} = \sum_k c_{k\sigma}\exp(i\mathbf{k}\mathbf{R}_j),$$

$$c_{k\sigma} = \frac{1}{N_0}\sum_j c_{j\sigma}\exp(-i\mathbf{k}\mathbf{R}_j),$$

$$\varepsilon_k = \sum_l t_{jl}\exp[i\mathbf{k}(\mathbf{R}_j - \mathbf{R}_l)].$$

Using the Stratonovich–Hubbard transformation we obtain for the free energy per unit cell

$$F = \Omega_0 + \Delta\Omega + \mu N, \tag{A4}$$

$$\exp(-\beta\Delta\Omega) = \text{const}\cdot\int\prod_{q\omega} d\eta_{q\omega}\exp(-\beta\psi\{\eta_q\}), \tag{A5}$$

$$\psi_0 = \left|\eta_{00}^Z - \frac{H_0}{2\sqrt{J}}\right|^2 + \left|\eta_{00}^X - \frac{H_Q^X}{2\sqrt{J}}\right|^2 + \left|\eta_{00}^Y - \frac{H_Q^Y}{2\sqrt{J}}\right|^2 + \sum_{q\omega\neq 0}(\boldsymbol{\eta}_{q\omega})^2, \tag{A6}$$

$$\psi_1 = -\frac{1}{\beta}\ln\left\langle T_\tau\exp\left(-\sum_\alpha \tilde{H}_1^\alpha\right)\right\rangle_{\tilde{H}_0} = -\frac{1}{\beta}\left\langle T_\tau\exp\left(-\sum_\alpha \tilde{H}_1^\alpha\right)\right\rangle_{\tilde{H}_0,\text{fr}}, \tag{A7}$$

$$\Omega_0 = -\frac{1}{\beta}\sum_{k,\sigma}\ln\{1+\exp[-\beta(\varepsilon_{k-1/2\sigma Q}-\mu)]\}, \tag{A8}$$

$$\eta_j(\tau) = \sum_{q,\omega}\eta_{q\omega}\exp[-i(qR_j+\omega\tau)],$$

$$\eta_{q\omega} = \frac{1}{N_0\beta}\sum_j\int_0^\beta \eta_j(\tau)\exp[-i(qR_j+\omega\tau)]d\tau,$$

where

$$\tilde{H}_1^\alpha = 2\sqrt{J}\sum_q\int_0^\beta (\eta_q^{\alpha^+}(\tau))^* S_q^\alpha(\tau)d\tau, \alpha = z, +, -,$$

q is a wave number in the first Brillouin zone, $\eta_q^\pm(\tau) = \eta_q^x(\tau) \pm \eta_q^y(\tau)$, $S_q^\alpha(\tau)$ and $(\eta_q^{\alpha^+}(\tau))^*$ are the α Fourier components of the spin operator and its conjugate component of the fluctuating exchange field. As one can see from Eq. (A6), switching to local coordinates X,Y,Z permits measuring the wave number of the spatial fluctuations of the exchange fields from the center of the Brillouin zone $q=0$.

Summing the infinite series (A7) in the uniform local field approximation, where the vertex parts $\varphi_{2p}^{\alpha_1\ldots\alpha_p}(q_1\ldots q_p,\omega_1\ldots\omega_p)$ are calculated with q_i, $\omega_i=0$, gives an approximate analytic expression for $\psi_1\equiv L(\eta)$. Taking account of the lowest-order corrections, describing the quadratic fluctuations of the field, $\psi_1\{\eta\}$ becomes

$$\psi_1\{\eta\}=L(\eta)+\sum_{q\omega\neq 0}(X_{q\omega}^{ZZ}|\eta_{q\omega}^{Z}|^2+X_{q\omega}^{+-}|\eta_{q\omega}^{X}|^2+X_{q\omega}^{+-}|\eta_{q\omega}^{Y}|^2), \tag{A9}$$

$$L\{\eta\}=-\frac{1}{\beta}\sum_{k,\sigma}\ln\{1+\exp[-\beta(E_\sigma(k,\eta)-\mu)]\}-\Omega_0, \tag{A10}$$

where

$$E_\sigma(k,\eta)=\frac{1}{2}\{\varepsilon_{k+Q/2}+\varepsilon_{k-Q/2}+\sigma\times\sqrt{(\varepsilon_{k+Q/2}-\varepsilon_{k-Q/2}+2\eta^Z\sqrt{J})^2+4J((\eta^X)^2+(\eta^Y)^2)}\}, \tag{A11}$$

$$X_{q\omega}^{ZZ}=\frac{J}{2}\sum_{k\sigma}\left(\frac{f(\varepsilon_{k+q-\sigma Q/2})-f(\varepsilon_{k-\sigma Q/2})}{\varepsilon_{k+q-\sigma Q/2}-\varepsilon_{k-\sigma Q/2}-i\omega}-\frac{\partial f(\varepsilon_{k\sigma})}{\partial\varepsilon_{k\sigma}}\right),$$

$$X_{q\omega}^{+-}=J\sum_{k}\left(\frac{f(\varepsilon_{k-Q/2})-f(\varepsilon_{k+q+Q/2})}{\varepsilon_{k-Q/2}-\varepsilon_{k+q+Q/2}+i\omega}-\frac{f(\varepsilon_{k-Q/2})-f(\varepsilon_{k+Q/2})}{\varepsilon_{k-Q/2}-\varepsilon_{k+Q/2}}\right), \tag{A12}$$

$$(\eta^\alpha)^2=\sum_{q\omega\neq 0}|\eta_{q\omega}^{\alpha}|+|\eta_{00}^{\alpha}|^2. \tag{A13}$$

After the substitution of variables $\eta_{q\omega}^{\alpha}=|\eta_{q\omega}^{\alpha}|e^{i\varphi_{q\omega}^{\alpha}}=r_{q\omega}^{\alpha}e^{i\varphi_{q\omega}^{\alpha}}$, $d\eta_{q\omega}^{\alpha}=r_{q\omega}^{\alpha}dr_{q\omega}^{\alpha}d\varphi_{q\omega}^{\alpha}$ and calculating the integrals over $\varphi_{q\omega}^{\alpha}$ the expression (A5) becomes

$$e^{-\beta\Delta\Omega}=\text{const}\cdot\int_0^\infty\prod_{\alpha=X,Y,Z}d\eta_{00}^{\alpha}\prod_{q\omega\neq 0}dr_{q\omega}^{\alpha}r_{q\omega}^{\alpha}e^{-\beta(\psi_0+\psi_1)}. \tag{A14}$$

The integrals over η_{00}^{α}, $r_{q\omega}^{\alpha}(\alpha=X,Y,Z)$ in Eq. (A14) can be evaluated by the saddle-point method. The equations $\partial\psi/\partial\eta_{00}^{\alpha}=0$ and $\partial\psi/\partial r_{q\omega}^{\alpha}=0$ describing the saddle points can be put into the form

$$\frac{\partial\psi}{\partial\eta_0^Z}=\eta_0^Z\left(1+\frac{\partial L}{\partial\eta_Z}\frac{1}{2\eta_Z}\right)-\frac{H_0}{2\sqrt{J}}=0,$$

$$\frac{\partial\psi}{\partial\eta_0^{X,Y}}=\eta_0^{X,Y}\left(1+\frac{\partial L}{\partial\eta_\perp}\frac{1}{2\eta_\perp}\right)-\frac{H_Q^{X,Y}}{2\sqrt{J}}=0,$$

$$\frac{\partial\psi}{\partial r_{q\omega}^Z}=r_{q\omega}^Z\left(1+X_{q\omega}^{ZZ}+\frac{\partial L}{\partial\eta_Z}\frac{1}{2\eta_Z}\right)-\frac{T}{2r_{q\omega}^Z}=0,$$

$$\frac{\partial\psi}{\partial r_{q\omega}^{X,Y}}=r_{q\omega}^{X,Y}\left(1+X_{q\omega}^{+-}+\frac{\partial L}{\partial\eta_\perp}\frac{1}{2\eta_\perp}\right)-\frac{T}{2r_{q\omega}^{X,Y}}=0, \tag{A15}$$

and the free energy is given by the expression

$$F=\psi_0+\psi_1+\mu N+\Omega_0, \tag{A16}$$

$$\psi_0=\left|\eta_{00}^Z-\frac{H_0}{2\sqrt{J}}\right|^2+\left|\eta_{00}^X-\frac{H_Q^X}{2\sqrt{J}}\right|^2+\left|\eta_{00}^Y-\frac{H_Q^Y}{2\sqrt{J}}\right|^2+\sum_{q\omega\neq 0}(\mathbf{r}_{q\omega})^2,$$

$$\psi_1=L+\sum_{q\omega\neq 0}\{X_{q\omega}^{ZZ}(r_{q\omega}^Z)^2+X_{q\omega}^{+-}[(r_{q\omega}^X)^2+(r_{q\omega}^Y)^2]\}-T\sum_{q\omega\neq 0}\sum_{\alpha=X,Y,Z}\ln r_{q\omega}^{\alpha}, \tag{A17}$$

where η and r are the solutions of the saddle-point equations (A15).

After switching to the density of states

$$g(\varepsilon)=\frac{V}{(2\pi)^3}\int d^3k\,\delta(\varepsilon-\varepsilon_k),$$

which is possible if the nesting condition is satisfied

$$\varepsilon_{k+Q/2}-\mu_0=\mu_0-\varepsilon_{k-Q/2},$$

the expression for L becomes

$$L\{\eta,\varphi,\varphi_1\}=-\frac{1}{\beta}\sum_\sigma\int g(\varepsilon)\ln\{1+\exp[-\beta(E_\sigma(\varepsilon,\eta)-\mu)]\}d\varepsilon-\Omega_0, \tag{A18}$$

where μ_0 is the center of the band,

$$E_\sigma(\varepsilon,\eta)=\mu_0+\sigma\sqrt{(\varepsilon-\mu_0+\eta_Z\sqrt{J})^2+J(\eta_\perp^2)}, \tag{A19}$$

$$\eta_Z=\sqrt{|\eta_{00}^Z|^2+\sum_{q\omega\neq 0}|r_{q\omega}^Z|^2},$$

$$\eta_{X,Y}=\sqrt{|\eta_{00}^{X,Y}|^2+\sum_{q\omega\neq 0}|r_{q\omega}^{X,Y}|^2},$$

$$\eta_\perp^2=\sum_{q\omega\neq 0}|r_{q\omega}^X|^2+\sum_{q\omega\neq 0}|r_{q\omega}^Y|^2+|\eta_{00}^X|^2+|\eta_{00}^Y|^2. \tag{A20}$$

The transition from the expression for the free energy as a function of the exchange fields η_Z and $\eta_\perp$ to an expression for the free energy as a function of the magnetic-order parameters M_0 and M is most effectively done by expanding the expression (A16) in a power series in the exchange fields η_Z and $\eta_\perp$:

$$F=\tilde{a}_1\eta_Z^2+\tilde{a}_3\eta_Z^4+\tilde{b}_1\eta_\perp^2+\tilde{b}_3\eta_\perp^4+\tilde{\delta}_3\eta_\perp^4\eta_Z^2+\left|\eta_0^Z-\frac{H_0^Z}{2\sqrt{J}}\right|^2+\left|\eta_0^X-\frac{H_Q^X}{2\sqrt{J}}\right|^2+\left|\eta_0^Y-\frac{H_Q^Y}{2\sqrt{J}}\right|^2+\sum_{q\omega\neq 0}(X_{q\omega}^{ZZ}|r_{q\omega}^Z|^2+X_{q\omega}^{+-}|r_{q\omega}^{\perp}|^2)-T\sum_{q\omega\neq 0}\sum_{\alpha=X,Y,Z}\ln r_{q\omega}^{\alpha}. \tag{A21}$$

The expansion coefficients $\tilde{a}_i$, $\tilde{b}_i$, and $\tilde{\delta}_3$

$$\tilde{a}_1=J\sum_k\frac{\partial f(\varepsilon_k)}{\partial\varepsilon_k}=-Jg(\mu),$$

$$\tilde{b}_1 = J\sum_k \frac{f(\varepsilon_{k+Q/2}) - f(\varepsilon_{k-Q/2})}{\varepsilon_{k+Q/2} - \varepsilon_{k-Q/2}},$$

$$\tilde{a}_3 = \frac{J^2}{12}\sum_k \frac{\partial^2 f(\varepsilon_k)}{\partial \varepsilon_k^2},$$

$$\tilde{b}_3 = \frac{J^2}{2}\sum_k \frac{\partial^2}{\partial \varepsilon_{k+Q/2}\partial \varepsilon_{k-Q/2}}\left(\frac{f(\varepsilon_{k+Q/2}) - f(\varepsilon_{k-Q/2})}{\varepsilon_{k+Q/2} - \varepsilon_{k-Q/2}}\right),$$

$$\tilde{\delta}_3 = \frac{J^2}{12}\sum_k \left(\frac{\partial^2}{\partial \varepsilon_{k+Q/2}^2} + \frac{\partial^2}{\partial \varepsilon_{k-Q/2}^2} + \frac{\partial^2}{\partial \varepsilon_{k+Q/2}\partial \varepsilon_{k-Q/2}}\right) \times \left(\frac{f(\varepsilon_{k+Q/2}) - f(\varepsilon_{k-Q/2})}{\varepsilon_{k+Q/2} - \varepsilon_{k-Q/2}}\right) \quad \text{(A22)}$$

are functions of the spectrum and are related with the coefficients a_i, b_i, and δ by the following relations:

$$a_1 = -2J\left(1 + \frac{1}{\tilde{a}_1 + 2\tilde{a}_3 x_z + \tilde{\delta}_3 x_\perp}\right),$$

$$b_1 = -2J\left(1 + \frac{1}{\tilde{b}_1 + 2\tilde{b}_3 x_\perp + \tilde{\delta}_3 x_z}\right),$$

$$a_3 = 6J^2 \frac{12\tilde{a}_3 + \left[\frac{\partial a_1}{\partial \mu}\frac{\partial^2 \mu}{\partial \eta_\perp^2} + \frac{\partial^2 a_1}{\partial \mu^2}\left(\frac{\partial \mu}{\partial \eta_\perp}\right)^2\right]}{a_1^4},$$

$$b_3 = 6J^2 \frac{12\tilde{b}_3 + \left[\frac{\partial b_1}{\partial \mu}\frac{\partial^2 \mu}{\partial \eta_\perp^2} + \frac{\partial^2 b_1}{\partial \mu^2}\left(\frac{\partial \mu}{\partial \eta_\perp}\right)^2\right]}{b_1^4},$$

$$\delta = J^2 \frac{4\tilde{\delta}_3 + 2\left[\frac{\partial^2 \tilde{a}_1}{\partial \mu^2}\left(\frac{\partial \mu}{\partial \eta_\perp}\right)^2 + \frac{\partial \tilde{a}_1}{\partial \mu}\frac{\partial^2 \mu}{\partial \eta_\perp^2}\right]}{\tilde{a}_1^2 \tilde{b}_1^2},$$

$$x_z = \sum_{q\omega \neq 0} |r_{q\omega}^Z|^2, \quad x_\perp = \sum_{q\omega \neq 0} |r_{q\omega}^\perp|^2.$$

We note that the series expansion $\Sigma_{k,\sigma} E_\sigma(k, \eta)$ with respect to η^Z and $\eta_\perp$ contains terms which are proportional to $(\eta^Z)^2 \eta_\perp^2$. This provides the fundamental possibility of the coexistence of ferromagnetism and antiferromagnetism. Such contributions to the energy of a system of localized d electrons can appear only if specific biquadratic exchange interactions are taken into account. The isotropic Heisenberg model, where the energy of the system can be expressed in the form $E = \Sigma_{q,\alpha} J(q) \langle |S^\alpha(q)|^2 \rangle$, does not describe the systematic appearance and coexistence of states with $\langle S^Z(0) \rangle \neq 0$ and $\langle S^{X,Y}(Q) \rangle \neq 0$.

[a)]E-mail: valkov@dpms.fti.ac.donetsk.ua

[1]A. A. Galkin, É. A. Zavadskiĭ, V. M. Smirnov, and V. I. Val'kov, JETP Lett. **20**, 111 (1974).
[2]A. A. Galkin, É. A. Zavadskiĭ, V. M. Smirnov, and V. I. Val'kov, Dokl. Akad. Nauk SSSR **218**, No. 3, 552 (1974) [Sov. Phys. Dokl. **19**, 593 (1975)].
[3]I. F. Gribanov, Fiz. Tverd. Tela (Leningrad) **17**, 2420 (1975) [Sov. Phys. Solid State **17**, 1008 (1975)].
[4]O. Tegus, E. Bruck, K. H. J. Bushow, and F. R. de Boer, Nature (London) **415**, 150 (2002).
[5]O. Tegus, E. Bruck, W. Daguta, X. W. Li, L. Zhang, K. H. J. Bushow, and F. R. de Boer, J. Appl. Phys. **93**, 7655 (2003).
[6]R. M. Rosenberg, W. H. Cloud, F. J. Darnell, and R. B. Flippen, Phys. Lett. A **28**, 723 (1967).
[7]R. M. Rosenberg, W. H. Cloud, F. J. Darnell, R. B. Flippen, and S. R. Butler, J. Appl. Phys. **40**, 1361 (1969).
[8]T. Goto, J. Magn. Magn. Mater. **51–57**, Pt. 2, 931 (1986).
[9]D. I. Khomskiĭ, Fiz. Met. Metalloved. **29**, No. 1, 31 (1970); T. Moriya and K. Usami, Solid State Commun. **23**, 935 (1977).
[10]I. F. Gribanov, É. A. Zavadskiĭ, and A. P. Sivachenko, Fiz. Nizk. Temp. **5**, 1219 (1979) [Sov. J. Low Temp. Phys. **5**, 577 (1979)].
[11]A. F. Vul' and B. M. Todris, Prib. Tekh. Éksp., No. 5, 208 (1989).
[12]I. N. Nechiporenko, Fiz. Nizk. Temp. **1**, 1481 (1975) [Sov. J. Low Temp. Phys. **1**, 712 (1975)].
[13]V. G. Barayakhtar', I. M. Vitebskiĭ, and D. A. Yablonskiĭ, Fiz. Tverd. Tela (Leningrad) **23**, 1448 (1981) [Sov. Phys. Solid State **23**, 843 (1981)].
[14]R. L. Stratonovich, Dokl. Akad. Nauk SSSR **157**, 1097 (1957) [Sov. Phys. Dokl. **2**, 416 (1958)].
[15]J. Hubbard, Phys. Rev. Lett. **3**, 77 (1959).
[16]J. A. Hertz and M. A. Klenin, Phys. Rev. B **10**, 1084 (1974).
[17]A. A. Povzner, A. G. Volkov, and P. V. Gel'd, Fiz. Met. Metalloved. **58**, 47 (1984).
[18]T. Moriya, *Spin Fluctuations in Itinerant Electron Magnetism*, Springer-Verlag, New York (1986), Mir, Moscow (1988).
[19]M. Isoda, J. Magn. Magn. Mater. **27**, 236 (1982).

Translated by M. E. Alferieff

LOW-DIMENSIONAL AND DISORDERED SYSTEMS

Kinetics of homogeneous crystallization of nitrogen according to electron diffraction data for free clusters

A. G. Danil'chenko,[a] S. I. Kovalenko, and V. N. Samovarov

B. I. Verkin Institute for Low Temperature Physics and Engineering of the National Academy of Sciences of Ukraine, pr. Lenina 47, Kharkov 61103, Ukraine

(Submitted April 24, 2005)
Fiz. Nizk. Temp. **31**, 1288–1292 (November 2005)

An electron diffraction investigation of the structure of free neon clusters $(N_2)_{\bar{n}}$ is performed in the average-size range $10^2 \leqslant \bar{n} \leqslant 10^5$ molecules/cluster. The first cluster beams of nitrogen consisting of monostructural aggregations with hexagonal close packing of the molecules are obtained. A sequence of structural transformations resulting in the formation of a high-temperature β phase of nitrogen in bulk samples with homogeneous nucleation is proposed on the basis of an analysis of the results obtained. © *2005 American Institute of Physics*.
[DOI: 10.1063/1.2127890]

I. INTRODUCTION

The great scientific interest in clusters is due to the fact that clusters fall between isolated microparticles and macrosystems. This makes it possible to use clusters to study the mechanisms and rates of formation of the structure and properties of a bulk substance at the earliest initial stages of its formation. Investigations of this type are ordinarily performed using aggregations containing several atoms (molecules) up to several hundreds of microparticles.

Together with these objects, it is of definite interest to study large aggregations (nanoclusters) containing 10^3 to 10^5 atoms (molecules)/cluster. The linear dimensions of such aggregations range from several tens to several hundreds of angstroms. The structure and properties of the kernels of nanoclusters are a good approximation to the properties and structure of bulk systems, in spite of the substantial number of surface atoms. If the nanoclusters are formed in an adiabatically expanding gas stream and are free of a substrate, then it is convenient to use them to study structural transformations which can occur in a condensed substance under conditions of deep supercooling and homogeneous nucleation. Metastable structures which form as a result of their growth kinetics can be obtained under these conditions.

The structure of nitrogen clusters has been studied in Refs. 1–4. As a result of these observations, the dimensional limits of existence of icosahedral clusters were estimated and a hypothesis was advanced concerning the mechanism of the transformation of an icosahedral structure into a crystal structure. However, it should be noted that all observations made in the above-cited works were performed on $(N_2)_{\bar{n}}$ clusters of small ($\bar{n} \leqslant 10^2$) and intermediate ($\bar{n} \sim 10^3$) sizes, while reliable data on the structure of larger aggregations are needed to obtain sufficiently complete and adequate information on the mechanisms of the formation of the crystal phase.

Our objective in the present work was to investigate structural transformations in free nitrogen clusters in a wide cluster-size range. The region of average sizes $\bar{n}$ of the aggregations studied was substantially increased in the direction of large clusters, up to $\bar{n} \sim 10^5$ molecules/cluster. As a result, the first monostructural nanoclusters of N_2 with hexagonal close packing (hcp) of molecules were obtained and the sequence of transformations resulting in the formation of the high-temperature β phase of nitrogen was traced in detail.

II. EXPERIMENTAL PROCEDURE

Substrate-free nitrogen clusters were formed in the process of isoentropic expansion of an ultrasonic jet of N_2 flowing into a vacuum. The observations were performed using a setup consisting of a standard electron diffraction apparatus, a supersonic cluster-beam generator, and a liquid hydrogen cooled cryogenic condensation pump, evacuating the jet gases. A conical nozzle with critical-section diameter 0.34 mm, cone angle 8.6°, and ratio of the area of the entrance section to that of the critical section 36.7 was used to produce a supersonic jet. The setup is described in detail in Ref. 3. Here we note only the most important points concerning the experimental procedure.

It is known that the size, flux density, and size distribution of the clusters are determined by the parameters of the nozzle, the temperature T_0 and the pressure P_0 of the gas at the entrance into the nozzle, and the thermodynamic properties of the gas itself. For a constant nozzle geometry, the size and flux density of the clusters increase with increasing P_0 and decreasing T_0.[5] In our case, for experimental convenience, the average cluster size was changed by varying P_0 up to 0.6 MPa, inclusively, at constant temperature $T_0 = 100$ K. The quite low temperature T_0, obtained for the first time for nitrogen, made it possible to produce cluster beams with large $\bar{n}$ using relatively low values of P_0. In this work the structure of aggregations with $\bar{n}$ in the range $5 \cdot 10^2 \leqslant \bar{n} \leqslant 1 \cdot 10^5$ molecules/cluster were investigated. In the diffraction zone, far from the cutoff of the nozzle at 100 mm, the cluster temperature was determined by comparing the measured values of the lattice parameters with the known temperature dependence of these parameters.[6] As a result, for the

clusters of the sizes studied, the temperature was $T_{eq}=38\pm5$ K, where 5 K is the maximum error in individual measurements. We note that the average cluster temperature 38 K was higher than the temperature of the phase transformation $T_{\alpha\to\beta}$ in bulk N_2, equal to 35.6 K. An independent argument showing that the average temperature of the clusters was determined correctly is that the crystal structure of large aggregations with $\bar{n}\geqslant10^4$ corresponded to the structure of the β phase of bulk N_2.[1)]

The average size of crystalline clusters with $10^3\leqslant\bar{n}\leqslant10^4$ molecules/clsuter was determined using the Selyakov-Scherrer relation (SSh). For small "noncrystalline" aggregations ($\bar{n}<10^3$ molecules/cluster) and for large crystalline nanoclusters ($\bar{n}\geqslant10^4$ molecules/cluster), where a polycrystalline state can obtain, the relation $\bar{n}=kP_0^{2.00}$ was used. This relation holds for $T_0=$const. The fact that this relation holds well in a wide range of values of $\bar{n}$ was confirmed for crystalline clusters of nitrogen in Ref. 3 by electron diffraction and in Ref. 5 by mass spectrometry for "noncrystalline" clusters ($\bar{n}\sim10^2$). The value of the coefficient k was determined from calculations of $\bar{n}$ using the SSh relation for crystalline structures of intermediate size.

The diffraction patterns were photographed in the course of the experiment. The electron diffraction patterns obtained were scanned with resolution 600 points/inch and processed on a computer. The method described in Ref. 7 was used to separate from the densitometer traces obtained the background due to the incoherent and gas components of the scattered electrons.

Figure 1 shows a series of our densitometer traces illustrating the evolution of the diffraction pattern as a function of the average cluster size. The diffraction pattern 1 corresponds to the smallest clusters, formed at $P_0=0.075$ MPa. The average cluster size in this case was 500–600 molecules/cluster. The overall features of the intensity distribution illustrated by the curve 1 generally correspond to the diffraction pattern characteristic for multilayer icosahedral clusters. Together with this, a special feature, previously not recorded in Refs. 2–4, is also observed. The essence of this feature is that the left-hand "wing" of the strongest peak ($s=1.92$ Å^{-1}) has a weak inflection, marked by an arrow in the figure. The position of the inflection $s=1.8$ Å^{-1} corresponds to the position of the diffraction peak (100) of the high-temperature β phase of nitrogen, which possesses hcp structure. Thus the character of the diffraction pattern shows that a cluster beam contains, in addition to a preponderance of icosahedral clusters, a neglible number of hcp aggregations whose size should be greater than the average value 500–600 molecules/cluster.

As $\bar{n}$ increases, substantial changes are observed to occur in the diffraction patterns. This is illustrated by the curve *2*, which corresponds to a cluster beam of nitrogen formed at $P_0=0.15$ MPa. The average cluster size in this case was 2200 molecules/cluster. The hcp peaks (100), (101), and (103) of the β phase of nitrogen are clearly recorded in the diffraction pattern. It is very interesting that together with this the diffraction pattern attests to the presence of aggregations with cubic structure in the cluster beam. This is indicated by the presence of the peak (200), characteristic only of this packing of the molecules, and by the anomalously

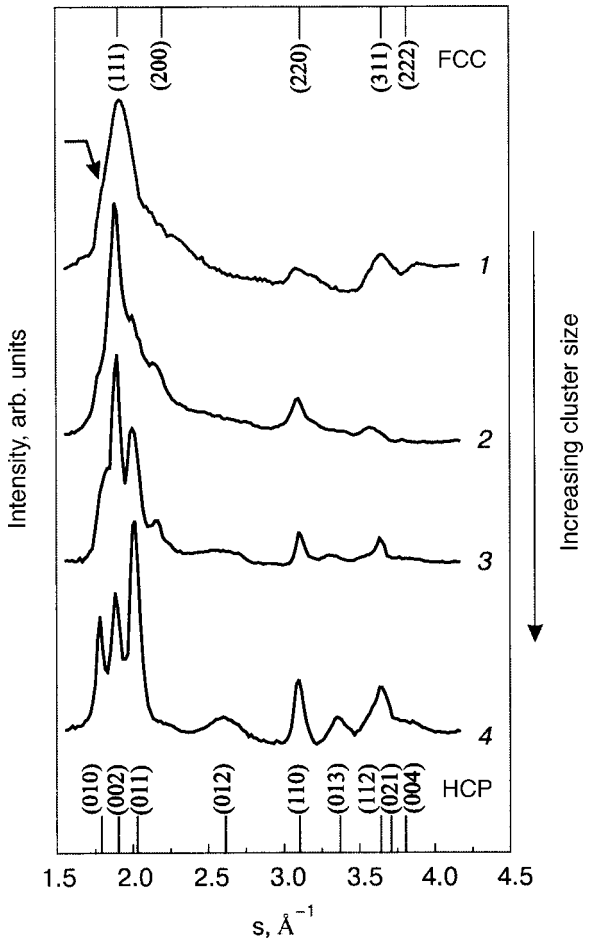

FIG. 1. Diffraction patterns after subtracting out the background from cluster beams of nitrogen with different $\bar{n}\cdot10^3$, molecules/cluster: 0.55 ($P_0=0.075$ MPa) (1); 2.2 ($P_0=0.15$ MPa) (2); 10 ($P_0=0.3$ MPa) (3); 50 ($P_0=0.55$ MPa) (4). $s=(4\pi\sin\theta)/\lambda$—diffraction wave number, θ—Bragg angle, λ—electron wavelength.

large height H_Σ of the peak at $s=1.92$ Å^{-1}, which can be explained by the superposition of the hcp peak (002) on the stronger peak (111) of the cubic phase. These peaks have the same position. We note that the ratio of the height H_{200} of the peak (200) of the cubic structure to the difference of the heights of the total peak H_Σ and the hcp peak H_{002} correlates well with the ratio of the intensities I_{200}/I_{111} of the peaks (200) and (111) of the cubic phase, i.e.

$$\frac{H_{200}}{H_\Sigma-H_{002}}\approx\frac{I_{200}}{I_{111}}.$$

The height H_{002} was calculated from the heights H_{100} and H_{101} which we observed for the hcp peaks (100) and (101). The equality obtained provides additional confirmation of the presence of the peak (111) of the cubic phase.

A further increase of the average cluster size was accompanied by an increase in the intensities of the hcp peaks and a decrease of the half-widths pf the peaks (see curve *3*). The observed transformation of the diffraction pattern indicates an increase in the number and sizes of aggregations with hcp structure. As one can see by comparing the curves *2* and *3*, as $\bar{n}$ increases, the peaks due to the cubic phase become sharper, but in the process their intensity decreases substantially, showing that the number of aggregations with cubic structure decreases. In the cases where the size $\bar{n}$ exceeded

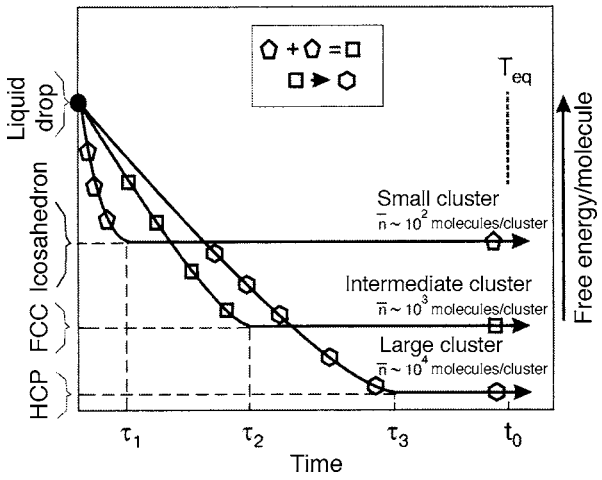

FIG. 2. Scheme of the time development of processes occurring in the clusters of a supersonic jet. The structure of the clusters: icosahedral (…..), cubic (…..), hcp (…..). τ_i—characteristic cooling times of clusters to the equilibrium temperature T_{eq} fixed in the diffraction zone; $t_0 \approx (2-4)$ μs—total time over which clusters are formed and traverse the diffraction zone. The horizontal thick lines correspond to temperature $T=T_{eq}$.

$1 \cdot 10^4$ molecules/cluster, nanoparticles only with hcp structure, stable for $T=38$K, were observed in the cluster beams. This is clearly illustrated by curve 4, which refers to cluster beams with $\bar{n} \approx (4\text{-}5) \cdot 10^4$ molecules/cluster. It should be noted that the first observation of supersonic nitrogen beams consisting only of aggregations with the equilibrium hcp structure for the given temperature was made in the present work.

Before analyzing the experimental data, the special features of the electron diffraction analysis of cluster beams, which in contrast to investigations on a substrate makes it possible to obtain important information on the structural transformations occurring over a very short time interval, need to be discussed in greater detail. Figure 2 illustrates qualitatively the time development of processes occurring in clusters of a supersonic jet, which are formed from liquid drops, which, as is well known, form inside the supersonic nozzle at the first stage of condensation of the gas. The time $t_0 \approx (2-4) \cdot 10^{-6}$ s in this figure is the total time over which the clusters are formed and traverse the electron diffraction zone. The times τ_i are the characteristic times over which clusters are cooled to the temperature T_{eq} fixed in the diffraction zone. The different states of the clusters are shown along the ordinate (actually, the free energy per molecule is plotted along the axis). For $T=T_{eq}$ the hcp structure is the equilibrium structure. For larger clusters the cooling time (τ_3) is longest, since the cooling rate v is inversely proportional to the characteristic linear size r of a cluster ($v \propto 1/r$ or $v \propto \sqrt[3]{1/\bar{n}}$). This is because substrate-free aggregations cool only as a result of the evaporation of their constituent microparticles. A "quenching" effect can occur for small clusters. This effect makes it possible to observe metastable structures in the diffraction zone.[2)] In this picture the formation kinetics of the high temperature hcp structure of nitrogen under conditions of homogeneous nucleation can be reconstructed in detail.

Virtually noninteracting clusters with icosahedral structure are formed even before the diffraction zone is reached at low values of P_0 (low density of cluster beams and small aggregation sizes $\bar{n} \approx 10^2$ molecules/cluster). As P_0 increases, the average cluster size and the density of the cluster beams increase. The probability of collisions of clusters followed by coalescence of the clusters becomes substantial. As a result of coalescence of icosahedral formations, regions of fcc structure with stacking faults arise.[8,9] The intersection of such regions creates on the surface of aggregations atomic steps which are not overgrown during the growth of the cluster; such steps subsequently make possible fast and defect-free growth of a cubic phase. The specific nature of such growth and the short residence time of a cluster in the superheated state ($\tau \ll t_0$) provide the conditions required to observe a cubic structure which is metastable at $T=38$ K. As $\bar{n}$ increases, the residence time of a cluster at temperatures far above T_{eq} increases, and as a result the probability of a cluster passing into the equilibrium state increases. It is this circumstance that is responsible for the increase of the relative contribution of the equilibrium hcp structure, observed to occur with increasing $\bar{n}$, and the decrease in the relative fraction of the metastable cubic phase, which vanishes completely for $\bar{n} \geqslant (4\text{-}5) \cdot 10^4$ molecules/cluster.

In our opinion the results of the electron diffraction analysis of a supersonic cluster beam shed light on the formation kinetics of the high-temperature β phase of N_2 under the conditions of homogeneous nucleation in bulk samples. Indeed, according to Frank's hypothesis,[10] which has recently been confirmed experimentally in Ref. 11 for metals and in Ref. 7 for inert gases, regions with icosahedral structure arise in a supercooled liquid drop. We believe that the coalescence of such regions results in rapid growth of the fcc phase which is metastable at $T > 35.6$ K and transforms subsequently into the equilibrium hcp β phase of nitrogen.

III. CONCLUSIONS

In the present work, for the first time, monostructural nitrogen clusters with hexagonal close packing of the molecules were observed and the size evolution of the structure of clusters was traced. Analysis of the experimental results made it possible to reconstruct the formation kinetics of the β phase of nitrogen in bulk samples under conditions of homogeneous nucleation. This process proceeds according to the following stages: liquid—appearance of regions with icosahedral structure—formation of a metastable cubic phase—formation of a stable β phase of nitrogen. The results obtained provide grounds for believing that the indicated sequence of transformations is fundamental for cryocrystals where the contribution of the anisotropic component to the total energy of the lattice is small.

a)E-mail: danylchenko@ilt.kharkov.ua

1)The value T_{eq} did not change with cluster size. This was indicated by the fact that the positions of the diffraction peaks were the same for different values of $\bar{n}$.

2)According to Ref. 2, for clusters with $\bar{n} \leqslant 10^2$ molecule/cluster the structure with a fivefold symmetry axis is the equilibrium structure.

[1]I. Farges, M. F. de Feraudy, B. Raoult, and G. Torchet, Ber. Bunsenges. Phys. Chem. **88**, 211 (1984).

[2]F. Calvo, G. Torchet, and M. F. de Feraudy, J. Chem. Phys. **111**, 4650 (1999).
[3]S. I. Kovalenko, D. D. Solnyshkin, É. T. Verkhovtseva, and V. V. Eremenko, Fiz. Nizk. Temp. **20**, 961 (1994) [Low Temp. Phys. **20**, 758 (1994)].
[4]S. J. Kovalenko, D. D. Solnyshkin, É T. Verkhovtseva, and V. V. Eremenko, J. Cryst. Growth **191**, 553 (1998).
[5]O. F. Hagena and O. Obert, J. Chem. Phys. **56**, 1793 (1972).
[6]*Physics of Cryocrystals*, V. Manzhelii and Yu. Freiman (eds.), AIP Press, American Institute of Physics, Woodbury, New York (1996).
[7]A. G. Danil'chenko, S. I. Kovalenko, and V. N. Samovarov, Fiz. Nizk. Temp. **30**, 226 (2004) [Low Temp. Phys. **30**, 166 (2004)].
[8]B. W. van de Waal, J. Cryst. Growth **158**, 153 (1996).
[9]S. I. Kovalenko, D. D. Solnyshkin, and É. T. Verkhovtseva, Fiz. Nizk. Temp. **26**, 279 (2000) [Low Temp. Phys. **26**, 207 (2000)].
[10]F. C. Frank, Proc. R. Soc. London, Ser. A **215**, 43 (1952).
[11]K. F. Kelton, G. W. Lee, A. K. Gangopadhyay, R. W. Hyers, T. J. Rathz, J. R. Rogers, M. B. Robinson, and D. S. Robinson, Phys. Rev. Lett. **90**, 195504 (2003).

Translated by M. E. Alferieff

QUANTUM EFFECTS IN SEMICONDUCTORS AND DIELECTRICS

Photoinduced absorption and anomalous dichroism in $NaCa_2Mn_2V_3O_{12}$ garnet as evidence for the formation of oxygen hole dynamics

V. V. Eremenko, S. L. Gnatchenko, I. S. Kachur, V. G. Piryatinskaya, A. M. Ratner, and V. V. Shapiro

B. Verkin Institute for Low Temperature Physics and Engineering of the National Academy of Sciences of Ukraine, 47 Lenin Ave., Kharkov 61103, Ukraine

M. B. Kosymna, B. P. Nazarenko, and V. M. Puzikov

STC "Institute for Single Crystals" of the National Academy of Sciences of Ukraine, 60 Lenin Ave., Kharkov 61001, Ukraine

(Submitted April 27, 2005; resubmitted May 25, 2005)
Fiz. Nizk. Temp. **31**, 1293–1301 (November 2005)

It is shown that long-lived photoinduced dichroism in garnets is caused by photoproduced charges with anisotropic structure, which retains a memory of the pumping light polarization for a long time, while photoinduced absorption is due to all photoproduced charges irrespective of their intrinsic structure. The charges with anisotropic structure are indentified as two-center oxygen holes. The formation of an oxygen hole is preceded by the excitation of a charge-transfer state with an electron partially transferred to a cation C (V^{5+} for $NaCa_2Mn_2V_3O_{12}$ garnet) from an adjacent oxygen anion. To turn this excited state into a free hole state requires a time τ_{hole} during which the hole axis can reorient, resulting in a diminution of dichroism. The time τ_{hole} decreases with increasing ionization potential of the cation C (very high for V^{5+}). Such a mechanism explains qualitatively a number of unusual experimental facts, specifically, very strong dichroism observed only in $NaCa_2Mn_2V_3O_{12}$ garnet, where after the irradiation is switched off the photoinduced changes in all optical properties disappear much more quickly than in the other garnets studied. © *2005 American Institute of Physics*. [DOI: 10.1063/1.2127891]

I. INTRODUCTION

Long-lived photoinduced phenomena in magnetic insulators have been extensively studied[1–10] and attributed to photoinduced charge transfer. In ferro-or ferrimagnets, whose Curie temperatures lie above the upper temperature limit of the existence of long-lived photoinduced phenomena, photoinduced changes in the optical properties can be observed only simultaneously with changes in the magnetic structure (specifically, illumination of the yttrium iron garnet $Y_3Fe_5O_{12}$ with linearly polarized light affects the magnetic anisotropy,[1–3] domain structure,[4] and optical dichroism[3]). The photoinduced changes in the optical and magnetic properties are deeply interconnected, which greatly complicates the mechanism of these changes and makes it more difficult to elucidate it.

To separate the photoinduced changes of the optical properties from those of the magnetic characteristics, the authors of Refs. 5–10 recently examined antiferromagnetic garnets ($Ca_3Mn_2Ge_3O_{12}$ and $NaCa_2Mn_2V_3O_{12}$ with low Néel temperature $T_N \sim 20$K) and the paramagnetic garnet $Ca_3Ga_{2-x}Mn_xGe_3O_{12}$ in a broad temperature range below the temperature at which long-lived photoinduced phenomena vanish (about 150 K). In the absence of magnetic ordering, photoinduced optical phenomena in the garnets mentioned above share well-pronounced features, which enabled us to elucidate their nature.[5–8]

A photoinduced addition to absorption, ΔK, and photoinduced dichroism were observed and analyzed in all the garnets examined—$Ca_3Mn_2Ge_3O_{12}$, $NaCa_2Mn_2V_3O_{12}$, and $Ca_3Ga_{2-x}Mn_xGe_3O_{12}$ ($x=0.01$ and 0.02). It was found that the corresponding relaxation curves, recorded after switching off the irradiation, are similar. Each relaxation curve contains a continuous set of exponential decay components with decay time varying from one minute up to many hours (a special analysis proved that the decay times cover this interval continuously). As the temperature is increased, the observed decay kinetics does not change noticeably, while ΔK diminishes by an order of magnitude. Such decay kinetics cannot be ascribed to some new irradiation-produced optical centers but is naturally explained by the random electric fields of the photoproduced localized charges. These fields play a dual role: they enhance the optical transition observed and strongly promote the delocalization of holes, thus accelerating their recombination with negative charges (localized electrons). The broad continuous set of decay times is conditioned by a continuous distribution of random electric fields over magnitude. This idea was quantitatively corroborated by the solving the corresponding kinetic equation with realistic values of the parameters.[5,6]

Photoinduced dichroism, observed simultaneously with photoinduced absorption ΔK, has the same relaxation kinetics but, unlike ΔK, sharply increases from $Ca_3Mn_2Ge_3O_{12}$ or $Ca_3Ga_{2-x}Mn_xGe_3O_{12}$ to $NaCa_2Mn_2V_3O_{12}$ (when the polarization direction of the pump light is varied, the difference $\Delta K_{max} - \Delta K_{min}$ between the maximum and minimum values of ΔK is 90% of ΔK_{max} for $NaCa_2Mn_2V_3O_{12}$ and only 10 to

20% for the other garnets mentioned). These and other facts suggested a mechanism where long-lived photoinduced dichroism is caused by two-center oxygen holes the direction of whose axis retains a memory of the pump polarization direction for a long time.[7,8] This mechanism is advanced in Sec. II.

The purpose of the present paper is to corroborate the proposed mechanism by new experimental data described in Sec. III. The main experimental result consists in separating the optical manifestations of photoproduced charges of opposite sign: electrons localized on lattice cations cause only photoinduced absorption, while two-center oxygen holes are responsible for photoinduced dichroism and absorption. Comparing dichroism and absorption, caused by charges of opposite sign, makes it possible to specify and confirm the mechanism proposed for dichroism, recorded through two-center holes when pumping a crystal with polarized light. Such an analysis is made in Sec. IV.

II. MAIN IDEA TO BE CORROBORATED EXPERIMENTALLY

Before describing the the experiment, to elucidate its goals it is helpful to summarize the main idea that is based on our previous results[7,8] and has to be corroborated by new experiments, which are discussed in Sec. III. This idea consists of the following.

(i) The role of oxygen holes as photoproduced charges in the formation of photoinduced absorption and dichroism follows from different independent considerations.[7,8] First, the motion and subsequent recombination of photoinduced charges is mirrored by the relaxation kinetics of photoinduced changes after switching off the irradiation. The similarity of the relaxation curves observed for the garnets $Ca_3Mn_2Ge_3O_{12}$, $Ca_3Ga_{2-x}Mn_xGe_3O_{12}$, and $NaCa_2Mn_2V_3O_{12}$ with different cation composition and the same anion group O_{12} suggests that the O^{2-} anion subsystem plays the main role in the motion of the photoinduced charges. This means that irradiation creates holes (O^-) moving in the oxygen subsystem.

Second, there is no alternative for the nature of the photoproduced positive charges. Indeed, in all the garnets examined photoinduced absorption can be excited by red light with photon energy (about 2 eV) much lower than the ionization potential of every lattice cation (>30 eV) but comparable to the dielectric gap, E_g, of the O^{2-} sublattice (the estimate $E_g \approx 2$ eV follows from the absorption spectrum given below in Fig. 1).

(ii) The structural features of the holes in the oxygen subsystem of garnets are predetermined by the closed-shell configuration of the O^{2-} ion, identical to that of Ne. It has been well established that in solid neon, as well as in other rare-gas solids, the stable lowest state of the hole ns^2np^5 is a two-atom molecule ns^2np^5–ns^2np^6 formed on adjacent lattice sites. The atomic valence p-hole, distributed between two atoms, produces strong exchange binding of the order of 1 eV.[11,12] The magnitude of such exchange binding mainly depends on the ratio of the valence p-state radius to the interatomic distance in an ideal lattice. This ratio is about 0.3 for the garnets studied, 0.17 for solid neon, and 0.25 for solid argon. For alkali halides (KCl, KI, NaI), where the existence of stable two-center holes in the anion subsystem is also reliably established, this ratio varies from 0.20 to 0.27. Hence, stable two-atom hole polarons must exist also in the O^{2-} subsystem of garnets.

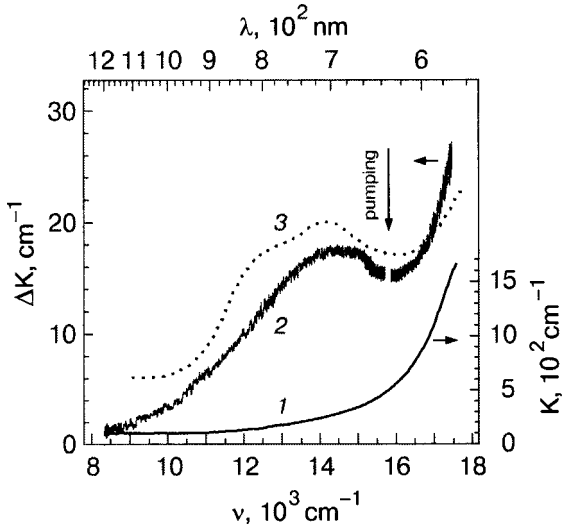

FIG. 1. Absorption spectrum of the garnet $NaCa_2Mn_2V_3O_{12}$ with pentavalent vanadium at 30 K: without pumping (curve *1*) and the photoinduced addition to absorption under pumping (curve *2*); the pumping light frequency is shown by an arrow, and the small spectral gap near it is caused by a light filter suppressing the scattered pump light.[9] For comparison, the dotted line 3 shows the absorption spectrum of the garnet $NaCa_2Mn_2V_3O_{12}$ with tetravalent vanadium.[13] A comparison of the curve *2* and *3* shows that the photoinduced absorption of $NaCa_2Mn_2V_3O_{12}$ at $\nu < 16000$ cm^{-1} is due to V^{5+} ions converted into V^{4+} by taking an electron away from O^{2-}.

(iii) Only charges with anisotropic structure can retain a long-time memory of the pumping polarization direction and, hence, be responsible for the long-lived photoinduced dichroism observed. A two-center hole in the oxygen subsystem is the only realistic candidate for a charge with anisotropic structure in garnets.

It is easy to trace how two-center holes created by polarized illumination cause dichroism. The latter is described by the difference, $\Delta K_\perp - \Delta K_\parallel$ in photoinduced absorption measured with the probe light polarized perpendicular and parallel to the pump light polarization. The photoinduced addition to absorption, ΔK, is determined by the photoinduced field **F** enhancing a weak optical transition in the lattice ions (obviously, Mn^{3+} or Mn^{4+}) serving as probe optical centers. The field **F** is produced mainly by a two-center hole, lying in the first coordination sphere of the probe ion A, and is perpendicular to the axis of the two-center hole (Fig. 2).

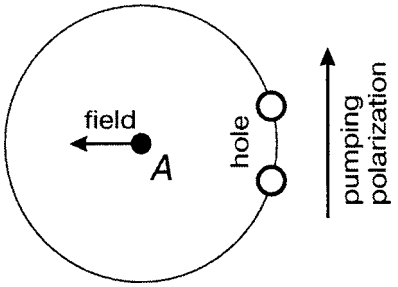

FIG. 2. Origin of photoinduced dichroism: a two-center oxygen hole, allocated in the first coordination sphere of the probe manganese ion A, creates at the point A an electric field perpendicular to the two-center hole axis and to the polarization direction of the pump.

Since the axis is oriented predominantly parallel to the pump polarization direction, the probe light undergoes stronger additional absorption if it is polarized perpendicularly to the pump polarization. Hence, $\Delta K_\perp > \Delta K_\parallel$ in accordance with experiment (see Sec. III).

(iv) The magnitude of dichroism is obviously dictated by the reorientation of the axes of two-center holes created by polarized light. Experiment shows that the reorientation of the axes of two-center holes after they are created is not of great importance. Indeed, very strong dichroism, much greater than that in other garnets studied, is observed in the garnet $NaCa_2Mn_2V_3O_{12}$, where after switching off the irradiation the dichroism disappears much faster than in the other garnets. Thus, the reorientation of the axes of two-center holes in the course of their creation by polarized light is of greatest importance. It occurs in the following way.

The initial excitation, caused by pump light polarized in the z direction, rearranges the binding between a lattice cation C (identified below as vanadium for $NaCa_2Mn_2V_3O_{12}$) and an adjacent anion O^{2-} lying on the z axis with respect to ion C. Such excitation is of a charge-transfer character: an electron is partially transferred from O^{2-} to a cation C with a high ionization potential. Such an excited state, denoted as $\langle j=1|$, is one of 6 degenerate states related to 6 oxygen ions in the first coordination sphere of ion C. Every excited state $\langle j|$ can pass during a time τ_{hole} into another type of excitation, somewhat lower in energy, with the completed electron transfer: a free hole appears in the oxygen sublattice and the charge of the cation C is 1 less than that at the regular sites. In addition, every excited state $\langle j|$ can pass during a time τ_j into another of 6 degenerate states $\langle j'|$ (such transitions are caused by random photoinduced electric fields, which are absent in the ideal lattice Hamiltonian with orthogonal eigenstates $\langle j|$). Under pumping with polarized light the strongest possible dichroism occurs if $\tau_{\text{hole}} \ll \tau_j$. In the opposite case $\tau_{\text{hole}} \gg \tau_j$, all the states $\langle j|$ become equally populated (as under unpolarized pumping), so that dichroism vanishes. Thus, the cause of the anomalous dichroism observed in $NaCa_2Mn_2V_3O_{12}$ should be sought in the small value of the time τ_{hole} required for the charge-transfer excitation to be transformed into an oxygen hole (the time τ_j dictated by the random fields is nearly the same for all garnets). In Sec. IV it will be explained why τ_{hole} takes on its lowest value only in the garnet $NaCa_2Mn_2V_3O_{12}$.

III. EXPERIMENT

A. Experimental technique

Single crystals of the garnet $NaCa_2Mn_2V_3O_{12}$ were grown from melt solution by the method of spontaneous crystallization.[10] A sample was cut in the form of a 50 ± 10 μm thick plane-parallel plate perpendicular to the [100] direction. Photoinduced phenomena were examined with an optical double-beam setup. The sample was illuminated by a He–Ne laser (with light wavelength $\lambda=633$ nm and flux density 0.13 W/cm^2). The stable wide-band emission from a xenon arc lamp, dispersed through a monochromator, served as the probe light. The intensity of the probe beam was low enough to cause no photoinduced phenomena. A special light filter was applied to suppress scattered illumination from the laser. The intensity of probe light passed through the sample was detected with a photomultiplier. The photoinduced absorption coefficient is defined as $\Delta K = (1/d)\ln(I_0/I)$, where d is the plate thickness, and I_0 and I denote the intensity of the probe beam passed through the plate in the ground state or exposed to radiation, respectively (photoinduced changes are not observed in the reflection coefficient).

The absorption spectrum of the illuminated sample was registered under pumping lasting 15 min (this time is sufficient for the photoinduced effect to reach saturation).

To examine photoinduced dichroism, the probe light was polarized in the lattice direction [110] and the photoinduced addition to the absorption coefficient was measured under irradiation with light polarized parallel ($\Delta K_\parallel$) and perpendicular ($\Delta K_\perp$) to the probe light polarization. Photoinduced dichroism is defined as the difference $\Delta K_\perp - \Delta K_\parallel$.

B. Spectra of photoinduced absorption and dichroism

The absorption spectrum of the garnet $NaCa_2Mn_2V_3O_{12}$ measured in the absence of pumping is shown in Fig. 1 (curve *1*). The figure presents the long-wavelength tail of strong absorption that increases rapidly with frequency (the position of the absorption band maximum, lying in the region of very strong absorption, could not be determined). To all appearances this absorption band is formed with the participation of manganese ions. Indeed, the garnet $NaCa_2Mg_2V_3O_{12}$, differing from the garnet $NaCa_2Mn_2V_3O_{12}$ under study only by Mg replacing Mn, is transparent in the same spectral region.[13] On the other hand, such a broad absorption band cannot be assigned to *d–d* transitions within the Mn subsystem, which manifest themselves as narrow absorption bands. The broad absorption band observed can be attributed to charge transfer transitions between a Mn ion and its crystalline surroundings (probably, adjacent oxygen anions). Note that the photoinduced dichroism considered below is connected with this absorption band.

Figure 1 also presents the spectrum of additional absorption caused by illumination (curve *2*).[9] For comparison, the dotted curve shows the absorption spectrum of the garnet $NaCa_2Mg_2V_3O_{12}$ exposed to thermal quenching that lowers the valence of some V^{5+} cations from 5 to 4[13] (the vanadium in regular $NaCa_2Mn_2V_3O_{12}$ and $NaCa_2Mg_2V_3O_{12}$ crystals is in the form V^{5+}). According to Ref. 13, transitions in V^{4+} ions manifest themselves in the absorption band shown by the dotted curve in Fig. 1. The close similarity between the photoinduced absorption band observed in $NaCa_2Mn_2V_3O_{12}$ near $\nu=14300$ cm^{-1} and the absorption band of V^{4+} ions in $NaCa_2Mg_2V_3O_{12}$ leads to the conclusion that in the former case this photoinduced absorption band belongs to photoproduced V^{4+} ions.[9] Thus, the photoproduction of an oxygen hole occurs via the localization of an electron, taken away from an O^{2-} anion, on a V^{5+} cation.

Figure 3 presents the spectrum of photoinduced dichroism described by the difference, $\Delta K_\perp - \Delta K_\parallel$, between the absorption measured with the probe light polarized perpendicular and parallel to the pump light polarization. As can be seen from the figure, this dichroism has a maximum at the point $\nu=16700$ cm^{-1} lying within the absorption band of manganese. Near this maximum $\Delta K_\perp$ is an order of magnitude greater than $\Delta K_\parallel$. This provides direct evidence that photoin-

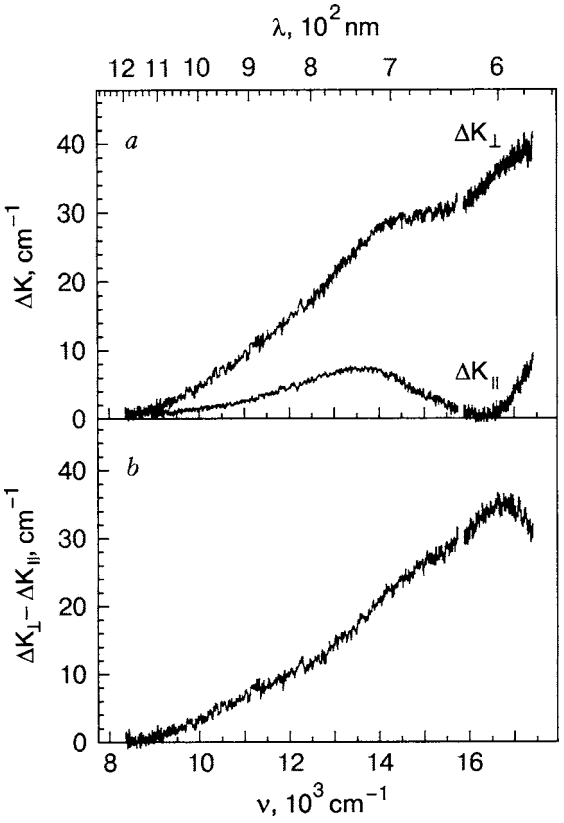

FIG. 3. The spectrum of the photoinduced addition to absorption in $NaCa_2Mn_2V_3O_{12}$ under irradiation with light polarized perpendicular and parallel to the probe light polarization ($\Delta K_\perp$ and $\Delta K_\parallel$, respectively) at 30 K (a). The difference spectrum, $\Delta K_\perp - \Delta K_\parallel$, describing the dichroism of $NaCa_2Mn_2V_3O_{12}$ (b).

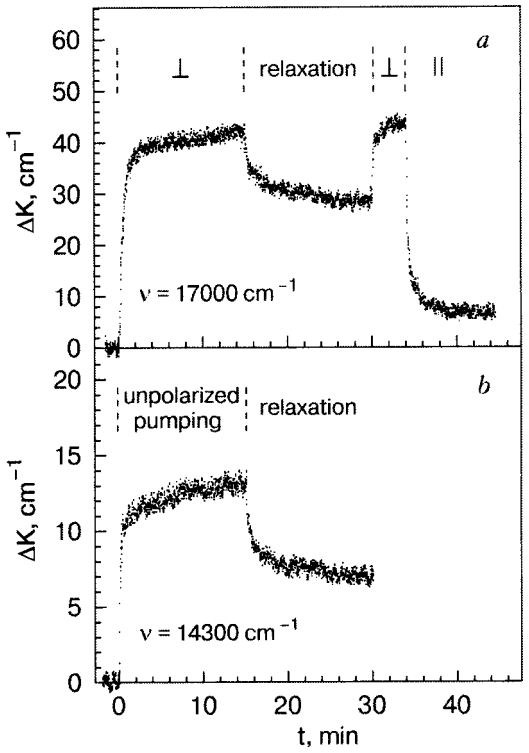

FIG. 4. Time dependence of the photoinduced addition to the absorption coefficient, ΔK, at $T=40$K measured at different frequencies: 17000 cm^{-1} (a) and 14300 cm^{-1} (b) under pumping conditions changed as indicated in the figure. The symbols $\perp$ and $\parallel$ denote a time interval when the sample was irradiated with light polarized perpendicular or parallel, respectively, to the probe light polarization. The relaxation regime in the absence of pumping is also shown.

duced absorption of probe light by manganese ions is highly sensitive to the angle between the polarizations of the probe and pump lights (Sec. II(iii), Fig. 2).

On the contrary, the absorption band of V^{4+} ions (shown in Fig. 1) is not sensitive to the polarizations of the pump and probe rays. Indeed, although the absorption of V^{4+} ions makes noticeable contributions to the curves $\Delta K_\perp$ and $\Delta K_\parallel$ presented in Fig. 3a, these contributions are equal and disappear from the difference curve shown in Fig. 3b. Actually, this difference curve has no maximum at the point $\nu = 14000$ cm^{-1} related to the absorption of V^{4+} ions and distinctly seen in Fig. 1 (curves *2* and *3*). The noticeable dichroism observed at $\nu \leqslant 14000$ cm^{-1} bears no relation to the absorption of V^{4+} ions and is due to the long-wavelength tail of the manganese absorption sensitive to the pump polarization. We shall return to this fact in Sec. IV.

C. Kinetics of photoinduced dichroism and absorption

Figure 4a demonstrates the measured dichroism and its kinetics under changing conditions of pumping. First, the photoinduced addition to absorption, $\Delta K_\perp$, was measured under pumping polarized perpendicularly to the probe light polarization. Then, at $t=15$ min when photoinduced dichroism approaches its saturation value, the pump was switched off and the relaxation of $\Delta K_\perp$ was observed during the next 15 min. At $t=30$ min the perpendicularly polarized pump was switched on again for 5 min, which was sufficient to achieve the same level of $\Delta K_\perp$ as before the pump had been switched off. At $t=35$ min the pump polarization direction was switched parallel to the probe light polarization, causing the diminution of ΔK down to a small value $\Delta K_\parallel \approx 0.1 \Delta K_\perp$; this indicates a high degree of dichroism $\Delta K_\perp / \Delta K_\parallel \approx 10$.

For comparison, Fig. 4b shows the time dependence of the photoinduced absorption observed under unpolarized pumping at the frequency $\nu = 14300$ cm^{-1}, i.e., at the maximum of the photoinduced absorption band of V^{4+} centers insensitive to the polarization of the pump (see Sec. II). Comparing Figs. 4b and 4a shows that the polarization of the pump influences only the magnitude of photoinduced absorption but not its kinetics under irradiation or after the irradiation is switched off. This comparison will be made in greater detail in Sec. IV.

It is also helpful to compare the relaxation rate of photoinduced absorption observed in two garnets at a low temperature after switching off the irradiation: in the garnet $NaCa_2Mn_2V_3O_{12}$ with strong dichroism and in the garnet $Ca_3Mn_2Ge_3O_{12}$ with weak dichroism.[5] To that end, making allowance for the close similarity between the relaxation kinetics of photoinduced absorption and dichroism, we define the mean relaxation rate as

$$R_{\text{relax}} = [\Delta K(0) - \Delta K(20 \text{ min})]/\Delta K(0) \quad (1)$$

where time is measured from the moment the irradiation is switched off. Figure 4 gives $R_{\text{relax}} \approx 0.35$ for $\Delta K_\perp$ in $NaCa_2Mn_2V_3O_{12}$. The value of R_{relax} in $Ca_3Mn_2Ge_3O_{12}$, equal to about 0.12,[5,6] indicates considerably slower relaxation.

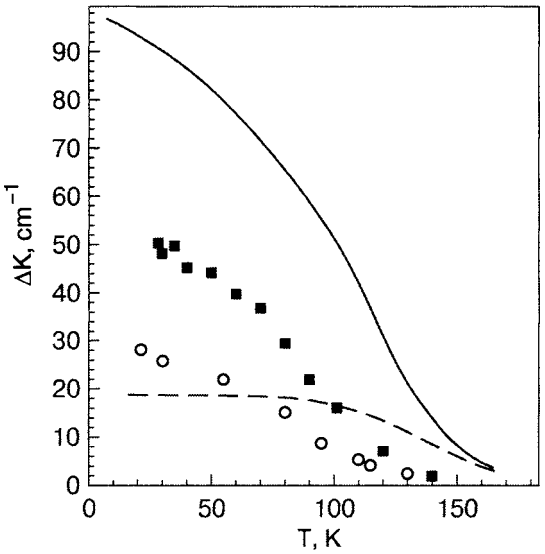

FIG. 5. Temperature dependence of photoinduced dichroism $\Delta K_\perp - \Delta K_\parallel$ measured for $NaCa_2Mn_2V_3O_{12}$ under polarized pumping (squares). The temperature dependence of photoinduced absorption measured under unpolarized pumping (circles) is of the same character. For comparison, the corresponding dependences of photoinduced dichroism and photoinduced absorption for the garnet $Ca_3Mn_2Ge_3O_{12}$[5] are shown by dashed and solid lines, respectively.

D. Temperature dependence of photoinduced dichroism and absorption

Figure 5 shows the temperature dependence of dichroism $K_{\text{dich}}=\Delta K_\perp - \Delta K_\parallel$ ($\Delta K_\perp$ and $\Delta K_\parallel$ were measured under irradiation lasting long enough so that $\Delta K_\perp$ and $\Delta K_\parallel$ become independent of time). For comparison, the dashed line shows the temperature dependence of the same quantity for $Ca_3Mn_2Ge_3O_{12}$.[5] Figure 5 demonstrates the different temperature behavior of dichroism for $NaCa_2Mn_2V_3O_{12}$ and $Ca_3Mn_2Ge_3O_{12}$. For $NaCa_2Mn_2V_3O_{12}$ K_{dich} decreases with temperature in the entire experimental temperature interval, quite similarly to photoinduced absorption ΔK observed under unpolarized pumping. For $Ca_3Mn_2Ge_3O_{12}$ K_{dich} diminishes with increasing temperature above the point $T_{\text{dim}}=90$ K only, while the temperature behavior of ΔK is quite similar for both garmets. For these garnets, Table I presents T_{dim} together with the degree of dichroism $\Delta K_\perp/\Delta K_\parallel$ and the relaxation rate (1).

IV. CORROBORATION OF THE MECHANISM OF PHOTOINDUCED DICHROISM AND OF THE ROLE OF TWO-CENTER HOLES

A. General conception of the enhancement of optical transitions by the electric fields of photoproduced charges

As mentioned in the introduction, long-lived photoinduced phenomena in garnets are generally caused by the enhancement of optical transitions in the manganese subsystem by the electric field of photoproduced charges.[5,6] In $NaCa_2Mn_2V_3O_{12}$ garnet, along with such a photoinduced contribution to absorption at $\nu \geqslant 16000$ cm^{-1} (Fig. 3), irradiation creates V^{4+} centers which give rise to the photoinduced absorption band near 14000 cm^{-1} (Fig. 1). The proposed mechanism of photoinduced absorption is illustratively corroborated by a comparison of these photoinduced contributions to absorption in $NaCa_2Mn_2V_3O_{12}$ garnet.

TABLE I. Characteristics of dichroism for the two garnets: relative degree of dichroism, the commencement T_{dim} of its temperature diminution, and the relaxation rate (1). Comment: *Dichroism decreases with temperature in the entire region examined.

Garnet	$\Delta K_\perp/\Delta K_\parallel - 1$	T_{dim}, K	R_{relax}
$NaCa_2Mn_2V_3O_{12}$	9	*	0.35
$Ca_3Mn_2Ge_3O_{12}$	0.2	90	0.12

Under irradiation with polarized light, an anisotropic electric field of two-center holes, influencing optical transition in the manganese subsystem, causes sharp dichroism of photoinduced absorption at $\nu \approx 17000$ cm^{-1} (Fig. 3). Note that these transitions can occur in all manganese ions, being enhanced by the applied field by a value proportional to the number of charges. But the V^{4+} absorption, proportional to a small photoproduced portion of V^{4+} ions, is practically insensitive to the field of photoproduced charges; this field changes the V^{4+} absorption by a negligibly small value quadric in the number of charges. Being insensitive to the anisotropic field of photoproduced two-center holes, the V^{4+} absorption exhibits no dichroism, as was spectroscopically evidenced in Sec. III B.

Thus, two different ions, labeled as C and A, are involved in photoinduced phenomena. Ion C (V^{5+} for $NaCa_2Mn_2V_3O_{12}$ garnet) participates in the creation of an oxygen hole O^- by taking an electron away from an adjacent O^{2-} cation. The created hole O^- undergoes two-site self-trapping and turns into a two-center hole with the initial orientation of its axis. Then the two-center hole, retaining the direction of orientation of its axis, reaches the first coordination sphere of the probe ion A ($\equiv$Mn) sensitive to the electric field of the hole and, hence, to the direction of its axis, which conditions dichroism. Note that V^{5+} ions with a very high ionization potential cannot play the role of probe ion A, since the oxygen holes created are more strongly attracted by Mn ions with a much lower ionization potential.

B. Creation of oxygen holes through complete transfer of an electron from an O^{2-} anion to a V^{5+} cation

As was shown in Sec. III B, an oxygen hole is created by taking an electron away from an O^{2-} anion and localizing it on a V^{5+} cation. Hence it follows that the number of photoproduced oxygen holes coincides with that of V^{4+} ions. This coincidence can be proved by comparing the absorption band of V^{4+} ions, created by unpolarized pumping with maximum at $\nu \approx 14000$ cm^{-1} (Fig. 1), with the absorption band of two-center oxygen holes created by pumping with light polarized perpendicularly to the polarization of the probe light (the reorientation of two-center holes after their creation can be neglected; see Sec. IV C). The ratio of the maximum ordinates of these absorption bands, $\rho=\Delta K_\perp(17000)/\Delta K(14300)$, must be independent of the number of holes and, hence, of temperature and irradiation time. Figure 6 presents the ratio $\rho=\Delta K_\perp(17000)/\Delta K(14300)$ observed under pumping and in the course of the subsequent relaxation. This ratio, measured under pumping with the same intensity, was found to be independent of temperature, to within the accuracy of the measurements, in the region examined, 40 K $\leqslant T$

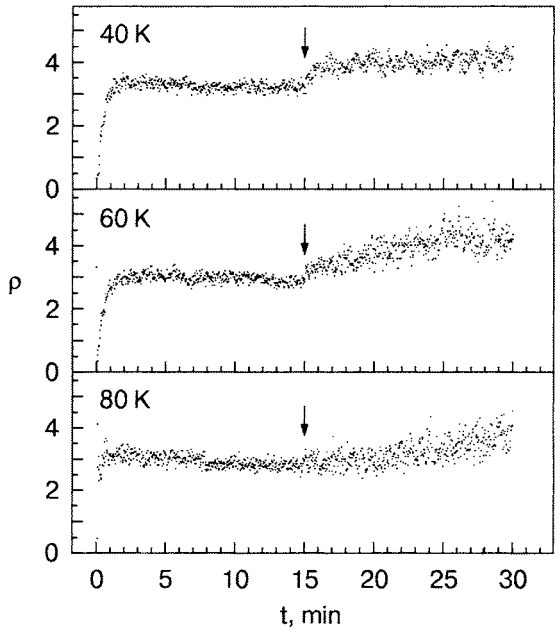

FIG. 6. Ratio $\rho=\Delta K(17000\ \mathrm{cm}^{-1})/\Delta K(14300\ \mathrm{cm}^{-1})$ measured under pumping and in the course of the subsequent relaxation at different temperatures (the moment when the irradiation is switched off is indicated by an arrow). This ratio mainly reproduces the ratio of the number of photoproduced oxygen holes to that of photoproduced V^{4+} ions. The approximate constancy of ρ confirms that oxygen holes are created by the trapping of an electron, taken away from an O^{2-} ion, by an adjacent V^{5+} cation (the slight enhancement of ρ after switching off the irradiation is explained in Sec. IV D(ii)).

$\leqslant 80$ K. After switching off the irradiation, ρ increases slightly, which provides additional evidence for the reorientation of holes at the stage of their creation [see Sec. IV D(ii)].

The constancy of the ratio ρ confirms that oxygen holes are created via trapping of an electron, taken away from an O^{2-} ion, by an adjacent vanadium cation of the lattice.

C. Conservation of the orientation of two-center holes after their formation

Experiment does not detect the reorientation of the axes of two-center holes after they are formed. Indeed, as seen from Fig. 6, after switching off the irradiation the dichroism relaxes (disappears) with the same (or even slightly slower) rate than the number of photoproduced charges. If this relaxation were accompanied by the reorientation of the axes of two-center holes, the dichroism would diminish faster than the number of photoproduced charges, and the ratio $\rho=\Delta K_{\perp}(17000)/\Delta K(14300)$ presented in Fig. 6 would be a decreasing function of time after switching off the irradiation.

Thus, Fig. 6 demonstrates that the time, τ_{reor}, required for a two-center hole to be reoriented is much greater than the hole-electron recombination time dictated by the hole hopping time τ_{hop}:

$$\tau_{\mathrm{reor}} \gg \tau_{\mathrm{hop}}. \tag{2}$$

Note that for two-center holes observed in alkali halide crystals the inequality (2) was also established experimentally.[14–16]

The physical reason for the relation (2) is elucidated by Fig. 7. Initially, a two-center hole was located on atoms A and B indicated by bold circles; the orbital of the p-hole at every atom (the absent p-electron) is schematically shown by the thin line. Immediately after a hop, the two-center hole occupies a new position BC or BD with the same orientation of the axes of the atomic p-holes. (In the latter case, the subsequent reorientation of the hole axis in the direction BD does not affect the hopping probability). The hop creating hole BD is much less probable than the hop creating hole BC. Indeed, the probability of hopping sharply depends on the exchange interaction between atom B and the adjacent atom C or D,[17] the exchange BC being much stronger due to the greater overlap of the wave functions.

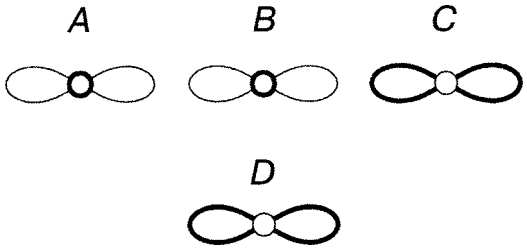

FIG. 7. Motion of a two-center hole, initially allocated on the atoms A and B, to a next position BC or BD. The motion rate is determined by the overlap of the atomic p-orbital not occupied at the atom B (thin line) with its orbital occupied at adjacent atoms (bold line); hence, the hop AB-BD has a much lower probability. In the latter case a hop is followed (in order to lower the resonance energy) by a reorientation the axes of the atomic p-holes and, hence, of the axis of the two-center hole.

D. Reorientation of the axes of oxygen holes in the course of their creation by polarized light

Experimental data corroborate the reorientation mechanism stated in Sec. II(iv). This mechanism involves excited states $\langle j|$ $(j=1,\ldots,6$ formed by partial electron transfer to cation C from any of 6 adjacent O^{2-} ions. The efficiency of this mechanism is characterized by the time ratio

$$u=\tau_{\mathrm{hole}}/\tau_j \tag{3}$$

where τ_j is the transition time between degenerate states $\langle j|$; the time τ_{hole} is required for complete electron transfer to ion C, resulting in the formation of a free oxygen hole. (As shown in Sec. IV B, for $NaCa_2Mn_2V_3O_{12}$ the ion C should be identified with V^{5+}). Let us trace how the variation of the numerator and denominator in (3) affects dichroism.

(i) The reorientation of two-center holes is due to transitions between its excited states caused by the random electric fields of photoproduced charges (in an ideal lattice the degenerate states $\langle j|$ are orthogonal to one another). These fields have a large straggling in magnitude, which is mirrored by the relaxation kinetics after switching off irradiation (Fig. 4): two-center holes formed at the locations of a strong field disappear rapidly and form the initial steep part of the relaxation curve, while its gently sloping part corresponds to holes formed at the locations of a weak field. In the latter csae, the reorientation rate, commensurable with the magnitude of random fields, is significantly lower. Thus, the gently sloping part of the relaxation curve pertains to holes that have undergone weak reorientation at their creation stage. This is mirrored by a slight enhancement of the ratio $\rho=\Delta K_{\perp}(17000)/\Delta K(14300)$ with an increase of time elapsed from the moment the irradiation is switched off (Fig. 6).

TABLE II. Ionization potentials of free ions of garnet constituents.

Garnet	$Ca_3Mn_2Ge_3O_{12}$			$NaCa_2Mn_2V_3O_{12}$			
Cation	Ca^{2+}	Mn^{3+}	Ge^{4+}	Na^{+}	Ca^{2+}	Mn^{2+}	$C=V^{5+}$
Ionization potential (eV)	I_2=11.9	I_3=33.7	I_4=45.7	I_1=5.1	I_2=11.9	I_2=15.6	I_5=65.3

(ii) Figure 5 presents the temperature dependences of photoinduced absorption and dichroism for $NaCa_2Mn_2V_3O_{12}$ (symbols) and $Ca_3Mn_2Ge_3O_{12}$ (lines). As seen from the figure, photoinduced absorption and dichroism vary with temperature in a similar way for $NaCa_2Mn_2V_3O_{12}$ and in a different manner for $Ca_3Mn_2Ge_3O_{12}$. Such a distinction between two garnets can be explained in terms of the ratio (3). An increase in temperature promotes overcoming the energy barrier between the initial excited state $\langle j|$ and the state with a free hole, so that the hole creation time τ_{hole} must decrease with increasing temperature. On the contrary, the time τ_j of the transitions between the degenerate excited states is determined by the random fields which cannot noticeably depend on the temperature. Hence, an increase in temperature entails a decrease of the ratio (3) and a diminution of the reorientation of two-center holes at the stage of their creation, which compensates the temperature acceleration of the recombination of photoproduced charges after their creation. In the case of the garnet $Ca_3Mn_2Ge_3O_{12}$, where the reorientation mechanism acts very efficiently (see Table I), this effect is well pronounced and results in a weakened temperature dependence of dichroism within a rather broad temperature interval $T<T_{\text{dim}}=90$ K (Fig. 5). But for $NaCa_2Mn_2V_3O_{12}$, the reorientation mechanism manifests itself very weakly and cannot cause a noticeable difference between the temperature dependences of dichroism and photoinduced absorption. Thus, the comparison of photoinduced phenomena in $NaCa_2Mn_2V_3O_{12}$ and $Ca_3Mn_2Ge_3O_{12}$ (a different temperature behavior of dichroism explainable only in terms of the initial stage of oxygen hole formation) corroborates the mechanism of the creation and reorientation of two-center holes stated in Sec. II(iv).

(iii) The sharp difference in the dichroism observed in $NaCa_2Mn_2V_3O_{12}$ and $Ca_3Mn_2Ge_3O_{12}$ (see Table I) can also be understood in terms of the relation (3) involving excited states $\langle j|$ with partial electron transfer to the ion C from adjacent O^{2-} ions. The degree of this electron transfer is dictated by the attractive potential of the ion C, which is commensurate with the ionization potential I_C of a separate ion C. On the other hand, the larger the fraction of an electron transferred to the cation C from an adjacent O^{2-} anion in an excited state, the more easily the electron can be completely localized at the ion C, resulting in the generation of a free oxygen hole. Thus, with an increase of I_C the hole formation time τ_{hole} decreases, which leads to a diminution of the oxygen hole reorientation and to a corresponding enhancement of dichroism. For the garnets $Ca_3Mn_2Ge_3O_{12}$ and $NaCa_2Mn_2V_3O_{12}$, Table II presents the nth ionization potential of each n-valence cation taken in a free state. The cation V^{5+}, playing the role of the ion C in $NaCa_2Mn_2V_3O_{12}$, has an ionization potential 65 eV, significantly exceeding the ionization potential of every cation in $Ca_3Mn_2Ge_3O_{12}$. The corresponding difference in the hole formation time τ_{hole} explains the strong difference in dichroism observed in $NaCa_2Mn_2V_3O_{12}$ and $Ca_3Mn_2Ge_3O_{12}$.

[1] R. W. Teale and D. W. Temple, Phys. Rev. Lett. **19**, 904 (1967).
[2] R. F. Pearson, A. D. Annis, and P. Kompfner, Phys. Rev. Lett. **21**, 1805 (1968).
[3] J. F. Dillon, E. M. Gyorgy, and J. P. Remeika, Phys. Rev. Lett. **23**, 643 (1969).
[4] V. F. Kovalenko, E. S. Kolezhuk, and P. S. Kuts, JETP **54**, 742 (1981).
[5] V. V. Eremenko, S. L. Gnatchenko, I. S. Kachur, V. G. Piryatinskaya, A. M. Ratner, and V. V. Shapiro, Phys. Rev. B **61**, 10670 (2000).
[6] V. V. Eremenko, S. L. Gnatchenko, I. S. Kachur, V. G. Piryatinskaya, A. M. Ratner, V. V. Shapiro, M. Fally, and R. A. Rupp, Low Temp. Phys. **27**, 22 (2001).
[7] V. V. Eremenko, S. L. Gnatchenko, I. S. Kachur, V. G. Piryatinskaya, A. M. Ratner, M. B. Kosmyna, B. P. Nazarenko, and V. M. Puzikov, J. Phys.: Condens. Matter **15**, 4025 (2003).
[8] V. V. Eremenko, S. L. Gnatchenko, I. S. Kachur, V. G. Piryatinskaya, A. M. Ratner, M. B. Kosmyna, B. P. Nazarenko, and V. M. Puzikov, Phys. Rev. B **69**, 233102 (2004).
[9] S. L. Gnatchenko, V. V. Eremenko, I. S. Kachur, V. G. Piryatinskaya, V. V. Slavin, V. V. Shapiro, M. B. Kosmyna, B. P. Nazarenko, and V. M. Puzikov, Fiz. Nizk. Temp. **30**, 1302 (2004) [Low Temp. Phys. **30**, 980 (2004)].
[10] V. V. Eremenko, S. L. Gnatchenko, I. S. Kachur, V. G. Piryatinskaya, A. M. Ratner, V. V. Shapiro, M. B. Kosmyna, B. P. Nazarenko, and V. M. Puzikov, Ukr. J. Phys. B **49**, 432 (2004).
[11] A. M. Ratner, Phys. Rep. **269**, 197 (1996).
[12] I. Ya. Fugol', Adv. Phys. **27**, 1 (1978).
[13] G. Oversluizen and R. Metselaar, J. Phys. C: Solid State Phys. **15**, 4869 (1982).
[14] H. B. Dietrich, A. E. Purdy, R. B. Murray, and R. T. Williams, Phys. Rev. B **8**, 5894 (1973).
[15] E. D. Aluker and D. J. Lusis, Phys. Status Solidi A **19**, 759 (1973).
[16] E. D. Aluker, D. Yu. Lusis, and S. A. Chernov, *Electronic Excitations and Radioluminescence of Alkali Halide Crystals* [in Russian], Zinatne, Riga, Latvia (1979).
[17] A. M. Ratner, Phys. Lett. A **298**, 422 (2002).

Translated by M. E. Alferieff

PHYSICAL PROPERTIES OF CRYOCRYSTALS

Isotopic effects in the heat capacity of concentrated orientationally disordered solid solutions of methane and deuteromethane in krypton

M. I. Bagatskiĭ,[a] V. V. Dudkin, D. A. Mashchenko, V. G. Manzheliĭ, and E. V. Manzheliĭ

B. I. Verkin Institute for Low Temperature Physics and Engineering of the National Academy of Sciences of Ukraine, pr. Lenina 47, Kharkov, 61103 Ukraine
(Submitted April 11, 2005; resubmitted June 7, 2005)
Fiz. Nizk. Temp. **31**, 1302–1311 (November 2005)

The heat capacity of orientationally disordered solid solutions $(CH_4)_nKr_{1-n}$ ($n=75$ and 78 mole% CH_4 in the temperature interval $\Delta T=0.8-20$ K) and $(CD_4)_nKr_{1-n}$ ($n=50$, 60, and 70 mole% CD_4, $\Delta T=0.6-30$ K) is investigated. At liquid-helium temperatures the temperature dependences of the molar heat capacities of the rotational subsystems of the solutions are qualitatively and quantitatively very different. One of the main reasons for the effect is that in the concentrated solutions investigated the CD_4 molecules are in a substantially stronger molecular field than the CH_4 molecules. This is because in low-energy states the effective octupole electric moment of CD_4 molecules, which determines the molecular field, is larger than the effective octupole moment of the more quantum molecules CH_4. The weak concentration dependences of the heat capacity of the solutions studied are due to the influence of frustration, which weakens the molecular fields produced at the lattice sites by the surrounding molecules. No evidence of the formation of orientational octupole glasses in the experimental systems was found. © *2005 American Institute of Physics*. [DOI: 10.1063/1.2127892]

INTRODUCTION

The behavior of an ensemble of methane in solid phases at low temperatures is ordinarily strikingly different from that of an ensemble of deuteromethane molecules.[1–4] This is due to the large difference of the moments of inertia of these molecules ($I_{CH_4}/I_{CD_4}=0.51$) and of their total nuclear spins and to the different manifestation of quantum effects in the rotational motion of CH_4 and CD_4 molecules in a crystal lattice. We recall that the total nuclear spins S of the spin-nuclear modifications A, T, and E of the CH_4 and CD_4 molecules are, respectively, $S_{CH_4}=2,1,0$ and $S_{CD_4}=4,2,0$. This means that the isotopic effects in the case studied will be determined, first and foremost, by the rotational motion of the CH_4 and CD_4 molecules.

Isotopic effects have been studied quite completely in two limiting cases: in pure solid methane and deuteromethane[1,2] and in the weak solutions of methane and deuteromethane in solidified inert gases.[3–7] In the latter case the situation is comparatively simple. The methane and deuteromethane molecules behave as weakly hindered rotors, and substantial information can be obtained by comparing their behavior with that of the free molecules.[4,6,7] In solid solutions of methane and deuteromethane with inert elements the properties of concentrated orientationally disordered solutions have been least studied and are most difficult to interpret. As far as we know, the isotopic effects in such solutions have not been studied directly. Even investigations devoted to concentrated orientationally disordered solutions are few in number. It is important to note that isotopic effects appear most clearly only at quite low temperatures. The following have been investigated in $(CH_4)_nKr_{1-n}$ solutions below 20 K: inelastic neutron scattering ($n=73\%$),[8] NMR spectra ($n=60-85\%$),[9,10] the spin-lattice relaxation time T_1 ($n<70\%$),[11,12] and the heat capacity ($n<60\%$).[13,14] X-Ray diffraction studies of $(CD_4)_nKr_{1-n}$ solutions with $n<70\%$ have been performed in Refs. 15–17.

What changes in the isotopic effects can be expected on switching from weak solutions to concentrated orientationally disordered solutions?

In weak solutions of methane and deuteromethane in solidified inert gases isolated impurity molecules are located in the crystal field of the matrix. The deformation introduced into the energy spectrum of free rotors by the crystal field is found to be much greater for CD_4 than CH_4. Thus, in weak solutions of methanes (CH_4,CD_4) in solid Kr the difference between the energies of the ground and first excited states of the molecules compared with the corresponding difference for the free molecules decreases by 23% for CH_4 molecules and 37% for CD_4 molecules.[7] In concentrated solutions a noncentral molecular field due to neighboring methane molecules acts on the methane molecules together with the crystal field.

For CD_4 molecules the molecular field at low temperatures is much stronger than for CH_4 molecules. The reason is that in low-energy states the effective octupole electric moment of CD_4 molecules, which determines the molecular field, is greater than the effective octupole moment of the more quantum CH_4 molecules.[4] Thus, as the methane concentration in the solution increases, greater deformation of the rotational spectrum of CD_4 molecules should be expected than for CH_4 molecules. Correspondingly, it should be expected that the isotopic effects in the properties which depend on the rotational motion of the molecules should increase.

The interest in the low-temperature properties of the solutions indicated above and the manifestation of isotopic effects in these properties is in part due to the possibility of orientational octupolar glasses forming in such systems[16,18] (see also the review in Ref. 19 and the literature cited there).

The present work is devoted to calorimetric investigations of the isotopic effects in the dynamics of the rotational motion of methane molecules in concentrated solid orientationally disordered solutions $(CH_4)_nKr_{1-n}$ ($n=75$ and 78 mole% CH_4, $\Delta T=0.8-20$ K) and $(CD_4)_nKr_{1-n}$ ($n=50$, 60, and 70 mole% CD_4, $\Delta T=0.6-30$ K).

The choice of the property to be studied (the heat capacity) and of the concentration and temperature intervals is based on the following considerations. In the first place the study of the structural and optical properties of disordered systems is ordinarily less informative than the study of the thermal properties, specifically, the heat capacity.[20] In the second place the solutions which have been studied are single-phase.[3] In the third place it is at low temperatures that the isotopic effect in the behavior of the solutions studied should be strongest.

EXPERIMENT

Heat capacity measurements at equilibrium vapor pressure of the above-indicated solid solutions were performed in a vacuum adiabatic calorimeter by the pulsed heating method.[21] In the experimental temperature range ($T<30$ K) the difference between the heat capacities at equilibrium vapor pressure and constant (zero) pressure can be neglected. The calorimetric heating time t_h was 2–6 min. The effective time t_m of one heat-capacity measurement is $t_m=t_h+t_e$, where t_e is the time over which a nearly stationary temperature variation in the calorimeter is established from the moment heating is switched off, varied from 50 to 10 min at temperatures from 0.6 to 30 K, respectively. The composition of the gases used was as follows: CH_4—chemical purity 99.94% (N_2-0.04%; O_2 and Ar$\leqslant$0.01%); CD_4—isotopic purity 99%, chemical purity 99.20% (N_2–0.50%; O_2–0.20%; CO–0.10%; Ar$<$0.01%); Kr—purity 99.79% (Xe-0.2%; N_2–0.01%, O_2 and Ar$<$0.01%). Solid samples were obtained in the calorimeter at $T\approx 80$ K by condensing gaseous mixtures directly into the solid phase. This gave a uniform composition of solutions and a random distribution of solution components. The measurement error of the heat capacity of the solutions was 8% at 0.6 K, 2% at 1 K, 1% at 2 K, and 0.5% above 4 K.

There are grounds for believing that in all cases the heat capacities which we measured refer to equilibrium systems, i.e. systems with an equilibrium distribution of the spin-nuclear modifications of the methanes. In the first place the experimental values of the heat capacity did not depend on the temperature history of the samples. In the second place the relaxation rate of the temperature after heating or cooling of the calorimeter showed that the spin-nuclear conversion in the experimental solutions (just as in the solution of CD_4 in Kr with $n=13\%$ CD_4[22]) is relatively fast. This agrees with the results of Ref. 10, according to which the characteristic conversion times in solutions of CH_4 in Kr with $n=60$ and 71% CH_4, as determined by the NMR method, are 0.03 and 0.047 h, respectively.

The heat capacity component C_{rot} due to the rotational motion of the CH_4 and CD_4 molecules in the solutions was determined by subtracting the translational heat capacity C_{tr} of the lattice from the experimental data on the solution heat capacities C_{sol}. It was assumed that $C_{tr}=C_{tr,CH_4}+\Delta C_{tr,CH_4}$ (or $C_{tr}=C_{tr,CD_4}+\Delta C_{tr,CD_4}$), where $C_{tr,CH_4}(C_{tr,CD_4})$ is the translational heat capacity of pure methane (deuteromethane) and $\Delta C_{tr,CH_4}(\Delta C_{tr,CD_4})$ is the change in the translational heat capacity as a result of introducing into the crystal lattice the heavier substitution impurity krypton. $C_{tr,CH_4}(C_{tr,CD_4})$ was calculated using the method of Jacobian matrices[23] and the characteristic temperatures $0_{CH_4}=140$ K and $0_{CD_4}=135$ K of CH_4 and CD_4 crystals, respectively. $\Delta C_{tr,CH_4}(\Delta C_{tr,CD_4})$ was calculated neglecting the changes in the force constants, using the method of Jacobian matrices[24] for mass ratios $M_{Kr}/M_{CH_4}=5$ and $M_{Kr}/M_{CD_4}=4$.

To separate more accurately the contribution of CH_4 and CD_4 molecules to $C_{sol}(T)$ the relatively small contribution of the rotational motion of the impurity molecules N_2 and O_2 to the solution heat capacity was subtracted out using the results of calorimetric studies of weak solutions of N_2 and O_2 in Kr.[25–27]

The correction C_P-C_V ($C_{rot}=C_{sol}-(C_P-C_V)-C_{tr}$) must also be taken into account at temperatures above 14 K. We could not reliably separate $C_{rot}(T)$ at $T>14$ K because the complete experimental data, needed for this, on the thermal expansion coefficients, compressibility, and molar volumes of our experimental solutions do not exist.

MEASUREMENT RESULTS. DISCUSSION

The experimental values of the heat capacity C_{sol} of solid concentrated orientationally disordered solutions $(CH_4)_nKr_{1-n}$ ($n=75$ and 78 mole% CH_4) and $(CD_4)_nKr_{1-n}$ ($n=50$, 60, and 70 mole% CD_4) at equilibrium vapor pressure are presented in Table I and Fig. 1. Figure 1 also shows the values given previously for the heat capacity of the solution $(CH_4)_nKr_{1-n}$ with $n=60\%$.[14]

According to Fig. 1, substantial changes of the temperature derivatives of $C_{sol}(T)$ are observed in the temperature range 18–21 K. These features are not due to the behavior of the translation subsystem (whose Debye temperature is of the order of 100 K) or solution decomposition processes. Krypton and deuteromethane at concentrations $n\leqslant 70\%$ form a continuous series of solid solutions.[15] Anomalous behavior of the lattice parameter and thermal expansion coefficients of orientationally disordered solid solutions CD_4–Kr was previously found in the concentration range $n<70\%$ at temperatures $T<20$ K.[15–17] The authors of Ref. 16 conjectured that these anomalies are due to the freezing of the short-range orientational order and formation of an orientational octupolar glass. We also believe that the features which we observed in $C_{sol}(T)$ in the temperature range 18–21 K are due to freezing of the short-range orientational order. The character of the rotational motion of a large fraction of the molecules changes from hindered rotation to localized orientational oscillations (librations). In Ref. 22 it was established experimentally that in solutions of CD_4 in Kr freezing of the short-range orientational order occurs in clusters with $k=3$ or more nearest-neighbor molecules.

TABLE I. Experimental values of the heat capacity C_{sol} of the solid solutions Kr-nCH$_4$ and Kr-nCD$_4$ at equilibrium vapor pressure.

T, K	C_{sol} J/(mole·K)	T, K	C_{sol}, J/(mole·K)	T, K	C_{sol}, J/(mole·K)	T, K	C_{sol}, J/(mole·K)
			Kr–74.7 % CH$_4$				
0.90914	0.2635	1.7437	2.357	2.8063	4.647	12.150	11.36
0.97826	0.3735	1.8318	2.708	2.9751	4.670	12.972	12.31
1.0251	0.5246	1.8543	2.808	3.3484	4.740	14.017	13.12
1.0841	0.6313	1.9669	3.098	3.9552	4.720	15.095	13.72
1.1478	0.7015	2.0538	2.920	4.4157	4.692	15.635	14.25
1.2153	0.9232	2.1276	3.347	5.0155	4.790	16.313	14.34
1.3021	1.164	2.1421	3.540	6.3339	5.264	17.046	14.67
1.4148	1.417	2.2177	2.941	6.9457	5.680	17.556	15.01
1.5112	1.611	2.2543	3.631	7.5581	6.232	18.746	15.89
1.5799	2.052	2.3394	4.010	8.2033	6.797	18.812	15.84
1.6116	1.862	2.3793	3.939	8.8788	7.491		
1.6221	2.353	2.5473	4.307	9.8652	8.593		
1.7090	2.412	2.5659	4.613	11.078	10.10		
1.7101	2.262	2.7350	4.442	11.685	10.84		
			Kr–78.8 % CH$_4$				
1.0403	0.5964	2.0263	3.246	5.7828	4.837	13.021	12.61
1.1189	0.6737	2.2096	3.824	6.6762	5.286	13.870	13.48
1.2350	0.9888	2.4110	4.071	7.5622	5.978	14.719	14.05
1.3570	1.286	2.6323	4.366	8.3955	6.750	16.213	14.62
1.4312	1.610	2.8635	4.318	9.3148	7.774	17.218	14.97
1.5050	1.851	3.1648	4.688	9.9678	8.593	18.344	15.60
1.5761	1.968	3.3861	4.321	9.9858	8.596		
1.6619	2.286	3.7836	4.541	10.388	9.119		
1.7730	2.490	4.3424	4.550	10.784	9.681		
1.8452	2.715	5.0476	4.639	11.489	10.62		
			Kr–50.3 % CD$_4$				
0.63665	0.8323	2.8879	0.5720	10.129	8.981	18.172	19.39
0.67259	0.7931	3.1765	0.6848	10.933	10.26	18.924	19.96
0.72131	0.7613	3.5193	0.8201	11.731	11.53	19.781	19.84
0.78006	0.8127	3.9152	1.035	12.543	12.87	20.371	20.16
0.94130	0.6885	4.3390	1.328	12.553	12.80	20.979	20.26
1.0429	0.6398	4.9129	1.837	13.026	13.53	21.533	20.31
1.1637	0.5723	5.4443	2.354	13.513	14.21	22.087	20.61
1.4015	0.5098	5.9711	2.889	14.023	14.87	22.701	20.92
1.5209	0.4799	6.5289	3.602	14.504	15.67	23.361	21.14
1.7143	0.4435	6.9789	4.127	15.010	16.04	24.012	21.36
1.9711	0.4248	7.1514	4.384	15.558	16.47	24.770	21.88
2.2225	0.4307	7.8207	5.368	16.205	17.30	25.697	21.89
2.4410	0.4690	8.6768	6.711	16.865	18.13	26.703	22.37
2.6616	0.5076	9.4012	7.708	17.494	18.65	27.758	22.88

Moreover, it is evident from Fig. 1 that at liquid-helium temperatures a very strong difference is observed in the temperature dependences and absolute values of the heat capacities of the systems $(CH_4)_nKr_{1-n}$ and $(CD_4)_nKr_{1-n}$.

As already mentioned above, isotopic effects should be sharpest in the rotational motion of methane molecules. Such effects should be sought in the heat capacity at temperatures which are low enough so that the values of C_{rot} would be substantially different from the classical values for free rotors. It is evident (see below, for example, Fig. 2) that we are talking about temperatures below 10 K. Fortunately, it is precisely at these temperatures that the rotational subsystem

T, K	C_{sol} J/(mole·K)	T, K	C_{sol}, J/(mole·K)	T, K	C_{sol}, J/(mole·K)	T, K	C_{sol}, J/(mole·K)
			Kr–60.1 % CD_4				
0.68560	0.7910	2.8273	0.5330	12.193	12.25	19.488	21.62
0.71522	0.7578	3.0716	0.6057	12.705	13.19	19.946	21.75
0.78850	0.7654	3.3045	0.6969	13.206	13.95	20.090	21.88
0.85937	0.7290	3.3643	0.7147	13.857	15.02	20.317	21.73
0.92187	0.7283	3.6504	0.8536	14.341	15.70	20.726	21.98
1.0053	0.6757	3.9722	1.031	14.544	16.05	20.818	21.92
1.1075	0.6208	4.2731	1.212	15.156	16.92	21.208	22.04
1.2268	0.5580	4.5790	1.464	15.436	17.24	21.449	22.22
1.2583	0.5328	5.4351	2.215	15.787	17.80	21.764	22.17
1.3597	0.5196	5.8504	2.623	16.443	18.62	22.006	22.16
1.3785	0.4906	6.2938	3.117	17.114	19.40	22.551	22.37
1.5092	0.4748	6.7505	3.670	17.365	19.72	23.075	22.34
1.6514	0.4410	7.2249	4.325	17.757	20.00	23.585	22.38
1.8018	0.4242	7.8693	5.254	18.062	20.50	24.084	22.61
2.0046	0.4128	8.4912	6.180	18.337	20.79	24.669	22.85
2.2114	0.4125	9.3288	7.502	18.739	21.08	27.362	23.66
2.4138	0.4443	10.318	9.174	18.921	20.98	28.406	24.30
2.6136	0.4813	11.250	10.73	19.402	21.41	29.384	24.45
			Kr–70.2 % CD_4				
0.61681	1.061	3.2453	0.6354	16.294	19.57	21.850	24.21
0.62042	0.9090	3.6160	0.7832	17.172	20.94	22.163	24.33
0.66269	0.9145	3.9988	0.9763	17.341	21.10	22.177	24.25
0.66756	0.8299	4.3303	1.182	17.869	22.07	22.473	24.41
0.70735	0.9594	4.7364	1.484	18.412	22.55	22.539	24.79
0.73729	0.8266	5.2890	1.953	18.538	23.00	22.835	24.61
0.80603	0.8101	5.8598	2.488	19.211	23.38	22.942	24.29
0.88167	0.7440	6.5894	3.287	19.212	23.50	23.283	24.60
0.97338	0.6954	7.4224	4.374	19.719	23.85	23.386	24.27
1.0868	0.7035	8.1486	5.405	19.734	23.80	24.206	24.65
1.2047	0.5930	8.9465	6.652	20.121	23.89	24.630	24.73
1.3362	0.5484	9.7179	7.863	20.206	24.15	25.046	24.74
1.4870	0.4918	10.479	9.222	20.522	24.09	25.447	25.04
1.6459	0.4618	11.240	10.61	20.620	24.45	25.852	24.95
1.8069	0.4207	11.994	11.98	21.024	24.45	26.253	24.81
1.9659	0.4272	12.662	13.23	21.378	24.38	26.971	25.17
2.3497	0.4267	13.428	14.69	21.416	24.50	28.110	25.52
2.6420	0.4740	14.277	16.19	21.771	24.39		
2.9361	0.5390	15.261	17.89	21.806	24.51		

makes the dominant contribution to the heat capacity $C_{sol}(T)$ of the experimental solid solutions of CH_4 and CD_4 in Kr. Thus, for a solution consisting of 60% CH_4 in Kr the contribution of $C_{rot}(T)$ to C_{sol} is 99% at $T=1$ K, 98% at $T=3$ K, 70% at $T=7$ K, and 55% at $T=10$ K. For a solution consisting of 60% CD_4 in Kr the contribution of $C_{rot}(T)$ to C_{sol} is 98% at $T=1$ K, 85% at $T=3$ K, 63% at $T=7$ K, and 60% at $T=10$ K.

On this basis, in what follows, to analyze the observed isotopic effect we shall concentrate on the low-temperature ($T<10$ K) contribution of the rotational motion of CH_4 and CD_4 molecules to the heat capacity.

Figure 2 shows the experimental data on the heat capacity $C_R=C_{rot}/(nR)$ of the rotational subsystem, normalized to concentration n of rotors and the universal gas constant R. The curves *1* and *3* are the values of C_R calculated for free CH_4[28] and CD_4[29] molecules, respectively, taking account of the energy levels up to values of the rotational quantum number $J=14$, inclusively. The values of the rotational heat capacity C_R calculated from the energy spectra of CH_4[30] and

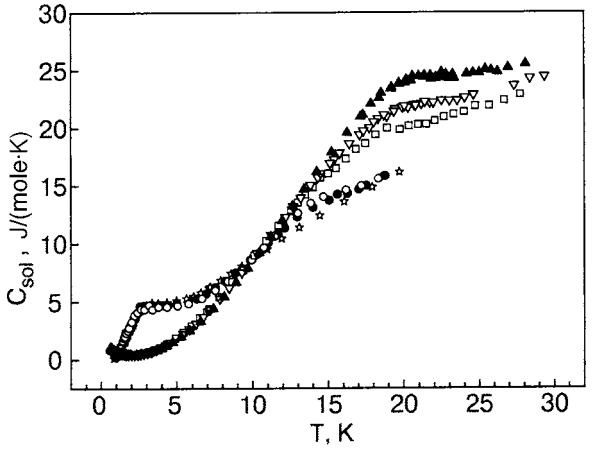

FIG. 1. Temperature dependence of the heat capacity pressure C_{sol} of the solid solutions $(CH_4)_nKr_{1-n}$ (n=60 (☆),[14] 75 (●), and 78 (○) mole%) and $(CD_4)_nKr_{1-n}$ (n=50 (□), 60 (▽), and 70 (▲) mole%) at equilibrium vapor.

CD_4[31] in the crystal field of krypton are shown in Fig. 2, curves 2 and 4, respectively. Since the energy spectrum of CD_4 rotors which is presented in Ref. 31 contains only levels with J=1 and 2 and, partially, J=3 and 4, the comparison of the experimental heat capacities C_R with the computed values is correct only for temperatures $T<2.2$ K.

According to Fig. 2, $C_R(T)$ of solutions of CH_4 and CD_4 in Kr are qualitatively and quantitatively very different. The heat capacity $C_R(T,n)$ is determined by the rotational spectrum of the molecules, which depends on the symmetry and magnitude of the potential (crystal and molecular) field at the lattice sites occupied by the molecules. The magnitude of the molecular field depends on the number k of nearest-neighbor molecules in the solution, their configuration, and the amplitude of the orientational oscillations. As shown in Refs. 4 and 7, the low-energy part of the spectra of the isolated molecules (k=0) is essentially identical to that of the molecules in isolated pair clusters (k=1). The spectra of molecules with

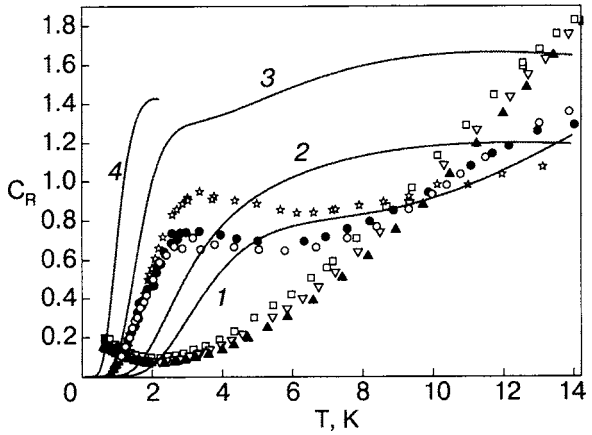

FIG. 2. Temperature dependence of the rotational heat capacity $C_R = C_{rot}/(nR)$ normalized to the molar concentration n of CH_4 and CD_4 molecules and the universal gas constant R: solid solutions $(CH_4)_nKr_{1-n}$ with n=60 (☆),[14] 75 (●), and 78 (○) mole% CH_4; solid solution $(CD_4)_nKr_{1-n}$ with n=50 (□), 60 (▽), and 70 (▲) mole% CD_4. The curves 1 and 3 were calculated according to spectra for free CH_4 rotors[28] and CD_4 rotors[29] taking account of the energy levels up to rotational quantum number J=14, inclusively; the curves 2 and 4 were calculated according to the spectra for the matrix-isolated CH_4 rotors[30] and CD_4 rotors[31] in Kr, respectively.

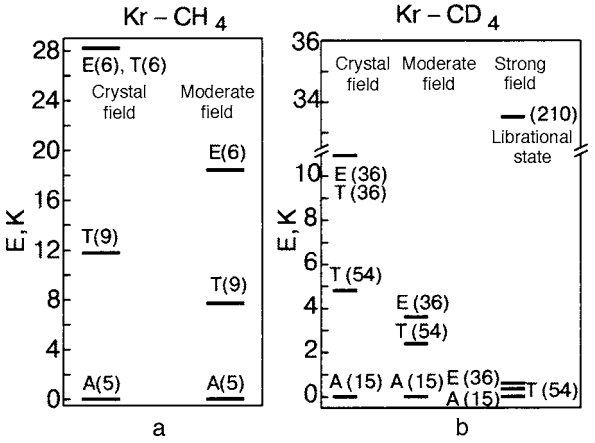

FIG. 3. Schematic representation of the low-energy part of the spectrum: a) matrix-isolated CH_4 rotors in Kr[30] and CH_4 rotors in a moderate effective (H rotors) field and b) matrix-isolated CD_4 rotors in Kr[31] and CD_4 rotors in a moderate effective (H rotors) and strong effective (SH rotors) fields. The spin-nuclear modifications A, T, and E and the degeneracy of the levels (in parentheses) are indicated. The positions of the levels of the spectrum were determined from an analysis of $C_R(T)$ for the solid solutions Kr—78% CH_4 (a) and Kr—70% CD_4 (b).

two or more neighboring isolated molecules differ substantially.[22] This means that an increase in the number of nearest-neighbor molecules from one to two or more results in a substantial increase of the potential field. However, for high concentrations n the noncentral forces exerted on a molecule by the molecules surrounding it (as a result of frustration) can completely or partially compensate one another.[1,4] The role of this effect for $n \geqslant 50\%$ increases with the concentration n of the molecules. As the molecular field increases, the low-energy part of the spectrum of a molecule in a crystal changes as follows: the lowest levels of the spin-nuclear modifications move downwards and approach one another, and in high fields they form a group of tunneling levels separated from the next group of levels by a substantial gap.[32–34] As the noncentral field increases, the character of the rotational motion of the molecule changes from weakly hindered to hindered and then to strongly hindered (orientational oscillations—librations).

In the system $(CH_4)_nKr_{1-n}$ the temperature dependences of the heat capacity $C_R(T)$ of matrix-isolated rotors CH_4 (curve 2) and CH_4 rotors in solutions with n=60,[14] 75, and 78% CH_4 are qualitatively similar (see Fig. 2). The experimental values of $C_R(T)$ in solutions at temperatures below 3 K are shifted to low temperatures relative to the curve 2 calculated for matrix-isolated rotors. This means that in the experimental solutions many molecules are in moderate potential fields and for them the gap E_{AT} between the nearest levels of the A and T modifications is smaller than for the matrix-isolated molecules CH_4 (see Fig. 3). The weak peak in $C_R(T)$ near 3 K indicates that on the average over all rotors the group of lowest energy levels of the A, T, and E modifications is separated by a relatively wide gap from all other levels.[32] This shows that the correlations between the more strongly hindered rotational motion of CH_4 rotors become stronger in solutions.

As one can see from Fig. 2, in the system $(CD_4)_nKr_{1-n}$ the behavior of the heat capacity $C_R(T)$ of matrix-isolated rotors (curve 4) is quantitatively and qualitatively very dif-

TABLE II. Effective gaps E_{AT} between the lowest energy levels of the A and T spin-nuclear modifications of CH_4 molecules in the solid solutions $(CH_4)_nKr_{1-n}$.

n, %	E_{AT}, K(H-rotors)
60	7.4±0.5 [14]
75	7.7±0.5
78	7.7±0.5

ferent from that of the rotors in solutions with $n=50$, 60, and 70% CD_4. At $T<2$ K the heat capacities $C_R(T)$ of the solutions increase with decreasing temperature. This indicates the existence, below 0.5 K, of peaks in $C_R(T)$ for solutions which are similar to the peaks in $C_R(T)$ for orientationally ordered sublattices in pure CH_4 and CD_4.[1] The existence of these peaks in $C_R(T)$ indicates that in concentrated solutions some rotors possess closely spaced tunneling levels A, T, and E, separated by a large energy gap E_L from the other (librational) levels. These rotors undergo localized orientational oscillations near randomly distributed equilibrium orientations, which are determined by the local configurations of the molecules. At $T<1.5$ K excitations of the tunneling levels determine the heat capacity $C_R(T)$, and at $T>3$ K the excitations of the librational levels determine $C_R(T)$. The experimental values of $C_R(T)$ determined by the librational excitations are strongly shifted to high temperatures relative to the values of $C_R(T)$ (curve 4) calculated for matrix-isolated rotors. It follows from this fact that the gap E_L is much greater than the splitting between the lowest levels of the A and T modifications of matrix-isolated rotors ($E_{AT}=4.8$ K[7]).

To give a quantitative description of $C_R(T,n)$ we shall confine our attention to the temperature range where the heat capacity $C_R(T,n)$ of the rotors is primarily due to excitations of several of the lowest energy levels of the spectrum of the rotors (see Fig. 3).

The heat capacity $C_R(T)$ of the system $(CH_4)_nKr_{1-n}$ at temperatures below 3 K is determined by the position of the first excited level (the lowest level of the T modification) of the rotational spectrum of methane molecules (see Fig. 3a). The weak dependence of $C_R(T)$ on the concentration n of CH_4 molecules in the concentration range 60–80% shows that as a result of the tetrahedral symmetry of the molecules and frustration the noncentral fields at the lattice sites are close for most molecules. Consequently, at temperatures far below the second excited rotational level (see Fig. 3a) there is hope of describing $C_R(T)$ as the heat capacity of a two-level system with an effective gap $\Delta E=E_{AT}$. We note that the NMR temperature dependences of the proton magnetic susceptibilities in the solid solutions $(CH_4)_nKr_{1-n}$ with $n=60-89\%$ CH_4 was described theoretically in Ref. 10 using one value of the effective gap $E_{AT}=5.8$ K. Table II gives the values of the effective gaps E_{AT} for solutions with 75 and 78% CH_4 in Kr, which we obtained from an analysis of $C_R(T,n)$, and the published data[14] for a solution with 60% CH_4. In Fig. 4 the experimental temperature dependences $C_R(T)$ in the temperature 0.8–3 K are compared with the temperature dependences calculated using the values of E_{AT} given in Table II. The values of E_{AT} for solutions with $n=60-78\%$ CH_4 in Kr agree within the limits of error.

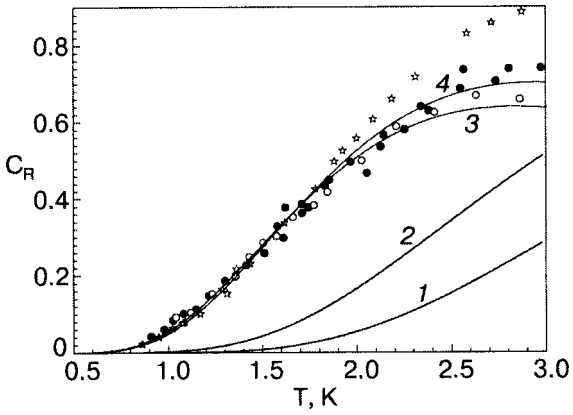

FIG. 4. Normalized rotational heat capacity $C_R=C_{rot}/(nR)$ of solid solutions $(CH_4)_nKr_{1-n}$ with $n=60$ (☆),[14] 75 (●), and 78 (○)% CH_4. The curves 1 and 2 were calculated, respectively, using the spectra for free CH_4 molecules[28] and matrix-isolated CH_4 molecules in Kr.[30] The curves 3 ($n=75$ and 78%) and 4 ($n=60\%$[14]) were calculated using a two-level model and the values of E_{AT} indicated in Table II.

An attempt to describe the heat capacity $C_R(T)$ of the solutions $(CD_4)_nKr_{1-n}$ assuming that for constant concentration n all CD_4 molecules are in the same effective noncentral field was unsuccessful. At the same time, using a simple model we were able to describe $C_R(T)$ in a quite wide temperature range (0.6–8 K). According to this model there are two groups of rotors: SH rotors, which are in a strong effective noncentral field, and H rotors, which are in a moderate effective noncentral field.[7] Qualitatively, the choice of this model is obvious. As already mentioned above, the character of the temperature dependence of C_R of the solutions $(CD_4)_nKr_{1-n}$ shows that the energy spectrum of the overwhelming majority of CD_4 molecules consists of groups of low-lying (tunneling) levels separated by a wide gap from the rest of the spectrum. Such a spectrum is characteristic for methane molecules in a strong molecular field.[1] This field can arise as a result of the effect of a large number of molecules located in the nearest-neighbor environment of the molecule being studied. It is precisely this situation that occurs for most CD_4 molecules in the concentrated solutions studied. At the same time comparatively few molecules in concentrated solutions have only a few nearest-neighbor molecules and the lowest levels in low-energy part of their spectrum are not separated by a wide gap from the rest of the spectrum. The temperature dependence of the contribution of such molecules to the heat capacity $C_R(T)$ should be reminiscent of $C_R(T)$ for nonconcentrated solutions of methanes in krypton. The arguments presented above are very general. Somewhat unexpectedly it was found that the experimental values of C_R could be described (see below) as the sum of two contributions, mentioned above, each of which is determined by a single effective energy spectrum.

Therefore we shall represent the normalized heat capacity of the rotational subsystem of the experimental solutions $(CD_4)_nKr_{1-n}$ at temperatures below 8 K in the form

$$C_R(T)=x_{SH}C_R(T)_{SH}+x_HC_R(T)_H, \tag{1}$$

where $C_R(T)_{SH}$ and $C_R(T)_H$ are the normalized rotational heat capacities due to strongly hindered and hindered rotors, re-

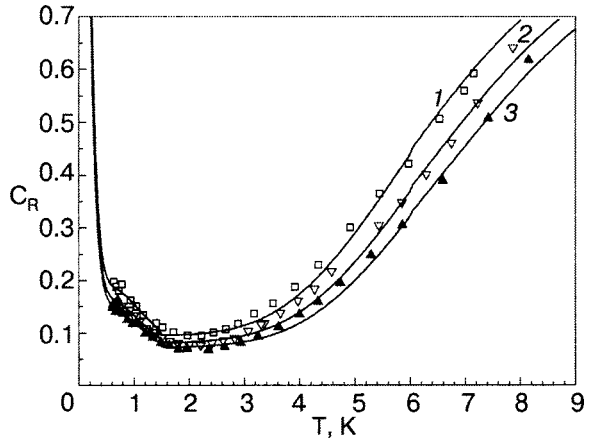

FIG. 5. Temperature dependence of the normalized rotational heat capacity $C_R = C_{\rm rot}/(nR)$ of solid solutions $(CD_4)_nKr_{1-n}$ with $n=50$ (□), 60 (▽), and 70 (▲)% CD_4. The curves 1, 2, and 3 were calculated using the parameters indicated in Table III for SH and H rotors.

spectively, and x_{SH} and x_H are the relative concentrations of SH and H rotors.

The good agreement between the experimental and computed values of $C_R(T)$, as shown in Fig. 5, was achieved under the following conditions. The first (dominant) term in the expression (1) was calculated using the spectrum presented in Fig. 3b and the parameters from Table III. The second term of the expression (1) was calculated at temperatures $T \leqslant 1.5$ K taking account of the values of E_{AT} and E_{AE} presented in Table III and assuming that C_R in the range 1.5–8 K varies linearly with temperature from 0.9 to the classical value 1.5.

The main qualitative results of the present work can be reduced to the following. A radical difference was found experimentally in the absolute values and temperature dependences of the low-temperature heat capacities C_R of the rotational subsystems in concentrated orientationally disordered solutions of methane and deuteromethane in solid krypton. Even though these solutions have the same crystal structure the observed isotopic effect cannot be explained solely by a uniform deformation of the energy spectrum because of the differences in the moments of inertia and the total nuclear spins of CH_4 and CD_4 molecules. The effect is mainly a solid-state effect and is due to the fact that for equal concentrations of CH_4 and CD_4 molecules in solutions the CD_4 molecules are in a much stronger molecular field than the CH_4 molecules. The point is that in the low-energy states the effective octupole electric moment of CD_4 molecules, which determines the molecular field, is greater than the effective octupole moment of the more quantum CH_4 molecules.

In $(CH_4)_nKr_{1-n}$ solutions the CH_4 molecules are in moderate effective molecular fields, and the correlated hindered rotational motion of virtually all molecules can be described using a single effective energy spectrum.

In $(CD_4)_nKr_{1-n}$ solutions the overwhelming majority of the CD_4 molecules are in strong molecular fields. Their effective energy spectrum is qualitatively reminiscent of the rotational spectrum of molecules in solid deuteromethane, which at low temperatures form an orientationally ordered lattice and undergo orientational oscillations. The remaining molecules (located, specifically, at the edges of clusters) are in moderate molecular fields, and their effective energy spectrum is qualitatively reminiscent of the spectrum of CH_4 molecules in $(CH_4)_nKr_{1-n}$ solutions.

The weak concentration dependences $C_R(T,n)$ in the experimental solutions are due to frustration, which weakens the molecular fields produced at the lattice sites by the surrounding molecules.

No evidence of the formation of orientational octupolar glasses in the systems investigated was found, i.e. a linear temperature dependence $C_R(T)$, characteristic of glasses of different nature,[19,35,36] was not found at the lowest temperature studied in the experiment. This result agrees with the results of investigations of $(CH_4)_nKr_{1-n}$ solutions by inelastic neutron scattering $(n=73\%)$[8] and NMR $(n=60-89\%)$.[13]

We thank Yu. A. Freĭman for helpful remarks concerning the text of this article. This work was supported by the Ministry of Education and Science of Ukraine (project "New quantum and anharmonic effects in solutions of cryocrystals," No. 02.07/00391-2004).

TABLE III. Parameters determining $C_R(T,n)$ in solid solutions $(CD_4)_nKr_{1-n}$ at $T<8$ K.

n, %	H-rotors			SH-rotors			
	x_H, %	E_{AT}, K	E_{AE}, K	x_{SH}, %	E_{AT}, K	E_{AE}, K	E_L, K
50	10	2.4	3.6	90	0.36	0.54	30
60	8.5	2.4	3.6	91.5	0.34	0.51	32
70	7.5	2.4	3.6	92.5	0.33	0.49	33.5

Notation: E_{AT} and E_{AE} are the effective gaps between the lowest energy levels of A, T and A, E spin-nuclear modifications, respectively, of CD_4 molecules; E_L is the effective energy of the first excited librational level; n is the concentration of CD_4; x_{SH} and x_H are the relative concentrations of SH and H rotors, respectively.

[a]E-mail: bagatskii@ilt.kharkov.ua

[1]V. G. Manzhelii, A. I. Prokhvatilov, V. G. Gavrilko, and A. P. Isakina, *Handbook and Structure and Thermodynamic Properties of Cryocrystals*, Begell House Inc., New York (1998).
[2]N. G. Parsonage and L. A. K. Staveley, *Disorder in Crystals*, Clarendon Press, Oxford (1978).
[3]V. G. Manzhelii, A. I. Prokhvatilov, I. Ya. Minchina, and L. D. Yantsevich, *Handbook of Binary Solutions of Cryocrystals*, Begell House Inc., New York (1996).
[4]W. Press, *Single-Particle Rotations in Molecular Crystals*, Vol. 92, Springer Tracts in Modern Physics, Springer-Verlag, New York (1981).
[5]R. Rohmer and A. Loidl, Z. Phys.: Condens. Matter **80**, 139 (1990).
[6]B. Asmussen, D. Balszunat, W. Press, M. Prager, C. J. Carlile, and H. Buttner, Physica B **202**, 224 (1994).
[7]M. I. Bagatskiĭ, V. G. Manzheliĭ, D. A. Mashchenko, and V. V. Dudkin, Fiz. Nizk. Temp. **29**, 1352 (2003) [Low Temp. Phys. **29**, 1028 (2003)].
[8]S. Grondey, M. Prager, W. Press, and A. Heidemann, J. Chem. Phys. **85**, 2204 (1986).
[9]P. Calvani and H. Glattli, Solid State Commun. **50**, 169 (1984).
[10]P. Calvani and H. Glattli, J. Chem. Phys. **83**, 1822 (1985).
[11]P. Calvani, C. Casierei, F. De Luca, and B. Maraviglia, Phys. Lett. A **86**, 490 (1981).
[12]P. Clavani, F. De Luca, and B. Maraviglia, Phys. Lett. A **96**, 212 (1983).
[13]I. Ya. Minchina, V. G. Manzhelii, M. I. Bagatskii, O. V. Sklyar, D. A. Mashchenko, and M. A. Pokhodenko, Fiz. Nizk. Temp. **27**, 773 (2001) [Low Temp. Phys. **27**, 568 (2001)].
[14]M. I. Bagatskii, V. G. Manzhelii, I. Ya. Minchina, D. A. Mashchenko, and

I. A. Gospodarev, J. Low Temp. Phys. **127**, 459 (2003).
[15]A. I. Prokhvatilov and A. P. Isakina, Fiz. Nizk. Temp. **11**, 1074 (1985) [Sov. J. Low Temp. Phys. **11**, 592 (1985)].
[16]A. P. Isakina, V. B. Kokshenev, and A. I. Prokhvatilov, Fiz. Nizk. Temp. **13**, 312 (1987) [Sov. J. Low Temp. Phys. **13**, 178 (1987)].
[17]A. P. Isakina, Fiz. Nizk. Temp. **19**, 1250 (1993) [Low Temp. Phys. **19**, 889 (1993)].
[18]F. De Luca and B. Maraviglia, Chem. Phys. Lett. **101**, 300 (1983).
[19]U. T. Hochli, K. Knorr, and A. Loidl, Adv. Phys. **39**, 405 (1990).
[20]Takasuke Matsuo, Pure Appl. Chem. **70**, 599 (1998).
[21]M. I. Bagatskiĭ, I. Ya. Minchina, and V. G. Manzheliĭ, Fiz. Nizk. Temp. **10**, 1039 (1984) [Sov. J. Low Temp. Phys. **10**, 542 (1984)].
[22]M. I. Bagatskiĭ, V. V. Dudkin, V. G. Manzheliĭ, D. A. Mashchenko, and S. B. Feodos'ev (in press).
[23]V. I. Pereseda, Zh. Eksp. Teor. Fiz. **53**, 605 (1967) [JETP **26**, 389 (1968)].
[24]V. I. Pereseda and V. P. Tolstoluzhskii, Fiz. Nizk. Temp. **3**, 788 (1977) [Sov. J. Low Temp. Phys. **3**, 783 (1977)].
[25]M. I. Bagatskiĭ, V. G. Manzheliĭ, M. A. Ivanov, P. I. Muromtsev, and I. Ya. Minchina, Fiz. Nizk. Temp. **18**, 1142 (1992) [Sov. J. Low Temp. Phys. **18**, 801 (1992)].
[26]P. I. Muromtsev, M. I. Bagatskiĭ, V. G. Manzheliĭ, and I. Ya. Minchina, Fiz. Nizk. Temp. **20**, 247 (1994) [Low Temp. Phys. **20**, 195 (1994)].
[27]M. I. Bagatskiĭ, *Doctoral Dissertation in Physical and Mathematical Sciences*, Kharkov (2000).
[28]G. Herzberg, *Infrared and Raman Spectra of Polyatomic Molecules*, New York (1945), p. 647.
[29]E. B. Wilson, J. Chem. Phys. **3**, 276 (1935).
[30]K. Nishiyama and T. Yamamoto, J. Chem. Phys. **58**, 1001 (1973).
[31]K. Nishiyama, J. Chem. Phys. **56**, 5096 (1972).
[32]T. Yamamoto, Y. Kataoka, and K. Okada, J. Chem. Phys. **66**, 2701 (1977).
[33]A. Hüller and J. Raich, J. Chem. Phys. **71**, 3851 (1979).
[34]A. Hüller and W. Press, Phys. Rev. B **24**, 17 (1981).
[35]V. G. Manzhelii, M. I. Bagatskii, I Ya. Minchina, and A. N. Aleksandrovskii, J. Low Temp. Phys. **111**, 257 (1998).
[36]U. T. Hochli, K. Knorr, and A. Loidl, Adv. Phys. **51**, 589 (2002).

Translated by M. E. Alferieff

TECHNIQUE OF SUPERLOW TEMPERATURES

Crystallization thermometer for ultralow temperatures with a cooled FET oscillator

V. A. Maĭdanov,[a] M. I. Mil'chenko, N. P. Mikhin, A. S. Neoneta, A. V. Polev, V. N. Repin, S. P. Rubets, A. S. Rybalko, S. F. Semenov, E. V. Syrnikov, V. A. Shilin, and E. O. Vekhov

B. I. Verkin Institute for Low Temperature Physics and Engineering of the National Academy of Sciences of Ukraine, pr. Lenina 47, Kharkov 61103, Ukraine
(Submitted April 26, 2005)
Fiz. Nizk. Temp. **31**, 1312–1316 (November 2005)

The existing methods of measuring pressure in a crystallization thermometer used for measuring ultralow temperatures are analyzed. It is shown that a method based on measuring the resonance frequency of a resonance circuit, which includes a capacitive pressure gauge, can be used to increase measurement sensitivity and accuracy. A low-temperature FET oscillator is described. This oscillator makes it possible to increase the sensitivity and accuracy of temperature measurements in the range 0.9 mK–1 K by more than an order of magnitude. © *2005 American Institute of Physics*. [DOI: 10.1063/1.2127893]

I. INTRODUCTION

Thermometry based on the temperature dependence of the melting pressure of ^{3}He has become in the last few years the most widely used method in physical studies in the millikelvin temperature range. The relation between the pressure and temperature of melting of pure ^{3}He is universal and has now been standardized to a high degree of accuracy. Since 2000, the new international temperature scale according to the melting curve of ^{3}He—PLTS-2000, which covers the temperature range from 0.9 mK to 1 K, has been recommended for laboratory practice.[1]

In crystallization thermometers where the working substance is a mixture of liquid and solid ^{3}He on the melting curve the measurement of temperature reduces to a corresponding measurement of pressure. The impossibility of measuring pressure directly *in situ* at low and ultralow temperatures has initiated the development of various transducers of the pressure in the experimental samples. The Straty-Adams membrane-type capacitive pressure gauge is currently widely used in low-temperature physics.[2,3]

The simplest method is a method of measuring directly the capacitance of a strain gauge of a crystallization thermometer using commercial automatic digital ac current bridges of the type E8-4, E7-8, and E7-12. As a rule, capacitive pressure gauges have a nominal capacitance $C = 30–40$ pF in the working tempreature range. The resolution of all the digital capacitance meters listed above is ~ 0.01 pF, i.e., $\Delta C/C \sim 10^{-4}–10^{-5}$. For the ordinary sensitivity of a capacitive pressure gauge ~ 1 pF/atm the temperature resolution in this case is about 0.4–0.5 mK (at 100 mK), which does not always satisfy the requirements for measuring temperature in experimental practice. In addition, the measuring voltage of such bridges (30–40 V and higher) causes the thermometer to overheat because of electromagnetic losses in the gauges, especially at temperatures of the order of several millikelvin.

The modern digital automatic bridges, fabricated abroad, for measuring capacitance have a high resolution $\Delta C/C \sim 10^{-6}–10^{-8}$ at low measurement voltage $\sim 0.1–1.5$ V (for example, the bridges manufactured by the Andeen-Hangerling Company). But they are expensive. This is why an alternative method of measuring the capacitance of pressure gauges is being developed—a resonance method in which the capacitive pressure gauge is an integral part of a LC circuit. A pressure change in this case changes the resonance frequency of the circuit,[4–7] which can be measured with a frequency meter to a high degree of accuracy. A modern frequency meter is one of the most accurate of all digital meters, gives measurements to eight significant figures, and makes it possible to reach a relative frequency resolution higher than $\sim 10^{-7}$.

The objective of the present work is to develop and realize a high-precision resonance method for measuring the capacitance of the pressure gauge of a crystallization thermometer in order to increase the accuracy of temperature measurements in the millikelvin range.

II. REQUIREMENTS FOR THE MEASURING SCHEME

The measuring scheme implementing the resonance method includes a parallel resonance LC circuit and an active part—a tunnel diode or transistor. While the measuring resonance LC circuit is always near the measuring cell, the active element can be located either at low temperatures right next to the circuit or held at room temperature. The advantages of the latter variant are obvious: any active and passive circuit elements can be used and the circuit is easily accessible during tuning and repair. However, the long line coupling the "warm" active part and the resonance circuit in the presence of the "microphone" effect and the dependence of the parasitic capacitance of the coupling line on the helium level in the Dewar become serious problems at relative frequency resolution better than 10^{-6}. The obvious solution is to decrease the coupling coefficient between the LC circuit and the active part, as a result of which the introduced capacitance of the coupling line decreases, but at the same time the

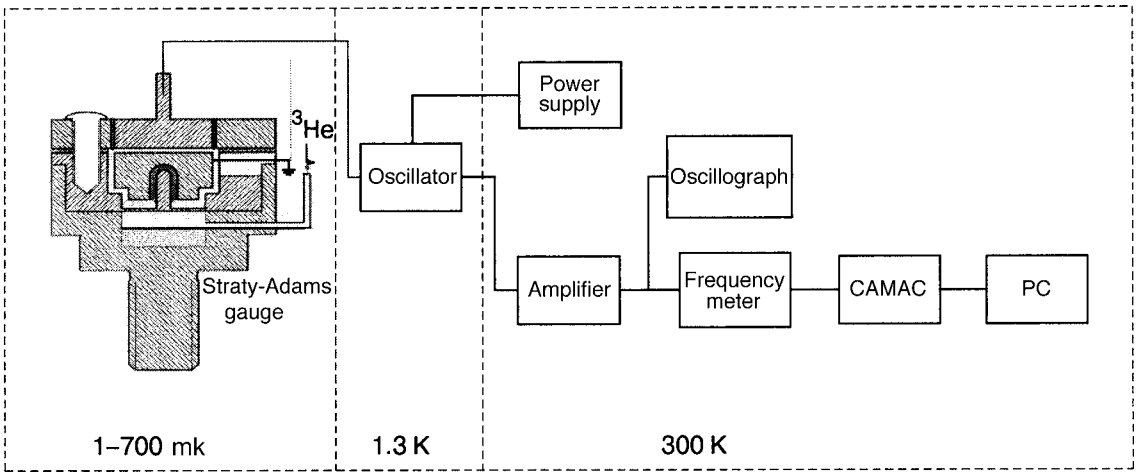

FIG. 1. Block diagram of the measuring system.

signal/noise ratio at the entrance of the active part decreases and, in consequence, the actual frequency stability becomes worse at the output of the oscillator.

For this reason the active part of the circuit, just as the resonance circuit, must be kept at low temperatures.

The experiments which have been performed have shown that all low-temperature components of the circuit cannot be placed in an open bath with liquid helium, whose temperature is 4.2 K, since bubbles of boiling helium strongly decrease the frequency stability of the apparatus, probably because of the "microphone effect" and because of the difference of the permittivities of helium gas and helium liquid. To avoid this all low-temperature components should be placed in the vacuum jacket of the refrigerator.

The following requirement is also due to the fact that the frequency generated must be highly stable. Our experiments with low-temperature tunnel-diode oscillators have shown that the instability (long- and short-time) of the frequency generated is determined primarily by the instability of the voltage of the power supply and is due to the steep slope and nonlinearity of the current-voltage characteristic of the tunnel diode at the working point. Inversed tunnel diodes, made of AI402 gallium arsenide, exhibited better stability ($\sim 3 \cdot 10^{-6}$).[7] Their current-voltage characteristic at liquid-helium temperatures at the working point is quite flat and nearly linear. The small improvements of the oscillator scheme[7] and the power supply and an increase of the generation frequency subsequently made it possible to increase the short-time frequency stability of the oscillator several-fold. Other experiments with low-temperature oscillators using domestically produced KP-350 field-effect transistors have shown that their frequency stability can be higher than that of the tunnel-diode oscillators. Moreover, field-effect transistors are much less demanding with respect to the stability of the supply voltage than are inversed tunnel diodes. However, most of these transistors broke down after several coolings.

In the present work a scheme for a harmonic signal generator using a modern NE25118 dual-gate field-effect MESFET transistor[8] is developed and investigated. It is shown that this scheme satisfies the requirements listed above, and at high relative resolution it is more stable than the previously used scheme.[7]

III. GENERAL APPARATUS AND SPECIAL SET-UP FEATURES

Figure 1 shows the general layout of the entire measurement apparatus and the arrangement of its individual components in a dilution refrigerator. The crystallization thermometer itself together with the capacitive pressure gauge are located on the plate of the dilution chamber.

The resonance circuit is mounted on a separate plate. It and the inductance coil placed on the plate of the one-degree bath. The location for the oscillator and, especially, the inductance coil is very important, since to achieve high stability when performing measurements all components of the oscillator (with the exception of the capacitive pressure gauge) must be at constant temperature and have adequate heat removal. The oscillator releases $\sim 3 \cdot 10^4$ W of heat, which is an order of magnitude lower than the cooling capacity of a one-degree bath. At the same time the cooling capacity of the dilution chamber ordinarily does not exceed several tens of microwatts. Thus the most convenient location for the oscillator is on the plate of the one-degree bath of the dilution refrigerator; this bath operates essentially at constant temperature.

The coil is wound on a ceramic framework, which an annealed copper support secures to the plate of the one-degree chamber. A 4 V source powers the oscillator; the stability of the source is no worse than ± 10 μV.

An important feature of including the crystallization thermometer in the LC circuit is that the stationary plate is connected with the inductance coil and the mobile plate is connected to ground. In this case the capacitance between the case and the mobile cover is not introduced into the LC circuit, thereby improving the frequency stability of the oscillator.

A $\sim$0.5 m long coaxial superconducting wire connects the pressure gauge with the oscillator. The wire has thermal contacts at each cooling step.

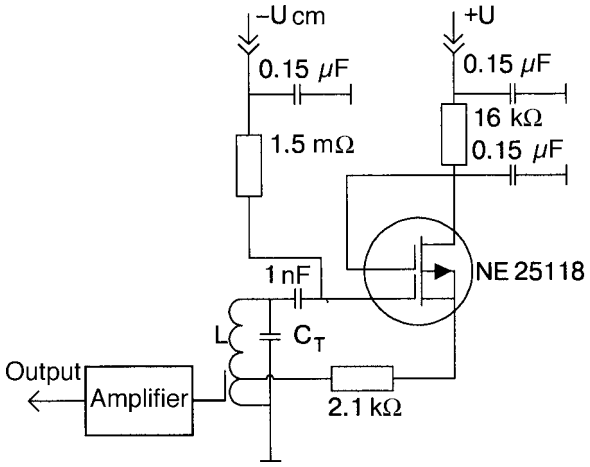

FIG. 2. Electrical circuit of the FET oscillator.

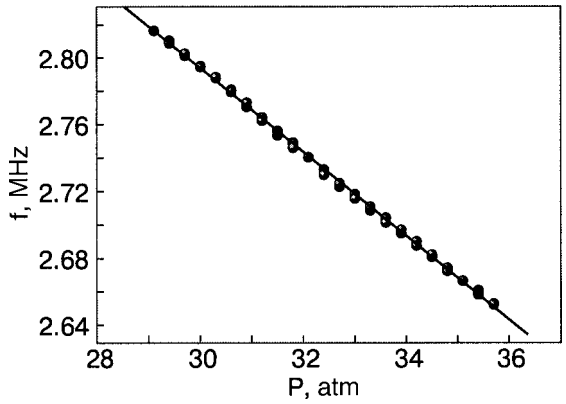

FIG. 3. Calibration curve of the pressure dependence of the frequency of the oscillator. Solid line—least-squares fit of the calibration data.

IV. FET OSCILLATOR

The oscillator is constructed according to a classical inductive three-point scheme (Fig. 2).[9] The measured capacitance of the crystallization thermometer $C_0(T)$ together with the inductance L determine the resonance frequency of the oscillator $f_{res}=1/2\pi(\sqrt{LC_0(T)}$.

A NE25118 dual-gate field-effect transistor was chosen as the active component of the high-frequency harmonic signal generator because this transistor possesses the following important features: regular reproduction of the electric characteristics at each cooldown to helium temperatures; temperature-independent current-voltage characteristic in the range 1–4.2 K; and, low intrinsic noise level.

To measure the capacitance $C_0(T)$ with high accuracy it is necessary to have, first and foremost, a highly stable oscillator, whose stability is in turn determined by the stability of the supply voltage, the intrinsic noise of the transistor, and vibrations. Important factors are a high Q of the circuit and the scheme used to extract the useful signal from the circuit for feeding to the measuring apparatus. The active losses in the circuit must be decreased in order to increase the Q of the coil. As a result of the skin effect the diameter d of the coil wire and the oscillator frequency play an important role. Since as d increases, on the one hand, the losses decrease as $1/d^2$ and, on the other hand, the losses to eddy currents (which are proportional to d) increase, there always exists an optimal diameter d_{opt}, which corresponds to minimum power losses in the coil winding. In addition, the optimal solution is to use a stranded high-frequency wire, which has an extended surface, but the diameter of each of the insulated strands is small.

Our analysis has shown that losses in the winding of a single-layer inductance coil are lowest when the ratio of the winding length to the outer diameter of the coil is 0.7. Ultimately, the circuit built and mounted in the cryostat was wound with LÉSHO 0.07×7 stranded high-frequency wire whose working frequency at room temperature $T=230$ K was 5 MHz.

To achieve the optimal ratio of the Q and the coupling constant k of the transmission line with the resonance circuit $kQ<1$ a coupling loop was placed inside the framework of the circuit coil; the weak oscillator signal from the coupling loop (2–6 mV) flows along a coaxial cable to a low-noise wide-band amplifier (see Fig. 1) with voltage gain 70 dB. The amplifier is assembled using series 235 microcircuits. This made it possible to eliminate almost completely any influence of the load on the frequency stability of the oscillations generated: even with temperatures changing from room to liquid-helium temperatures, when the parameters of the resonance circuit, transistor, and transmission line vary especially strongly, the stability of the oscillator remained essentially unchanged.

The useful signal of the oscillator amplified up to ~100 mV enters a frequency meter. The signal shape and amplitude are monitored with an oscillograph. For further recording and processing, the signal from the digital output of the frequency meter is fed into a CAMAC interface complex and displayed on a computer monitor screen.

V. CALIBRATION OF THE GAUGE

The gauge of the crystallization thermometer was calibrated at temperature ~1.3 K. Under these conditions ^{3}He remains liquid in the entire working pressure range ($P<3.8$ MPa). The dependence of the oscillator frequency on the indications of a standard manometer, which is at room temperature, was recorded. Before the calibration procedure was started the capacitive gauge was "conditioned," which consisted of varying the pressure cyclically (~10 cycles) in the working range. Practice shows that this is necessary in order to remove any possible hysteresis with the increase (decrease) of pressure.

For convenience in further use, the calibration data were described by a polynomial of degree five. A typical plot of the frequency versus pressure is presented in Fig. 3.

Thus, knowing the frequency it is possible to determine uniquely the pressure in the crystallization chamber of a thermometer after the filling capillary is blocked. The temperature of the cold plate of the refrigerator in the range 0.9 mK–1 K can be determined using an equation which relates the melting pressure ^{3}He and the temperature.[10] The use of superconducting reference points[11] in a wide temperature range makes it possible to refine this relationship and eliminate the systematic error in temperature measurements that is associated with the error due to the manometer.

Analyzing the calibration data it is easy to calculate the temperature resolution for this apparatus taking account of the fact that a change in pressure by one atmosphere ($\sim 10^5$ Pa) changes the resonance frequency by $\Delta f = 25$ kHz.

Since the long-time frequency stability of the oscillator at low temperatures is ±1 Hz, the minimum resolvable pressure change is ±4 Pa. This value can be used to estimate the temperature measurement accuracy on any interval of the temperature range as a function of the slope dP/dT of the melting curve of ^{3}He. For example, the resolution at 100 mK ($dP/dT = -2.16$ MPa/K)[10] is 2 μK. This is more than two orders of magnitude better than in conventional measurements of the capacitance of the gauge in a crystallization thermometer performed using E8-4, E7-8, and E7-12 commercial measuring bridges.

The repeated coolings performed down to temperature 1 K showed that the cryogenic oscillator based on a field-effect transistor combined with a capacitive gauge of a crystallization thermometer operates well and gives reproducible results. This method is promising for ultralow-temperature thermometry and for physical investigations involving high-precision measurements of pressure or electrical capacitance at ultralow temperatures.

We thank É. Ya. Rudavskiĭ and V. N. Grigor'ev for their interest in this work.

This work was supported by the Ukrainian Foundation for Fundamental Research 02.07/00391 (project No. F12-7/286-2004).

[a)]E-mail: maidanov@ilt.kharkov.ua

[1]R. L. Rusby, M. Durieux, A. L. Reesink, R. P. Hudson, G. Schuster, H. Kuhne, W. E. Fogle, R. J. Soulen, and E. D. Adams, J. Low Temp. Phys. **126**, 633 (2002).
[2]G. C. Straty and E. D. Adams, Rev. Sci. Instrum. **40**, 1393 (1969).
[3]A. A. Scribner and E. D. Adams, Rev. Sci. Instrum. **41**, 287 (1970).
[4]H. Chester, Rev. Sci. Instrum. **39**, 719 (1968).
[5]J. Janis, Phys. Rev. **170**, 320 (1968).
[6]C. T. Van Degniff, Rev. Sci. Instrum. **46**, 599 (1975).
[7]B. A. Mikheev, G. R. Movsesyan, K. Z. Kabayan, R. T. Mina, V. A. Maĭdanov, N. P. Mikhin, V. K. Chagovets, and G. A. Sheshin, Prib. Tekh. Éksp., No. 1, 226 (1989).
[8]General Purpose Dual-Gate Ga-As MESFET NE25118, Exclusive North American Agent NEC RF, Microwave & Optoelectronic Semiconductors, California Eastern Laboratories, Headquarters, 4590 Patrick Henry Drive, Santa Clara, CA 95054-1817.
[9]V. A. Kotel'nikov and A. N. Nikolaev, *Principles of Radio Engineering*, Gos. izd.-vo literatury po voprosam svyazi radio, Moscow (1950), pp. 57–70.
[10]B. I. Verkin, V. N. Grigor'ev, V. G. Ivantsov, V. A. Koval', É. Ya. Rudavskiĭ, A. A. Golub, and N. M. Zvyagina, *Handbook of Methods for Obtaining and Measuring Low and Ultralow Temperatures*, Naukova dumka, Kiev (1987).
[11]S. Schottl, R. Rushby, H. Godfrin, M. Meschke, V. Goudon, S. Triqueneaux, A. Peruzzi, M. de Groot, R. Jochemsen, W. Bisch, Y. Hermier, L. Pitre, C. Rives, B. Fellmuth, and J. Engert, J. Low Temp. Phys. **138**, 941 (2002).

Translated by M. E. Alferieff